Die Suche nach den Higgs Teilchen bei LEP2

[The search for Higgs particles at LEP 2]

HABILITATIONSSCHRIFT

vorgelegt an der
Naturwissenschaftlichen Fakultät
der
Leopold–Franzens–Universität Innsbruck

eingereicht von
Mag. Dr. Emmerich KNERINGER

Innsbruck, im September 2003

Contents

List of Figures

List of Tables

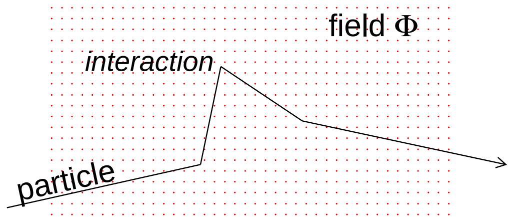

What is the origin of mass?

Chapter 1

Introduction

1.1 Motivation

This *Habilitationsschrift* is about the search for Higgs bosons, as predicted by various theoretical models, which try to explain the origin of mass. In this section I want to give some arguments why the search for Higgs bosons is one of the most important subjects of present experimental as well as theoretical particle physics.

In the standard model of elementary particle physics the Higgs particle naturally arises as a result of spontaneous symmetry breaking, which allows to give masses to particles in a gauge invariant way. This is what is generally understood by the term Higgs mechanism. While symmetry breaking is an experimental fact in the context of the standard model (given through the existence of massive particles), the mechanism which causes the symmetry breaking is still speculation. The Higgs mechanism is one possibility and convincing alternative models do not yet exist. The discovery of the Higgs boson would be the ultimate triumph of the standard model. However, since this could also mean the end of interesting new discoveries in high energy physics, many people would be excited, if no Higgs boson is found in the mass range up to 1 TeV/c^2 (see below). Therefore excluding the existence of the Higgs boson in certain mass ranges is also important.

From a more mathematical point of view theorists do not like a light Higgs boson (with a mass of the order of the electroweak scale). To make this look more natural they have constructed the elaborate edifice of the supersymmetric standard model in which all observed particles have (yet) unobserved superpartners. This model predicts one Higgs boson to have a mass below ~ 130 GeV/c^2. Therefore, excluding the existence of Higgs bosons in this mass range would signify the collapse of this model.

Clearly, experimental input is needed to guide the development of theoretical models. This is the main motivation for building the LHC. Moreover, the so-called *no-lose* theorem (*cf.* Sec. 2.5) says that if no Higgs boson is found in the mass range up to

1 TeV/c^2, then the standard model is not correct and new physics processes are expected in the TeV energy range — which LHC is able to cover with its centre-of-mass energy of 14 TeV.

1.2 Overview

This section shortly describes to contents of the individual chapters. The basics of the working of this Higgs mechanism, where particles aquire mass through the interaction with a scalar field Φ pervading the vacuum, are detailed in Chapter 2 (*cf.* the illustration in the upper right corner of the previous page).

Chapter 3 is devoted to a phenomenological description of the production and decay modes of the standard model Higgs boson, which is the basis for an experimental search for the Higgs particle. This chapter also contains the first paper to which I contributed, entitled "Search for the Standard Model Higgs boson in e^+e^- collisions at $\sqrt{s} = 161, 170$ and 172 GeV." This was just the beginning of the search for Higgs bosons at LEP2. It was planned to increase the centre-of-mass energy of the LEP collider each year, as more and more superconducting cavities were available to replace to conventional ones. The paper describing the analyses of the data taken at $\sqrt{s} = 183$ GeV finishes this chapter.

An overview over the whole LEP2 period — concerning the collider, the various centre-of-mass energies, the amount of data collected with the ALEPH detector and the question on the ultimate energy achievable at LEP2 — are presented at the beginning of Chapter 4. This is followed by a more general description of the physics of the ALEPH detector relevant for the Higgs search analyses.

Chapter 5 introduces extensions to the standard model. First it discusses general two Higgs doublet models (2HDM), then it specializes to the minimal supersymmetric standard model (MSSM). This is followed by the presentation of the paper "Search for the neutral Higgs bosons of the MSSM in e^+e^- collisions at $\sqrt{s}$ from 130 to 172 GeV." The next paper summarizes the results of all ALEPH Higgs boson searches obtained from data taken at the LEP collider up to a centre-of-mass energy of 189 GeV. Besides new results on the mass bounds of the neutral Higgs bosons of the standard model and the MSSM, it includes results on the searches for charged Higgs bosons and an invisibly decaying Higgs boson.

As the energy of the LEP collider was increased during the years it became more and more important to combine the results of the individual LEP experiments. Therefore a (to become) standard procedure had to be found which ideally was expected to have the best discovery and exclusion potential for particle searches. Chapter 6 is devoted to explaining the statistical method that was finally used at LEP.

Complementary to the direct search for the standard model Higgs boson an indirect method based on a fit of the standard model parameters to precision electroweak data exists. The physics input to this method is discussed in Chapter 7.

The final Chapter 8 gives an outlook of what can be expected in this field of research in the short term future.

In Appendix A a graphical display of a Higgs boson candidate event as seen with the ALEPH detector is presented. Appendix B contains an amusing explanation of the Higgs mechanism for the layman.

1.3 Final results at the end of LEP2

Though an excess of events compatible with the production of a standard model Higgs boson is found in the data of the last year of LEP running, this is not sufficient to claim a discovery. As the LEP collider has to give way to the new LHC machine, future experiments have to answer the question on the existence of the Higgs boson.

Table 1.1 displays the final ALEPH and combined LEP results for the 95% confidence level lower limits on the masses of Higgs bosons as obtained in the context of various models. For the MSSM also the excluded range for the parameter $\tan\beta$ is given (for details see Chapter 5). It is interesting to note that the LEP combined exclusion limit on the mass of the standard model Higgs boson ($m_{\mathrm{H}} > 114.4$ GeV/c^2) is very close to the kinematic limit[1] $E - m_{\mathrm{Z}} = 206.7 - 91.2 = 115.5$ GeV/c^2 for Higgs production, which is an indiction that the search analyses have really been pushed to their limits.

Higgs boson	model	ALEPH limit (GeV/c^2)	LEP limit (GeV/c^2)
H	standard model	111.5	114.4
h	MSSM	89.8	91.0
A	MSSM	90.1	91.9
$\mathrm{H}^{\pm}$	2HDM	79.3	
invisible	2HDM	114.1	
fermiophobic	2HDM	105.4	109.7
	MSSM	$0.7 < \tan\beta < 2.3$	$0.5 < \tan\beta < 2.4$

Table 1.1: Final 95% confidence level lower limits on the Higgs boson masses from direct searches with the ALEPH detector. The corresponding limits from the combination of the results of the four LEP collaborations are also shown. The limit quoted for the invisible Higgs is for the standard model cross section and 100% branching ratio to invisible decays. Fermiophobic Higgs bosons are the physical states of the Higgs sector in 2HDM of type I with couplings only to gauge bosons, *e.g.* $\mathrm{h} \to \gamma\gamma$ via $\mathrm{W}^+\mathrm{W}^-$ loops.

[1] For the energy the highest value where still a substantial amount of data has been collected is inserted (see Table 4.2).

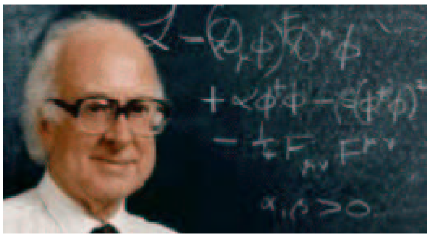

Peter Higgs

Chapter 2

The Standard Model

2.1 History

The first theory of the weak interaction (in nuclear β-decay) was the Fermi model [1], which described β-decay as an effective four-fermion interaction. However, it turned out that high energy behavior of this theory was not well defined, *i.e.* the S-matrix was not unitary. This was reminiscent of the ultraviolet catastrophe of the classical theory of blackbody radiation. While the ultraviolet catastrophe went away by quantizing the energy spectrum of the radiation, the S-matrix problem was tackled by introducing massive vector bosons W and Z (see, for example, [2]). Further problems arose when higher order corrections were calculated in this improved Fermi model. The results turned out to be infinite. In quantum electrodynamics (QED) this problem had already been solved by the so-called renormalization procedure. A theory is called renormalizable if all infinities that occur in calculations (mainly of higher order processes) can be absorbed in a finite number of constants [1] in each order of perturbation theory. In other words, renormalizability of a field theory is important if the theory should make sense beyond the Born level. QED was already known to be renormalizable since the end of the 1940's. By introducing the massive exchange particles, a theory with a similar structure as QED was obtained, because in the high energy limit the exchanged bosons can be regarded as being massless — like the photon. However, a detailed analysis showed that the intermediate vector boson theory of the weak interaction was not renormalizable. For example [3], the amplitude of inelastic $2 \to 2$ scattering processes violates unitarity at high energies through contributions from longitudinally polarized vector bosons.

The reason for QED to be renormalizable was known to be its gauge invariance. A consequence of the gauge symmetry is the masslessness of the gauge particles. On

[1] These constants are the parameters in the Lagrangian or associated with the fields, but also certain operators need a renormalization constant.

the other hand massive gauge particles (W,Z) were needed to explain the short range of the weak interaction. Therefore, if the weak interaction was to be described by a gauge theory the gauge symmetry had to be broken. Explicitly breaking the symmetry via mass terms in the Lagrangian of a field theory destroys the renormalizability of the theory. At the time (around 1960) another way of breaking the symmetry was found by J. Goldstone, which came to be known under the term "spontaneous symmetry breaking", described in detail in Section 2.3. It was also found that in a field theory with a spontaneously broken symmetry at least one massless spin 0 field must exist. The particle associated with such a field is called a Goldstone boson. Since no massless scalar particles were known at the time (the pion was and still is the spin 0 particle with the lowest mass – more than 200 times heavier than the electron) gauge theories with spontaneous symmetry breaking were not paid much attention.

It was only after the discovery of the so-called Higgs mechanism [4] that theorists [2] seriously tried to describe the electroweak interaction by models with a spontaneously broken symmetry. The Higgs mechanism elegantly got rid of massless scalar particles by putting these degrees of freedom into the longitudinal polarization states of the massive gauge bosons, but it generated also at least one massive scalar particle, hereafter called Higgs boson. One of the proposed models was the Glashow-Salam-Weinberg (GSW) theory for leptons [5]. This unified theory of electromagnetic and weak interactions became very popular when t'Hooft [6] demonstrated that spontaneously broken gauge theories are renormalizable. Moreover, the Renormalizability of such theories requires the existence of the Higgs boson. Referring to the above mentioned example of the inelastic scattering process, it is found that with the addition of Feynman diagrams with a Higgs boson the whole process is well behaved in the high energy limit.

After one of the predictions of the GSW theory, namely the existence of the weak neutral current, had been verified by experiment (CERN, 1973), the three physicists Glashow, Salam and Weinberg were awarded the nobel prize in 1979 "for their contributions to the theory of the unified weak and electromagnetic interaction between elementary particles." This was 4 years before direct evidence for the existence of the intermediate vector bosons $W^{\pm}$ and Z was found by the UA1 and UA2 collaborations at the SPS proton-antiproton collider at CERN.

Together with quantum chromodynamics the GSW theory, extended to the hadronic sector, forms today's standard model of elementary particle physics.

[2]Higgs and Kibble extended the work of Goldstone to gauge theories. However, as mentioned in the nobel lecture of S. Glashow, "these workers never thought to apply their work on formal field theory to a phenomenologically relevant model."

2.2 The standard model is a gauge theory

At present, the standard model of elementary particle theory describes three of the four known forces of nature (electromagnetism, weak and strong interaction, but not gravitation). It is based on quantum fields that are generalizations of Yang-Mills [7] gauge fields. Yang-Mills theories are based on the principle of local gauge symmetry, that is, a symmetry believed to be present in a physical system is already built into the Lagrangian density [3] of the system.

The electroweak part of the standard model is based on the gauge group $SU(2)_L \times U(1)_Y$, which consists of two independent sets of gauge transformations with gauge couplings g and g'. $U(1)_Y$ is the gauge group of the weak hypercharge, and $SU(2)_L$ is the gauge group of the weak isospin, where the index L reminds one that only the left handed fields participate in the weak interaction ("parity violation").

The gauge fields associated with the gauge groups are identified with the mediators of the interactions between matter particles. These objects are called gauge bosons and in order not to violate gauge invariance they should all be massless — in contradiction to what is required by the experiment. The way massive gauge bosons can be introduced into a gauge theory without spoiling the gauge symmetry will be explained in the next section for the simple case of the U(1) gauge group [4]. This can then be easily extended to the SU(2) × U(1) group.

2.3 The Higgs mechanism

Let $\phi(x) = (\phi_1(x) + i\phi_2(x))/\sqrt{2}$ be a complex scalar field and $A_\mu(x)$ be the massless gauge field of the U(1) gauge group, where x denotes the 4-dimensional space-time coordinates. The Lagrangian of the theory is taken to be [5]

$$\mathcal{L} = (D_\mu\phi)^*(D^\mu\phi) - V(|\phi|) - \frac{1}{4}F_{\mu\nu}F^{\mu\nu}, \tag{2.1}$$

where $F_{\mu\nu} = \partial_\mu A_\nu - \partial_\nu A_\mu$ is the antisymmetric tensor of the gauge field and $D_\mu = \partial_\mu - igA_\mu$ is the covariant derivative that ensures invariance of the Lagrangian under the local gauge transformation

$$\begin{aligned} \phi &\rightarrow \phi' = e^{ig\chi(x)}\phi \\ A_\mu &\rightarrow A'_\mu = A_\mu - \partial_\mu\chi(x) \ . \end{aligned} \tag{2.2}$$

An explicit mass term of the form $m^2/2 \cdot A_\mu A^\mu$, on the other hand, would break local gauge invariance and is therefore not allowed in $\mathcal{L}$. The potential V in (2.1) has the

[3] The Lagrangian density is the starting point of any field theory containing a symmetry.

[4] The non-Abelian nature of the gauge group of the electroweak theory is not relevant for the working of the Higgs mechanism.

[5] The dependence of the fields on x in only shown the first time, *i.e.* when the field is introduced.

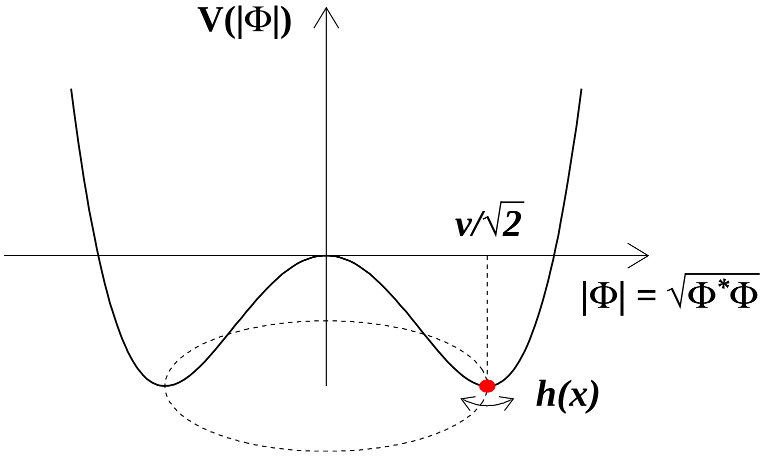

Figure 2.1: A graphical illustration of the so-called Higgs potential. For a complex scalar field ϕ there exist an infinite number of minima of the potential V, as indicated by the dashed ellipse. The real field $h(x)$ can be interpreted as an excitation of ϕ around the value at its minimum.

form

$$V(|\phi|) = -\mu^2(\phi^*\phi) + \lambda(\phi^*\phi)^2, \tag{2.3}$$

where the parameters μ^2 and λ are chosen to be positive (this choice results in the potential to have the form shown in Fig. 2.1). To find the ground state of the field ϕ one has to calculate the minimum of the potential. The absolute value of ϕ at the minimum is $|\phi| = \sqrt{\mu^2/2\lambda} =: v/\sqrt{2}$. The constant $v/\sqrt{2}$ is called the vacuum expectation value of the field ϕ. Since ϕ is complex the ground state is degenerate and the set of minima is described by $\phi_1^2 + \phi_2^2 = v^2$. One of these possible ground states has to be selected as the true ground state (usually called the vacuum) of the theory. Without loss of generality it will be taken as the real field $\phi_{\text{g.s.}} := v/\sqrt{2}$. Whereas the Lagrangian of the theory is invariant under the gauge transformation, the ground state is not [6]. This is commonly referred to as *spontaneous symmetry breaking* [7].

In the next step the fields are investigated in the vicinity of the ground state. Let the field ϕ be expanded as follows:

$$\phi(x) = \phi_{\text{g.s.}} + \frac{1}{\sqrt{2}}[h(x) + i\xi(x)]. \tag{2.4}$$

When this is substituted into (2.1) one obtains the following expression

$$\mathcal{L} = \frac{1}{2}(\partial_\mu - igA_\mu)(v + h - i\xi)(\partial^\mu + igA^\mu)(v + h + i\xi) - V(h, \xi) - \frac{1}{4}F_{\mu\nu}F^{\mu\nu}, \tag{2.5}$$

[6] Through a U(1) transformation the vacuum can end up anywhere on the circle of Fig. 2.1.

[7] The term spontaneous symmetry breaking was first used by Baker and Glashow in [8].

with the potential

$$V(h, \xi) = \frac{\mu^2}{2} \left[(v + h)^2 + \xi^2 \right] - \frac{\lambda}{4} \left[(v + h)^2 + \xi^2 \right]^2 . \tag{2.6}$$

The masses of the field quanta ($m^2/2$, to be precise) are given by the coefficients in front of the quadratic terms of the fields. The first term on the right hand side of (2.5) contains the expression $g^2 v^2/2 \cdot A_\mu A^\mu$, which can be interpreted as a massive gauge boson with mass

$$m_A = gv. \tag{2.7}$$

To second order in the fields (2.6) can be written as $V^{(2)} = \text{const} + 2\lambda v^2/2 \cdot h^2$, which yields a scalar boson with mass

$$m_h = \sqrt{2\lambda} v. \tag{2.8}$$

Since all terms proportional to ξ^2 cancel this scalar particle is massless. To summarize: for a simple parabolic potential $V = \mu^2 \phi^* \phi$ in (2.1) the theory contains two massive scalar particles ϕ_1 and ϕ_2 and a massless gauge boson A. If the potential is deformed (by whatever mechanism) to the form shown in Fig. 2.1 the mass of one of the scalar particles shifts to the gauge boson. This is generalized in the *Goldstone theorem* [9, 10] which states that for each spontaneously broken dimension of the gauge symmetry group there exists a massless scalar field, called a Goldstone boson.

Whereas the h field, called Higgs field after one of its inventors, is a real field and should be observable in experiments, the ξ field (and the Goldstone bosons in general) can be eliminated from the Lagrangian by a special gauge transformation [12]. In other words, the Goldstone bosons are unphysical states corresponding to the gauge freedom of the theory.

This section will be concluded by listing some important properties of the dynamical Higgs field (not to be mixed up with the constant field v that pervades space-time) and in the next section it will be discussed how the Higgs mechanism works in the context of the gauge group of the unified electroweak theory.

- The Higgs field cannot be gauged away and should therefore be observable as a physical particle H.
- The mass of the Higgs particle is given through the parameters v and λ. Whereas v is determined by the gauge boson mass and the generalized charge quantum number of the theory, the parameter λ of the Higgs potential is unknown. As a consequence the Higgs boson mass is not predicted by the theory.
- The interaction terms of the Higgs boson with other particles only depend on v which means that the production cross sections and the decay rates are known.
- There are self-interaction terms of the Higgs boson (*e.g.* four h fields with the coupling λ).

- The number of degrees of freedom of the fields is conserved. A massless gauge boson has two degrees of freedom (the transverse polarization states) and a complex scalar field also has two. When the Higgs mechanism comes into action we are left with a massive gauge boson with three polarization states and one real Higgs boson.

2.3.1 The Higgs mechanism for the SU(2) × U(1) gauge group of the GSW model

The first attempts (Schwinger 1958) to unify the weak and the electromagnetic interactions used the SU(2) gauge group. This group was chosen to accommodate the three known gauge bosons, two vector bosons of the charged current of the weak interaction and the photon. At the time parity violation of the weak interaction had already been discovered and things had to be arranged so that the charged current, but not the neutral (electromagnetic) current violated parity. This was not easily possible and it was concluded that a group of larger dimension was needed. Physicists were led to the SU(2) × U(1) group in analogy to the approximate isospin-hypercharge symmetry [8] which characterized the strong interaction. Having one dimension more than the SU(2) group alone this gauge theory predicted another neutral gauge boson, known as the neutral current of the weak interaction. Since all the gauge bosons of the weak interaction had to be massive, in a theory with spontaneous symmetry breaking three dimensions of the symmetry group must be broken, thereby introducing three Goldstone bosons. In the GSW model this is achieved by breaking $\mathrm{SU}(2)_L\times\mathrm{U}(1)_Y$ to $\mathrm{U}(1)_{em}$, where $\mathrm{U}(1)_{em}$ is the gauge group of the electric charge (with the massless photon as gauge boson). To obtain three Goldstone bosons one has to start out with four degrees of freedom for the scalar fields. The four fields are arranged as an SU(2) doublet Φ in the following way:

$$\Phi = \begin{pmatrix} \phi^+ \\ \phi^0 \end{pmatrix} = \frac{1}{\sqrt{2}} \begin{pmatrix} \phi_3 + i\phi_4 \\ \phi_1 + i\phi_2 \end{pmatrix}. \tag{2.9}$$

The superscript of the complex field ϕ^0 denotes that it is neutral, in contrast to ϕ^+, which is charged. The field ϕ^+ must be charged in order to give masses to the charged gauge bosons. Formally the Lagrangian of the theory is similar to (2.1), with the additions of a kinetic energy term for the three SU(2) gauge fields $W^{\mathrm{a}}(x)$ and terms needed because the GSW model includes matter fermions [9] ($\mathcal{L}_{\mathrm{fermion}}$ for the kinetic

[8] The SU(2) × U(1) isospin-hypercharge symmetry group was later extended to local $\mathrm{SU}(3)_{\mathrm{flavor}}$ and then reinterpreted as $\mathrm{SU}(3)_{\mathrm{color}}$.

[9] The original GSW model only described leptons, because the quark model only had been invented three years before. The extension of the GSW model to the hadronic sector was straightforward after more quarks had been discovered and when it became clear that the quarks could also be arranged in weak isospin doublets.

energy and the interaction with the gauge fields and $\mathcal{L}_{\text{Yukawa}}$ for generating masses for the fermions):

$$\begin{aligned}\mathcal{L} &= (D_\mu\Phi)^\dagger(D^\mu\Phi) + \mu^2(\Phi^\dagger\Phi) - \lambda(\Phi^\dagger\Phi)^2 \\ &\quad - \frac{1}{4}B_{\mu\nu}B^{\mu\nu} - \frac{1}{2}\text{tr}(W_{\mu\nu}W^{\mu\nu}) \\ &\quad + \mathcal{L}_{\text{fermion}} + \mathcal{L}_{\text{Yukawa}} \ . \end{aligned} \tag{2.10}$$

This is the full Lagrangian of the electroweak sector of the standard model. Invariance of $\mathcal{L}$ under local SU(2) $\times$ U(1) gauge transformations requires the covariant derivative to have the form

$$D_\mu = \partial_\mu - igT\tau^{\text{a}}W_\mu^{\text{a}} - ig'\frac{Y}{2}B_\mu, \tag{2.11}$$

where τ^{a} (a=1,2,3) are the Pauli matrices and (T,Y) are the weak isospin and hypercharge[10] quantum numbers of the field in question. For doublets $T = 1/2$ and for singlets $T = 0$. The weak hypercharge Y has to be chosen such as to get the electric charges correct for the fields. The electric charge is given by the relation $Q = e(T^3 + Y/2)$, where T^3 is quantum number of the z-component of the weak isospin. Since the Higgs field is neutral and has $T^3 = -1/2$ it follows that $Y = Y_\Phi = 1$. With the definition[11] $W_\mu := W_\mu^{\text{a}}\,\tau^{\text{a}}/2$ the fields $W_{\mu\nu} := W_{\mu\nu}^{\text{a}}\,\tau^{\text{a}}/2$ in (2.10) are given by

$$W_{\mu\nu} = \partial_\mu W_\nu - \partial_\nu W_\mu - ig[W_\mu, W_\nu], \tag{2.12}$$

where the commutator is due to the non-Abelian character of SU(2). Spontaneous symmetry breaking generates a 3-dimensional manifold of minima of the potential V given by

$$\Phi^\dagger\Phi = \frac{1}{2}(\phi_1^2 + \phi_2^2 + \phi_3^2 + \phi_4^2) = \frac{\mu^2}{2\lambda} =: \frac{v^2}{2}. \tag{2.13}$$

The true vacuum is chosen as

$$\Phi_{\text{g.s.}} = \frac{1}{\sqrt{2}}\begin{pmatrix} 0 \\ v \end{pmatrix}, \tag{2.14}$$

i.e. $\phi_1 = v$ and $\phi_2 = \phi_3 = \phi_4 = 0$. Expanding Φ around this particular vacuum,

$$\Phi = \frac{1}{\sqrt{2}}\begin{pmatrix} 0 \\ v + h(x) \end{pmatrix} \tag{2.15}$$

(where the unphysical Goldstone fields have already been gauged away), and inserting this expression into the Lagrangian yields the masses for the Higgs boson and the gauge bosons in the same way as before. Whereas the formula for m_{H} in (2.8) is also valid

[10]In the literature sometimes $\tilde{Y} = Y/2$ is defined as the hypercharge.

[11]The fields W_μ and $W_{\mu\nu}$ are elements of the Lie algebra of SU(2) and the Pauli matrices are a representation of the generators of this Lie algebra.

here, the formula for the mass of the gauge boson is modified by a factor of 2 due to the introduction of the quantum numbers in (2.11). (this is equivalent to a redefinition of the couplings). By inspecting the quadratic term in the W fields one obtains

$$m_{\mathrm{W}} = \frac{gv}{2} \tag{2.16}$$

for the mass of the charged gauge bosons. Together with the relation

$$\frac{G_F}{\sqrt{2}} = \frac{g^2}{8m_{\mathrm{W}}^2}, \tag{2.17}$$

which is obtained when muon decay is calculated in the context of the electroweak theory, (2.16) can be used to calculate the vacuum expectation value from the Fermi constant:

$$v = (\sqrt{2}G_F)^{-1/2} \simeq 246\,\mathrm{GeV}. \tag{2.18}$$

The Lagrangian also contains trilinear hW^+W^- and quadrilinear hhW^+W^- terms that determine the Higgs boson coupling to W boson. The coefficients of these terms are the so-called vertex factors and the results are

$$g_{_{hW^+W^-}} = igm_{\mathrm{W}} = i\frac{2m_{\mathrm{W}}^2}{v} \tag{2.19}$$

and

$$g_{_{hhW^+W^-}} = i\frac{g^2}{4} = i\frac{m_{\mathrm{W}}^2}{v^2}. \tag{2.20}$$

When calculating the masses of the neutral gauge bosons there is a complication because the neutral fields W_μ^3 and B_μ mix. In this case the masses of the observable particles can be found by diagonalizing the mass matrix. As expected, one linear combination of the fields has zero mass (to be identified with the photon) and the orthogonal combination (the neutral Z boson) has a mass given by

$$m_{\mathrm{Z}} = \frac{v}{2}\sqrt{g^2 + g'^2}. \tag{2.21}$$

Only the Z boson couples to the Higgs boson and the vertex factors $g_{_{hZZ}}$ and $g_{_{hhZZ}}$ are obtained by replacing m_{W}^2 with m_{Z}^2 in (2.19) and (2.20). The electroweak mixing angle is calculated to be $\tan\theta_W = g'/g$ and by building the ratio of the gauge boson masses one obtains the important relation

$$\frac{m_{\mathrm{W}}}{m_{\mathrm{Z}}} = \cos\theta_W. \tag{2.22}$$

Since alle quantities in this equation are independently measurable, it serves as an experimental test of the theory. To good precision measurements confirm the above equation, however, it turns out that the right hand side ($\sin^2\theta_W$, to be exact) is renormalization scheme dependent (as well as scale dependent), which makes the comparison more difficult.

Finally the question will be discussed, whether other multiplets than doublets could have been chosen for the scalar field. For this purpose the above result is written in the following form:

$$\rho := \frac{m_{\rm W}}{m_{\rm Z}\cos\theta_W} = 1. \tag{2.23}$$

It turns out [13] that doublets are the only case where $\rho = 1$ (triplets, for example, have $\rho = 1/2$). This is another strong argument which supports the validity of the structure of the GSW model and the Higgs mechanism. In particular, it says that extensions of the standard model only should add doublets, as far as the Higgs sector is concerned.

2.3.2 Mass generation for fermions

A free fermion is described by the Dirac equation $(i\gamma^\mu\partial_\mu - m)\psi = 0$. In QED the mass m was put in by hand but after the discovery of the Higgs mechanism it was natural to try to generate masses for the fermions by using the non-vanishing vacuum expectation value of the scalar field. In the GSW model fermions are embedded as left-handed $\mathrm{SU}(2)_L$ doublets and right-handed singlets, *e.g.* $\Psi_e \equiv \begin{pmatrix} \nu_{e_L} \\ e_L \end{pmatrix}$ and e_R. Each singlet or doublet Θ contributes a term

$$\overline{\Theta}\, i\gamma^\mu D_\mu \Theta \tag{2.24}$$

to $\mathcal{L}_{\rm fermion}$ of (2.10). For D_μ of (2.11) the weak hypercharge has to be chosen correctly, *e.g.* $Y = -1$ for left-handed lepton doublets and $Y = -2$ for right-handed lepton singlets. Explicit mass terms of the form $-m\overline{\psi}\psi$ are not allowed in $\mathcal{L}_{\rm fermion}$ because they break the gauge symmetry [12]. Inspection of the Lagrangian reveals that terms with an even number of SU(2) doublets are gauge invariant. Therefore the following combination, called Yukawa coupling [13], of the scalar doublet Φ with the fermionic doublet Ψ and the corresponding right-handed fermion singlet as well as a coupling constant (everything given for the case of the electron)

$$\mathcal{L}^e_{\rm Yukawa} = -g_e \left(\overline{\Psi}_e \Phi e_R + \overline{e}_R \overline{\Phi} \Psi_e \right), \tag{2.25}$$

is invariant under local SU(2) × U(1) gauge transformations. It will be shown that this expression contains a mass term for fermion e. Thus for each massive fermion a term of this type has to be added to the Lagrangian. With $\overline{\Psi}_e = (\overline{\nu}_{e_L}, \overline{e}_L)$ and (2.15)

[12] With a bit of algebra a mass term of the form $-m_e\overline{e}e$ can be transformed into $-m_e(\overline{e}_L e_R + \overline{e}_R e_L)$. Under an SU(2) transformation the right-handed fields are invariant, but the left-handed fields rotate in SU(2) space, which means that an electron becomes a linear combination of a neutrino and an electron.

[13] This expression is named after Yukawa, because he used a similar term to couple the pion to the nucleon.

one obtains

$$\mathcal{L}^e_{\text{Yukawa}} = -\frac{g_e v}{\sqrt{2}}(\overline{e}_L e_R + \overline{e}_R e_L) - \frac{g_e}{\sqrt{2}}(\overline{e}_L e_R + \overline{e}_R e_L)h(x). \tag{2.26}$$

The coupling constant g_e is chosen such that the fermion mass is given by

$$m_e = \frac{g_e v}{\sqrt{2}}. \tag{2.27}$$

Substituting this into (2.26) and using the identity $\overline{e}_L e_R + \overline{e}_R e_L = \overline{e}e$ the final result is

$$\mathcal{L}^e_{\text{Yukawa}} = -m_e \overline{e}e - \frac{m_e}{v}\overline{e}eh. \tag{2.28}$$

Besides the mass term there is an interaction term $\overline{e}eh$, coupling the Higgs scalar to the fermion with a coupling strength proportional to the mass of the fermion. This is in contrast to the coupling of the Higgs to the gauge bosons, (2.19), which is proportional to the mass squared of the gauge boson. Whereas the usage of the Yukawa coupling allows to introduce massive fermions into the GSW model in a consistent way, it does not predict the masses. It just shifts the ignorance of the mass of a fermion to the ignorance of the strength of the coupling to the Higgs boson. On the other hand, this coupling is proportional to the fermion mass which is a prediction that can be well tested when the Higgs boson is discovered.

With (2.25) a mass can only be generated for the lower member of a doublet. The reason being (2.14), which shows that the vacuum expectation value v also sits at the lower component of the doublet. This is sufficient for lepton doublets (with massless neutrinos), but in order to give a mass to the upper member of a quark doublet a scalar doublet is needed that after spontaneous symmetry breaking is equal to $\frac{1}{\sqrt{2}}\begin{pmatrix} v \\ 0 \end{pmatrix}$. The field $\Phi_c = -i\tau_2\Phi^*$ has this property, and since it transforms identically to Φ it can be used to construct a gauge invariant contribution to the Lagrangian.

Finally it is anticipated how the Higgs mechanism works in the context of a minimal supersymmetric theory (*cf.* the first section of Chapter 5). The added symmetry implies that two $SU(2)_L$ doublets with hypercharge $Y = \pm 1$ are required to give masses to the fermions. Since there are no additional gauge bosons which need masses the four new fields directly show up [14] as two charged and two neutral Higgs bosons, so that there are five Higgs bosons altogether in such a theory.

[14] Actually it is a bit more complicated because the fields of the two doublets mix.

2.4 Parameters and particles

For the case of massless neutrinos the standard model has 18 independent parameters: 3 gauge couplings for the 3 interactions (e, g, g_S, or an equivalent set: α, $\sin^2\theta_W$, α_S), 2 parameters in the Higgs sector (μ^2, λ; or $m_{\rm H}$, v) and 13 parameters in the flavor sector (6 quark masses, 3 lepton masses and 4 parameters from the CKM-matrix: 3 angles and one phase). All but one parameter, namely the mass $m_{\rm H}$ of the Higgs boson, have been measured in experiments. For the values of the parameters see Ref. [15]. The particle content of the standard model is displayed in Figure 2.2. Precise measurements

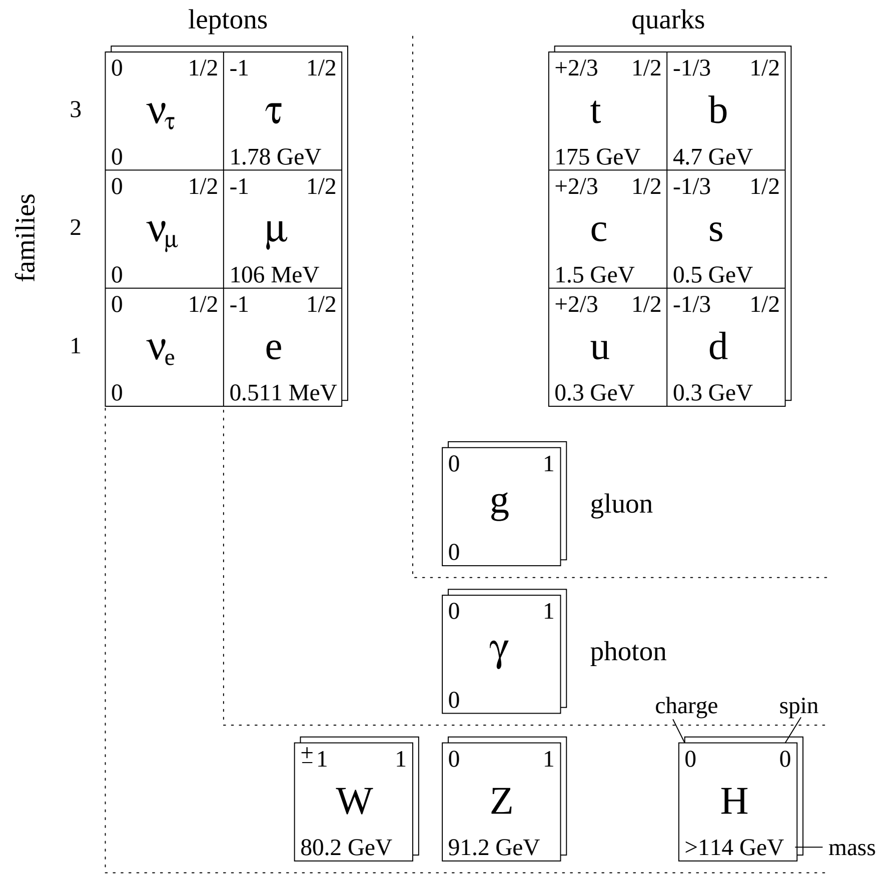

Figure 2.2: This chart shows the particles of the standard model. The matter particles consist of three families of fermions (quarks and leptons). The gauge particles are arranged such as to show the hierarchy of interactions (by means of the dotted lines): eight gluons, differing in the color quantum numbers, mediate the strong interaction and couple only to quarks; the photon is responsible for the electromagnetic interaction and couples to quarks and charged leptons; the W and Z particles mediate the weak interaction and couple to all fermions. Bosons of the same row also couple among themselves and the charged W's couple to the photon in addition. By definition the Higgs particle (shown in the lower right corner) couples directly only to particles which have a nonzero mass.

of electroweak observables (*cf.* Chapter 7) are used to check the validity of the standard model and to constrain its parameters, especially the mass of the Higgs boson, which is contained in the electroweak observables through loop corrections. Since it is the logarithm of the Higgs mass which enters the corrections (see Eq. 7.7), the constraint is rather weak.

The standard model makes no prediction for the mass m_{H} of the Higgs boson. In Section 2.5 it is shown that upper and lower limits for m_{H} as a function of the energy scale Λ up to which the standard model should be valid follow from theoretical principles (validity of perturbation theory and stability of the effective potential).

2.5 Mass bounds

It should be pointed out that the standard model is neither final nor fundamental, but it is commonly viewed as an "effective" scale-dependent theory, which is valid up to some energy scale $\Lambda < \Lambda_{\mathrm{Planck}}$, where $\Lambda_{\mathrm{Planck}} = 10^{19}$ GeV is the energy scale when gravitation can no longer be neglected in quantum theories. Since the standard model does not include gravitation at all it cannot describe the physics processes at the Planck scale, or equivalently, the time up to 10^{-43} s after the big bang. However, the breakdown of the standard model can already occur at some lower scale, defined as Λ. In the following a relation between Λ and the upper bound on m_{H} will be derived from theoretical considerations.

In the same way as the running of the gauge couplings of the standard model is determined by renormalization group equations (RGE), this is also true for the quartic coupling λ of the Higgs potential (2.3), which is responsible for the self-coupling of the Higgs field. The evolution of λ with the energy scale Q^2 (starting from a fixed scale Q_0^2) is determined by the RGE [13]

$$\frac{\mathrm{d}\lambda}{\mathrm{d}t} = \frac{1}{16\pi^2}(12\lambda^2 + 6\lambda g_t^2 - 3g_t^4) + \text{electroweak corr.}, \tag{2.29}$$

where $t = \ln Q^2/Q_0^2$ and g_t is the top quark Yukawa coupling constant defined according to (2.27), which accidentally gives $g_t \simeq 1$. First (2.29) is investigated in the limit of large λ, where λ is expected to increase[15] with Q^2. Neglecting everything but the leading term (which is equivalent to the pure ϕ^4 theory) gives

$$\frac{\mathrm{d}\lambda}{\lambda^2} = \frac{3}{4\pi^2}\,\mathrm{d}(\ln Q^2). \tag{2.30}$$

Integrating between the scales v and Q yields

$$\frac{1}{\lambda(v)} - \frac{1}{\lambda(Q)} = \frac{3}{4\pi^2}\,\ln\frac{Q^2}{v^2}. \tag{2.31}$$

[15] This is in contrast to QCD, where the coupling α_S decreases with increasing Q^2 as a result of a minus sign in front of the first term of the RGE.

When the scale Λ is introduced, where λ diverges, *i.e.* $\lambda(\Lambda) \to \infty$ (called the Landau pole), the following result is obtained:

$$\lambda(v) = \frac{2\pi^2}{3}\left(\ln\frac{\Lambda}{v}\right)^{-1}. \tag{2.32}$$

This equation relates the coupling λ at the electroweak scale v to the scale Λ beyond which the electroweak theory is no longer applicable (in the perturbative sense). It is usually understood, that Λ is the scale of "new physics", because the self-coupling of the Higgs becomes so large when approaching the scale Λ that new physics phenomena are unavoidable. Equation (2.32) implies that for all scales $\Lambda' > \Lambda$ one has $\lambda'(v) < \lambda(v) =: \lambda_\Lambda^{\max}$. Therefore $\lambda_\Lambda^{\max}$ is the maximum value allowed for the quartic coupling if the standard model should be perturbatively valid at least up to Λ (*cf.* Fig. 2.3a).

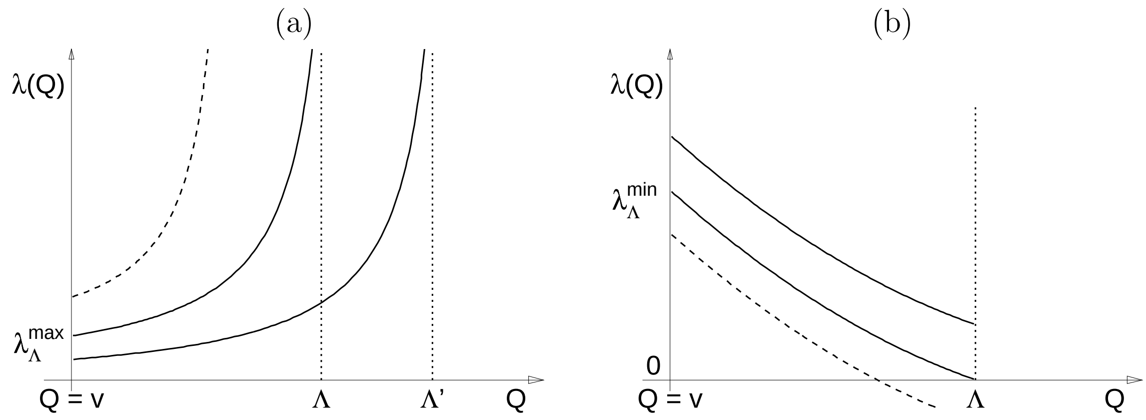

Figure 2.3: Graphical illustration of the theoretical considerations on the evolution of the quartic coupling leading to the mass bounds of the standard model Higgs boson as a function of the energy scale Λ where λ (a) diverges (b) becomes negative.

Through (2.8) this can be directly translated into an upper bound on the Higgs boson mass:

$$m_{\mathrm{H}}^{\max}(\Lambda) = \frac{2\pi v}{\sqrt{3}}\left(\ln\frac{\Lambda}{v}\right)^{-1/2}. \tag{2.33}$$

An absolute upper bound of m_{H} independent of Λ can be derived from the scenario where m_{H} itself approaches Λ. For $m_{\mathrm{H}} > \Lambda$ new physics would appear before the Higgs boson can manifest itself. This is in contradiction to the assumption. Setting $m_{\mathrm{H}}^{\max}(\Lambda) = \Lambda$ in (2.33) on obtains $m_{\mathrm{H}}^{\max} = 815$ GeV, where the value should be regarded as a rough estimate. As shown in Figure 3.5b for $m_{\mathrm{H}} = 1000$ GeV the width is $\Gamma_{\mathrm{H}} \simeq 600$ GeV, and it becomes experimentally very difficult (if not impossible) to separate the Higgs resonance pole from the continuum of VV finale states (V=W,Z).

The result on $m_{\mathrm{H}}^{\max}(\Lambda)$ from a calculation including higher orders [16] is shown in Figure 2.4, together with bounds from direct (*cf.* Sec. 6.1.5) and indirect (see Sec. 7.3) searches and a lower bound from considerations of vacuum stability [17]. For the vacuum to be stable the Higgs potential is required to have an absolute minimum. This is fulfilled if $\lambda > 0$. But looking at (2.29) in the case of small λ one can see that the top Yukawa coupling drives λ to negative values, thereby destabilizing the vacuum. While λ was not allowed to diverge before the scale Λ is reached, here λ is not allowed to be negative up to the scale Λ.

The stability bound on m_{H} is defined (for a given value of the top quark mass) as the lowest value of $\lambda(v)$ (called $\lambda_\Lambda^{\mathrm{min}}$) for which $\lambda(\Lambda) \geq 0$ for any value of Q below the scale Λ. For a graphical illustration of this definition see Fig. 2.3b. Again the lower bound on m_{H} is obtained through $m_{\mathrm{H}}^{\mathrm{min}}(\Lambda) = \sqrt{2\lambda_\Lambda^{\mathrm{min}}}\, v$. For $m_{\mathrm{t}} = 175$ GeV and $\alpha_S = 0.118$ the absolute lower bound is $m_{\mathrm{H}}^{\mathrm{min}} = 52$ GeV/c^2.

Present 95% confidence limit bounds from direct and indirect searches for the Higgs boson are fully compatible with the possibility that the standard model is valid up to the Planck scale — as can be nicely seen in Figure 2.4. While the theoretical upper bound is irrelevant for LEP energies the lower theoretical bound would give a hint for new physics at $\Lambda \simeq 100$ TeV if $m_{\mathrm{H}} \simeq 115$ GeV/c^2.

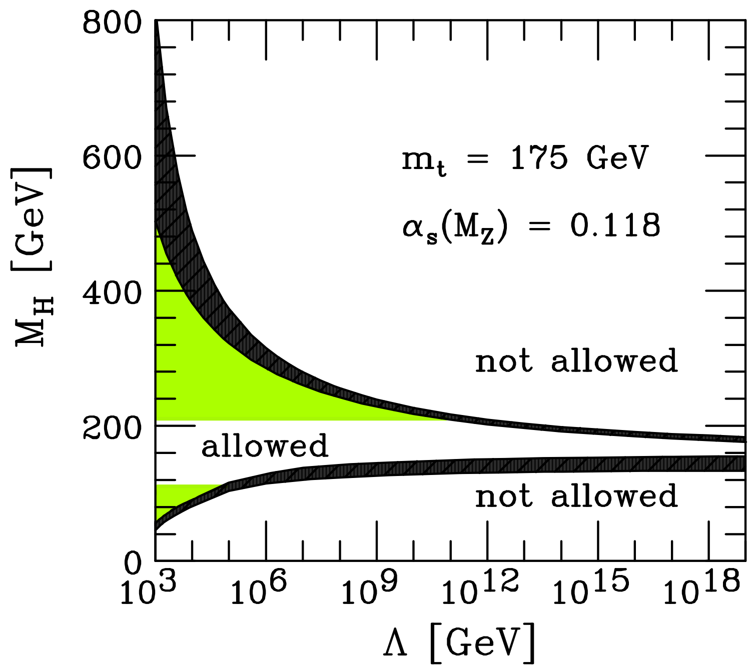

Figure 2.4: Bounds on the standard model Higgs boson mass as a function of the scale Λ of new physics for perturbativity (upper curved band) and vacuum stability (lower curved band) considerations. The width of the bands is an estimate of the theoretical uncertainties. The region in between is theoretically allowed, but part of it is experimentally excluded (upper and lower light shaded areas) by electroweak precision measurements and direct searches. For 130 GeV/$c^2 \lesssim m_{\mathrm{H}} \lesssim 180$ GeV/c^2 no new physics is needed up to the Planck scale.

Chapter 3

The Search for the Standard Model Higgs Boson at LEP2

Following the review of electroweak theory in Chapter 2, this chapter presents some of the basic physics behind the experimental search for the Higgs boson at the LEP collider. The cross section plot below gives an idea of the relative number of background and signal events expected. Not all background processes are listed.

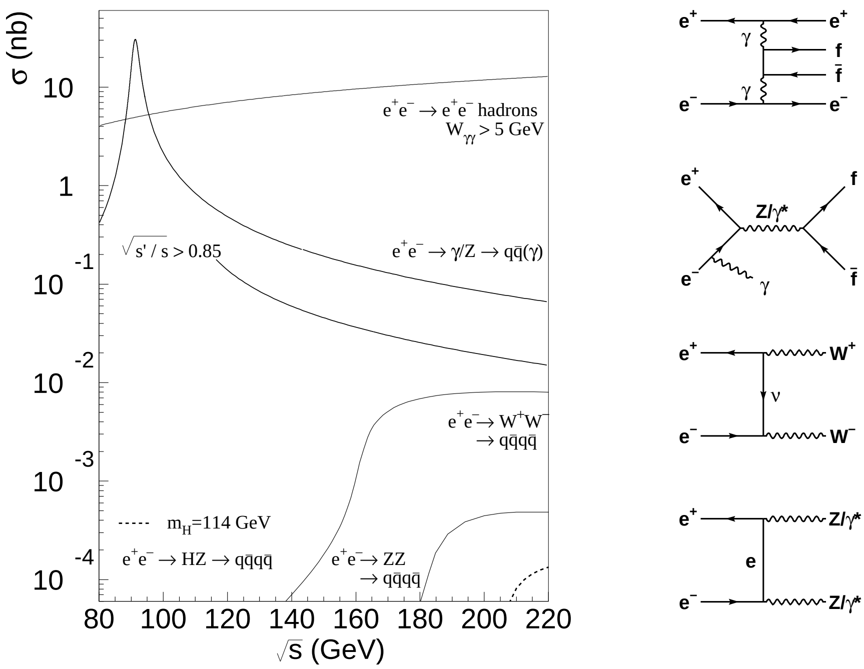

Figure 3.1: Cross sections (for the quark final states) of various processes in e^+e^- annihilation as a function of (LEP) energy. On the right side the corresponding Feynman diagrams are displayed. The cross section for the Higgs-strahlung process (diagram on the next page) with $m_H = 114$ GeV/c^2 is the dashed curve in the lower right corner. Here and in the following plots for the mass of the standard model Higgs boson a value of 114 GeV/c^2 is used which corresponds approximately to the present lower limit from searches at LEP.

3.1 Production processes in e^+e^- annihilation

As explained in Sec. 2.3 the couplings of the Higgs boson to fermions and gauge bosons are known. The only unknown parameter in the production cross sections and decay rates of the Higgs boson is the mass $m_{\rm H}$. The Feynman diagrams for the Higgs boson production processes relevant at LEP2, called Higgs-strahlung and gauge boson fusion, are shown in Figure 3.2a-c. For comparison, Figures 3.2d represents a typical production process at a $p\overline{p}$ collider.

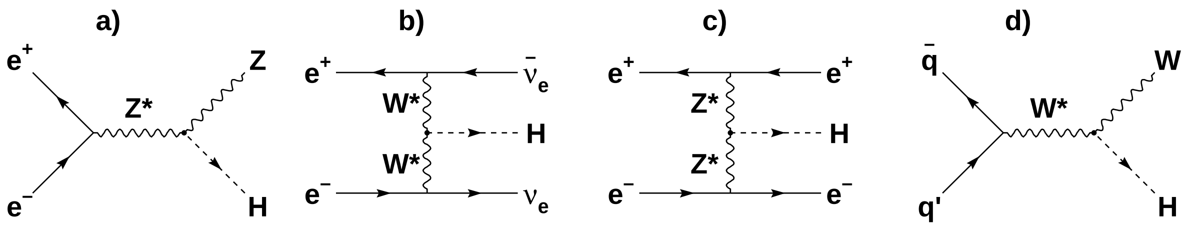

Figure 3.2: Feynman diagrams for a) the Higgs–strahlung process, b) WW fusion and c) ZZ fusion in e^+e^- collisions and d) HW production in $p\overline{p}$ collisions.

3.1.1 Higgs-strahlung

The cross section for Higgs-strahlung in e^+e^- annihilation can be written in compact form as [18]

$$\sigma(e^+e^-\to HZ) = \frac{g^4\,(v_e^2 + a_e^2)}{32^2\,3\pi\cos^4\theta_W}\,\frac{\beta}{s}\,\frac{\beta^2 + 12m_Z^2/s}{(1-m_Z^2/s)^2}\,, \tag{3.1}$$

where $v_e = -1 + 4\sin^2\theta_W$ and $a_e = -1$ are the vector and axial-vector electroweak couplings of the Z to the electron, s is the centre-of-mass energy squared and $\beta = [1-(m_H+m_Z)^2/s][1-(m_H-m_Z)^2/s]$ is the usual two-particle phase-space factor (normalized to 1 for massless decay products).

This formula is only valid in lowest order and for $\sqrt{s} \geq m_H + m_Z$. Moreover, it does not include the width of the Z boson. Higher order corrections have been calculated and are implemented in the event generator HZHA [23], which is also used for cross section calculations. The effects of higher order corrections to (3.1) are displayed in Figure 3.3. While photon radiation gives the largest correction to the cross section (*cf.* the 30% reduction of $\sigma(e^+e^-\to f\overline{f})$ at the Z peak due to initial state radiation), the genuine electroweak corrections are small at LEP energies (less than 1.5% [20]). Figure 3.3 also shows one of the main characteristics of the Higgs-strahlung process at LEP2 energies, namely its threshold behavior. Whereas the threshold is sharp in (3.1), the width of the Z boson ($\Gamma_Z \simeq 2.5$ GeV) allows for the cross section to be non-zero below the threshold, *i.e.* for $\sqrt{s} < m_Z + m_H$. The width of the Higgs boson, on the other hand, is negligible for masses $m_{\rm H} < 150$ GeV/c^2 (*cf.* Fig. 3.5b). After reaching a maximum about 25 GeV above threshold (at LEP2 energies) the cross section falls off at high energies according to the scaling law $\sim g^4/s$ asymptotically (as it should do for this s-channel process of point-like particles).

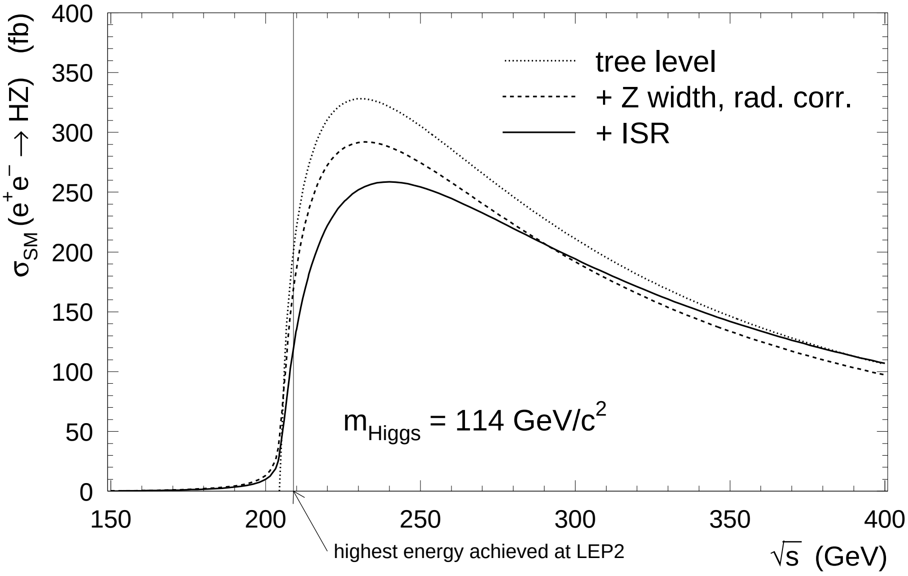

Figure 3.3: Cross section of the Higgs-strahlung process as a function of the centre-of-mass energy for a Higgs boson of mass $m_{\rm H} = 114$ GeV/c^2: the dotted line gives the cross section according to (3.1); the dashed line includes the effect of the Z width and all known QED, weak and QCD corrections, but without initial state radiation (ISR); the full line, in addition, includes ISR to $\mathcal{O}(\alpha^2)$, called double ISR. The latter two curves are obtained with the HZHA program.

3.1.2 The WW fusion process

The final state in which the Higgs particle is produced together with two neutrinos, $\rm e^+e^- \to H\nu\overline{\nu}$ (called the missing final state), consists of two different contributions: Higgs-strahlung with the Z decaying into the three types of neutrinos and WW fusion of the Higgs boson (*cf.* Fig. 3.2b). The cross section for the latter process is given by [19]

$$\sigma(\mathrm{e^+e^-\to H\nu_e\overline{\nu}_e}) = \frac{g^6}{32^2\pi^3 m_{\rm W}^2}\int_{x_{\rm H}}^1 \mathrm{d}x \int_x^1 \frac{F(x,y)\mathrm{d}y}{[1+(y-x)/x_{\rm W}]^2} \tag{3.2}$$

$$F(x,y) = [\frac{2x}{y^3} - \frac{1+3x}{y^2} + \frac{2+x}{y} - 1][\frac{z}{1+z} - \ln(1+z)] + \frac{x}{y^3}\frac{z^2(1-y)}{1+z} \tag{3.3}$$

with $x_{\rm H} = m_{\rm H}^2/s$, $x_{\rm W} = m_{\rm W}^2/s$ and $z = y(x-x_{\rm H})/(x x_{\rm W})$.

For the $e^+e^- \rightarrow H\nu_e\overline{\nu}_e$ process the two amplitudes of Higgs-strahlung and WW-fusion interfere. The three individual contributions to the total cross section are depicted in Figure 3.4. At energies above the HZ threshold for on-shell Z production, Higgs-strahlung is the dominant process, while below the threshold the fusion process is dominant. Correspondingly, the interference term is most important near the threshold were the cross-over between the two processes occurs. For moderate Higgs masses (around 100 GeV/c^2) and at LEP2 energies the WW-fusion process, being $\mathcal{O}(g^6)$, is suppressed with respect to Higgs-strahlung by the additional electroweak coupling. However, at higher energies the WW-fusion process becomes leading due to the logarithmic rise of its cross section — as expected for this t-channel exchange process: $\sigma(e^+e^- \rightarrow H\nu_e\overline{\nu}_e) \sim \log(s/m_H^2)$.

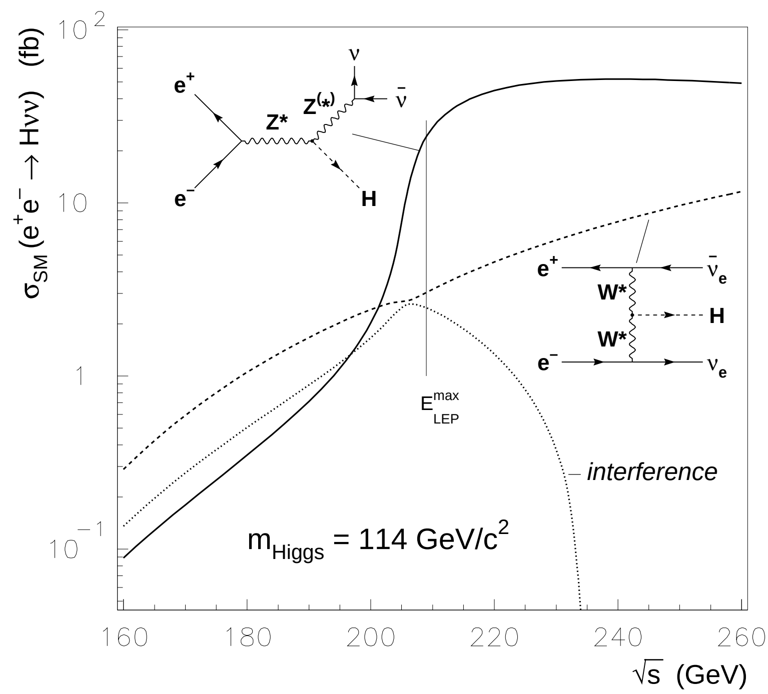

Figure 3.4: Individual cross sections for the $H\nu\overline{\nu}$ final state as a function of the centre-of-mass energy for a fixed value of m_H = 114 GeV/c^2: Higgs-strahlung (solid), WW-fusion (dashed) and the interference term (dotted). Calculations were done with the HZHA program.

3.1.3 The ZZ fusion process

The cross section for ZZ fusion is reduced by an order of magnitude with respect to WW fusion since the leptonic neutral current couplings are considerably smaller than the corresponding charged current couplings. Therefore this process gives only a minor contribution to the $H\,e^+e^-$ final state.

3.2 Decay modes

The decay modes of the standard model Higgs boson at LEP2 energies are defined by the couplings $g_{\rm f}$ of the Higgs boson to fermions. From (2.27) and (2.16) it follows that

$$g_{\rm f} \sim \frac{g m_{\rm f}}{m_{\rm W}}. \tag{3.4}$$

The decay width for $\rm H \rightarrow f\bar{f}$ is proportional to $g_{\rm f}^2$ and in lowest order [20] is given by

$$\Gamma({\rm H} \rightarrow {\rm f\bar{f}}) = N_{\rm f}^c \frac{g^2 m_{\rm f}^2}{32\pi m_{\rm W}^2} \beta^3 m_{\rm H}, \tag{3.5}$$

where $N_c^{\rm f}$ is the color factor (3 for quarks and 1 for leptons) and $\beta = (1 - 4m_{\rm f}^2/m_{\rm H}^2)^{1/2}$ is the velocity of the fermion. When (3.5) is considered as a function of $m_{\rm H}$ one finds the following peculiar behavior: due to the quadratic dependence on the fermion mass the decay rate into a specific fermion pair $\rm f\bar{f}$ always dominates as soon as $m_{\rm H}$ is raised slightly above the threshold $2m_{\rm f}$. When the Higgs boson was searched for at LEP1 in the mass range $0 < m_{\rm H} < m_{\rm Z}$ this effect resulted in numerous different search strategies [22]. At the end of LEP1 all four LEP collaborations reported negative search results, *i.e.* they quoted a lower limit of $m_{\rm H} \gtrsim 60$ GeV/c^2. Therefore the Higgs boson mass range relevant at LEP2 is defined by 60 GeV/$c^2 < m_{\rm H} \lesssim \sqrt{s} - m_{\rm Z}$, where the upper limit follows from the threshold behavior of the Higgs-strahlung process (*cf.* Sec. 3.1.1).

The relevant decay modes of the Higgs boson at LEP2 are

- $\rm H \rightarrow b\bar{b}$ (86.2 – 81.7%)
- $\rm H \rightarrow \tau^+\tau^-$ (7.5 – 7.8%)
- $\rm H \rightarrow c\bar{c}$ (3.9 – 3.6%)
- $\rm H \rightarrow gg$ (2.3 – 5.5%),

where the two numbers in the brackets give the corresponding branching ratios at the values of $m_{\rm H} = 60$ GeV/c^2 and 100 GeV/c^2 (*cf.* Fig. 3.5a, which shows the branching ratios up to $m_{\rm H} = 1$ TeV/c^2). The $\rm b\bar{b}$ decays are by far the leading decay mode, followed by τ, charm and gluon decays at the level of a few percent. In the calculation of the above numbers (by means of the HZHA program) QCD radiative corrections have been included for the decay into $\rm b\bar{b}$ and $\rm c\bar{c}$ quark pairs. The bulk of these corrections can be absorbed by defining the quark masses $m_{\rm q}$ to evolve with the scale of the process, which is $m_{\rm H}$ in this case. For quarks (3.5) is known to second order in α_S and reads

$$\Gamma({\rm H} \rightarrow {\rm q\bar{q}}) = 3 \frac{g^2 m_{\rm q}^2(m_{\rm H})}{32\pi m_{\rm W}^2} \beta^3 m_{\rm H} \left[1 + \frac{17}{3}\left(\frac{\alpha_S}{\pi}\right) + F \cdot \left(\frac{\alpha_S}{\pi}\right)^2\right], \tag{3.6}$$

where the expressions for $m_{\rm q}(m_{\rm H})$ and F can be found, for example, in Ref. [20].

The total decay width of the Higgs boson Γ_{H} is given by the sum of all individual contributions and presented as a double-logarithmic plot in Figure 3.5b in order to easily recognize the power laws

- $\Gamma_{\mathrm{H}} \sim m_{\mathrm{H}}$ for $m_{\mathrm{H}} \lesssim 100$ GeV/c^2 and
- $\Gamma_{\mathrm{H}} \sim m_{\mathrm{H}}^3$ for $m_{\mathrm{H}} \gtrsim 200$ GeV/c^2,

with a transition region in between defined by the onset of the decays H → WW and H → ZZ. The scaling $\Gamma_{\mathrm{H}} \sim {m_{\mathrm{H}}}^3$ in the high mass region (accessible only to future colliders) reflects that the coupling of the Higgs boson to the longitudinal components of W and Z becomes strong.

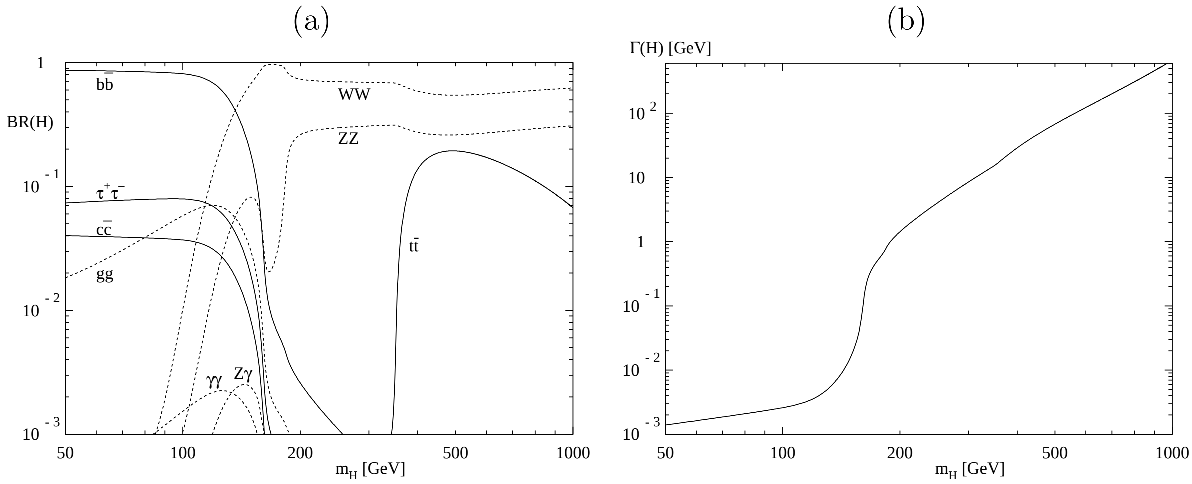

Figure 3.5: (a) Branching ratios of the standard model Higgs boson into fermions (solid lines) and gauge bosons (dashed lines) and (b) the decay width as a function of the Higgs boson mass (plots taken from [21]).

3.3 P1: Search for the standard model Higgs boson in e^+e^- collisions at $\sqrt{s} = 161$, 170 and 172 GeV

[24] The search for the standard model Higgs boson in the Higgs-strahlung process is based on the study of four distinct topologies determined by the decay products of the H and Z bosons (see also Fig. 3.6):

(a) $\mathrm{HZ} \to (\mathrm{q\overline{q}},\, \tau^+\tau^-)\, \ell^+\ell^-$ (leptonic final state, $\ell = \mathrm{e},\mu$),
(b) $\mathrm{HZ} \to \mathrm{q\overline{q}}\nu\overline{\nu}$ (missing energy final state),
(c) $\mathrm{HZ} \to \mathrm{q\overline{q}q\overline{q}}$ (four-jet final state),
(d) $\mathrm{HZ} \to \mathrm{q\overline{q}}\tau^+\tau^-$ or $\tau^+\tau^-\mathrm{q\overline{q}}$ (tau channel).

With the exception of the $\mathrm{HZ} \to \mathrm{q\overline{q}}\ell^+\ell^-$ and $\mathrm{HZ} \to \tau^+\tau^-\mathrm{q\overline{q}}$ channels, all analyses are optimized for the decay mode $\mathrm{H} \to \mathrm{b\overline{b}}$ which dominates in the mass range of interest.

Below each topology is characterized briefly and it is mentioned how the mass of the Higgs boson is calculated. This reconstructed Higgs boson mass is used to define the estimator that is needed for the calculation of the confidence levels for the search hypotheses. In paper 1 a method different from the one described in Chapter 6 is used. However, in the context of the statistical method detailed in Chapter 6 the reconstructed Higgs boson mass would be called the discriminating variable.

The leptonic final state is searched for in events which contain two isolated and oppositely charged high energetic electrons or muons as well as two hadronic jets. In this case the tau decay channel of the Higgs boson is also included. The mass of the Higgs boson is calculated as the mass recoiling to the lepton pair and the invariant mass of the lepton pair is checked for its consistency with the Z boson mass.

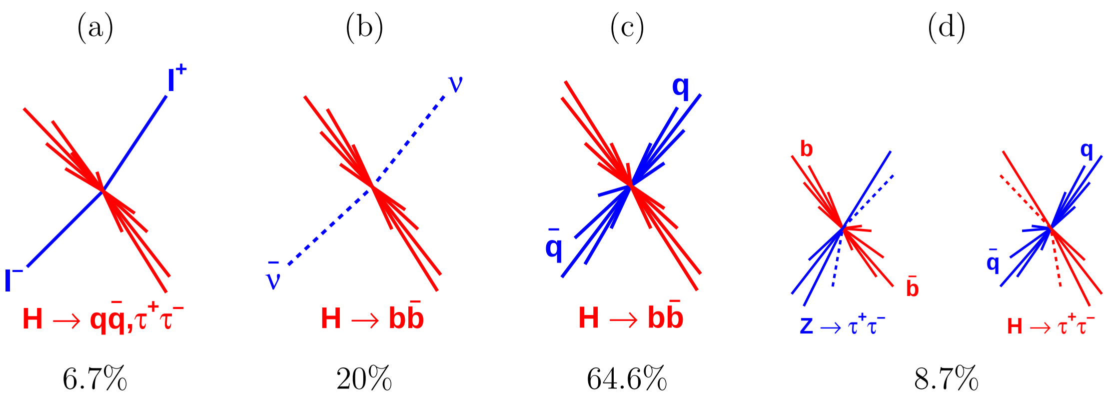

Figure 3.6: The standard model Higgs boson is searched for in these four characteristic event topologies. The branching ratios of the HZ decay topologies are determined by the Z decay branching ratios which are shown below the figures, with the small subtlety that the 5.3% from (c) where $\mathrm{H} \to \tau^+\tau^-$ have been moved to (d).

The HZ $\rightarrow$ $\mathrm{q\overline{q}}\nu\overline{\nu}$ signal topology is characterized by large missing energy due to the undetectable neutrinos and two acoplanar hadronic jets containing the decay products of B-hadrons. While naively the mass of the Higgs boson would be calculated from all reconstructed tracks, here one can do better by using the constraint that the missing mass[1] should be equal to m_{Z}.

The signature of the pure hadronic final state, HZ $\rightarrow$ $\mathrm{q\overline{q}q\overline{q}}$, is four high multiplicity hadronic jets and the presence of B-hadron decay products, in particular, in the jets assigned to the Higgs boson. All combinations of jet pairings are tried and the one is chosen where the invariant mass m_{12} on one di-jet system is closest to m_{Z}. In this channel the mass of the Higgs boson is defined as m_{12} + m_{34} - m_{Z}, where m_{34} is the invariant mass of the other two jets, assumed to come from the Higgs boson decay.

Finally, the tau channel is characterized by four jets, two of which have low multiplicity as expected for tau jets. Since the tau's can originate either from the H or the Z two subanalyses are used in this channel.

All the analyses presented in the paper extensively use Monte Carlo simulations of the signal and the background processes, *e.g.* for setting cuts, for the training of the b-tag neural net and for testing the performance of discriminating variables. The analyses in the individual channels are optimized in order to get the best combined analysis, *i.e.* the best Higgs mass exclusion limit in case there is no hint for a signal.

[1] The missing mass is defined as $m_{\mathrm{miss}} = \mathrm{sign}(x)\sqrt{|x|}$ with $x = E^2_{\mathrm{miss}} - p^2_{\mathrm{miss}}$, where p_{miss} is the momentum unbalance of the event and the missing energy E_{miss} is defined as $\sqrt{s} - E_{\mathrm{vis}}$, E_{vis} being the visible energy.

ELSEVIER

23 October 1997

PHYSICS LETTERS B

Physics Letters B 412 (1997) 155–172

Search for the Standard Model Higgs boson in e^+e^- collisions at $\sqrt{s} = 161$, 170 and 172 GeV

ALEPH Collaboration

R. Barate [a], D. Buskulic [a], D. Decamp [a], P. Ghez [a], C. Goy [a], J.-P. Lees [a], A. Lucotte [a], M.-N. Minard [a], J.-Y. Nief [a], B. Pietrzyk [a], M.P. Casado [b], M. Chmeissani [b], P. Comas [b], J.M. Crespo [b], M. Delfino, [b], E. Fernandez [b], M. Fernandez-Bosman [b], Ll. Garrido [b,1], A. Juste [b], M. Martinez [b], G. Merino [b], R. Miquel [b], Ll.M. Mir [b], C. Padilla [b], I.C. Park [b], A. Pascual [b], J.A. Perlas [b], I. Riu [b], F. Sanchez [b], F. Teubert [b], A. Colaleo [c], D. Creanza [c], M. de Palma [c], G. Gelao [c], G. Iaselli [c], G. Maggi [c], M. Maggi [c], N. Marinelli [c], S. Nuzzo [c], A. Ranieri [c], G. Raso [c], F. Ruggieri [c], G. Selvaggi [c], L. Silvestris [c], P. Tempesta [c], A. Tricomi [c,2], G. Zito [c], X. Huang [d], J. Lin [d], Q. Ouyang [d], T. Wang [d], Y. Xie [d], R. Xu [d], S. Xue [d], J. Zhang [d], L. Zhang [d], W. Zhao [d], D. Abbaneo [e], R. Alemany [e], A.O. Bazarko [e,3], U. Becker [e], P. Bright-Thomas [e], M. Cattaneo [e], F. Cerutti [e], G. Dissertori [e], H. Drevermann [e], R.W. Forty [e], M. Frank [e], R. Hagelberg [e], J.B. Hansen [e], J. Harvey [e], P. Janot [e], B. Jost [e], E. Kneringer [e], J. Knobloch [e], I. Lehraus [e], G. Lutters [e], P. Mato [e], A. Minten [e], L. Moneta [e], A. Pacheco [e], J.-F. Pusztaszeri [e,4], F. Ranjard [e], G. Rizzo [e], L. Rolandi [e], D. Rousseau [e], D. Schlatter [e], M. Schmitt [e], O. Schneider [e], W. Tejessy [e], I.R. Tomalin [e], H. Wachsmuth [e], A. Wagner [e,5], Z. Ajaltouni [f], A. Barrès [f], C. Boyer [f], A. Falvard [f], C. Ferdi [f], P. Gay [f], C. Guicheney [f], P. Henrard [f], J. Jousset [f], B. Michel [f], S. Monteil [f], J-C. Montret [f], D. Pallin [f], P. Perret [f], F. Podlyski [f], J. Proriol [f], P. Rosnet [f], J.-M. Rossignol [f], T. Fearnley [g], J.D. Hansen [g], J.R. Hansen [g], P.H. Hansen [g], B.S. Nilsson [g], B. Rensch [g], A. Wäänänen [g], G. Daskalakis [h],

[1] Permanent address: Universitat de Barcelona, 08208 Barcelona, Spain.
[2] Also at Dipartimento di Fisica, INFN Sezione di Catania, Catania, Italy.
[3] Now at Princeton University, Princeton, NJ 08544, USA.
[4] Now at School of Operations Research and Industrial Engireering, Cornell University, Ithaca, NY 14853-3801, USA.
[5] Now at Schweizerischer Bankverein, Basel, Switzerland.

PII S0370-2693(97)01110-6

156 R. Barate et al. / Physics Letters B 412 (1997) 155–172

A. Kyriakis [h], C. Markou [h], E. Simopoulou [h], A. Vayaki [h], A. Blondel [i], J.C. Brient [i], F. Machefert [i], A. Rougé [i], M. Rumpf [i], A. Valassi [i,6], H. Videau [i], E. Focardi [j], G. Parrini [j], K. Zachariadou [j], R. Cavanaugh [k], M. Corden [k], C. Georgiopoulos [k], T. Huehn [k], D.E. Jaffe [k], A. Antonelli [l], G. Bencivenni [l], G. Bologna [l,7], F. Bossi [l], P. Campana [l], G. Capon [l], D. Casper [l], V. Chiarella [l], G. Felici [l], P. Laurelli [l], G. Mannocchi [l,8], F. Murtas [l], G.P. Murtas [l], L. Passalacqua [l], M. Pepe-Altarelli [l], L. Curtis [m], S.J. Dorris [m], A.W. Halley [m], I.G. Knowles [m], J.G. Lynch [m], V. O'Shea [m], C. Raine [m], J.M. Scarr [m], K. Smith [m], P. Teixeira-Dias [m], A.S. Thompson [m], E. Thomson [m], F. Thomson [m], R.M. Turnbull [m], O. Buchmüller [n], S. Dhamotharan [n], C. Geweniger [n], G. Graefe [n], P. Hanke [n], G. Hansper [n], V. Hepp [n], E.E. Kluge [n], A. Putzer [n], J. Sommer [n], K. Tittel [n], S. Werner [n], M. Wunsch [n], R. Beuselinck [o], D.M. Binnie [o], W. Cameron [o], P.J. Dornan [o], M. Girone [o], S. Goodsir [o], E.B. Martin [o], P. Morawitz [o], A. Moutoussi [o], J. Nash [o], J.K. Sedgbeer [o], P. Spagnolo [o], A.M. Stacey [o], M.D. Williams [o], V.M. Ghete [p], P. Girtler [p], D. Kuhn [p], G. Rudolph [p], A.P. Betteridge [q], C.K. Bowdery [q], P. Colrain [q], G. Crawford [q], A.J. Finch [q], F. Foster [q], G. Hughes [q], R.W. Jones [q], T. Sloan [q], E.P. Whelan [q], M.I. Williams [q], C. Hoffmann [r], K. Jakobs [r], K. Kleinknecht [r], G. Quast [r], B. Renk [r], E. Rohne [r], H.-G. Sander [r], P. van Gemmeren [r], C. Zeitnitz [r], J.J. Aubert [s], C. Benchouk [s], A. Bonissent [s], G. Bujosa [s], J. Carr [s], P. Coyle [s], C. Diaconu [s], A. Ealet [s], D. Fouchez [s], N. Konstantinidis [s], O. Leroy [s], F. Motsch [s], P. Payre [s], M. Talby [s], A. Sadouki [s], M. Thulasidas [s], A. Tilquin [s], K. Trabelsi [s], M. Aleppo [t], M. Antonelli [t], F. Ragusa [t,9], R. Berlich [u], W. Blum [u], V. Büscher [u], H. Dietl [u], G. Ganis [u], C. Gotzhein [u], H. Kroha [u], G. Lütjens [u], G. Lutz [u], W. Männer [u], H.-G. Moser [u], R. Richter [u], A. Rosado-Schlosser [u], S. Schael [u], R. Settles [u], H. Seywerd [u], R. St. Denis [u], H. Stenzel [u], W. Wiedenmann [u], G. Wolf [u], J. Boucrot [v], O. Callot [v,9], S. Chen [v], A. Cordier [v], M. Davier [v], L. Duflot [v], J.-F. Grivaz [v], Ph. Heusse [v], A. Höcker [v], A. Jacholkowska [v], M. Jacquet [v], M. Kado [v], D.W. Kim [v,10], F. Le Diberder [v], J. Lefrançois [v], A.-M. Lutz [v], I. Nikolic [v], M.-H. Schune [v], L. Serin [v], S. Simion [v], E. Tournefier [v], J.-J. Veillet [v], I. Videau [v], D. Zerwas [v], P. Azzurri [w], G. Bagliesi [w], S. Bettarini [w], C. Bozzi [w], G. Calderini [w], V. Ciulli [w], R. Dell'Orso [w], R. Fantechi [w], I. Ferrante [w], A. Giassi [w], A. Gregorio [w], F. Ligabue [w], A. Lusiani [w], P.S. Marrocchesi [w], A. Messineo [w],

[6] Supported by the Commission of the European Communities, contract ERBCHBICT941234.

[7] Also Istituto di Fisica Generale, Università di Torino, Torino, Italy.
[8] Also Istituto di Cosmo-Geofisica del C.N.R., Torino, Italy.
[9] Also at CERN, 1211 Geneva 23, Switzerland.
[10] Permanent address: Kangnung National University, Kangnung, Korea.

R. Barate et al. / Physics Letters B 412 (1997) 155–172 157

F. Palla [w], G. Sanguinetti [w], A. Sciabà [w], J. Steinberger [w], R. Tenchini [w], C. Vannini [w], A. Venturi [w], P.G. Verdini [w], G.A. Blair [x], L.M. Bryant [x], J.T. Chambers [x], Y. Gao [x], M.G. Green [x], T. Medcalf [x], P. Perrodo [x], J.A. Strong [x], J.H. von Wimmersperg-Toeller [x], D.R. Botterill [y], R.W. Clifft [y], T.R. Edgecock [y], S. Haywood [y], P. Maley [y], P.R. Norton [y], J.C. Thompson [y], A.E. Wright [y], B. Bloch-Devaux [z], P. Colas [z], B. Fabbro [z], W. Kozanecki [z], E. Lançon [z], M.C. Lemaire [z], E. Locci [z], P. Perez [z], J. Rander [z], J.-F. Renardy [z], A. Rosowsky [z], A. Roussarie [z], J.-P. Schuller [z], J. Schwindling [z], A. Trabelsi [z], B. Vallage [z], S.N. Black [aa], J.H. Dann [aa], H.Y. Kim [aa], A.M. Litke [aa], M.A. McNeil [aa], G. Taylor [aa], C.N. Booth [ab], R. Boswell [ab], C.A.J. Brew [ab], S. Cartwright [ab], F. Combley [ab], M.S. Kelly [ab], M. Lehto [ab], W.M. Newton [ab], J. Reeve [ab], L.F. Thompson [ab], K. Affholderbach [ac], A. Böhrer [ac], S. Brandt [ac], G. Cowan [ac], J. Foss [ac], C. Grupen [ac], P. Saraiva [ac], L. Smolik [ac], F. Stephan [ac], M. Apollonio [ad], L. Bosisio [ad], R. Della Marina [ad], G. Giannini [ad], B. Gobbo [ad], G. Musolino [ad], J. Putz [ae], J. Rothberg [ae], S. Wasserbaech [ae], R.W. Williams [ae], S.R. Armstrong [af], E. Charles [af], P. Elmer [af], D.P.S. Ferguson [af], S. González [af], T.C. Greening [af], O.J. Hayes [af], H. Hu [af], S. Jin [af], P.A. McNamara III [af], J.M. Nachtman [af], J. Nielsen [af], W. Orejudos [af], Y.B. Pan [af], Y. Saadi [af], I.J. Scott [af], J. Walsh [af], Sau Lan Wu [af], X. Wu [af], J.M. Yamartino [af], G. Zobernig [af]

[a] *Laboratoire de Physique des Particules (LAPP), IN2P3-CNRS, 74019 Annecy-le-Vieux Cedex, France*
[b] *Institut de Física d'Altes Energies, Universitat Autònoma de Barcelona, 08193 Bellaterra (Barcelona), Spain* [11]
[c] *Dipartimento di Fisica, INFN Sezione di Bari, 70126 Bari, Italy*
[d] *Institute of High-Energy Physics, Academia Sinica, Beijing, People's Republic of China* [12]
[e] *European Laboratory for Particle Physics (CERN), 1211 Geneva 23, Switzerland*
[f] *Laboratoire de Physique Corpusculaire, Université Blaise Pascal, IN2P3-CNRS, Clermont-Ferrand, 63177 Aubière, France*
[g] *Niels Bohr Institute, 2100 Copenhagen, Denmark* [13]
[h] *Nuclear Research Center Demokritos (NRCD), Athens, Greece*
[i] *Laboratoire de Physique Nucléaire et des Hautes Energies, Ecole Polytechnique, IN2P3-CNRS, 91128 Palaiseau Cedex, France*
[j] *Dipartimento di Fisica, Università di Firenze, INFN Sezione di Firenze, 50125 Firenze, Italy*
[k] *Supercomputer Computations Research Institute, Florida State University, Tallahassee, FL 32306-4052, USA* [14,15]
[l] *Laboratori Nazionali dell'INFN (LNF-INFN), 00044 Frascati, Italy*
[m] *Department of Physics and Astronomy, University of Glasgow, Glasgow G12 8QQ, United Kingdom* [16]
[n] *Institut für Hochenergiephysik, Universität Heidelberg, 69120 Heidelberg, Germany* [17]
[o] *Department of Physics, Imperial College, London SW7 2BZ, United Kingdom* [16]
[p] *Institut für Experimentalphysik, Universität Innsbruck, 6020 Innsbruck, Austria* [18]
[q] *Department of Physics, University of Lancaster, Lancaster LA1 4YB, United Kingdom* [16]

[11] Supported by CICYT, Spain.
[12] Supported by the National Science Foundation of China.
[13] Supported by the Danish Natural Science Research Council.
[14] Supported by the US Department of Energy, contract DE-FG05-92ER40742.
[15] Supported by the US Department of Energy, contract DE-FC05-85ER250000.
[16] Supported by the UK Particle Physics and Astronomy Research Council.
[17] Supported by the Bundesministerium für Bildung, Wissenschaft, Forschung und Technologie, Germany.
[18] Supported by Fonds zur Förderung der wissenschaftlichen Forschung, Austria.

158 R. Barate et al. / Physics Letters B 412 (1997) 155–172

[r] Institut für Physik, Universität Mainz, 55099 Mainz, Germany [17]
[s] Centre de Physique des Particules, Faculté des Sciences de Luminy, IN2P3-CNRS, 13288 Marseille, France
[t] Dipartimento di Fisica, Università di Milano e INFN Sezione di Milano, 20133 Milano, Italy
[u] Max-Planck-Institut für Physik, Werner-Heisenberg-Institut, 80805 München, Germany [17]
[v] Laboratoire de l'Accélérateur Linéaire, Université de Paris-Sud, IN2P3-CNRS, 91405 Orsay Cedex, France
[w] Dipartimento di Fisica dell'Università, INFN Sezione di Pisa, e Scuola Normale Superiore, 56010 Pisa, Italy
[x] Department of Physics, Royal Holloway & Bedford New College, University of London, Surrey TW20 OEX, United Kingdom [16]
[y] Particle Physics Dept., Rutherford Appleton Laboratory, Chilton, Didcot, Oxon OX11 OQX, United Kingdom [16]
[z] CEA, DAPNIA / Service de Physique des Particules, CE-Saclay, 91191 Gif-sur-Yvette Cedex, France [19]
[aa] Institute for Particle Physics, University of California at Santa Cruz, Santa Cruz, CA 95064, USA [20]
[ab] Department of Physics, University of Sheffield, Sheffield S3 7RH, United Kingdom [16]
[ac] Fachbereich Physik, Universität Siegen, 57068 Siegen, Germany [17]
[ad] Dipartimento di Fisica, Università di Trieste e INFN Sezione di Trieste, 34127 Trieste, Italy
[ae] Experimental Elementary Particle Physics, University of Washington, Seattle, WA 98195, USA
[af] Department of Physics, University of Wisconsin, Madison, WI 53706, USA [21]

Received 23 June 1997
Editor: K. Winter

Abstract

The reaction $e^+e^- \to HZ$ is used to search for the Standard Model Higgs boson. The data sample consists of integrated luminosities of $10.9\,pb^{-1}$, $1.1\,pb^{-1}$, and $9.5\,pb^{-1}$ collected by the ALEPH experiment at LEP during 1996, at centre-of-mass energies of 161, 170 and 172 GeV, respectively. No candidate events were found, in agreement with the expected background of 0.84 events from all Standard Model processes. This search results in a 95% C.L. lower limit on the Higgs boson mass of $69.4\,GeV/c^2$. When combined with earlier ALEPH searches performed at energies at and around the Z peak, this limit increases to $70.7\,GeV/c^2$.

[19] Supported by the Direction des Sciences de la Matière, C.E.A.
[20] Supported by the US Department of Energy, grant DE-FG03-92ER40689.
[21] Supported by the US Department of Energy, grant DE-FG0295-ER40896.

1. Introduction

In the minimal Standard Model, the spontaneous breaking of $SU(2)_L \times U(1)_Y$ is achieved at the expense of the introduction of a doublet of complex scalar fields ϕ in self-interaction. As ϕ develops a vacuum expectation value, the W and Z bosons acquire their masses while three of the four initial degrees of freedom are absorbed. A single neutral scalar particle remains, the Higgs boson H. The mass of the Higgs boson is not specified by the theory, but for a given mass the theory predicts its production rates and partial decay widths unambiguously [1].

At LEP 1, the Higgs-strahlung process $e^+e^- \to HZ^* \to Hf\bar{f}$ (Fig. 1a) was the dominant Higgs boson production mechanism. This process was investigated by ALEPH [2] in the $H\nu\bar{\nu}$ and $H\ell^+\ell^-$ channels (throughout this paper ℓ denotes an electron or a muon) with the whole data sample collected at centre-of-mass energies in the vicinity of the Z peak. This sample corresponds to over 4.5 million hadronic Z decays. Three events were observed, in agreement with the expected background, and a 95% C.L. lower limit on the Standard Model Higgs boson mass was set at $63.9\,GeV/c^2$. Excluded domains up to $60.2\,GeV/c^2$ were also reported by the other LEP

R. Barate et al. / Physics Letters B 412 (1997) 155–172 159

experiments [3]. The LEP 1 analyses, however, were slowly reaching their limit in terms of search sensitivity, because the production cross section rapidly vanishes with increasing m_H (see Fig. 1b).

During 1996, the LEP centre-of-mass energy was increased to 161 GeV, and subsequently to 172 GeV. Due to the possibility of producing an on-shell Z boson in association with a Higgs boson, still via the Higgs-strahlung process $e^+e^- \to HZ$, the production cross section is sizeable for Higgs boson masses up to $m_H \simeq \sqrt{s} - m_Z$. The production cross sections at the Z peak and at the higher energies are displayed in Fig. 1b as a function of the Higgs boson mass, including a small contribution from WW and ZZ fusion (Fig. 1a). A sensitivity to $m_H \sim 60$ GeV/c^2 has already been achieved by OPAL [4] with an integrated luminosity of 10 pb^{-1} collected at 161 GeV.

With the integrated luminosity recorded by ALEPH at 161.3 GeV (10.9 pb^{-1}), 170.3 GeV (1.1 pb^{-1}) and 172.3 GeV (9.5 pb^{-1}), about ten events are expected to be produced if $m_H = 70$ GeV/c^2. To be able to select a significant fraction of these ten events, all the final states are considered. These final states depend on the decay modes of the Z ($\ell^+\ell^-$, $\tau^+\tau^-$, $\nu\bar{\nu}$ and $q\bar{q}$) and the Higgs boson ($b\bar{b}$, $\tau^+\tau^-$, $c\bar{c}$ and gg). These final states are addressed by five selections, namely $H\ell^+\ell^-$, $H\nu\bar{\nu}$, $Hq\bar{q}$, $H\tau^+\tau^-$ and $\tau^+\tau^-q\bar{q}$. The $\tau^+\tau^-q\bar{q}$ analysis supplements the $Hq\bar{q}$ selection in cases where the Higgs boson decays to $\tau^+\tau^-$. The $H\tau^+\tau^-$ and $\tau^+\tau^-q\bar{q}$ selections are treated together due to the similar topology.

Several differences between the situation at LEP 2 and at the Z peak can be pointed out. Due to the larger number of channels, the statistical treatment of analysis optimization and combination is more involved. Also, at LEP 1 the background to the Higgs boson search in the $H\nu\bar{\nu}$ channel consists mainly of $e^+e^- \to q\bar{q}$ events with extreme energy losses due to detector effects or exotic heavy quark semileptonic decays. Since the production cross section of these processes is several orders of magnitude smaller at LEP 2 than at the Z peak, background of this type is no longer significant. Instead, the background is due mainly to calculable physics processes. Conse-

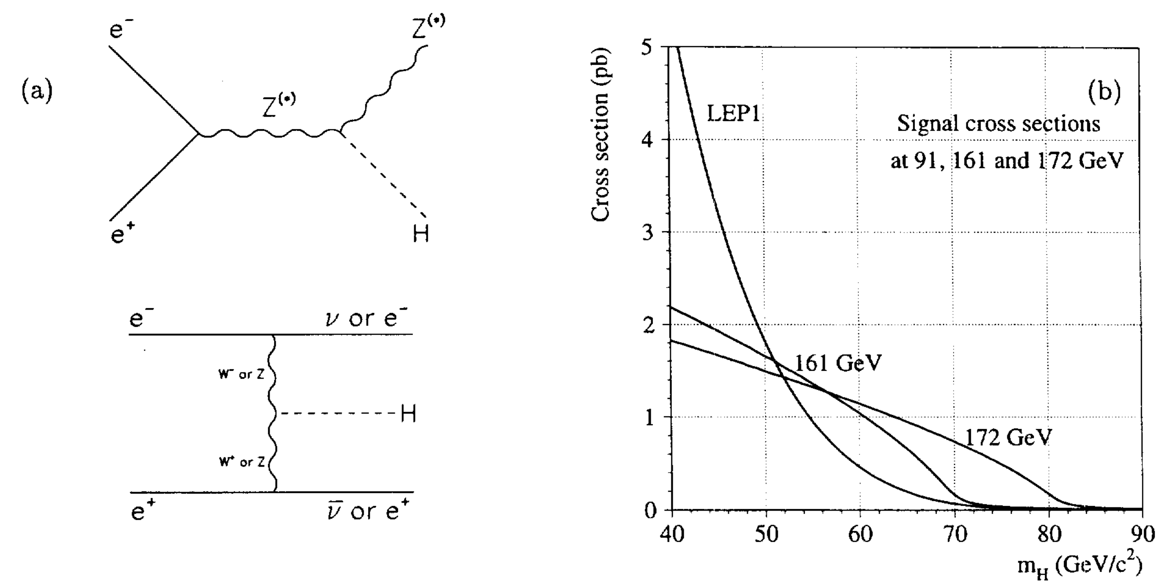

Fig. 1. (a) Feynman diagrams for the Higgs-strahlung process (top) and for the WW or ZZ fusion process (bottom); and (b) corresponding production cross sections as a function of the Higgs boson mass at LEP 1 energies, at 161 GeV and at 172 GeV.

quently, the prediction of the background no longer depends upon details of the detector simulation or the knowledge of rare physical processes. It is therefore more reliable at LEP 2 than at LEP 1, and the analysis can be designed to exploit this good theoretical knowledge. A similar situation holds in the other decay channels as well. The lower cross sections for the background processes also allow Monte Carlo samples to be produced with an equivalent luminosity much larger than the actual recorded luminosity.

Finally, the Z boson produced in association with the Higgs boson via the Higgs-strahlung process is produced on-shell at LEP 2 energies, while it was highly virtual at LEP 1. This additional mass constraint allows the Higgs boson mass to be reconstructed with a good resolution in all channels, thus enhancing the discriminating power of all analyses with respect to simple event counting.

This letter is organized as follows. After a brief description of the ALEPH detector in Section 2, the important issues relevant for the search strategy, the selection optimization and the analysis combination, are addressed in Section 3. In Section 4, the background studies and the searches for the various final states are presented in detail. The combination and the final results are described in Section 5.

2. The ALEPH detector

A detailed description of the ALEPH detector and its performance can be found in Refs. [5] and [6]. The only major modification to the apparatus took place in October 1995 when the vertex detector was replaced by a new device [7], twice as long as the previous one. The new device extends the acceptance to lower polar angles and has less material in the active region. Charged particle tracking is achieved with the new vertex detector, a cylindrical drift chamber and a large time projection chamber. A 1.5 T axial magnetic field is provided by a superconducting solenoidal coil. A $1/p_t$ resolution of $6 \times 10^{-4}\,(\mathrm{GeV}/c)^{-1} \oplus 5 \times 10^{-3}/p_t$ is achieved, and the three-dimensional impact parameter resolution can be parametrized as $(34 + 70/p) \times (1 + 1.6\cos^4\theta)\,\mu$m, with p in GeV/c. Hereafter, charged particle tracks reconstructed with at least four hits in the time projection chamber and originating from within a cylinder of length 20 cm and radius 2 cm coaxial with the beam and centred at the nominal collision point are called *good tracks*. Throughout this letter, events with at least five good tracks accounting for more than 10% of the centre-of-mass energy are referred to as *hadronic events*.

Electrons and photons are identified in the electromagnetic calorimeter by their characteristic longitudinal and transverse shower developments [6]. The calorimeter, a lead/wire-plane sampling device with fine readout segmentation and total thickness of 22 radiation lengths at normal incidence, provides a relative energy resolution of $0.18/\sqrt{E} + 0.009$ (E in GeV).

Muons are identified by their characteristic penetration pattern in the hadron calorimeter [6], a 1.2 m thick yoke instrumented with 23 layers of streamer tubes, together with two surrounding layers of muon chambers. In association with the electromagnetic calorimeter, the hadron calorimeter also provides a measurement of the energy of charged and neutral hadrons with a relative resolution of $0.85/\sqrt{E}$ (E in GeV).

The total visible energy, and therefore also the missing energy, is measured with an energy-flow reconstruction algorithm [6] which combines all of the above measurements, supplemented by the energy detected at low polar angles by two additional electromagnetic calorimeters which are used principally for the luminosity determination. In addition to the total energy measurement, the energy-flow reconstruction algorithm also provides a list of charged and neutral reconstructed objects, called *energy-flow particles*, allowing jets to be reconstructed with a typical angular resolution of 20 mrad both for the polar and azimuthal angles, and a relatively uniform energy resolution over the whole detector acceptance. The latter can be parametrized as $\sigma_E = (0.60\sqrt{E} + 0.6)\,\mathrm{GeV} \times (1 + \cos^2\theta)$ where E (in GeV) and θ are the jet energy and polar angle, respectively.

Finally, jets originating from b quarks are identified from lifetime b tagging algorithms [8], from high transverse momentum leptons coming from semileptonic decays [9], and from jet shape variables such as charged multiplicity, boosted sphericity, and sum of the transverse momenta squared with respect to the jet axes. These quantities are combined with a neural network into a single variable η_i for each jet i, where η_i is near unity for tagged b jets and near zero for other jets. The neural network b tagging is described in detail in Ref. [10].

In the data sample used for the analysis reported here, all major components of the detector were required to be simultaneously operational, and all major trigger logic had to be enabled.

3. Search strategy

3.1. Monte Carlo samples

To design the selection algorithms, large Monte Carlo samples were generated for all background and signal processes, and processed through the complete detector simulation and event reconstruction. To fully benefit from the good theoretical knowledge of the background, a luminosity equivalent in most cases to about 100 times the luminosity recorded in ALEPH was simulated for each process. The samples available at 172 GeV are summarized in Table 1.

Signal events were generated with the HZHA program [13]. At least 2000 events were simulated for each of the various final states, for Higgs boson masses varying from 45 to 80 GeV/c^2, and at each centre-of-mass energy.

Table 1
Number of events generated (in thousands) for each background process, and the equivalent luminosity (with the corresponding scaling factor with respect to the actual data sample), at a centre-of-mass energy of 172 GeV. A private generator was used for the process $e^+e^- \to Z\nu\bar{\nu}$ [11]. All other processes were generated with PYTHIA [12]. In this table, Z is used to represent Z or γ^*. Cuts of 0.2 GeV/c^2 and 12 GeV/c^2 are placed on the Z mass for the ZZ and Ze^+e^- final states, respectively. The mass of the hadronic system was required to be larger than 30 GeV/c^2 for the process $\gamma\gamma \to q\bar{q}$.

Process	No. Events (10^3)	$\mathscr{L}$ (fb^{-1})
$e^+e^- \to q\bar{q}$	325	2.68 (253)
$e^+e^- \to W^+W^-$	12	1.02 (96)
$e^+e^- \to ZZ$	3	0.98 (92)
$e^-e^- \to We\nu$	1	2.07 (195)
$e^+e^- \to Ze^+e^-$	7	1.07 (101)
$e^+e^- \to Z\nu\bar{\nu}$	0.1	10.0 (943)
$\gamma\gamma \to q\bar{q}$	200	0.25 (24)

3.2. Selection optimization

The above Monte Carlo samples are first used to identify variables discriminating signal and background events. These quantities are described in detail in the following sections, for each of the final states. As had already been the case for LEP 1 analyses [2], the locations of the cuts on the most critical variables are placed in such a way that, if the Higgs boson is too heavy to be produced at LEP (the null hypothesis), the highest 95% C.L. lower limit on its mass is achieved, on average.

To do so, an estimator, inspired by Ref. [14], is built to rank all possible experiment outcomes from the least to the most signal-like, using both the number of selected events and their distribution of reconstructed Higgs boson candidate masses [15]. For any experiment outcome, a confidence level $c(m_H)$ is determined as a function of the Higgs boson mass hypothesis: this is the fraction of outcomes of all possible experiments *with signal only* of mass m_H for which the estimator value would be smaller than or equal to that of the experiment under consideration.

The expected confidence level for the null hypothesis, $\langle c \rangle_\infty(m_H)$, is the average value of $c(m_H)$ for experiments *with background only*. The mass for which $\langle c \rangle_\infty(m_H)$ crosses the 5% level represents the mass value which, on average, is "excluded at the 95% confidence level" if the true Higgs boson mass is out of reach. The optimization of an analysis is achieved by minimizing $\langle c \rangle_\infty(m_H)$ with respect to the selection cut values, with m_H chosen at the edge of the expected sensitivity domain.

When several analyses are to be combined, the individual optimization of each of them following the method described above does not guarantee that the combination is in turn optimal. In general, this depends on how the combination is performed. The optimal combination method can be defined, as above, as the combination leading to the smallest expected combined confidence level. Therefore, the expected confidence level $\langle c_i \rangle_\infty$ has to be computed for each analysis i as a function of the selection cut values, and the expected combined confidence level simultaneously minimized with respect to the selection cuts of all analyses. The combination procedure is briefly described in the following subsection.

3.3. Analysis combination

To merge the analyses, the prescription of Ref. [15] is chosen. Let $c_i(m_{\rm H})$, $i = 1,\ldots,n$, be the confidence levels determined on the actual data sample from the n analyses, as a function of the Higgs boson mass hypothesis. If no other information as to the intrinsic capabilities of each of the n analyses is known, it can be shown [15] that the optimal way to combine the n confidence levels is to use the product

$$f(m_{\rm H}) = \prod_{i=1}^{n} c_i(m_{\rm H}).$$

The combined confidence level is obtained by calculating the fraction of outcomes of experiments *with signal only* that would lead to a value of f less than or equal to the measured one.

Although optimal when the qualities of the various analyses are unknown, this democratic approach can lead to an average dilution of the performance of a superior analysis by an inferior one.

According to the prescription that the expected combined confidence level has to be minimized, the poor analysis would have to be rejected and ignored in the combination.

To keep such an analysis in the combination, this approach can be refined into an elitist approach by merging the different confidence levels, taking into account the intrinsic capabilities of each of the analyses:

$$f(m_{\rm H}) = \prod_{i=1}^{n} c_i^{a_i}(m_{\rm H}).$$

The optimal "weights" a_i are obtained by minimizing the expected combined confidence level, calculated from the individual expected confidence levels $\langle c_i \rangle_\infty(m_{\rm H})$.

These weights guarantee that the confidence level, and hence the mass limit, is never degraded, on average, by the inclusion of additional analyses.

The Higgs boson mass hypothesis $m_{\rm H}^{\rm min}$ that leads to a value of 5% for the measured compound confi-

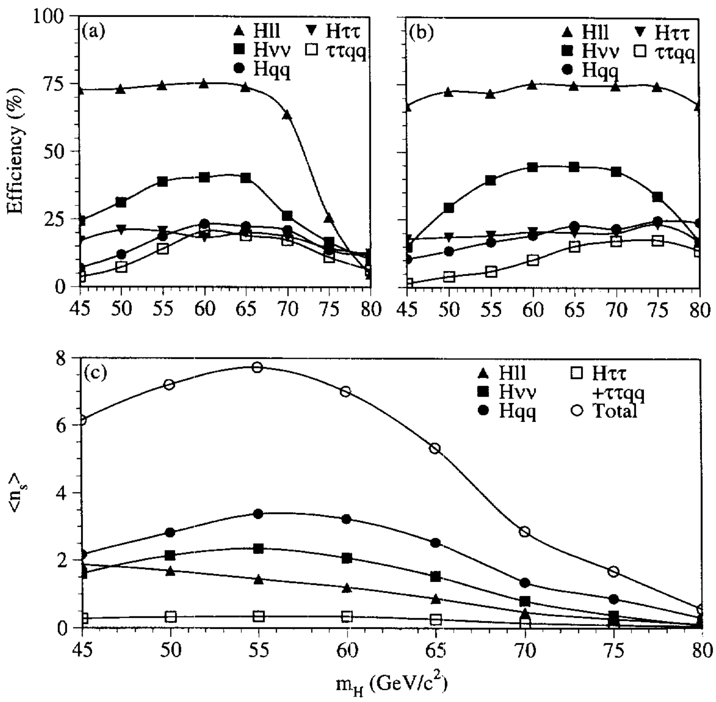

Fig. 2. The reconstruction efficiency as a function of the Higgs boson mass at (a) 161 GeV and (b) 172 GeV. (c) The number of expected events for all energies as a function of the Higgs boson mass.

R. Barate et al. / Physics Letters B 412 (1997) 155–172 163

Table 2
The Higgs-strahlung branching ratio, background, signal efficiency, and the number of signal events expected for a Higgs boson mass of $m_H = 70\,\mathrm{GeV}/c^2$. The left-hand entries are for 161 GeV and the right-hand entries are for 170–172 GeV. The expected number of signal events takes into account the small contributions from WW and ZZ fusion

Final State	Br.(%)	Background		Efficiency(%)		$\langle n_s \rangle$	
$H\ell^+\ell^-$	6.7	0.06	0.11	64.2	74.8	0.08	0.40
$H\nu\bar{\nu}$	20.0	0.06	0.09	26.3	42.9	0.11	0.70
$Hq\bar{q}$	64.6	0.17	0.23	21.1	21.9	0.24	1.12
$H\tau^+\tau^-$	3.4	0.02	0.02	18.8	20.4	0.01	0.05
$\tau^+\tau^- q\bar{q}$	5.3	0.05	0.03	17.4	17.4	0.02	0.07
Total	100	0.36	0.48	24.7	29.6	0.46	2.34

dence level is the 95% C.L. lower limit on the Higgs boson mass.

4. Event selection

The selections of the various final states are described in the following subsections. The expected background, efficiency and expected number of signal events for each channel are summarized in Table 2 for a $70\,\mathrm{GeV}/c^2$ Higgs boson. The variation of the efficiency and the expected number of signal events with the Higgs boson mass is shown in Fig. 2. In the $e^+e^- \to Hq\bar{q}$ channel, events in which the Higgs boson decays to tau leptons are explicitly removed, as this final state is selected by the $\tau^+\tau^- q\bar{q}$ analysis.

In the following subsections, the distributions of simulated data are normalized to the collected luminosity and the distributions for the simulated signal are for a Higgs boson mass of $70\,\mathrm{GeV}/c^2$, unless otherwise indicated.

4.1. The $H\ell^+\ell^-$ final state

The $H\ell^+\ell^-$ final state represents 6.7% of the Higgs-strahlung cross section. Most of the signal events are characterized by two leptons with an invariant mass close to m_Z and a large hadronic recoil mass. The case in which the Higgs boson decays to a tau pair is also considered. Although this channel has a low branching ratio, the experimental signature is clean and the Higgs boson mass can be reconstructed with a good resolution.

4.1.1. Selection

Events are required to have at least four good tracks with $|\cos\theta| < 0.95$ (θ is the polar angle with respect to the beam axis), with a total charged energy larger than $10\%\sqrt{s}$. The selection procedure attempts

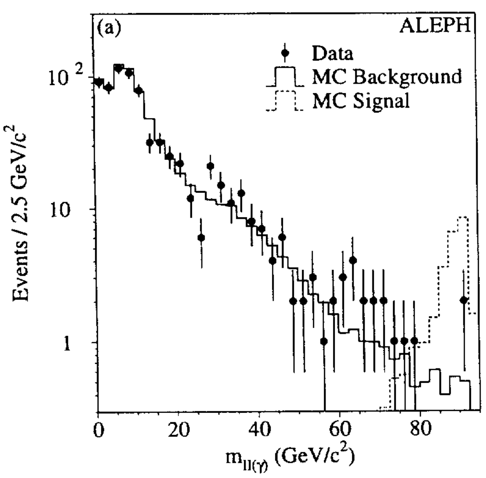

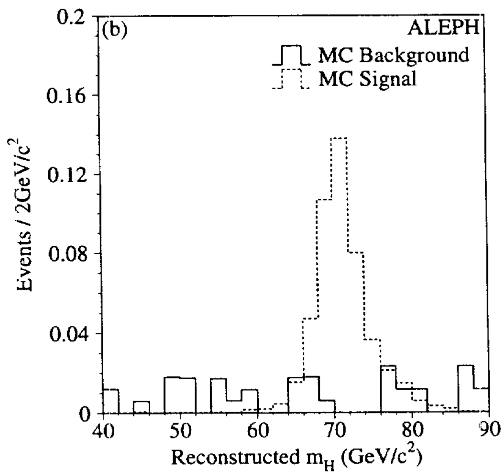

Fig. 3. (a) The $\ell^+\ell^-(\gamma)$ mass distribution for the data (points), the background (solid histogram), and the expected signal (dashed histogram), with loosened selection criteria. (b) The distribution of the mass recoiling to the lepton pair after all the selection criteria are applied. The solid histogram is the background and the dashed histogram is the signal.

to reconstruct the Z boson by finding pairs of oppositely charged particles, hereafter referred to as "leptons", which are either identified as electrons or muons [6] or isolated. The isolation angle of a particle is defined as the half-angle of the largest cone around the particle direction containing less than 5% of the total energy of the other particles in the event. In this analysis a particle is isolated if the isolation angle is larger than 10°. To account for possible Bremsstrahlung photons, neutral energy-flow particles within 2° of the directions of the lepton momenta are excluded from the isolation calculation. In events with an identified electron, the energy of these neutral particles is added to the electron energy. Combinations with no identified lepton, or with an identified e-μ pair, are rejected.

The Higgs boson mass is calculated as the mass recoiling to the lepton pair. The resolution is improved by including a possible radiative photon from the decay of the Z boson. Such a photon must be isolated and have an energy greater than 2 GeV. The isolation angle is determined in the same way as above, but excluding the leptons from the calculation. If more than one photon is identified, the photon which forms with the leptons the invariant mass closest to m_Z is chosen. The reconstructed $\ell^+\ell^-(\gamma)$ mass is required to be greater than $80\,\mathrm{GeV}/c^2$. Fig. 3a shows the $\ell^+\ell^-(\gamma)$ invariant mass distribution for the data and the simulation.

To reject events with an energetic photon from a radiative return to the Z, the most energetic isolated photon must have an energy less than 40 GeV at $\sqrt{s}$ = 161 GeV, and 45 GeV at $\sqrt{s}$ = 172 GeV. These values correspond to about 75% of the most probable energy of the photon in $e^+e^- \to q\bar{q}\gamma$ events.

After selection of the lepton pair, the remaining particles are clustered into two jets using the Durham algorithm. To reject $e^+e^- \to q\bar{q}$ events where the leptons are close to the jets, the sum of the transverse momenta of the leptons with respect to their nearest jet is required to be greater than $20\,\mathrm{GeV}/c$.

The visible mass, excluding the particles attributed to the Z decay, must be larger than $15\,\mathrm{GeV}/c^2$. This rejects $e^+e^-\gamma^*$ and $Z\gamma^*$ processes with a low γ^* mass. To further reduce this background in events which have only one identified lepton, the track closest in angle to each lepton candidate must lie within 110°.

Events with exactly four good tracks are candidates for $(H \to \tau^+\tau^-)\ell^+\ell^-$ and are required to have a missing energy of at least $7\%\sqrt{s}$.

In events with only one identified lepton, both leptons are required to be isolated and their invariant mass should be greater than $85\,\mathrm{GeV}/c^2$. Furthermore, the background from $WW \to q q \ell\nu$ events is rejected by explicitly reconstructing the W's. The missing four-momentum (neutrino) and the lepton are assigned to the leptonic W, and the remaining energy flow particles to the hadronic W. Events where the mass sum of the reconstructed W's is greater than $150\,\mathrm{GeV}/c^2$ and where the mass of the hadronic W is less than $90\,\mathrm{GeV}/c^2$ are rejected.

The background expected with a mass recoiling against the lepton pair larger than $50\,\mathrm{GeV}/c^2$ is 0.06 and 0.11 events at 161 GeV and 170–172 GeV, respectively. Fig. 3b shows the Higgs boson mass distribution for the simulation. No events are observed in the data.

4.1.2. Systematic uncertainties

Potential sources of systematic uncertainties include lepton identification, lepton isolation, and energy and momentum reconstruction. The lepton identification efficiency has been studied and the effect on the selection efficiency is less than 0.2%. The lepton isolation criterion is tested by studying hadronic events with identified leptons. Good agreement is observed between the data and simulation and no uncertainty is assigned. The energy resolution of photons and electrons in the electromagnetic calorimeter and the momentum resolution for muons are studied using $e^+e^- \to \ell^+\ell^-$ events and are found to be slightly better in the simulation. Corrections are applied and the uncertainty on the efficiency is estimated to be less than 0.3%. Taking the aforementioned uncertainties as independent, the total relative systematic uncertainty on the selection efficiency is 0.4%.

4.2. The $H\nu\bar{\nu}$ final state

The $H\nu\bar{\nu}$ final state comprises 20.0% of the total Higgs-strahlung cross section. These events are characterized by large missing mass compatible with the Z mass, and two acoplanar jets.

R. Barate et al. / Physics Letters B 412 (1997) 155–172 165

4.2.1. Selection

The event selection requires hadronic events with a missing mass larger than $80\,\mathrm{GeV}/c^2$, and a visible mass less than $75\,\mathrm{GeV}/c^2$. Background from two-photon collisions is reduced by requiring the visible mass to be larger than $30\%\sqrt{s}$ or the total transverse momentum to be larger than $5\%\sqrt{s}$.

Events with undetected energetic particles at low polar angles are rejected by requiring the angle between the missing momentum and the beam axis to be larger than 25°. Also, the longitudinal missing momentum must be less than $20\,\mathrm{GeV}/c$ and $30\,\mathrm{GeV}/c$, respectively, at 161 GeV and 170–172 GeV.

Background from radiative returns to the Z is further reduced by means of the event acoplanarity. Events are first divided into hemispheres using the plane perpendicular to the thrust axis and non-zero energy is required in each of the hemispheres. The event acoplanarity is defined as the absolute value of the triple product of the normalized momentum vector of each hemisphere and the unit vector along the beam axis. This can be expressed as $|\sin\theta_1 \sin\theta_2 \sin(\phi_1 - \phi_2)|$, where $\theta_{1,2}$ and $\phi_{1,2}$ are respectively the polar and azimuthal angles of the momentum vectors. The acoplanarity is required to be larger than 0.12. Fig. 4a shows the distribution of the acoplanarity for the data and the simulation.

Events from processes such as $\mathrm{We}\nu$, Zee and two-photon collisions where energetic electrons are scattered into the detector are removed by the requirement that the observed energy within 12° of the beam axis be less than $3\%\sqrt{s}$.

To remove background from hadronic events with energetic neutrinos from semileptonic decays of b or c hadrons, the energy contained in an azimuthal wedge of half angle 30° with respect to the plane defined by the beam and the missing momentum direction must be less than $10\%\sqrt{s}$.

The remaining background is reduced using b tagging. The b tagging algorithm described in Ref. [10] is slightly modified, however, to avoid associating a hadron jet from one W in $\mathrm{WW} \to \mathrm{qq}\ell\nu$ events with the lepton from the other W, and possibly tagging the hadron jet as a b quark jet. Leptons with $p_t > 1.5\,\mathrm{GeV}/c$ with respect to the associated jet are not considered for the purposes of b tagging. The sum of the neural network outputs for the two hemisphere jets is required to satisfy $\eta_1 + \eta_2 > 1.1$.

To further reduce background from $\mathrm{WW} \to \mathrm{qq}\tau\nu$

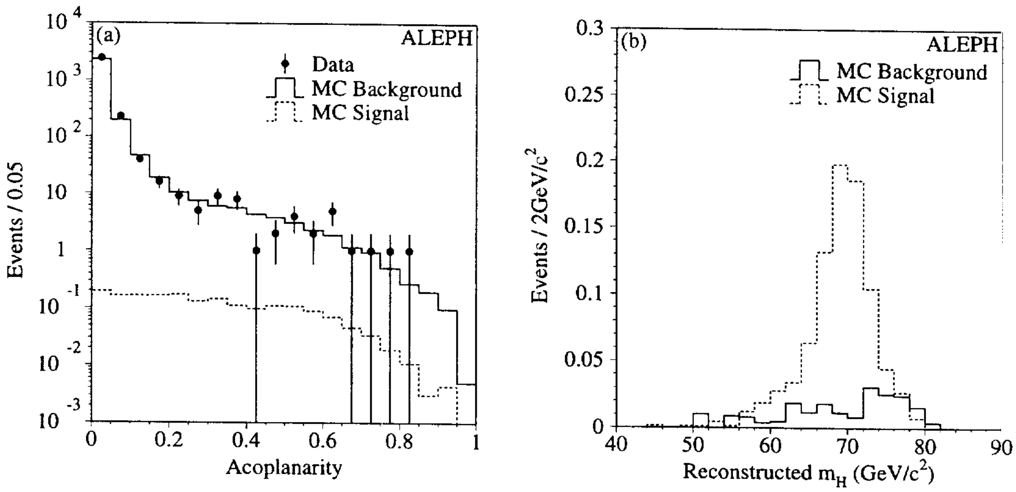

Fig. 4. (a) The event acoplanarity distribution for the data (points), background (solid histogram), and signal (dashed histogram). (b) The distribution of the reconstructed Higgs boson mass for background (solid histogram), and signal (dashed histogram). All selection criteria are applied except the requirement on the visible mass.

events, jets are reconstructed using the jade clustering algorithm with a y_{cut} of m_τ^2/s. The most isolated jet is required to have an energy less than 5 GeV.

The expected background is 0.06 and 0.09 events at 161 GeV and 170–172 GeV, respectively. Fig. 4b shows the reconstructed Higgs boson mass distribution for the simulation. No events are observed in the data.

4.2.2. Systematic uncertainties

The requirement on the maximum observed energy within 12° of the beam axis was studied in random trigger events and is found to reduce the signal efficiency by 0.5%.

The effect of the underlying physics distributions on the b tagging is studied by varying the momenta and lifetimes of the b hadrons in the simulation within their uncertainties. The b hadron momentum spectrum in the simulation is varied within the uncertainties quoted in Ref. [16] and the effect on the selection efficiency is 0.4%. The lifetimes of the weakly-decaying b hadrons are varied about the world-average lifetime of 1.55 ± 0.02 ps [17], and the effect is found to be negligible. The uncertainty on the b tagging efficiency due to the simulation of the detector response is investigated by studying the track impact parameter resolution, since it provides the bulk of the b tagging information. An additional smearing of the track parameters, described in Ref. [10], is introduced in the simulation to correct for discrepancies in the impact parameter resolution. This decreases the efficiency in the simulation by 0.4%, and a systematic uncertainty corresponding to half of this variation is assigned.

Uncertainties coming from the simulation of non-b tagging variables have been extensively studied [2]. The overall uncertainty was found to be less than 1%.

Taking these uncertainties as independent, the total relative systematic uncertainty on the selection efficiency is 1.1%.

4.3. The $Hq\bar{q}$ *final state*

The $Hq\bar{q}$ final state accounts for 64.6% of the Higgs-strahlung cross section, not including the case where the Higgs boson decays to tau leptons. The events are characterized by two jets from the Z decay accompanied by two jets from the Higgs boson decay. The main sources of background are $e^+e^- \to q\bar{q}(\gamma)$, $e^+e^- \to W^+W^-$ and $e^+e^- \to ZZ$.

4.3.1. Selection

The standard hadronic event selection criteria are tightened to at least eight good tracks satisfying $|\cos\theta| < 0.95$. The events are forced to form four jets by the Durham jet-clustering algorithm and the y_{cut} value where the transition from four to three jets occurs (y_{34}) must be larger than 0.004.

Radiative returns to the Z with energetic undetected photons at low polar angles are removed by requiring the missing momentum along the beam direction to be smaller than $1.5(m_{vis} - 90)$, where m_{vis} is the invariant mass in GeV$/c^2$ of all the energy-flow particles. Radiative returns to the Z where energetic photons are observed in the detector are removed by identifying the electromagnetic clusters due to these photons. The electromagnetic energy is computed from identified photons and electrons, charged particle pairs consistent with photon conversions, neutral particles passing through an electromagnetic calorimeter crack region and detected in the hadron calorimeter, and particles detected in the luminosity monitors. If the fraction of electromagnetic energy in a one degree cone around any energy flow particle in a given jet is larger than 80% of the jet energy, the event is rejected. Each jet is further required to contain at least one good track.

In order to reject background events in which three of the jets are close in angle, as expected in $e^+e^- \to q\bar{q}$ events, the sum Θ of the four smallest jet-jet angles must be larger than 350°.

Near threshold the Higgs and Z bosons decay into a pair of approximately back-to-back jets. The sum of the cosines of the opening angles of the two jet pairs, therefore, discriminates between a signal close to threshold and the background from Z decays to hadrons. Since the correct pairing is not known a priori, the minimum value over all possible jet-jet combinations is used: $\gamma = \min(\cos\theta_{ij} + \cos\theta_{kl})$ for all permutations of *ijkl*. Events are required to satisfy $\gamma < -1.2$ at 161 GeV and $\gamma < -0.9$ at 170–172 GeV.

The energies of the four jets are rescaled by imposing energy-momentum conservation, fixing the four jet velocities to their measured values. If any of the rescaled energies is negative because the measured jet directions are not compatible with a four-body final state, the observed momentum and energy of all four jets are used instead.

At 161 GeV, at least one of the six possible jet pairing combinations is required to satisfy either of the following sets of criteria, referred to as a) and b):

a) • $y_{34} > 0.008$
- $m_{12} > 82\,\mathrm{GeV}/c^2$ (Z boson candidate)
- $m_{34} > 45\,\mathrm{GeV}/c^2$ (Higgs boson candidate)
- $\min(\eta_3, \eta_4) > 0.6$
- $(1-\eta_3)(1-\eta_4) < 8 \times 10^{-3}$

b) $1.9\,y_{34} + 0.14 \sum_{i=1}^{4} \eta_i > 0.48$.

The variables m_{12} and m_{34} are respectively the invariant masses of jet pairs corresponding to the Z and Higgs boson candidates and $\{\eta_i\}$ are the b tagging neural network outputs [10]. The requirement b) is similar to that used in Ref. [10] and is designed to select four b quark final states.

At 170–172 GeV, the requirements on the Z boson mass and the b tagging are modified to take into account the different level and composition of the background:

a′) • $y_{34} > 0.008$
- $m_{12} > 80\,\mathrm{GeV}/c^2$
- $m_{34} > 45\,\mathrm{GeV}/c^2$
- $\min(\eta_3, \eta_4) > 0.6$
- $(1-\eta_3)(1-\eta_4) < 4 \times 10^{-3}$

b′) $1.9\,y_{34} + 0.14 \sum_{i=1}^{4} \eta_i > 0.52$.

Fig. 5a shows the distribution of the b tagging variable $(1-\eta_3)(1-\eta_4)$. The expected background is 0.17 and 0.23 events at 161 GeV and 170–172 GeV, respectively. Fig. 5b shows the reconstructed Higgs boson mass distribution. No events are observed in the data.

An alternative event selection based on a neural network has also been developed. Its performance is similar to the standard analysis described above, though it is not used to derive the final result presented in this letter because it leads to a minimum value of $\langle c \rangle_\infty$ slightly larger than the standard selection.

In the neural network analysis, the selection of hadronic events, the determination of the jet four-momenta, and the rejection of background from radiative returns to the Z are adopted from the standard selection. Only events satisfying $y_{34} > 0.008$ are considered.

The neural network inputs include the following variables, used in the standard analysis: $\{\eta_i\}$, y_{34}, Θ,

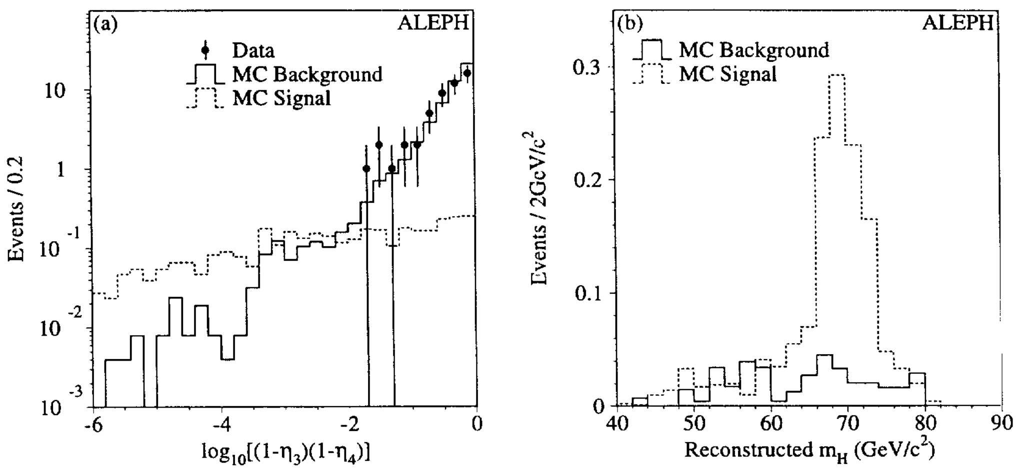

Fig. 5. (a) The distribution of the b tagging variable $(1-\eta_3)(1-\eta_4)$ at 170–172 GeV, for the data (points), the simulated background (solid histogram), and the signal (dashed histogram). All cuts are applied except the b tagging criteria in a′). If more than one combination in an event is selected, the combination with the smallest value of $(1-\eta_3)(1-\eta_4)$ is plotted. (b) The distribution of the reconstructed Higgs boson mass $m_{12} + m_{34} - 91.2\,\mathrm{GeV}/c^2$ for the background (solid histogram) and the signal (dashed histogram), summed over the centre-of-mass energies. The plot shows only the combination for which m_{12} is closest to the nominal Z mass.

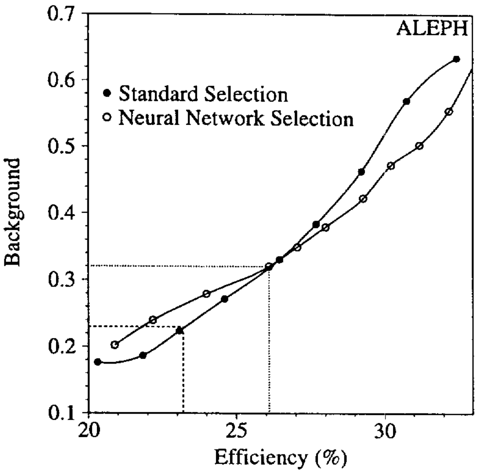

Fig. 6. The expected background as a function of the efficiency for the two four-jet analyses for a Higgs boson of mass 67 GeV/c^2 and a centre-of-mass energy of 172 GeV. The dashed and dotted lines indicate the working points of the standard and the neural network analyses, respectively. The curve for the standard analysis (solid points) is obtained by varying the cuts on m_{12} and the b tagging variables. The curve for the neural network analysis (hollow points) is obtained by varying the cut on the neural network output.

and γ. The reconstructed Higgs boson mass variable m_{34} is not used, to avoid biasing of the neural network selection toward a given m_{H} value. Additional inputs to the neural network include the probability that the impact parameters of the tracks in the event are consistent with zero lifetime [8], the event thrust and sphericity, the track multiplicity, the minimum dijet mass, and the minimum values of the following jet properties: mass, energy and track multiplicity.

These variables discriminate between signal and background without assigning the jets to the Higgs or Z boson candidates. This information is used together with the mass m_{12} of the Z boson candidate and the b tagging information for each of the six possible jet pairings. The neural network discriminates signal from background and selects the most probable H and Z candidates among the six combinations in each event. Events are selected by placing a cut on the output of the neural network.

The expected background is 0.12 and 0.32 events at 161 GeV and 170–172 GeV, respectively. The background as a function of the reconstruction efficiency is shown for the standard analysis and the neural network analysis in Fig. 6. This selection also does not select any events in the data.

4.3.2. Systematic uncertainties

The determination of the systematic uncertainty arising from the b tagging follows the prescription of Section 4.2.2. The variation of the b hadron momentum spectrum in the simulation results in a 1.0% uncertainty. The lifetime uncertainty is negligible, as was the case previously. The uncertainty due to impact parameter resolution is 0.8%.

The modelling of the non-b tagging variables is studied using the sample of events obtained after the selection of hadronic events and the rejection of radiative returns to the Z. The signal distributions are reweighted using weights calculated from a comparison of the data and the background simulation. No statistically significant deviations are found and a systematic uncertainty of 1.2% is attributed to this source.

Adding the above uncertainties in quadrature results in an overall relative systematic uncertainty on the selection efficiency of 1.8%.

4.4. The $\mathrm{H}\tau^+\tau^-$ *and* $\tau^+\tau^-\mathrm{q\bar{q}}$ *final states*

The $\mathrm{H}\tau^+\tau^-$ final state accounts for 3.4% of signal decays, including final states with four tau leptons. The $\tau^+\tau^-\mathrm{q\bar{q}}$ channel has a branching ratio of 5.3%, including the hadronic branching ratio of the Z. Non-hadronic decays of the Z are not considered here as they are addressed by other channels described in this letter.

The selection procedure begins with a common set of criteria sensitive to $\tau^+\tau^-\mathrm{q\bar{q}}$ final states produced via either process. This preselection is similar to the track based selection developed for hA $\to$ $\tau^+\tau^-\mathrm{q\bar{q}}$ [10], but with looser criteria. Further criteria are then applied, tailored to the channel under consideration.

4.4.1. Preselection

Hadronic events are selected by requiring at least five good tracks with $|\cos\theta| < 0.95$ which account for at least 10% of $\sqrt{s}$. Radiative returns with undetected photons at low polar angles are rejected by requiring the longitudinal missing momentum to be less than 40 GeV/c. The signal events are also characterized by missing energy due to the undetected neutrinos. This is exploited by requiring the measured missing energy to be positive.

The identification and reconstruction of tau lepton candidates is identical to that of Ref. [10]. Events are required to have at least two tau candidates of opposite charge, and at least one of the tau jets is required to have unit charged multiplicity. The sum of the isolation angles of the tau candidates is required to be larger than 50°. The isolation angle is defined as the half-angle of the largest cone about the tau candidate direction containing less than 5% of the total energy of the particles in the event excluding the particles (neutral and charged) making up the tau.

In events with one identified lepton, background from WW $\to$ qq$\ell\nu$ events is rejected using the method described in Section 4.1. The cuts on the mass sum and the hadronic mass are set to 140 GeV/c^2 and 85 GeV/c^2, respectively.

Energy-flow particles not included in the tau jets are clustered into two jets with the Durham algorithm. A χ^2 fit is performed on the event using a modified version of the method described in Ref. [10]. Here, a constraint on the compatibility of the $\tau^+\tau^-$ or q$\bar{\text{q}}$ pair masses with the nominal Z mass is imposed, depending on the channel under consideration. If more than one combination passes the selection criteria, the combination with the smallest χ^2 is kept. The fitted mass of the pair assigned to the Higgs boson decay is required to lie between 40 GeV/c^2 and 80 GeV/c^2. Fig. 7a shows the distribution of the χ^2 variable for the data and the simulation after the preselection.

4.4.2. H$\tau^+\tau^-$

Two further criteria are applied to select signal decays in this channel. The χ^2 of the fit is required to be less than 20 and the neural network b tag values for the non-tau jets are required to satisfy $\eta_1 + \eta_2 > 1$.

The expected background for the collected luminosity is 0.02 and 0.02 events at 161 GeV and 170–172 GeV, respectively. No events are selected in the data.

4.4.3. $\tau^-\tau^-$q$\bar{\text{q}}$

The inapplicability of b tagging in this channel leads to a tightening of the preselection requirements and a larger set of additional selection criteria.

To reduce background from low multiplicity hadron jets misidentified as tau jets, no good tracks are allowed to fall within a 30° cone around the tau candidate direction. Furthermore, the sum of the masses of the tau candidates must not exceed 1.5 GeV/c^2.

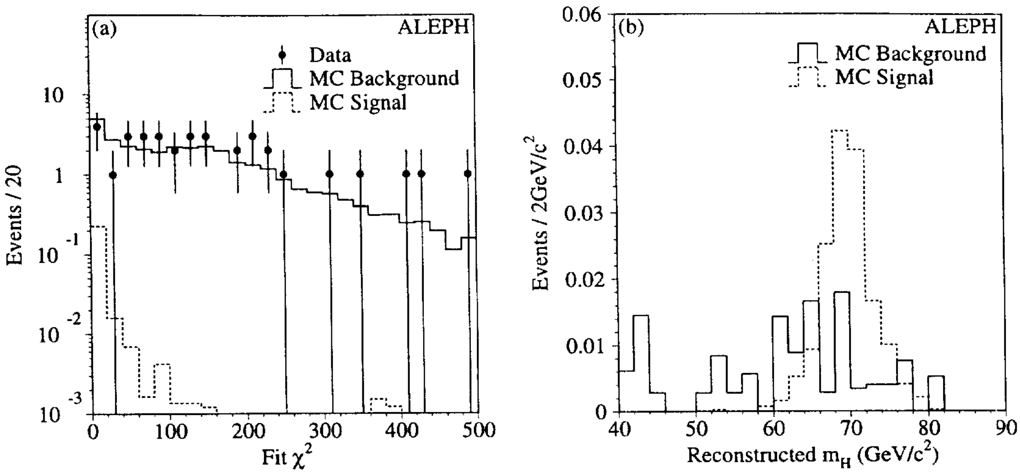

Fig. 7. (a) The fit χ^2 variable for the H $\to \tau^+\tau^-$, Z $\to$ q$\bar{\text{q}}$ channel after the preselection. The points are the data, the solid histogram is the expected background, and the dashed histogram is the signal. (b) The distribution of the fitted Higgs boson mass for both channels after the selection criteria have been applied. The solid histogram is the expected background and the dotted histogram is the signal. The cuts on the reconstructed Higgs boson mass are relaxed.

The χ^2 of the fit is required to be less than 10 and the fitted energies of the non-tau jets must be larger than 85% of the measured values. The angle between the two tau candidates is required to be larger than 120°. To reduce the background from the process $e^+e^- \to e^+e^-Z$ where typically one high momentum electron is unobserved due to its low polar angle, the missing energy is required to be less than 75 GeV.

The expected background for the collected luminosity is 0.05 and 0.03 events at 161 GeV and 170–172 GeV, respectively. No events are observed in the data.

Fig. 7b shows the reconstructed Higgs boson mass distribution for the simulation. The results of the selections of both channels contributing to this final state have been added.

4.4.4. Systematic uncertainties

The main sources of systematic uncertainty are energy flow reconstruction and b tagging. Inaccuracies of the simulation of the reconstructed energy flow particles can cause systematic differences in the simulated efficiency. In particular, they might affect the efficiency of a cut on the reconstructed Higgs boson mass and also the requirements on the value of the fit χ^2. This is studied by introducing additional smearing to the measured momenta of the reconstructed tau and non-tau jets and redoing the fit. The effect is found to be negligible even when the additional smearing is much larger than the effect of any possible inaccuracies of the simulation.

The simulation of the b tagging affects only the $H\tau^+\tau^-$ channel. The determination of the systematic uncertainty has already been described in Section 4.2.2 and results in a 3.0% relative error on the efficiency.

Therefore, a relative uncertainty of 3.0% for the $H\tau^+\tau^-$ channel results, with no significant uncertainty for the $\tau^+\tau^- q\bar{q}$ channel.

5. Combined results

No candidate events are retained in any of the selections presented in the previous section, in agreement with the 0.84 events expected from Standard Model processes. In the absence of any signal, the results of the five selections are combined as outlined in Section 3.3 to set a 95% C.L. lower limit on the Higgs boson mass.

The measured and expected confidence levels are computed at both centre-of-mass energies (161 and 170–172 GeV) for each of the five analyses. Since no candidate events are selected by any analysis, the measured confidence levels are simply $\exp(-s_i)$, where s_i is the number of signal events expected to be selected by the i-th analysis. The two centre-of-

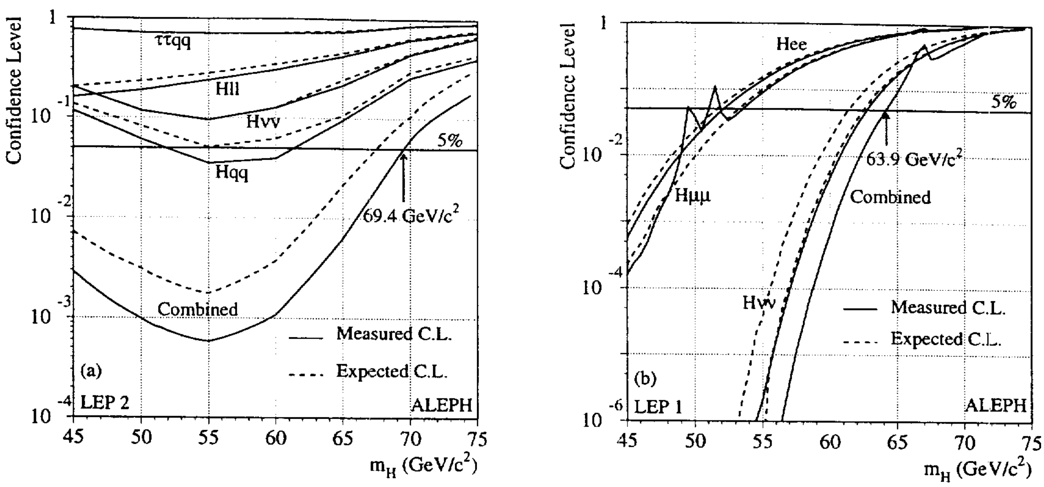

Fig. 8. The measured (full curves) and expected (dashed curves) confidence levels for each of the final states, and their combination, (a) at high energy and (b) at LEP 1. The $H\tau^+\tau^-$ and $\tau^+\tau^- q\bar{q}$ analyses are combined into a single $\tau^+\tau^- q\bar{q}$ result.

mass energies are first combined for each of the final states, and then the five analyses together. In these two successive combinations, the democratic ($a_i = 1$) and the elitist (optimal a_i's) approaches give essentially identical results. This is due to the analysis optimization procedure that optimizes the expected combined confidence level rather than the individual ones, as already described in Section 3.2. The result is displayed in Fig. 8a. While no single analysis allows a confidence level smaller than 5% to be reached in a significant mass domain, the combination excludes the whole range between 45 and $69.4\,\mathrm{GeV}/c^2$ at more than 95% C.L.

The same procedure is then applied to the three selections (for the $\mathrm{He^+e^-}$, $\mathrm{H}\mu^+\mu^-$ and $\mathrm{H}\nu\bar{\nu}$ final states) developed for the LEP 1 data analysis [2]. Here, three candidate events were observed in the $\mathrm{H}\mu^+\mu^-$ channel. They can be seen as bumps in the measured confidence levels displayed in Fig. 8b. The weight assigned to the $\mathrm{H}\nu\bar{\nu}$ final state turns out to be about five times smaller than the weights assigned to the $\mathrm{H}\ell^+\ell^-$ final states, mainly due to the superior mass resolution achieved in the leptonic channels. A 95% C.L. lower limit on the Higgs boson mass of $63.9\,\mathrm{GeV}/c^2$ is found, the same as in Ref. [2].

Finally, the LEP 1 and LEP 2 results are combined. The weight assigned to the high energy part is

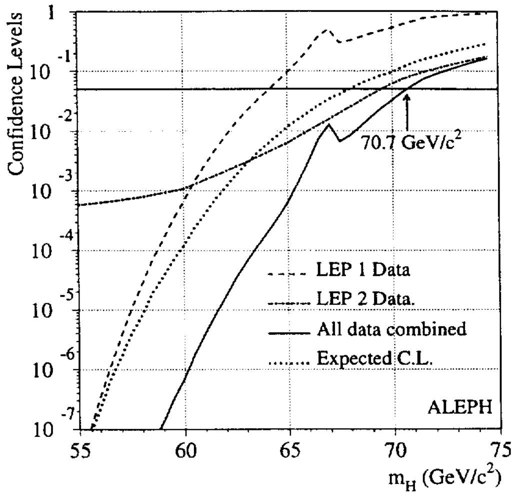

Fig. 9. Measured confidence level curves for the high energy data (dash-dotted), the LEP 1 data (dashed), and the combination (full). The dotted curve shows the expectation for the combination.

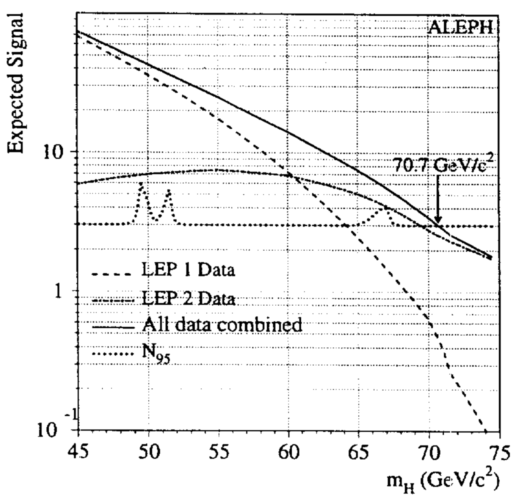

Fig. 10. Number of events expected for signal from high energy data (dash-dotted curve), LEP 1 data (dashed curve), and the combination (full curve). The dotted curve indicates the number of signal events needed to reach a confidence level of 5%. The bumps are due to the three candidate events found at LEP 1 in the $\mathrm{H}\mu^+\mu^-$ channel.

found to be at least 20% larger than that assigned to LEP 1, slowly increasing with the Higgs boson mass hypothesis and becoming very large above $71\,\mathrm{GeV}/c^2$, where the $\mathrm{H}\ell^+\ell^-$ LEP 1 selection has no efficiency. The resulting confidence levels (measured and expected) are shown in Fig. 9. Higgs boson masses below $70.7\,\mathrm{GeV}/c^2$ are excluded at more than 95% C.L.

This result can also be viewed in Fig. 10, where the number of signal events expected is displayed as a function of the Higgs boson mass, together with N_{95}, the number of signal events needed to exclude the corresponding mass hypothesis at 95% C.L.

The sources of systematic uncertainties on the number of signal events expected are

- An uncertainty of $\pm 0.5\%$ from the total integrated luminosity measurement.
- The centre-of-mass energy is affected by an uncertainty of $\pm 0.054\,\mathrm{GeV}$ [18], which corresponds to a $\pm 0.3\%$ variation in the signal cross section.
- The knowledge of the top quark mass, $m_{\mathrm{top}} = 175 \pm 6\,\mathrm{GeV}/c^2$ [19], the simulation of the initial state radiation, and the comparisons between different Monte Carlo programs [20] result in an uncertainty of $\pm 1\%$ in the signal cross section.

- The ambiguities on the values of the b and c quark masses entering the calculation of the ($H \to b\bar{b}$) and ($H \to c\bar{c}$) decay partial widths introduce a $\pm 1\%$ uncertainty on the corresponding branching ratios. This translates into $\pm 0.7\%$ for the number of signal events expected.
- The limited signal Monte Carlo statistics induce an uncertainty of 0.5%.
- The uncertainty related to the selection procedures, detailed in the previous sections, is smaller than 2%.

The overall systematic uncertainty is therefore below $\pm 3\%$. Following the method of Ref. [21], this results in a small increase of the measured confidence level, corresponding to a change of the mass limit by about $10\,\mathrm{MeV}/c^2$.

6. Conclusion

The reaction $e^+e^- \to HZ$ was used to search for the Standard Model Higgs boson. The data sample consists of integrated luminosities of $10.9\,\mathrm{pb}^{-1}$, $1.1\,\mathrm{pb}^{-1}$ and $9.5\,\mathrm{pb}^{-1}$, collected at centre-of-mass energies of 161 GeV, 170 GeV and 172 GeV, respectively. No candidate events were found in any of the final states, in agreement with the 0.84 events expected from all Standard Model processes. The 95% C.L. lower limit on the Higgs boson mass is $69.4\,\mathrm{GeV}/c^2$. When combined with earlier ALEPH searches performed at LEP 1, the limit increases to $70.7\,\mathrm{GeV}/c^2$.

Acknowledgements

We wish to thank our colleagues from the accelerator divisions for the successful high energy operation of LEP. We are indebted to the engineers and technicians in all our institutions for their contribution to the excellent performance of ALEPH. Those of us from non-member countries thank CERN for its hospitality.

References

[1] See for instance, J.F. Gunion, H.E. Haber, G. Kane, S. Dawson, The Higgs Hunter's Guide (Addison-Wesley, 1990); P.J. Franzini et al., in: Z Physics at LEP 1, Eds. G. Altarelli, R. Kleiss, C. Verzegnassi, CERN 89-08 (1989); E. Gross, B.A. Kniehl, G. Wolf, Z. Phys. C 63 (1994) 417; C 66 (1995) 321 (E).
[2] ALEPH Collaboration, Phys. Lett. B 384 (1996) 427.
[3] OPAL Collaboration, Z. Phys. C 73 (1997) 189; L3 Collaboration, Phys. Lett. B 385 (1996) 454; DELPHI Collaboration, Nucl. Phys. B 421 (1994) 3.
[4] OPAL Collaboration, Phys. Lett. B 393 (1997) 231.
[5] ALEPH Collaboration, Nucl. Instrum. Methods A 294 (1990) 121.
[6] ALEPH Collaboration, Nucl. Instrum. Methods A 360 (1995) 481.
[7] D. Creanza et al., Construction and Performance of the New ALEPH Vertex Detector, to appear in the Proceedings of the Conference on Advanced Technology and Particle Physics, Como, Italy (October 7–11, 1996).
[8] ALEPH Collaboration, Phys. Lett. B 313 (1993) 535.
[9] ALEPH Collaboration, Nucl. Instrum. Methods A 346 (1994) 461.
[10] ALEPH Collaboration, Phys. Lett. B 412 (1997) 173.
[11] This generator is based on the differential cross-section published in: S. Ambrosanio, B. Mele, Nucl. Phys. B 374 (1992) 3.
[12] T. Sjöstrand, The PYTHIA 5.7 and JETSET 7.4 Manual, LU-TP.95/20, CERN-TH.7112/93; Comput. Phys. Commun. 82 (1994) 74.
[13] P. Janot, The HZHA generator, in Physics at LEP2, Eds. G. Altarelli, T. Sjöstrand, F. Zwirner, CERN 96-01 (1996), Vol. 2, p. 309.
[14] J.-F. Grivaz, F. Le Diberder, Nucl. Instrum. Methods A 333 (1993) 320.
[15] P. Janot, F. Le Diberder, Combining 'Limits', CERN PPE 97-053 and LPNHE 97-01, to be submitted to Nucl. Instrum. Methods.
[16] ALEPH Collaboration, Phys. Lett. B 357 (1995) 699.
[17] Particle Data Group, R.M. Barnett et al., Phys. Rev. D 54 (1996).
[18] Working group on LEP energy, private communication.
[19] J. Lys, S. Protopopescu, P. Tipton, Proceedings of the 28th International Conference on High Energy Physics, Warsaw, Poland (25–31 July, 1996), Eds. Z. Ajduk, A.K. Wróblewski (World Scientific, 1997) pp. 23–32, 1192–1199.
[20] M. Carena, P.M. Zerwas et al., Higgs Physics, in: Physics at LEP 2, Eds. G. Altarelli, T. Sjöstrand, F. Zwirner, CERN 96-01 (1996) p. 351.
[21] R.D. Cousins, V.L. Highland, Nucl. Instrum. Methods A 320 (1992) 331.

3.4 P2 [25]: Search for the standard model Higgs boson at the LEP2 collider near $\sqrt{s} = 183$ GeV

In the previous section a search for the standard model Higgs boson in LEP data taken at centre-of-mass energies of 161, 170 and 172 GeV was presented. Since no candidate events were found that matched the selection criteria of any of the HZ final states, a lower limit of 70.7 GeV/c^2 was set on the mass of the standard model Higgs boson. For the analyses presented in this paper new data collected at the upgraded LEP collider are used. For an overview of the centre-of-mass energies of the collider and the amount of data that have been collected with the ALEPH detector at LEP see Sec. 4.1.

While the adaption of the analyses to the higher centre-of-mass energy is straightforward the new analyses contain several improvements. For example, the two final states with the largest branching ratio ($\mathrm{q\bar{q}q\bar{q}}$ and $\mathrm{q\bar{q}}\nu\bar{\nu}$) are each supplemented by an additional analysis. While the original analyses are all cut based the new analyses are mainly based on neural networks. These supplemental analyses are not complementary but overlap with the cut analyses. Therefore a more involved procedure is needed for the combination of a cut analysis and a neural net analysis of the same final state, which shortly can be described as follows: let A and B denote the sets of events selected by the two overlapping analyses, then the three statistically independent sub-analyses which select the events $\mathrm{A}\wedge\mathrm{B}$, $\mathrm{A}\backslash\mathrm{B}$ and $\mathrm{B}\backslash\mathrm{A}$ are combined, where the symbols have the same meaning as in the theory of sets.

A comment is also due on background subtraction. In the previous as well as in this paper no background subtraction is performed in deriving the final result. This means that in the context of the confidence level calculation all candidate events selected by the analyses are interpreted as signal events, even when the probability is high that they are background events. In a simple event counting experiment this would on the one hand degrade any exclusion limits that are set, and on the other hand make a discovery impossible. However, here a more elaborate method is used for setting limits. Confidence levels are calculated by using information on the number of candidates and on the values of a discriminating variables for each candidate (the reconstructed Higgs mass $m_{\mathrm{H}}^{\mathrm{rec}}$ is one of them). As long as the candidate events do not cluster at a specific value of $m_{\mathrm{H}}^{\mathrm{rec}}$ the limits are only slightly degraded. Not performing background subtraction means that the resulting limit is conservative and not affected by systematic uncertainties related to the poor knowledge of the residual background.

In the analysis of 57 pb^{-1} of data collected at $\sqrt{s} = 183$ GeV seven candidate events were found, equally distributed in $m_{\mathrm{H}}^{\mathrm{rec}}$. Though the centre-of-mass energy was only increased by 11 GeV compared to the previous year, the exclusion region for the Higgs mass could be extended by 17 GeV/c^2, namely from 70.7 up to 87.9 GeV/c^2.

11 February 1999

PHYSICS LETTERS B

ELSEVIER

Physics Letters B 447 (1999) 336–351

Search for the standard model Higgs boson at the LEP2 Collider near $\sqrt{s} = 183$ GeV [1]

ALEPH Collaboration

R. Barate [a], D. Buskulic [a], D. Decamp [a], P. Ghez [a], C. Goy [a], S. Jezequel [a], J.-P. Lees [a], A. Lucotte [a], F. Martin [a], E. Merle [a], M.-N. Minard [a], J.-Y. Nief [a], P. Perrodo [a], B. Pietrzyk [a], R. Alemany [b], M.P. Casado [b], M. Chmeissani [b], J.M. Crespo [b], M. Delfino [b], E. Fernandez [b], M. Fernandez-Bosman [b], Ll. Garrido [b,2], E. Graugès [b], A. Juste [b], M. Martinez [b], G. Merino [b], R. Miquel [b], Ll.M. Mir [b], P. Morawitz [b], A. Pacheco [b], I.C. Park [b], A. Pascual [b], I. Riu [b], F. Sanchez [b], A. Colaleo [c], D. Creanza [c], M. de Palma [c], G. Gelao [c], G. Iaselli [c], G. Maggi [c], M. Maggi [c], S. Nuzzo [c], A. Ranieri [c], G. Raso [c], F. Ruggieri [c], G. Selvaggi [c], L. Silvestris [c], P. Tempesta [c], A. Tricomi [c,3], G. Zito [c], X. Huang [d], J. Lin [d], Q. Ouyang [d], T. Wang [d], Y. Xie [d], R. Xu [d], S. Xue [d], J. Zhang [d], L. Zhang [d], W. Zhao [d], D. Abbaneo [e], U. Becker [e,4], G. Boix [e,5], M. Cattaneo [e], F. Cerutti [e], V. Ciulli [e], G. Dissertori [e], H. Drevermann [e], R.W. Forty [e], M. Frank [e], F. Gianotti [e], R. Hagelberg [e], A.W. Halley [e], J.B. Hansen [e], J. Harvey [e], P. Janot [e], B. Jost [e], I. Lehraus [e], O. Leroy [e], C. Loomis [e], P. Maley [e], P. Mato [e], A. Minten [e], L. Moneta [e,6],A. Moutoussi [e], F. Ranjard [e], L. Rolandi [e], D. Rousseau [e], D. Schlatter [e], M. Schmitt [e,7], O. Schneider [e], W. Tejessy [e], F. Teubert [e], I.R. Tomalin [e], E. Tournefier [e], M. Vreeswijk [e], H. Wachsmuth [e], Z. Ajaltouni [f], F. Badaud [f], G. Chazelle [f], O. Deschamps [f], S. Dessagne [f], A. Falvard [f], C. Ferdi [f], P. Gay [f], C. Guicheney [f], P. Henrard [f], J. Jousset [f], B. Michel [f], S. Monteil [f], J-C. Montret [f], D. Pallin [f], P. Perret [f], F. Podlyski [f], J.D. Hansen [g], J.R. Hansen [g],

[1] This is the correct version replacing the misprinted article appearing in Phys. Lett. B 440 (1998) 403.
[2] Permanent address: Universitat de Barcelona, 08208 Barcelona, Spain.
[3] Also at Dipartimento di Fisica, INFN Sezione di Catania, Catania, Italy.
[4] Now at SAP AG, D-69185 Walldorf, Germany.
[5] Supported by the Commission of the European Communities, contract ERBFMBICT982894.
[6] Now at University of Geneva, 1211 Geneva 4, Switzerland.
[7] Now at Harvard University, Cambridge, MA 02138, USA.

PII: S0370-2693(98)01506-8

R. Barate et al. / Physics Letters B 447 (1999) 336–351 337

P.H. Hansen [g], B.S. Nilsson [g], B. Rensch [g], A. Wäänänen [g], G. Daskalakis [h], A. Kyriakis [h], C. Markou [h], E. Simopoulou [h], A. Vayaki [h], A. Blondel [i], J.-C. Brient [i], F. Machefert [i], A. Rougé [i], M. Rumpf [i], R. Tanaka [i], A. Valassi [i,8], H. Videau [i], E. Focardi [j], G. Parrini [j], K. Zachariadou [j], R. Cavanaugh [k], M. Corden [k], C. Georgiopoulos [k], T. Huehn [k], D.E. Jaffe [k], A. Antonelli [l], G. Bencivenni [l], G. Bologna [l,9], F. Bossi [l], P. Campana [l], G. Capon [l], V. Chiarella [l], P. Laurelli [l], G. Mannocchi [l,10], F. Murtas [l], G.P. Murtas [l], L. Passalacqua [l], M. Pepe-Altarelli [l,11], M. Chalmers [m], L. Curtis [m], J.G. Lynch [m], P. Negus [m], V. O'Shea [m], C. Raine [m], J.M. Scarr [m], P. Teixeira-Dias [m], A.S. Thompson [m], E. Thomson [m], J.J. Ward [m], O. Buchmüller [n], S. Dhamotharan [n], C. Geweniger [n], P. Hanke [n], G. Hansper [n], V. Hepp [n], E.E. Kluge [n], A. Putzer [n], J. Sommer [n], K. Tittel [n], S. Werner [n], M. Wunsch [n], R. Beuselinck [o], D.M. Binnie [o], W. Cameron [o], P.J. Dornan [o,11], M. Girone [o], S. Goodsir [o], N. Marinelli [o], E.B. Martin [o], J. Nash [o], J.K. Sedgbeer [o], P. Spagnolo [o], M.D. Williams [o], V.M. Ghete [p], P. Girtler [p], E. Kneringer [p], D. Kuhn [p], G. Rudolph [p], A.P. Betteridge [q], C.K. Bowdery [q], P.G. Buck [q], P. Colrain [q], G. Crawford [q], G. Ellis [q], A.J. Finch [q], F. Foster [q], G. Hughes [q], R.W.L. Jones [q], A.N. Robertson [q], M.I. Williams [q], P. van Gemmeren [r], I. Giehl [r], C. Hoffmann [r], K. Jakobs [r], K. Kleinknecht [r], M. Kröcker [r], H.-A. Nürnberger [r], G. Quast [r], B. Renk [r], E. Rohne [r], H.-G. Sander [r], S. Schmeling [r], C. Zeitnitz [r], T. Ziegler [r], J.J. Aubert [s], C. Benchouk [s], A. Bonissent [s], J. Carr [s,11], P. Coyle [s], A. Ealet [s], D. Fouchez [s], F. Motsch [s], P. Payre [s], M. Talby [s], M. Thulasidas [s], A. Tilquin [s], M. Aleppo [t], M. Antonelli [t], F. Ragusa [t], R. Berlich [u], V. Büscher [u], H. Dietl [u], G. Ganis [u], K. Hüttmann [u], G. Lütjens [u], C. Mannert [u], W. Männer [u], H.-G. Moser [u], S. Schael [u], R. Settles [u], H. Seywerd [u], H. Stenzel [u], W. Wiedenmann [u], G. Wolf [u], J. Boucrot [v], O. Callot [v], S. Chen [v], M. Davier [v], L. Duflot [v], J.-F. Grivaz [v], Ph. Heusse [v], A. Höcker [v], A. Jacholkowska [v], M. Kado [v], D.W. Kim [v,12], F. Le Diberder [v], J. Lefrançois [v], L. Serin [v], J.-J. Veillet [v], I. Videau [v,11], J.-B. de Vivie de Régie [v], D. Zerwas [v], P. Azzurri [w], G. Bagliesi [w,11], S. Bettarini [w], T. Boccali [w], C. Bozzi [w], G. Calderini [w], R. Dell'Orso [w], R. Fantechi [w], I. Ferrante [w], A. Giassi [w], A. Gregorio [w], F. Ligabue [w], A. Lusiani [w], P.S. Marrocchesi [w], A. Messineo [w], F. Palla [w], G. Rizzo [w], G. Sanguinetti [w], A. Sciabà [w], G. Sguazzoni [w], R. Tenchini [w], C. Vannini [w], A. Venturi [w], P.G. Verdini [w], G.A. Blair [x], J.T. Chambers [x], J. Coles [x],

[8] Now at LAL, Orsay.
[9] Also Istituto di Fisica Generale, Università di Torino, Torino, Italy.
[10] Also Istituto di Cosmo-Geofisica del C.N.R., Torino, Italy.
[11] Also at CERN, 1211 Geneva 23, Switzerland.
[12] Permanent address: Kangnung National University, Kangnung, Korea.

338 R. Barate et al. / Physics Letters B 447 (1999) 336–351

G. Cowan [x], M.G. Green [x], T. Medcalf [x], J.A. Strong [x],
J.H. von Wimmersperg-Toeller [x], D.R. Botterill [y], R.W. Clifft [y], T.R. Edgecock [y],
P.R. Norton [y], J.C. Thompson [y], A.E. Wright [y], B. Bloch-Devaux [z], P. Colas [z],
B. Fabbro [z], G. Faïf [z], E. Lançon [z,11], M.-C. Lemaire [z], E. Locci [z], P. Perez [z],
H. Przysiezniak [z], J. Rander [z], J.-F. Renardy [z], A. Rosowsky [z], A. Trabelsi [z,13],
B. Tuchming [z], B. Vallage [z], S.N. Black [aa], J.H. Dann [aa], H.Y. Kim [aa],
N. Konstantinidis [aa], A.M. Litke [aa], M.A. McNeil [aa], G. Taylor [aa], C.N. Booth [ab],
S. Cartwright [ab], F. Combley [ab], M.S. Kelly [ab], M. Lehto [ab], L.F. Thompson [ab],
K. Affholderbach [ac], A. Böhrer [ac], S. Brandt [ac], J. Foss [ac], C. Grupen [ac], G. Prange [ac],
L. Smolik [ac], F. Stephan [ac], G. Giannini [ad], B. Gobbo [ad], J. Putz [ae], J. Rothberg [ae],
S. Wasserbaech [ae], R.W. Williams [ae], S.R. Armstrong [af], E. Charles [af], P. Elmer [af],
D.P.S. Ferguson [af], Y. Gao [af], S. González [af], T.C. Greening [af], O.J. Hayes [af],
H. Hu [af], S. Jin [af], G. Mamier [af], P.A. McNamara III [af], J.M. Nachtman [af,14],
J. Nielsen [af], W. Orejudos [af], Y.B. Pan [af], Y. Saadi [af], I.J. Scott [af], M. Vogt [af],
J. Walsh [af], Sau Lan Wu [af], X. Wu [af], G. Zobernig [af]

[a] *Laboratoire de Physique des Particules (LAPP), IN2P3-CNRS, F-74019 Annecy-le-Vieux Cedex, France*
[b] *Institut de Física d'Altes Energies, Universitat Autònoma de Barcelona, 08193 Bellaterra (Barcelona), Spain* [15]
[c] *Dipartimento di Fisica, INFN Sezione di Bari, I-70126 Bari, Italy*
[d] *Institute of High-Energy Physics, Academia Sinica, Beijing, China* [16]
[e] *European Laboratory for Particle Physics (CERN), CH-1211 Geneva 23, Switzerland*
[f] *Laboratoire de Physique Corpusculaire, Université Blaise Pascal, IN2P3-CNRS, Clermont-Ferrand, F-63177 Aubière, France*
[g] *Niels Bohr Institute, 2100 Copenhagen, Denmark* [17]
[h] *Nuclear Research Center Demokritos (NRCD), GR-15310 Attiki, Greece*
[i] *Laboratoire de Physique Nucléaire et des Hautes Energies, Ecole Polytechnique, IN2P3-CNRS, F-91128 Palaiseau Cedex, France*
[j] *Dipartimento di Fisica, Università di Firenze, INFN Sezione di Firenze, I-50125 Firenze, Italy*
[k] *Supercomputer Computations Research Institute, Florida State University, Tallahassee, FL 32306-4052, USA* [18,19]
[l] *Laboratori Nazionali dell'INFN (LNF-INFN), I-00044 Frascati, Italy*
[m] *Department of Physics and Astronomy, University of Glasgow, Glasgow G12 8QQ, UK* [20]
[n] *Institut für Hochenergiephysik, Universität Heidelberg, D-69120 Heidelberg, Germany* [21]
[o] *Department of Physics, Imperial College, London SW7 2BZ, UK* [20]
[p] *Institut für Experimentalphysik, Universität Innsbruck, A-6020 Innsbruck, Austria* [22]
[q] *Department of Physics, University of Lancaster, Lancaster LA1 4YB, UK* [20]
[r] *Institut für Physik, Universität Mainz, D-55099 Mainz, Germany* [21]
[s] *Centre de Physique des Particules, Faculté des Sciences de Luminy, IN2P3-CNRS, F-13288 Marseille, France*
[t] *Dipartimento di Fisica, Università di Milano e INFN Sezione di Milano, I-20133 Milano, Italy*
[u] *Max-Planck-Institut für Physik, Werner-Heisenberg-Institut, D-80805 München, Germany* [21]
[v] *Laboratoire de l'Accélérateur Linéaire, Université de Paris-Sud, IN2P3-CNRS, F-91898 Orsay Cedex, France*

---

[13] Now at Département de Physique, Faculté des Sciences de Tunis, 1060 Le Belvédère, Tunisia.
[14] Now at University of California at Los Angeles (UCLA), Los Angeles, CA 90024, USA.
[15] Supported by CICYT, Spain.
[16] Supported by the National Science Foundation of China.
[17] Supported by the Danish Natural Science Research Council.
[18] Supported by the US Department of Energy, contract DE-FG05-92ER40742.
[19] Supported by the US Department of Energy, contract DE-FC05-85ER250000.
[20] Supported by the UK Particle Physics and Astronomy Research Council.
[21] Supported by the Bundesministerium für Bildung, Wissenschaft, Forschung und Technologie, Germany.
[22] Supported by Fonds zur Förderung der wissenschaftlichen Forschung, Austria.

[w] *Dipartimento di Fisica dell'Università, INFN Sezione di Pisa, e Scuola Normale Superiore, I-56010 Pisa, Italy*
[x] *Department of Physics, Royal Holloway & Bedford New College, University of London, Surrey TW20 OEX, UK* [20]
[y] *Particle Physics Dept., Rutherford Appleton Laboratory, Chilton, Didcot, Oxon OX11 OQX, UK* [20]
[z] *CEA, DAPNIA / Service de Physique des Particules, CE-Saclay, F-91191 Gif-sur-Yvette Cedex, France* [23]
[aa] *Institute for Particle Physics, University of California at Santa Cruz, Santa Cruz, CA 95064, USA* [24]
[ab] *Department of Physics, University of Sheffield, Sheffield S3 7RH, UK* [20]
[ac] *Fachbereich Physik, Universität Siegen, D-57068 Siegen, Germany* [21]
[ad] *Dipartimento di Fisica, Università di Trieste e INFN Sezione di Trieste, I-34127 Trieste, Italy*
[ae] *Experimental Elementary Particle Physics, University of Washington, Seattle, WA 98195, USA*
[af] *Department of Physics, University of Wisconsin, Madison, WI 53706, USA* [25]

Dedicated to the memory of Colin Raine who died suddenly on September 16, 1998

Received 17 September 1998
Editor: L. Montanet

Abstract

During 1997 the ALEPH experiment at LEP gathered 57 pb^{-1} of data at centre-of-mass energies near 183 GeV. These data are used to look for possible signals from the production of the Standard Model Higgs boson in the reaction $e^+e^- \to HZ$. No evidence of a signal is found in the data; seven events are selected, in agreement with the expectation of 7.2 events from background processes. This observation results in an improved lower limit on the mass of the Higgs boson: $m_H > 87.9\ \mathrm{GeV}/c^2$ at 95% confidence level.

1. Introduction

The Standard Model is very successful in describing the interactions of elementary particles. However, the origin of the particle masses remains an open question. The Higgs mechanism directly addresses this problem, with the $W^\pm$ and Z gauge bosons acquiring mass via spontaneous symmetry breaking. A consequence of the Higgs mechanism is the addition of a neutral scalar particle, the Higgs boson, to the spectrum of elementary particles. While the Higgs boson mass m_H is not predicted by the theory, recent results of fits to experimental electroweak data favour low mass values [1].

At LEP2, the Higgs boson can be produced through the Higgs-strahlung process, $e^+e^- \to HZ$, with smaller contributions to the $H\nu\bar{\nu}$ and He^+e^- channels from W- and Z-fusion processes. In the Standard Model, the Higgs boson production rate and decay branching ratios are calculable as a function of m_H [2]. In the mass region relevant to LEP2 searches, the Higgs boson decays mostly into $b\bar{b}$ and, to a lesser extent, into $\tau^+\tau^-$. The searches described in this paper cover most of the topologies arising from the HZ process, with $H \to$ hadrons or $\tau^+\tau^-$, and $Z \to e^+e^-, \mu^+\mu^-, \tau^+\tau^-, \nu\bar{\nu}$, or $q\bar{q}$.

The LEP Collider has been operating at centre-of-mass energies above the W^+W^- production threshold since 1996. The ALEPH Collaboration has searched for the Higgs boson with $\sim 20\ \mathrm{pb}^{-1}$ of data accumulated at $\sqrt{s} = 161$ and 170–172 GeV: no evidence of a signal was detected, and a lower limit of $70.7\ \mathrm{GeV}/c^2$ at 95% confidence level was set on the Higgs boson mass [3]. The other three LEP experiments have reported similar results [4–6].

A total integrated luminosity of 57 pb^{-1} was accumulated by ALEPH in 1997 at centre-of-mass energies near 183 GeV: 0.2 pb^{-1} at 180.8 GeV, 3.9 pb^{-1} at 181.7 GeV, 51.0 pb^{-1} at 182.7 GeV, and 1.9 pb^{-1} at 183.8 GeV. In this letter, these data are referred to as ‘‘the 183 GeV data’’. The higher centre-of-mass energies and the larger total luminosity increase the experimental detection sensitivity for the Higgs boson to a mass around $85\ \mathrm{GeV}/c^2$.

[23] Supported by the Direction des Sciences de la Matière, C.E.A.
[24] Supported by the US Department of Energy, grant DE-FG03-92ER40689.
[25] Supported by the US Department of Energy, grant DE-FG0295-ER40896.

Therefore a reference signal with $m_H = 85\,\mathrm{GeV}/c^2$ and $\sqrt{s} = 183$ GeV is used when optimizing the event selections and quoting signal detection efficiencies. The total production cross section for the reference signal is 0.37 pb.

To improve the discriminating power between signal and background processes, the previously published selections [3] are updated, and new event selections based on artificial neural networks are introduced. Another new feature of Higgs boson searches at $\sqrt{s} \sim 183$ GeV is the higher and partly irreducible ZZ background; since these centre-of-mass energies lie on the threshold for ZZ production, a significant fraction of these events have only one on-shell Z boson.

This letter is organized in the following manner. Section 2 provides a brief description of the ALEPH detector and the b-tagging scheme used in the searches. An overview of the search strategy and of the method used to combine the event selections in all the channels is presented in Section 3. The event selection criteria for each of the signal final states are described in Section 4.1 through 4.4; new developments with respect to the previous publications [3,7] are emphasized and systematic uncertainties specific to each channel are also summarized. In Section 5 the combination of all search channels is presented and the final result is derived. A summary follows in Section 6.

2. The ALEPH detector

In this section the ALEPH detector parts which are most relevant for the analyses that follow are succinctly described. A more comprehensive description of the detector and its performance is given in Refs. [8] and [9].

Three coaxial tracking devices surround the beam line. The innermost device is a silicon microstrip vertex detector (VDET) [10]. It consists of two cylindrical layers of silicon wafers situated at average radii of 6.3 and 11.0 cm. Charged particles with polar angle in the range $|\cos\theta| < 0.88$ traverse both VDET layers. The VDET is surrounded by a 2 m long inner tracking wire chamber (ITC) which provides up to eight hits between radii of 16 and 26 cm. Outside of the ITC is the main tracking detector, a large time projection chamber (TPC) which measures up to 21 three-dimensional coordinates per charged particle. The TPC also measures up to 338 samples of the specific energy loss per track, allowing charged particle identification. A superconducting solenoid immerses the central tracking volume in a 1.5 T axial magnetic field.

In this letter, charged particle tracks reconstructed with at least four hits in the TPC and which originate from within a cylinder of 2 cm radius and 20 cm length centred on the nominal interaction point are called *good tracks*. The tracking ensemble achieves a momentum resolution $\sigma(p_t)/p_t$ of $6 \times 10^{-4}\,(\mathrm{GeV}/c)^{-1}\,p_t \oplus 0.005$. The three-dimensional resolution on the impact parameter of tracks can be parameterized as $(34 + 70/p) \times (1 + 1.6\cos^4\theta)$ μm, with p in GeV/c.

The precise measurement of track parameters plays an essential rôle in the identification of jets containing b hadrons. Weakly decaying b hadrons are long-lived, typically flying several millimetres before decaying. The tagging of b-quark jets relies on six variables reflecting the impact parameter of tracks in the jet, reconstructed secondary vertices, identified electrons and muons with large transverse momentum with respect to the jet axis, and jet shape and multiplicity variables. A neural network is used to combine this information into an output η for each jet. The network is trained to have a response near zero for light quark jets and near one for b quark jets [7].

A lead/proportional-chamber electromagnetic calorimeter (ECAL) is also situated inside the superconducting coil. It is finely segmented into projective towers of $0.9° \times 0.9°$, allowing the identification of electrons and photons within jets. Luminosity calorimeters are installed between the ECAL endcaps and the beam pipe. These calorimeters are of similar construction to ECAL and are treated as an extension of it. A relative energy resolution of $0.18/\sqrt{E(\mathrm{GeV})} + 0.009$ is achieved. A silicon-tungsten sampling calorimeter completes the electromagnetic calorimeter coverage down to 34 mrad.

The ECAL is surrounded by a hadron calorimeter (HCAL) consisting of 5 cm thick iron slabs instrumented with streamer tubes; this structure serves as the return yoke for the magnetic field. The HCAL has the dual purpose of measuring hadronic energy deposition as well as acting as a filter for the identification of muons. When used in conjunction with the ECAL, a relative energy resolution of $0.85/\sqrt{E(\mathrm{GeV})}$ is achieved for hadrons. The outermost detectors are two double layers of muon chambers. Muons are identified as charged particles which penetrate the whole depth of the HCAL or which have associated hits in the outer chambers.

The measurements of charged particle tracks and of energy deposition in the calorimeters, combined with the identification of photons, electrons, and muons, are used to produce a list of charged and neutral *energy flow particles* which are used in all the analyses which follow. Hadronic jets are clustered from these objects with a resolution approximately described as $\sigma(E) = (0.60\sqrt{E} + 0.6)\,\mathrm{GeV} \times (1 + \cos^2\theta)$, where E is the jet energy in GeV and θ is its polar angle. The resolution on the jet angles is approximately 20 mrad in both θ and ϕ.

The total uncertainty on the integrated luminosity of the accumulated data is less than 0.6%.

3. Search strategy

Event selections have been previously developed [3] for the various topologies arising from the HZ process. These selections address the $\mathrm{H}\ell^+\ell^-$ channel (here and in the following, ℓ denotes an electron or a muon, collectively referred to as ''leptons''), the $\mathrm{H}\nu\bar{\nu}$ channel, the $\mathrm{Hq\bar{q}}$ channel where $\mathrm{H} \to \tau^+\tau^-$ decays are not included, the $\mathrm{H}\tau^+\tau^-$ channel, and the $\tau^+\tau^-\mathrm{q\bar{q}}$ channel which complements the $\mathrm{Hq\bar{q}}$ channel when H decays to a $\tau^+\tau^-$ pair. These selections are reoptimized for the increased centre-of-mass energy and integrated luminosity and are supplemented with new event selections. In the $\mathrm{H}\ell^+\ell^-$ final state the selection is improved to extend the acceptance into an angular region not considered previously. In final states with τ leptons, the previous track-based τ candidate selection is replaced by a minijet-based selection, and the previous cut-based event selection algorithms are replaced with new selections based upon neural network (NN) combinations of discriminating variables. In the $\mathrm{H}\nu\bar{\nu}$ and the $\mathrm{Hq\bar{q}}$ channels, new NN-based event selections complement the published cut-based selections [3].

The various selections are optimized to maximize the sensitivity to a Higgs boson signal with mass 85 GeV/c^2, which is near the expected experimental sensitivity. The expected combined confidence level on the signal hypothesis that would be obtained on average if no signal were present [11] is minimized with respect to the position of the cuts on the most relevant selection variables:

- the reconstructed Z mass in the $\mathrm{H}\ell^+\ell^-$ selection;
- the b-quark content of the event and the event acoplanarity in the $\mathrm{H}\nu\bar{\nu}$ cut-based selection;
- the b-quark content of the jets from a candidate Higgs boson and the invariant mass of jets from the Z boson in the $\mathrm{Hq\bar{q}}$ cut-based selection;
- the neural network outputs in the $\mathrm{H}\nu\bar{\nu}$ and the $\mathrm{Hq\bar{q}}$ neural network selections, and in the $\mathrm{H}\tau^+\tau^-$ and $\tau^+\tau^-\mathrm{q\bar{q}}$ selections.

The confidence level for each channel is computed without performing any background subtraction. All channels are subsequently combined using the elitist prescription described in Ref. [11]. This combination prescription assigns different weights to the various search channels in an optimal manner according to their sensitivities to the signal hypothesis.

When two selections are available for a given final state, their results are combined instead of keeping only the selection leading to the (often marginally) better expected confidence level. The gain from this combination procedure is significant since, when two analyses are aimed at selecting the same signal and have similar performance, they often have a large overlap in signal efficiency but not so large an overlap in terms of background. Signal events are, unlike reducible background events, signal-like in *many* variables. The selection of a background event by both selections is therefore less probable, as it depends on the specific choice of variables in each of the selections. The two four-jet final state selections illustrate this point, as is summarized in Table 1. The two original selections are therefore separated into three statistically independent and thus easily combinable sub-selections. The first sub-selection, corresponding to the overlap of the two original analyses, is very pure. The two less pure exclusive selections contain additional information and are combined with the first, decreasing

Table 1
Signal efficiency and the number of signal and background events expected to be selected by each of two four-jet event selections (cuts and neural network), by the two selections simultaneously, and by each of the two exclusively. In this table the selection criteria of the cut-based and neural network selections are optimized independently of one another, and together with all other channels

Selection	Efficiency (%)	Signal	Background
NN	25.7	3.53	1.50
Cuts	24.1	3.31	1.48
Cuts and NN	19.8	2.72	0.88
Cuts only	4.3	0.59	0.60
NN only	5.9	0.81	0.62
Total	30.0	4.12	2.10

further the overall expected confidence level. The combination of the three sub-selections is also done with the elitist prescription. As a result, the events selected by both original analyses receive a larger weight (being more signal-like) than those selected exclusively by one of the two (being more background-like).

Systematic uncertainties related to the knowledge of the residual background shape and normalization do not affect the results presented in this letter since no background subtraction is performed. As is also the case in Ref. [3], the reconstructed Higgs boson mass for all final states is a discriminating variable entering the calculation of the confidence levels. Here, the power of the confidence levels determined from the various searches is improved by including more discriminating variables in the test statistic. These new variables are

- the b content of the event in the $H\nu\bar{\nu}$ channel for the cut-based selection;
- the neural network output in the $H\nu\bar{\nu}$ channel for the NN selection;
- the b content of the hadronic jets for the $H\ell^+\ell^-$ channel.

A global optimization is performed in the manner described above with the criteria of the two $Hq\bar{q}$, the two $H\nu\bar{\nu}$, the $H\ell^+\ell^-$, and the $\tau^+\tau^- q\bar{q}$ and $H\tau^+\tau^-$ selections varied simultaneously. The final sets of selection cuts, leading to the overall smallest expected combined confidence level for $m_H = 85$ GeV$/c^2$, are described in the following section.

4. Event selections

In addition to the cut-based analyses described below, NN-based analyses are introduced for the $Hq\bar{q}$, $H\nu\bar{\nu}$, $H\tau^+\tau^-$ and $\tau^+\tau^- q\bar{q}$ channels to enhance the event selection performance. Variables which alone show marginal separation between signal and background and would be difficult to incorporate into a cut-based analysis can be effectively used in the neural network framework [12].

In the following subsections, the distributions of simulated background processes are normalized to the collected integrated luminosity, and the distributions of the simulated signal are for a Higgs boson mass of 85 GeV$/c^2$. The background processes were simulated as described in Ref. [3], with sample sizes typically exceeding the collected data luminosity by a factor ~ 100. Samples of 10 000 signal events are simulated at several Higgs boson mass values using the HZHA program [13]. In the case of the $H\nu\bar{\nu}$ final state, the W-fusion process as well as its interference with the Higgs-strahlung process are taken into account. Independent training and performance evaluation samples are used for the neural network selections.

The selection efficiencies quoted in this letter are always calculated as the fraction of events in the given channel that pass the selection cuts. Table 2 shows, for each event selection, the variation of efficiency for several Higgs boson masses as well as the expected number of signal events for $m_H = 85$ GeV$/c^2$, the expected number of background events and the number of events selected in the data.

Although the selections differ between the various analyses, they share common systematic uncertainties. For the $Hq\bar{q}$, $H\nu\bar{\nu}$, and $H\tau^+\tau^-$ analyses these common systematic effects relate to the tagging of b-quark jets. Systematic effects related to the simulation of track reconstruction and to the modelling of b-hadron physics are the dominant source of uncertainty in both the cut-based and NN-based analyses. The systematic effect arising from the uncertainty on the b-quark fragmentation hardness (modelled with the Peterson function [14]) is determined by reweighting signal events to cover the experimental uncertainty on the parameter $\epsilon_b = 0.0045 \pm 0.0014$ [15]. Differences in the b-hadron lifetimes and decay multiplicities between the simulation and the world

Table 2
Signal detection efficiencies (in percent) for different Higgs boson mass values. For the $\mathrm{Hq\bar{q}}$ and $\mathrm{H}\nu\bar{\nu}$ channels three independent sub-selections are used: events selected by both the cut-based and the neural network-based selections, and events selected exclusively by either of them. The number of expected background events (n_{b}), the number of events selected in the data (n_{obs}), and the number of expected signal events for $m_{\mathrm{H}} = 85$ GeV$/c^2$ (n_{s}) are also given

m_{H}	$\mathrm{H}\ell^+\ell^-$	$\mathrm{H}\nu\bar{\nu}$			$\mathrm{Hq\bar{q}}$			$\mathrm{H}\tau^+\tau^-$	$\tau^+\tau^-\mathrm{q\bar{q}}$
(GeV$/c^2$)		Cuts + NN	Cuts	NN	Cuts + NN	Cuts	NN		
60	79.6	8.8	8.7	4.7	9.3	5.4	8.1	18.1	0.93
70	77.8	15.8	4.4	7.9	12.4	8.6	9.0	22.9	2.9
80	78.3	20.9	2.8	10.9	23.5	7.4	5.2	22.7	9.8
85	76.2	17.9	4.0	12.2	26.1	7.8	5.2	20.7	12.6
90	71.9	11.1	5.2	7.0	24.6	9.4	4.6	17.4	13.6
95	31.1	9.5	2.6	7.2	19.1	7.6	6.0	12.7	11.6
100	4.0	6.0	1.7	5.7	14.2	6.6	6.9	6.8	5.7
Numbers of events									
n_{b}	2.0	0.16	0.08	0.18	1.4	2.1	1.00	0.17	0.16
n_{obs}	3	0	0	0	1	2	1	0	0
n_{s}	1.1	0.82	0.18	0.56	3.6	1.1	0.71	0.14	0.16

averages are also incorporated in the systematic uncertainty. The uncertainty due to the modelling of the detector tracking is estimated by varying track parameters in accordance with the experimentally measured resolution.

Systematic effects from possible uncertainties in the simulation of the non-b-tagging selection variables are estimated by recomputing the detection efficiency with reweighted signal event samples. The weights are determined from a direct comparison of data and simulated background event distributions at a preselection level with suitably large statistics. Further studies of systematic uncertainties specific to each selection are given below in the corresponding sections.

4.1. The leptonic final states

The $\mathrm{H}\ell^+\ell^-$ channel represents 6.7% of the Higgs-strahlung cross section. The signal events are characterized by two leptons with an invariant mass close to m_{Z} and a recoil mass equal to the Higgs boson mass. Although the branching ratio of this channel is small, the experimental signature is very clear and the Higgs boson mass can be reconstructed with high resolution.

The event selection follows closely that of Ref. [3]. To be considered as lepton candidates charged particles must either be identified as electrons or muons, or else must be isolated from other particles by more than 10°. All accepted combinations of oppositely charged lepton candidates must have at least one identified lepton. Mixed e-μ pairs are not considered. Final state radiation photons from the Z boson decay products are identified and added to isolated lepton candidates to improve the Higgs boson mass resolution.

The analysis algorithm has been simplified with respect to [3] regarding the treatment of events with only one identified lepton. In such cases, the requirement on the angles of the tracks closest to the lepton candidates as well as the requirement that both lepton candidates be isolated have been dropped.

The definition of lepton candidates has been improved with respect to [3] to include leptons below the main tracking acceptance of $|\cos\theta| \leq 0.95$. Low angle muons are identified down to 7.5° from the beam line by finding hit patterns in the hadronic calorimeter consistent with a muon. The momentum of such a low angle muon is calculated from an over-constrained fit to the event using energy and momentum conservation. Low angle electrons are identified down to 12.4° from the beam line by finding large isolated energy deposits in the electromagnetic calorimeters. To separate these electrons from photons, an electron candidate must have at least two consistent hits in the ITC. The new definition of lepton candidates improves the $H\ell^+\ell^-$ signal efficiency by approximately 4% for the same purity.

The selection criteria remain unchanged with respect to those published in Ref. [3] with the sole exception of the requirement on the reconstructed Z boson mass which is reoptimized from $m_{\ell\ell^{+}_{-}(\gamma)} > 80\,\mathrm{GeV}/c^2$ to $m_{\ell^+\ell^-(\gamma)} > 82.75\,\mathrm{GeV}/c^2$.

4.1.1. Systematic uncertainties

Several potential sources of systematic uncertainty are investigated. These include the identification of electrons and muons, the isolation criterion, and the simulation of the energy and momentum resolution of jets and leptons [3]. Some limitations are found in the simulation of the background to low angle electrons which, however, do not contribute any systematic effect. The total relative systematic uncertainty in the signal detection efficiency is 0.4%.

4.2. The missing energy final state

The HZ signal where the Z boson decays invisibly to two neutrinos constitutes 20% of the total Higgs-strahlung cross section. A large missing mass and two b jets from the Higgs boson decay characterize this final state. Two independent analyses are used to search for a signal in this final state: a cut-based analysis modelled on the previous selection [3] and an analysis based on a neural network.

Both analyses share a common hadronic event preselection. The plane perpendicular to the thrust axis is used to divide the event into two hemispheres. All energy flow particles in a hemisphere are considered to belong to a jet, and both jets are required to have nonzero energy. To reduce background from $\gamma\gamma$ interactions, the preselection requires either $P_t > 5\%\sqrt{s}$ or $m_{vis} > 30\%\sqrt{s}$, where P_t is the total transverse momentum of the event and m_{vis} is the visible mass. Finally, the missing mass of the event must be larger than 80 GeV/c^2.

4.2.1. Event selection with cuts

In order to reject radiative returns to the Z, the missing momentum vector is required to point into the apparatus ($\theta_{\not p} > 20°$), and its component along the beam line is not allowed to be large ($|\not p_z| < 26$ GeV/c). The event acoplanarity [3] is used to reduce further the contamination from radiative return events ($\tilde{A} > 0.13$). The energy deposited within a 12° cone around the beam axis is required to be small ($E_{12} < 1.2\%\sqrt{s}$) to reject Weν and Zee events with an energetic electron deflected at a low angle into the detector. In order to suppress background from $W^+W^- \to q\bar{q}'\tau\nu$ decays, the whole event is reclustered into τ minijets [3], and the most isolated jet is required to have a low energy ($E_\tau < 7$ GeV). Finally, b-tagging information from the jets (Fig. 1a) is used to enhance the signal-to-background ratio ($\eta_1 + \eta_2 > 1.1$).

4.2.2. Event selection with a neural network

The analysis described above is complemented with a neural network selection using the six variables of the cut selection and five additional ones. The new variables include the fraction of the energy deposited beyond 30° of the beam line, the total energy within a 30° azimuthal wedge around the missing momentum direction, the acollinearity of the jets, and an additional combination of the b-tagging variables, $\log_{10}(1 - \eta_1\eta_2/2)$. Finally, the isolation angle of the most isolated track (with $p > 1$ GeV/c) provides additional discriminating power against $W^+W^- \to q\bar{q}'\tau\nu$ background.

Further details of the $H\nu\bar{\nu}$ neural network are discussed in the Appendix. Fig. 1b shows the neural network output. Events are selected if the neural network response exceeds 0.983.

4.2.3. Systematic uncertainties

Based on deviations between data and Monte Carlo simulation of the kinematic variable distributions, a relative systematic uncertainty of 2.4% on the signal efficiency is determined. The events from Monte Carlo simulation of the HZ signal are reweighted to simulate changes in b fragmentation, lifetime, and decay multiplicity, giving a relative systematic uncertainty of 3.0%. The relative systematic uncertainty from discrepancies between the tracking in the simulated data and real data is 6.1%.

R. Barate et al. / Physics Letters B 447 (1999) 336–351 345

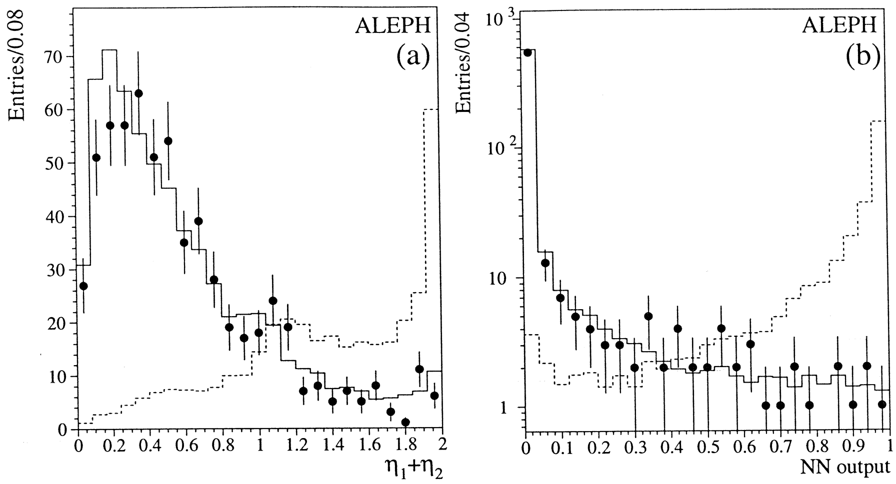

Fig. 1. The distributions in the missing energy channel of (a) the sum of the two neural network b-tag outputs and (b) the output of the neural network used for event selection. The distributions are shown for the data (points), the total simulated background (solid histogram) and the reference signal sample (dashed histogram) after the preselection cuts. The signal distributions have an arbitrary normalization.

The total relative systematic uncertainty on the signal selection efficiency is 7.2%.

4.3. The four-jet final state

Although the $b\bar{b}q\bar{q}$ final state is not as distinctive as the leptonic and missing energy final states, its large branching ratio, 64.4%, compensates for this drawback. The dominant background processes $e^+e^- \to q\bar{q}$, W^+W^-, ZZ are reduced using event topology, kinematic criteria, and b-tagging information. Two analyses are used to search for this final state: a cut-based analysis [3] and a neural network based analysis.

Common event preselection criteria are used for both the cut-based and neural network analyses. Events are required to have at least eight good tracks satisfying $|\cos\theta| \leq 0.95$. Radiative returns to the Z resonance are rejected when the initial state photon is observed in the apparatus as well as when it escapes down the beam pipe. The events are then forced to form four jets with the Durham jet-clustering algorithm [16]. The y_{cut} value where the transition from four to three jets occurs (y_{34}) must be larger than 0.004. Each jet is required to contain at least one good track. The energies and masses of the four jets are then rescaled in accordance with energy and momentum conservation. The measured jet velocities are preserved in this process.

4.3.1. Event selection with cuts

The analysis algorithm and the selection criteria are identical to those found in Ref. [3] except where explicitly stated otherwise.

The sum Θ of the four smallest interjet angles in the event (Fig. 2a) must be larger than 350°; this significantly reduces the background contribution from $q\bar{q}$ events where an energetic jet recoils against three softer jets. Since the sensitivity of this analysis approaches the HZ kinematic limit, signal events are expected to have two nearly back-to-back pairs of jets. This event topology is selected by requiring $\gamma = \min(\cos\theta_{ij} + \cos\theta_{kl}) < -1.30$, where the minimum is over all possible *ijkl* jet permutations.

Further event selection criteria are based upon the six possible jet-pairing combinations. An event is selected if at least one of the jet-pairing combinations conforms to either one of the two following sets of criteria (labelled a and b).

For the first case, events with four well-isolated jets are required. One di-jet system is required to have an invariant mass consistent with the Z mass. The other di-jet is required to have an invariant mass

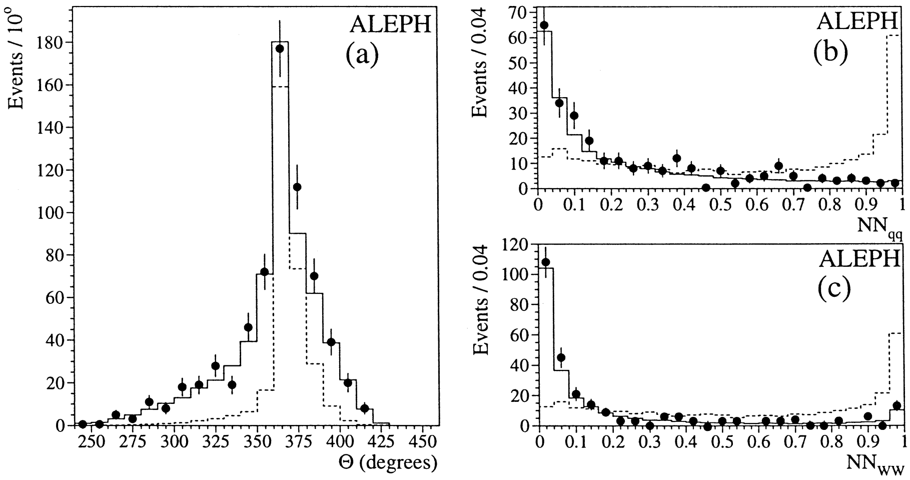

Fig. 2. The four-jet channel distributions for preselected events of (a) Θ, and of the outputs of (b) the anti-q$\bar{\text{q}}$ and (c) anti-W^+W^- neural networks. The points are the data and the solid histogram is the simulated total background normalized to the data integrated luminosity. The signal distributions (dashed histograms) are shown with an arbitrary normalization.

within the Higgs boson mass range of interest and also to have well b-tagged jets. Hence the selection criteria are the following:

(a) • $y_{34} > 0.008$;
- $m_{12} > 78\,\text{GeV}/c^2$ (Z candidate jets);
- $m_{34} > 55\,\text{GeV}/c^2$ (Higgs candidate jets);
- $\min(\eta_3,\eta_4) > 0.30$ (Higgs candidate jets);
- $(1-\eta_3)(1-\eta_4) < 6\times10^{-3}$ (Higgs candidate jets).

Selection criteria for the second case are designed for the HZ $\to \text{b}\bar{\text{b}}\text{b}\bar{\text{b}}$ final state. These events are almost background free and are selected by requiring that the event as a whole has a high b-quark content and a clear four-jet structure:

(b) $9.5y_{34} + \sum_{i=1}^{4}\eta_i > 2.90$.

4.3.2. Event selection with neural networks

Two neural networks are trained to identify the HZ $\to \text{b}\bar{\text{b}}\text{q}\bar{\text{q}}$ signal while rejecting the q$\bar{\text{q}}$ and W^+W^- backgrounds: one network is specifically designed to reject q$\bar{\text{q}}$ events, while the other is designed to reject W^+W^- events. Details related to the training of the neural networks are discussed in the Appendix.

The input patterns to the neural networks consist of the different di-jet pairing combinations within each event. Only pairings that survive the preselection criteria described in Section 4.3 as well as the requirements $\sum_{i=1}^{4}\eta_i > 1.0$ and $m_{34} > 45\,\text{GeV}/c^2$ are input to the neural networks.

The inputs for both neural networks include several of the selection variables used in the cut-based selection: y_{34}, γ, m_{12}, $\min(\eta_3,\eta_4)$, $(1-\eta_3)(1-\eta_4)$, and $\sum_{i=1}^{4}\eta_i$. The invariant mass of the Higgs candidate jets m_{34} is not included to avoid biasing the selection efficiency towards the signal mass hypotheses used for training.

The average QCD four-jet matrix element squared [17] and Θ are especially powerful discriminating variables for eliminating q$\bar{\text{q}}$ background events and hence are also used as inputs to the anti-q$\bar{\text{q}}$ neural network. A vast majority of four-jet events from $e^+e^- \to \text{q}\bar{\text{q}}$ are q$\bar{\text{q}}$gg. The following observables offer additional discriminating power between light quark and gluon jets and are included as inputs to the anti-q$\bar{\text{q}}$ neural network: the boosted aplanarity and the boosted sphericity (both calculated in the rest frame of the jet), and the multiplicity of tracks with large rapidity with respect to the jet axis, for the two Z candidate jets. Additional kinematic variables (e.g., jet energies and di-jet masses, smallest interjet angle and angle of the missing momentum with respect to the beam axis) are also included to improve the overall discriminating power. The complete list of input variables for the anti-$q\bar{q}$ neural network is given in the Appendix.

Important characteristics of W^+W^- events compared to $HZ \rightarrow b\bar{b}q\bar{q}$ signal events include the lack of b jet production and the comparative abundance of c jets. In order to exploit these differences, the common neural network input variables listed above are complemented with the b-tagging information from the two Z candidate jets (η_1 and η_2) and with charm rejection variables for the Higgs candidate jets (μ_3 and μ_4). The charm rejection variables are computed in a similar way to the track impact-parameter-based uds-jet probability $P_{\rm jet}$ [7] but using only tracks with low rapidity with respect to the jet axis ($y < 4.9$) [18]. This rapidity criterion is effective since charmed meson decays result in particles with transverse momentum lower than those from b-hadron decays. The lowest di-jet mass, the lowest jet energy in the event, and the event broadening variable (defined in the Appendix) are also used. The complete list of input variables for the anti-W^+W^- neural network is given in the Appendix.

The neural network output distributions are shown in Fig. 2b and Fig. 2c for signal, background, and data. An event is selected when at least one of its jet pairing combinations has neural network outputs which satisfy both $NN_{q\bar{q}} > 0.940$ and $NN_{W^+W^-} > 0.964$.

4.3.3. Systematic uncertainties

The systematic uncertainties affecting the signal detection efficiency are determined using the method outlined in Section 4. The relative uncertainty from b tagging is 6.5%. The systematic uncertainty corresponding to possible limitations in the description of the most important non-b-tagging selection variables ($y_{34}, \gamma, \Theta, m_{12}, m_{34}, NN_{q\bar{q}}$, and $NN_{W^+W^-}$) is determined to be 2.5%. Conservatively increasing the jet angular resolution in θ and ϕ by 10% in the Monte Carlo simulation results in an additional uncertainty of 0.8%. The correlations between all pairs of variables used in each of the neural networks are compared between the data and the simulated background event sample used for training; no significant discrepancies are observed.

Adding the above contributions in quadrature, the total relative systematic uncertainty assigned to the signal detection efficiency is 7.0%.

4.4. The final states with τ leptons

Two signal channels contribute to final states with at least one $\tau^+\tau^-$ pair. The process $HZ \rightarrow H\tau^+\tau^-$ corresponds to 3.4% of the total Higgs-strahlung process, and $H \rightarrow \tau^+\tau^-, Z \rightarrow q\bar{q}$ corresponds to an additional 5.5%. These events are expected to have two oppositely charged low multiplicity jets in association with missing energy from the τ decays. The main background processes are ZZ and W^+W^-.

Multihadronic events are selected by requiring at least eight good tracks. The total charged track energy in the event is required to exceed 20% of the centre-of-mass energy.

Events from radiative returns to the Z peak, $q\bar{q}(\gamma)$, are rejected with the requirement $|P_z| + E_{\rm miss} < 1.8\gamma_{\rm peak}$. Here, P_z and $E_{\rm miss}$ are the total longitudinal momentum of the event and its missing energy. The mean of the initial state radiation (ISR) photon spectrum peak is denoted as $\gamma_{\rm peak}$ and is defined as $\gamma_{\rm peak} = \sqrt{s}/2 - m_Z^2/2\sqrt{s}$. In addition, $|P_z|$ is required not to exceed $0.6\gamma_{\rm peak}$. In order to exploit the missing energy expected in this final state, the total missing transverse momentum of the event is required to be at least $2.5\%\sqrt{s}$.

A new method for identifying τ lepton candidates replaces the previously published track-based approach [3]. The event is clustered into a large number of jets, referred to as *minijets*, with mass consistent with m_τ. The τ candidates are then selected from these minijets according to the procedure described in detail in Ref. [19]. This minijet method offers a performance similar to the track-based selection but is simpler.

Events with at least two oppositely charged τ candidates are selected. At least one of the candidates must be single-prong. The remainder of the event is forced to form two jets using the Durham clustering algorithm. Events which have more than one τ-pair candidate yield multiple $\tau^+\tau^-q\bar{q}$ combinations. A χ^2 is determined for each event combination with a kinematic consistency fit [19]. This fit requires energy-momentum conservation while keeping the four jet directions fixed. In the fit, the mass of the candidate τ jets is fixed to the nominal τ lepton mass, and the energy resolution of the two non-τ jets is taken into account. The invariant mass of either the $\tau^+\tau^-$ or the $q\bar{q}$ pair is constrained to be compatible with the Z mass, depending on the channel. In addition, the non-τ jet momenta are constrained to be larger than 75% of the measured value. The combination with the lowest χ^2 is chosen and presented to the neural networks described below.

4.4.1. The $HZ \to H\tau^+\tau^-$ *channel*

To discriminate between $H\tau^+\tau^-$ and background events, a neural network is used with five input variables: the total missing transverse momentum of the event, the sum of the two τ jet isolation angles, the sum of the fitted transverse momenta of the τ jets with respect to their nearest hadronic jet, the kinematic consistency χ^2, and $(\eta_1 + \eta_2)$. The jet isolation angle definition for the second variable is the same as for the $H\ell^+\ell^-$ selection [3]. The last variable reflects the b-quark content of the two non-τ jets. Details of the neural network are discussed in the Appendix.

Fig. 3a shows the response of the $H\tau^+\tau^-$ neural network in the data and in simulated signal and background events. The optimal point for this selection corresponds to neural network output values larger than 0.979.

4.4.2. The $HZ \to \tau^+\tau^- q\bar{q}$ *channel*

A neural network is also used to select $HZ \to \tau^+\tau^- q\bar{q}$ events. The input variables are identical to those described in the previous subsection except that the b-tagging variable is not used. This is a limiting factor in the performance of the selection. Fig. 3b shows the neural network output in the data and simulated signal and background events. Events which have a neural network output larger than 0.980 are selected.

4.4.3. Systematic uncertainties

The main sources of systematic uncertainty in the final states with τ leptons are the reconstruction of the kinematic variables, the clustering of jets and the tagging of jets containing b quarks.

From a comparison of multihadronic events with an identified lepton, in the data and in simulated events, a slight discrepancy in the total transverse momentum distribution is observed which translates into an absolute uncertainty of 0.3% (0.2%) in the signal detection efficiency for the $H\tau^+\tau^-$ ($\tau^+\tau^- q\bar{q}$) channel. The effects from jet reconstruction are evaluated by smearing the reconstructed jet angles and energies according to the expected measurement errors. The systematic effect on the detection efficiency is 0.4% (0.1%) from the jet directions and 0.1% (0.1%) from the jet energies, in absolute terms. Uncertainties arising from the tagging of b-quark jets affect only the $H\tau^+\tau^-$ selection and are evaluated, as is described in Section 4, to be 0.9%. Therefore,

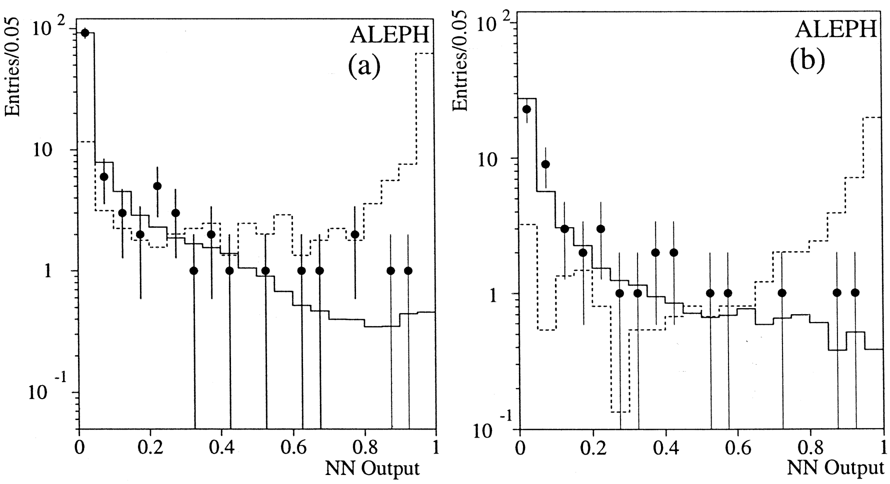

Fig. 3. The distributions of the neural network outputs for (a) the $H\tau^+\tau^-$ channel and (b) the $\tau^+\tau^- q\bar{q}$ channel. The distributions are shown for the data (points), the total simulated background (solid histogram), and the reference signal sample (dashed histogram) after the preselection cuts. The signal distributions have an arbitrary normalization.

total relative systematic uncertainties of 5.0% and 1.9% are respectively assigned to the $H\tau^+\tau^-$ and $\tau^+\tau^- q\bar{q}$ signal detection efficiencies.

5. Combined result

Seven events are selected in the data by the various selections, in agreement with the 7.2 events expected from all Standard Model background processes. Four of these events are selected in the four-jet final state. One event, selected by both the selection with cuts and the selection with neural networks, has a reconstructed Higgs boson mass of 71.5 GeV/c^2 while the other events selected with cuts (neural networks) only, have mass values of 76.1 and 85.0 GeV/c^2 (85.2 GeV/c^2). The other three candidate events are found in the leptonic final state, with masses of 67.0, 82.2, and 96.5 GeV/c^2. Fig. 4 shows the reconstructed Higgs boson mass distribution for the selected events in all channels.

The result obtained when all sub-selections are combined is displayed in Fig. 5. This result includes the lower energy ALEPH data taken at LEP1 [20] and at $\sqrt{s}$ = 161,170, and 172 GeV [3]. The lower energy data has an impact on the confidence level only for mass values lower than ~ 75 GeV/c^2. The HZ searches exclude all Higgs boson masses below 88.0 GeV/c^2 at the 95% confidence level. The average limit expected in the absence of signal is 85.3 GeV/c^2. With this expected limit, the probability to observe a limit at least as high as 88.0 GeV/c^2 is 22%.

As explained in the previous sections, a number of possible systematic effects are studied and their impacts evaluated. The uncertainties related to the selection procedure and to the inadequacies of the Monte Carlo dominate, translating into uncertainties on the selection efficiencies ranging from ~ 0.5% to 7%, depending on the final state. Following the method of Ref. [21], a small increase of the confidence level results, corresponding to a change in the mass limit of −0.1 GeV/c^2.

The mass of the Standard Model Higgs boson therefore exceeds 87.9 GeV/c^2 at the 95% confidence level. Had background subtraction been performed — with the same set of selection criteria and ignoring the related systematic uncertainties — a 95% confidence level limit of 88.3 GeV/c^2 would have been derived, with 88.3 GeV/c^2 expected.

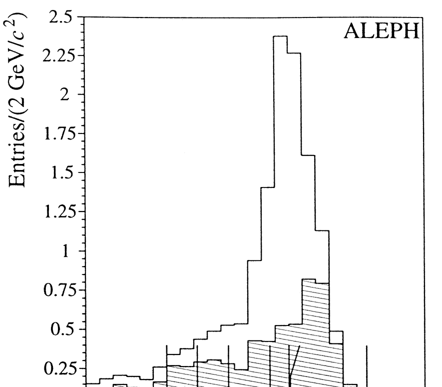

Fig. 4. The distribution of the reconstructed Higgs boson mass of the selected events in all search channels. The histogram shows the expected distribution, with the contribution from background processes (shaded) and from the reference signal (m_H = 85 GeV/c^2), normalized to the collected data luminosity. The data events are indicated with arrows. The selected events do not have equal weights in the combination procedure but have been plotted here with unit weight for convenience.

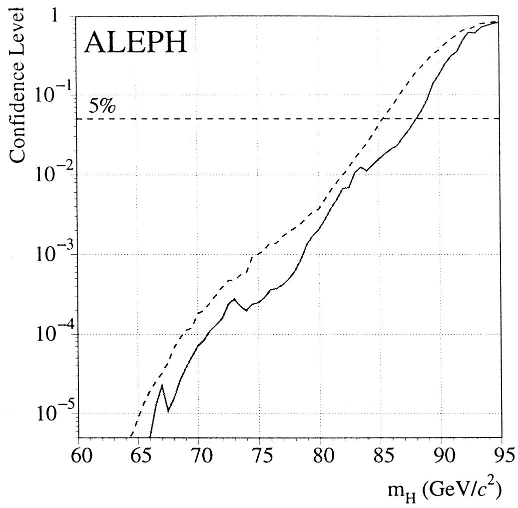

Fig. 5. The observed (solid line) and expected (dashed line) confidence level curves after all channels are combined, using the 183 GeV data as well as the results obtained at lower energies.

Table 3
A summary of the architecture and the HZ signal and background process training samples used for the neural networks described in the text

Final state	Network architecture	m_H in signal training samples (GeV/c^2)	Background training samples
$Hq\bar{q}$ (anti-$q\bar{q}$)	22-10-10-1	70, 80, 85	$q\bar{q}(\gamma)$
$Hq\bar{q}$ (anti-W^+W^-)	14-12-10-2	80	W^+W^-
$H\nu\bar{\nu}$	11-20-3	80, 85	W^+W^-, $q\bar{q}(\gamma)$
$H\tau^+\tau^-$	5-10-1	80, 85, 90	W^+W^-, ZZ
$\tau^+\tau^-q\bar{q}$	4-10-1	80, 85, 90	W^+W^-, ZZ

6. Summary

A search for evidence of the production of Higgs bosons in e^+e^- collisions at centre-of-mass energies between 181 and 184 GeV has been performed with the ALEPH detector. The major event topologies have been covered: the leptonic and missing energy final states as well as the final states with four hadronic jets and those including τ leptons. The previously published search algorithms have been improved and new selections using artificial neural networks were introduced.

In the collected data sample, corresponding to a total of $57\,pb^{-1}$, seven events were selected, in agreement with 7.2 events expected from Standard Model background processes. From this observation, a 95% confidence level lower limit on the mass of the Higgs boson is set at $87.9\,GeV/c^2$. A similar result has been reported by the L3 experiment at LEP [22].

Acknowledgements

We wish to congratulate our colleagues from the accelerator divisions for the very successful operation of LEP at high energy. We are indebted to the engineers and technicians in all of our institutions for their contribution to the excellent performance of ALEPH. Those of us from non-member countries thank CERN for its hospitality.

Appendix A

This Appendix offers more details on the neural networks used for the $H\nu\bar{\nu}$, $Hq\bar{q}$, $H\tau^+\tau^-$, and

Table 4
The complete list of inputs to the anti-$q\bar{q}$ neural network

Variable	
1.	y_{34} †
2.	γ †
3.	m_{12} †
4.	$\min(\eta_3,\eta_4)$†
5.	$(1-\eta_3)(1-\eta_4)$†
6.	$\sum_{i=1}^{4}\eta_i$ †
7.	Θ †
8.	$\langle \mathscr{M} \rangle$, average four-jet QCD matrix element.
9–10.	Boosted aplanarity of Z candidate jets.
11–12.	Boosted sphericity of Z candidate jets.
13–14.	Multiplicity of tracks with rapidity larger than 1.6, in the Z candidate jets.
15.	$\min(\theta_{ij})$, lowest interjet angle.
16.	$\cos\theta_{\not{p}}$, cosine of the polar angle of the event missing momentum vector.
17.	$\min(m_{ij}+m_{kl})$, lowest di-jet mass sum.
18–19.	$m_{\min}$,$m_{\min 2}$, the two lowest jet masses.
20–21.	$E_{\min}$,$E_{\min 2}$, the two lowest jet energies.
22.	$E_{\max}$, largest jet energy.

The variables marked with † are common to the NN-based and cut-based selections and are described in Sections 4.3 and 4.3.1.

Table 5
The complete list of inputs to the anti-W^+W^- neural network

Variable	
1.	y_{34} †
2.	γ †
3.	m_{12} †
4–5.	$\min(\eta_3,\eta_4)$,$\max(\eta_3,\eta_4)$†
6.	$(1-\eta_3)(1-\eta_4)$†
7.	$\sum_{i=1}^{4}\eta_i$ †
8–9.	$\min(\eta_1,\eta_2)$,$\max(\eta_1,\eta_2)$
10–11.	$\min(\mu_3,\mu_4)$,$\max(\mu_3,\mu_4)$
12.	B, event broadening.
13.	$E_{\min}$, lowest jet energy.
14.	$\min(m_{ij})$, lowest di-jet mass.

The variables marked with † are common to the NN-based and cut-based selections and are described in Sections 4.3 and 4.3.1.

$\tau^+\tau^- q\bar{q}$ selections. All of the neural networks are fully-connected multi-layer feed-forward networks trained with back-propagation algorithms using existing programs [23]. During an initial training phase, patterns composed of sets of discriminating variables are presented to the neural network, and the network weights are optimized to produce an output near one for signal patterns and near zero for background patterns.

The architecture and training details of the neural networks are summarized in Table 3. These parameters are chosen based upon optimal performance in Monte Carlo simulation. Each network is trained with Monte Carlo simulation of HZ signal samples as well as samples of background processes.

For the four-jet final state, only the correct pairing in $HZ \to b\bar{b}q\bar{q}$ events is presented to the neural network as the signal pattern during the training phase.

The input variables used for the anti-$q\bar{q}$ neural network in the $Hq\bar{q}$ channel are listed in Table 4.

The input variables used for the anti-W^+W^-neural network in the $Hq\bar{q}$ channel are listed in Table 5. The event broadening is computed using the two event hemispheres defined by the plane perpendicular to the event thrust axis; the quantity $B_{\rm hemi}$ is computed for each hemisphere:

$$B_{\rm hemi} = \frac{\sum_{i=1}^{N_{\rm tracks}} |p_{ti}|}{\sum_{i=1}^{N_{\rm tracks}} |p_i|},$$

where $N_{\rm tracks}$ is the number of tracks in the hemisphere, p_i is the momentum of the ith track, and p_{ti} is the transverse momentum of the ith track with respect to the thrust axis. The event broadening B is the smaller of the two $B_{\rm hemi}$ values.

References

[1] M. Grünewald, Combined Analysis of Electroweak Precision Results, talk presented at the ICHEP, Vancouver, August 1998, to appear in the proceedings.

[2] For reviews see: J.F. Gunion, H.E. Haber, G. Kane, S. Dawson, The Higgs Hunter's Guide, Addison-Wesley, 1990, and references therein. P.J. Franzini et al., in: G. Altarelli, R. Kleiss, C. Verzegnassi (Eds.), Z Physics at LEP 1, CERN 89-08, 1989. M. Carena, P. Zerwas (Conveners) et al., Higgs Physics, in: G. Altarelli, T. Sjöstrand, F. Zwirner (Eds.), Physics at LEP 2, CERN 96-01, 1996, p. 351.

[3] ALEPH Collaboration, Phys. Lett. B 412 (1997) 155.

[4] DELPHI Collaboration, E. Phys. J. 2 (1998) 1.

[5] L3 Collaboration, Phys. Lett. B 411 (1997) 373.

[6] OPAL Collaboration, E. Phys. J. 1 (1998) 425.

[7] ALEPH Collaboration, Phys. Lett. B 412 (1997) 173.

[8] ALEPH Collaboration, Nucl. Instrum. Methods A 294 (1990) 121.

[9] ALEPH Collaboration, Nucl. Instrum. Methods A 360 (1995) 481.

[10] D. Creanza et al., Construction and Performance of the New ALEPH Vertex Detector, to appear in the Proceedings of the Conference on Advanced Technology and Particle Physics, Como, Italy, October 1996.

[11] P. Janot, F. Le Diberder, Nucl. Instrum. Methods A 411 (1998) 449.

[12] See for instance: C. Peterson, T. Rögnvaldsson, An Introduction to Artificial Neural Networks, 1991 CERN School of Computing, C. Verkerk (Ed.), p. 113; L. Lönnblad, C. Peterson, T. Rögnvaldsson, Comput. Phys. Commun. 70 (1992) 167; S.R. Amendolia, Neural Networks, 1993 CERN School of Computing, C.E. Vandoni, C. Verkerk (Eds.), p. 1.

[13] P. Janot, The HZHA generator, in: G. Altarelli, T. Sjöstrand, F. Zwirner (Eds.), Physics at LEP2, CERN 96-01, 1996, vol. 2, p. 309.

[14] C. Peterson, D. Schlatter, I. Schmitt, P.M. Zerwas, Phys. Rev. D 27 (1983) 105.

[15] ALEPH Collaboration, Phys. Lett. B 357 (1995) 699; ALEPH Collaboration, Inclusive Heavy Flavour Lifetime and Mixing Measurements at ALEPH, paper #596 submitted to the EPS-HEP97 Conference, Jerusalem, August 1997.

[16] W.J. Stirling, J. Phys. G 17 (1991) 1567.

[17] D. Danckaert et al., Phys. Lett. B 114 (1982) 203.

[18] ALEPH Collaboration, Phys. Lett. B 401 (1997) 163.

[19] ALEPH Collaboration, Phys. Lett. B 440 (1998) 419.

[20] ALEPH Collaboration, Phys. Lett. B 384 (1996) 427.

[21] R.D. Cousins, V.L. Highland, Nucl. Instrum. Methods A 320 (1992) 331.

[22] L3 Collaboration, Search for the Standard Model Higgs Boson in e^+e^- Interactions at $\sqrt{s} = 183$ GeV, CERN-EP/98-052 (to appear in Phys. Lett. B).

[23] A. Zell et al., SNNS - Stuttgart Neural Network Simulator User Manual, Version 4.0, University of Stuttgart, Institute for Parallel and Distributed High Performance Computing (IPVR), Department of Computer Science, Report 6/95, 1995; L. Lönnblad, C. Peterson, T. Rögnvaldsson, JETNET 3.0: A Versatile Artificial Neural Network Package, CERN-TH 7135/94, 1994; J. Proriol, Nucl. Instrum. Methods A 337 (1994) 566.

Chapter 4

The ALEPH Experiment

4.1 LEP

LEP (1989-2000), the **L**arge **E**lectron–**P**ositron storage ring at CERN, has been built in order to make precision studies of the electroweak interaction and, if possible, to discover new physics phenomena. It can be looked upon as a factory for the production of the electroweak gauge bosons Z and $W^\pm$ through e^+e^- annihilation. LEP was operated in two phases. During phase 1, also called LEP1 (1989-1995), when LEP was mainly [1] running at a centre-of-mass energy of 91.2 GeV ($\approx m_Z$), the Z boson was mass-produced with up to about ten thousand Z particles created per day. During phase 2, also called LEP2 (1996-2000), when the centre-of-mass energy was increased beyond the threshold for the pair production of the W boson, of the order of ten $W^\pm$ pairs were produced per day. For the cross sections of these and other processes see Figure 3.1. Because electrons and positrons have opposite charges they can circulate in opposite directions in the same arrangement of focusing and bending magnets. Hence, LEP consisted of a single ring, with the shape of an octagon with rounded corners (eight straight sections of about 500 m each and eight arcs alternating around the circumference of 27 km). The 3368 dipole magnets in the arcs bend the e^+ and e^- beams, whereas the focusing is done with 808 quadrupole and 504 sextupole magnets installed both in the straight sections and in the arcs. The e^+ and e^- beams are concentrated in 4 bunches [2], where a bunch of particles is about 1 cm long, has a width of $\sim$ 350 μm and a height of $\sim$ 10 μm. For counterpropagating beams this gives 8 collision points which are arranged in the centers of the straight sections. Detectors measuring the products of the collisions were installed at every second collision point (see Fig. 4.1).

[1] In the years 1989, 1990 and 1991 energy scans were performed at 1 GeV intervals over a 7 GeV range centred at the Z peak, whereas in the years 1993 and 1995 the scans were limited to running at energies of 91.2 and 91.2±2 GeV.

[2] Also other schemes have been tried, like using bunch trains.

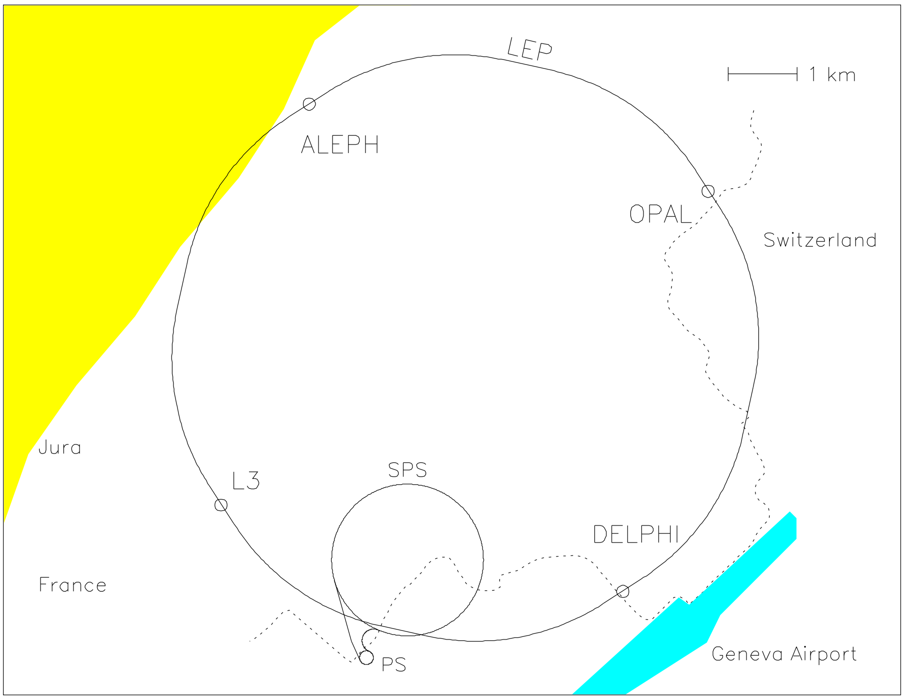

Figure 4.1: The layout of the CERN LEP collider at the French-Swiss border near Geneva. The ALEPH experiment was situated near the Jura mountains, 140 meters below surface.

During phase 1 the acceleration was performed using a copper radio-frequency (RF) system working at room temperature and consisting of 128 five-cell RF cavities with a potential voltage of 400 MV. In parallel with the successful operation at the Z peak until 1995, research and development was being carried out to provide the technology and production techniques for high gradient superconducting (SC) cavities. In 1995 few test modules of SC cavities were installed which allowed the energy to be raised to 70 GeV/beam (LEP1.5).

Phase 2 officially began in 1996 when the energy reached the threshold for the production of $W^{\pm}$ pairs for the first time, after about half of the SC cavities forseen had been installed. Physics data was taken at centre-of-mass energies of 161 and 172 GeV. During the winter shutdowns of the next two years most of the remaining superconducting cavities were installed, raising the total number to 272. In the year 1998 LEP was operated at the single energy of 94.5 GeV per beam and delivered a record integrated luminosity of almost 200 pb^{-1} per experiment. One year later, in August 1999, LEP achieved its unofficial design energy for phase 2 when it was running at 100 GeV per beam, *i.e.* at a collision energy of 200 GeV. At this energy LEP operated at the limit on many fronts; in particular the radio-frequency system which, optimistically designed for accelerating gradients of 6 MV/m, had to operate all

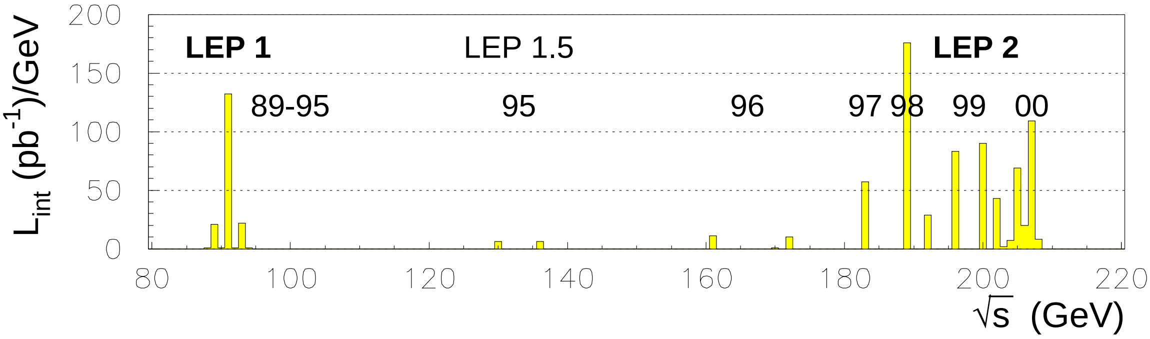

Figure 4.2: The integrated luminosity collected with the ALEPH detector at LEP in the years 1989-2000 as a function of the centre-of-mass energy (the histogram is in bins of 1 GeV). The total integrated luminosity is $\sim$ 179 pb^{-1} around the Z peak and $\sim$ 715 pb^{-1} at LEP2 energies. The increase of the centre-of-mass energy during the LEP2 phase is indicated by the year numbers.

288 cavities at an average gradient of 7 MV/m. The total RF voltage per turn needed was 3400 MV, and the synchrotron radiation beam power at this energy was 18 MW. An overview of the various energies, the number of SC cavities installed and the total RF voltage available is given in Table 4.1. The steps of increase in energy during the years can also be seen in Figure 4.2, which shows the integrated luminosity collected by the ALEPH experiment as a function of $\sqrt{s}$.

In the final year of LEP running, *i.e.* the year 2000, with the utmost effort [3] more than 200 pb^{-1} of data were collected at centre-of-mass energies greater than 205 GeV and the highest energy achieved for a short time was 209.2 GeV. Despite a request from the physics community to continue in 2001, CERN's Director General decided to shut down LEP forever on November 17$^{\text{th}}$, 2000.

4.2 The cavity story

A significant increase in energy in the year 2001 would not have been possible (though there was space for putting more cavities), because the production of SC cavities was stopped [4] already in 1997, and no spare ones were available. It was estimated that an energy of 220 GeV could have been reached, if all the space available would have been

[3] For example, the nominal radio-frequency of 352 MHz was reduced by about 100 Hz to benefit from the dipolar magnetic field seen by the beams in the focusing quadrupoles, effectively increasing the bending radius of LEP (*cf.* next section). Using (otherwise unused) orbit correctors to act as magnetic dipoles had a similar effect.

[4] The production was stopped mainly as a result of the pressure on getting LHC approved and because it was claimed (*cf.* Chapter 7 on indirect searches) that the Higgs boson would most probably be lighter than 100 GeV anyway. To get new SC cavities produced would have taken more than a year, as stated by the CERN accelerator director [28].

filled with SC cavities. Since for the discovery of the Higgs boson at LEP it is crucial to run at the highest possible energy, in the remaining part of this section the theory behind the question on the maximum energy of a collider is briefly discussed.

A relativistic charged particle with energy E moving on a circle with radius r loses energy by synchrotron radiation according to the formula [29]

$$\delta E = \frac{1}{4\pi\epsilon_0}\frac{4\pi}{3}\frac{e^2\beta^3\gamma^4}{r} \approx 8.85\cdot 10^{-2}\,\frac{(E[\text{GeV}])^4}{r[\text{m}]}, \tag{4.1}$$

where δE is the energy loss per turn (in units of MeV for the term on the right hand side). Using the bending radius $r = 3.1$ km in the dipole magnets at LEP, the relative energy loss $\delta E/E$ for typical beam energies at the two LEP phases is given in the following table:

LEP 1:	$E_{\text{beam}} =$	45.6 GeV	$\delta E_{\text{beam}}/E_{\text{beam}} =$	0.27%
LEP 2:		100 GeV		2.85%.

This means, for example, that in order to maintain stable beams at $\sqrt{s} = 200$ GeV in theory a minimum RF voltage of 2850 MV is necessary to compensate for the energy losses. In reality, with this RF voltage the LEP accelerator was only operated at an energy of $\sqrt{s} = 189$ GeV (*cf.* Table 4.1), with a safety margin of 200 MV (allowing two klystrons to trip without losing the beams). In the final year of LEP running the beam energy was increased slightly by reducing this safety margin to 100 MV, with only a moderate reduction of the average fill duration.

Year	$\sqrt{s}$ (GeV)	# Cu cavities	# SC cavities	RF (MV)
1989-1995	m_Z	128	none	400
1996	161, 172	128	144, 176	1600, 2000
1997	183	52	240	2500
1998	189	52	272	2850
1999	192 $\rightarrow$ 202	48	288	3000 $\rightarrow$ 3550
2000	205 $\rightarrow$ 209.2	56	288	3650

Table 4.1: Number of copper and superconducting cavities installed in the LEP tunnel in various years of running at the energies given in column two. The last column shows the total RF voltage available.

4.3 The ALEPH detector

The papers presented in this *Habilitationsschrift* are based on data taken with the ALEPH detector [5]. This general-purpose detector for measuring particles created in e^+e^- collisions is shown in Fig. 4.3 and described in detail in [30–32]. It can briefly be characterized as a universal detector fitted with a very large-diameter track chamber, a high magnetic field from a superconducting coil and gas calorimeters.

Interesting physics events are selected using a flexible three stage trigger system. The Level-1 trigger makes a decision within 5 μs based on analog signals from the main detector components (energy deposition in the calorimeters, track segments from the tracking devices). Since the time between two successive beam crossings is 22 μs (with four bunches per beam), this trigger level operates with no dead time. If the Level-1 answer is positive, the Level-2 trigger, based on hard-wired processors, looks for tracks in the time projection chamber (TPC) coming from the beam interaction region. It has to make a decision whether the event should be thrown away or kept for further

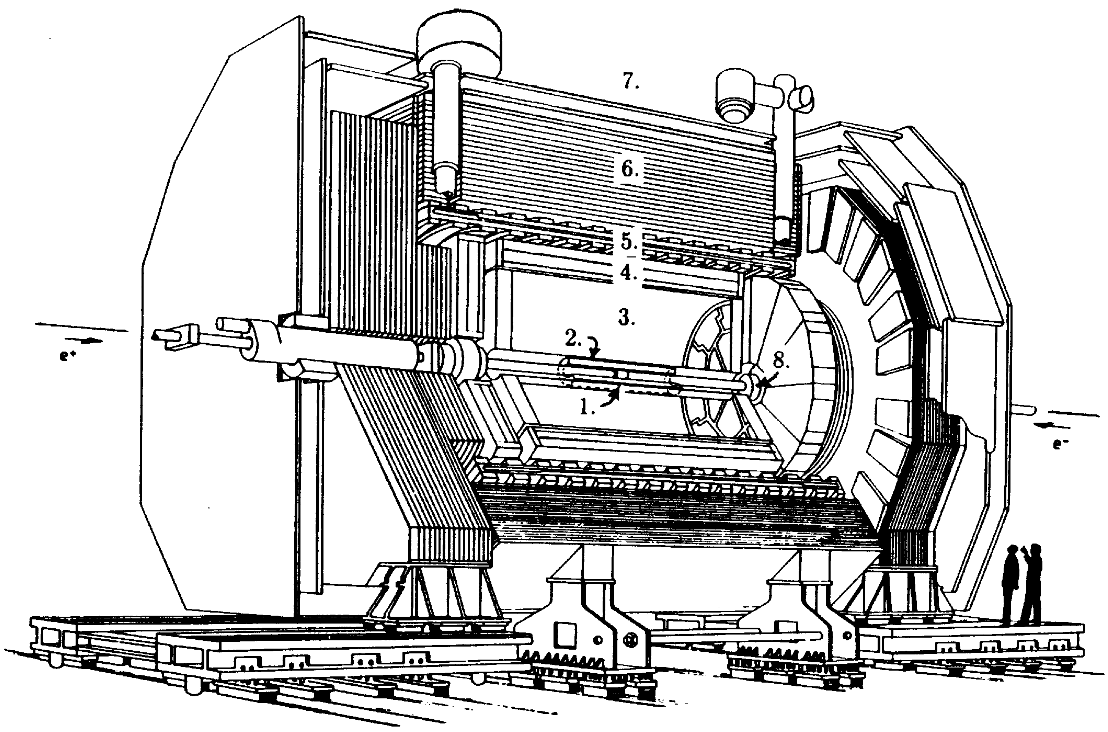

Figure 4.3: The ALEPH detector: 1. silicon vertex detector, 2. drift chamber, 3. time projection chamber, 4. electromagnetic calorimeter, 5. superconducting magnet coil, 6. hadron calorimeter, 7. muon chambers, 8. luminosity monitors.

[5] By the time of this writing the ALEPH detector has already been dismantled and parts of it have been distributed to various institutes that have participated in the ALEPH experiment.

inspection by the Level-3 trigger system within 50 μs. Finally, the Level-3 trigger tries to identify genuine e^+e^- interactions with the help of information from all detector components. If positive, the event is read out and written on a storage medium, where is it then available for offline reconstruction.

Event rates were already low at LEP1 (with a rate of ~ 0.5 Hz for Z events at the peak), but they are even lower at LEP2. Therefore the trigger system just has to reduce the background, mainly coming from beam gas interactions and off momentum beam particles hitting the vacuum pipe or the collimators somewhere close to the detector, to a manageable level. The trigger efficiency for hadronic Z decays was measured [31] to be practically 100%. As a consequence at LEP2 the efficiency for triggering events which contain a standard model Higgs boson of a mass comparable to m_Z is also close to 100%, mainly because in about 92% of these events the Higgs boson decays hadronically (*cf.* Sec. 3.2) and because for the majority of the remaining events (where $H \to \tau^+\tau^-$) there is a Z particle that decays hadronically. These are practically the only topologies that the standard model Higgs boson is searched for at LEP2 anyway (except for $HZ \to \tau^+\tau^-\ell^+\ell^-$; for details see Sec. 3.3).

4.3.1 Energy flow

Offline reconstruction of an event yields the 4-momenta of charged and neutral particles that best fit the signals registered with the detector. Charged particles reconstructed in the tracking devices are assumed to be pions if they are not identified as electrons (by their shower profile in the electromagnetic calorimeter) or muons (with the help of the hadron calorimeter and the muon chambers). Neutral particles are reconstructed from energy deposits in the calorimeters. However, also charged particles lose energy in the calorimeters. To solve this problem, but also in order to calculate the total energy of an event (which ideally should be $2E_{\mathrm{beam}}$), the so-called energy flow algorithm [31] has been developed. It subtracts the energy that the charged particles are expected to deposit in the calorimeters from the energy of the measured calorimeter objects. The remaining energy in the calorimeters is used to identify photons (neutral electromagnetic energy) and neutral hadrons.

The output of the energy flow algorithm is a set of *energy flow objects* (electrons, muons, photons, charged and neutral hadrons). These energy flow objects in turn are the input to the Higgs search analyses, *e.g.* they are used to define jets, calculate event shape variables and invariant masses, or any other event characteristic. In the context of the energy flow algorithm the ALEPH detector as a whole effectively behaves like a single big calorimeter with a relative energy resolution of [31]

$$\frac{\sigma(E)}{E} = \frac{0.60}{\sqrt{E}} + \frac{0.6}{E} \qquad (E \text{ in GeV}) \tag{4.2}$$

as obtained for well contained[6] hadronic Z decays (*cf.* Fig. 4.4). This lies in between the ideal performances (particles at normal incidence) of the electromagnetic and the hadron calorimeters, where the corresponding coefficients in front of the $1/\sqrt{E}$ term are 0.18 and 0.85, respectively, but is a factor of two better then the energy resolution obtained by simply summing up all the energy deposits in the calorimeters.

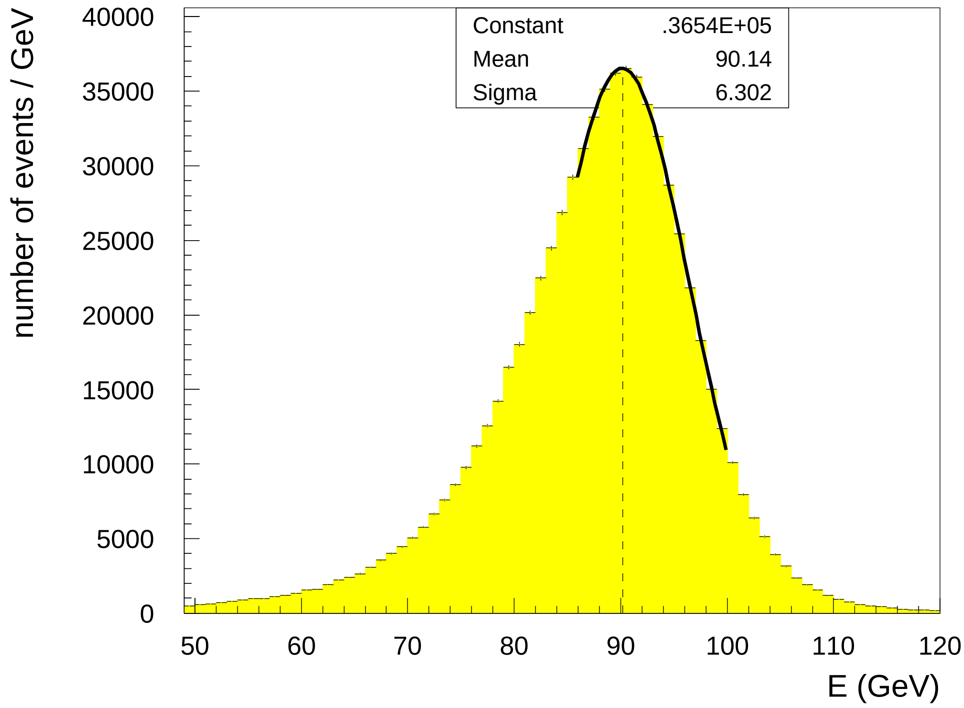

Figure 4.4: Distribution of the total energy for hadronic Z decays as calculated with the energy flow algorithm in the context of an analysis [33] of ALEPH data taken in 1992 at the Z peak. A Gaussian fit (shown on top of the histogram) has been performed in the range 86 GeV $< E <$ 100 GeV, giving a mean value[7] of 90.14 GeV (vertical line) and a width of 6.3 GeV, in agreement with Eq. (4.2). This range has been chosen because for $E \lesssim 86$ GeV the distribution quickly gets asymmetric due to energy losses, not due to the detector or the algorithm, but due to physics processes like initial state radiation or neutrinos from heavy quark decays. This distribution is nicely reproduced [31] with the Monte Carlo simulation of the ALEPH experiment by using events from an event generator.

[6]Well contained means: no energy deposit within a cone of 12° around the beam axis and less than 10% of the total energy within a cone of 30° around the beam axis.

[7]The mean value of the fit is lower than the nominal centre-of-mass energy used in 1992 by about 1 GeV. A Monte Carlo study shows that half of this is due to the neutrinos and the other half is due to energy escaping undetected at very low angles to the beam axis. The latter can be improved by requesting well contained events (which was not done in [33]).

4.3.2 b-tagging

For masses $10 \lesssim m_{\mathrm{H}} \lesssim 130$ GeV/c^2 the standard model Higgs boson decays predominantly into a pair of b-quarks. Therefore a key element for finding the Higgs boson at LEP2 is a tool (hardware and software) that allows the detection of B-hadrons, *i.e.* particles containing a b-quark. B-hadrons can manifest themselves in several ways. Their mean lifetime of about 1.5 ps, for example, allows them to travel (on average) a few mm away from the interaction point before they decay at a separate vertex. Another indication for the presence of a B-hadron in an event is a lepton with a relatively high transverse momentum with respect to the jet axis (as a result of a semileptonic B-decay).

On the hardware side a so-called vertex detector (VDET) serves the purpose of detecting B-hadrons by very precisely [8] measuring charged tracks near the interaction point, which allows to reconstruct the displaced vertices of the B-decays. Motivated

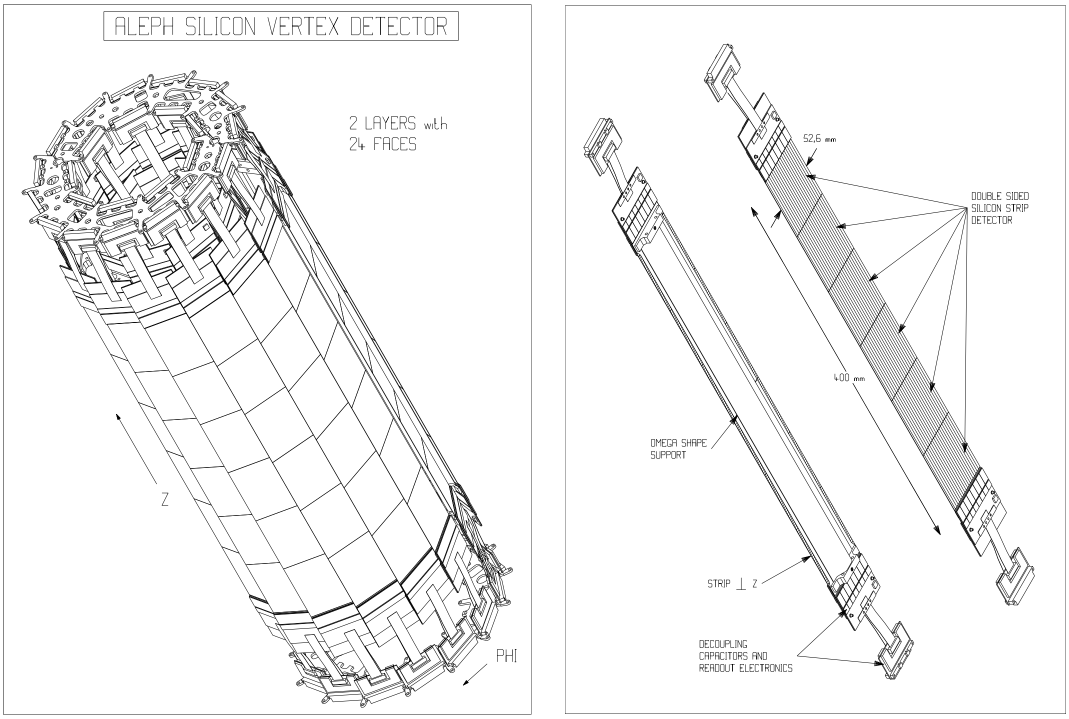

Figure 4.5: VDET2, the upgraded ALEPH silicon vertex detector.
Left: The cylindrical detector consists of two concentric shells of so-called VDET faces, with average radii of 6.3 cm (9 faces) and 11 cm (15 faces). Right: Two views of a VDET face. Each face consists of 6 double sided silicon strip detectors with dimensions $52.6 \times 65.4 \times 0.3$ mm.

[8] The hit resolution of the upgraded VDET is 12 μm in the azimuthal direction and 15-50 μm in the z-direction (along the beam line) for incident angles between 0° and 70°.

by the desire to increase the efficiency for the detection of the Higgs boson decay into pairs of b-quarks, the ALEPH collaboration decided to upgrade the previously installed VDET for the LEP2 data taking. The new silicon vertex detector, called VDET2 (see Fig. 4.5), was installed during the spring of 1996. VDET2 extended the angular coverage up to $|\cos\theta| \leq 0.95$ (being twice as long as before) and reduced the material present in the tracking volume by about a factor of two.

On the software side so-called b-tagging algorithms have been developed that give a measure of the probability that a jet originates from a primary b-quark. They use information available through special detector components (like the VDET), but also global event information (like the multiplicity and the transverse momenta of particles in a jet) available through the energy flow objects. To benefit from all the information simultaneously, in the searches for the Higgs bosons up to six variables discriminating between b-jets and light quark jets are combined into one global variable. The task of deciding how much weight to give to each discriminating variable is performed by a so-called Neural Network on an event by event basis. Details of this procedure are given in the paper of Sec 5.4.

Chapter 5

General Two Higgs Doublet Models

One Higgs doublet is the minimum number needed for the Higgs mechanism to work, but there is no strong theoretical argument which favors this minimal choice. On the other hand, given the fact that at the moment there is no experimental information concerning the Higgs sector, it is difficult to judge how the standard model should be extended. To be clear: from an experimental point of view at the moment there is no reason to be unhappy with the standard model since it successfully describes all measurements within the statistical scatter. Arguments that try to "discredit" the standard model are mainly of a theoretical nature. As a consequence, in deciding which options are worthy of discussion theoretical arguments must be a guideline.

As mentioned earlier, doublets are the only SU(2) representations of the Higgs fields that lead to $m_{\mathrm{W}} = m_{\mathrm{Z}} \cos\theta_W$ at tree level, as favored by the experiment. Therefore this chapter will be restricted to the discussion of the implications of models with just one more Higgs doublet, called two Higgs doublet models (2HDM). A special case of a 2HDM is the so-called minimal supersymmetric extension of the standard model (MSSM), which explicitly requires two doublets of scalar Higgs fields (*cf.* next section).

Two Higgs doublet models are usually built in such a way as to guarantee the absence of tree level flavor-changing neutral currents, which have not been observed experimentally. This is achieved by requiring that all fermions of a given charge couple to no more than one Higgs doublet. With this restriction there are basically four different ways [13] in which the Higgs doublets can couple to fermions in the framework of 2HDM. The most common choice, called type II models (which is also the structure assumed in the MSSM), is where one of the Higgs doublets couples both to down type quarks and to leptons, and the other doublet couples to up type quarks. Another choice is the type I models, where only one of the Higgs doublets is allowed to couple to fermions (a special case of such a model leads to a so-called fermiophobic Higgs boson, which is also searched for in the ALEPH experiment). The remaining two types are of minor importance.

Given the two complex SU(2) doublet scalar fields Φ_1 and Φ_2 one has to define the Higgs potential, which in the most general gauge invariant form is given by [13]

$$\begin{aligned} V(\Phi_1,\Phi_2) &= \lambda_1(\Phi_1^\dagger\Phi_1 - v_1^2)^2 + \lambda_2(\Phi_2^\dagger\Phi_2 - v_2^2)^2 \\ &+\lambda_3\left[(\Phi_1^\dagger\Phi_1 - v_1^2) + (\Phi_2^\dagger\Phi_2 - v_2^2)\right]^2 \\ &+\lambda_4\left[(\Phi_1^\dagger\Phi_1)(\Phi_2^\dagger\Phi_2) - (\Phi_1^\dagger\Phi_2)(\Phi_2^\dagger\Phi_1)\right] \\ &+\lambda_5\left[\mathrm{Re}(\Phi_1^\dagger\Phi_2) - v_1 v_2\cos\xi\right]^2 \\ &+\lambda_6\left[\mathrm{Im}(\Phi_1^\dagger\Phi_2) - v_1 v_2\sin\xi\right]^2 . \end{aligned} \tag{5.1}$$

Here the λ_i are real parameters and the v_i are the vacuum expectation values of the two doublets. The phase ξ has to be introduced if the Higgs sector should accommodate CP-violation, which is not considered further here. To have a non-trivial absolute minimum of the Higgs potential the λ_i are required to be non-negative. At this minimum the two doublet fields are given by

$$\Phi_{1,\,\mathrm{g.s.}} = \begin{pmatrix} 0 \\ v_1 \end{pmatrix} \quad \text{and} \quad \Phi_{2,\,\mathrm{g.s.}} = \begin{pmatrix} 0 \\ v_2 \end{pmatrix}, \tag{5.2}$$

where there are no factors of $\sqrt{2}$ compared to (2.14) because of the special parametrization of the potential V in terms of the v_i. The Higgs and Goldstone fields are obtained by expanding the fields Φ_i around the minima. One of the most important parameters in the phenomenology of 2HDM (especially in the MSSM) is the ratio of the vacuum expectation values for the two scalar fields, defined as

$$\tan\beta := \frac{v_2}{v_1}. \tag{5.3}$$

It is also convenient to define

$$v := \sqrt{v_1^2 + v_2^2}\,, \tag{5.4}$$

where v has the same meaning and the same value as in the standard model, *i.e.* it is fixed by the W mass through (2.16). The next step, namely extracting the masses and the couplings of the fields, closely follows the procedure outlined in Sec. 2.3.1 for the standard model, though in the case of two doublets it is more complicated. For details see Ref. [13]. Here only the most important results are quoted. Spontaneous symmetry breaking puts three out of the eight degrees of freedom of the scalar fields into the longitudinal polarization states of the W and Z bosons. The remaining five give rise to the following scalar particles:

- a pair of charged Higgs bosons $H^\pm$,
- a CP-odd neutral Higgs boson A
- and two CP-even neutral Higgs bosons h and H, with the usual convention that h is the lighter of the two.

The physical Higgs mass eigenstates h and H are orthogonal linear combinations of the neutral CP-even Higgs fields $(\mathrm{Re}\,\phi_1^0 - v_1)$ and $(\mathrm{Re}\,\phi_2^0 - v_2)$, where ϕ_i^0 is defined as the lower component of the scalar doublet Φ_i (*cf.* Eq. 2.15):

$$\begin{aligned} \mathrm{H} &= \sqrt{2}\left[(\mathrm{Re}\,\phi_1^0 - v_1)\cos\alpha + (\mathrm{Re}\,\phi_2^0 - v_2)\sin\alpha\right], \\ \mathrm{h} &= \sqrt{2}\left[-(\mathrm{Re}\,\phi_1^0 - v_1)\sin\alpha + (\mathrm{Re}\,\phi_2^0 - v_2)\cos\alpha\right]. \end{aligned} \tag{5.5}$$

Whereas the standard model has only one unknown parameter, CP-conserving 2HDM have six free parameters in the Higgs sector, which are

- the four Higgs boson masses m_h, m_H, m_A and $m_{\mathrm{H}^\pm}$,
- the ratio of the vacuum expectation values $\tan\beta$
- and the mixing angle α of (5.5).

The angles α and β are chosen such that $-\pi/2 \le \alpha \le 0 \le \beta \le \pi/2$. Fermion masses arise due to Yukawa coupling. Equations similar to (2.27) hold, where v has to be replaced by either v_1 or v_2, depending on which Higgs doublet couples to the fermion in question. As mentioned above, the CP-even neutral Higgs fields mix. Rotating the weak eigenstates to the mass eigenstates one obtains the dependence of the Higgs boson couplings to the fermions and gauge bosons on the parameters α and β. In the case of the gauge bosons the Higgs couplings follow from gauge invariance and thus are model independent. Here we are interested in the hZZ vertex (*cf.* Fig. 5.1a), which is the relevant one for the experimental Higgs boson searches at LEP2 (the Higgs boson H is too heavy to be produced at LEP2). The vertex factor is given by (leaving out possible factors of i)

$$g_\mathrm{hzz} = \frac{g m_\mathrm{Z}}{\cos\theta_W}\sin(\beta - \alpha). \tag{5.6}$$

There are no tree level couplings of A or $\mathrm{H}^\pm$ to WW or ZZ. However, trilinear couplings of two different Higgs bosons to one gauge boson exist. At LEP2 the hAZ vertex is relevant (*cf.* Fig. 5.1b). Also in this case gauge invariance determines the strength of

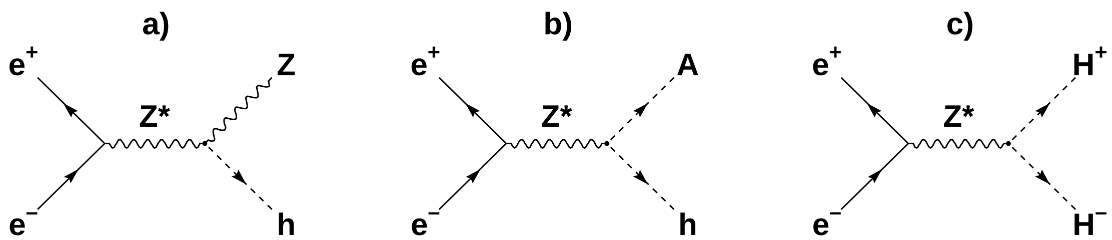

Figure 5.1: Tree level Feynman diagrams for Higgs boson production in 2HDM: a) the Higgs–strahlung process, b) associated production and c) pair production of charged Higgs bosons.

the coupling:

$$g_{\mathrm{hAZ}} = \frac{g}{2\cos\theta_W}\ \cos(\beta - \alpha). \tag{5.7}$$

In (5.6) and (5.7) one of the couplings can be suppressed if either $\sin(\beta-\alpha)$ or $\cos(\beta-\alpha)$ is small, but they cannot both vanish simultaneously. This feature is exploited in the search for the neutral Higgs bosons h and A. The tree level Feynman diagram for the production of charged Higgs bosons in given in Fig. 5.1c.

5.1 Supersymmetry and the MSSM

As shown above, it is relatively straightforward to extend the minimal (one-doublet) Higgs sector of the standard model. However, there are a number of theoretical reasons to suppose that the standard model itself is only part of a more general theory. Indeed, it is some deep-rooted problems in the Higgs sector of the standard model, referred to as naturalness, fine tuning and hierarchy problems (reviewed *e.g.* in [34,35]), that have led people to look beyond the standard model. Another shortcoming of the standard model comes from its inability to include in a consistent way gravity. Attempts to include gravity within the framework of quantum field theories lead to a non-renormalizable theory. Radiative corrections become more and more divergent in higher orders of perturbation theory, which is also at the heart of the problems mentioned above.

Symmetries have proven to be very useful in physics. As mentioned in Chapter 2, the symmetry of gauge theories allowed to get rid of divergencies when calculating higher order processes ("renormalization procedure"). Below it will be shown that introducing a new symmetry can solve the hierarchy problem, thereby restoring naturalness.

5.1.1 The hierarchy problem of the standard model

In the standard model, the calculation of first order corrections to the Higgs boson mass squared yields the following quadratically divergent expression arising from standard model particle loop graphs (*cf.* Fig. 5.2):

$$\delta m_{\mathrm{H}}^2 \sim g^2 \int^{\Lambda} \frac{\mathrm{d}^4 k}{k^2} \sim g^2 \Lambda^2 \tag{5.8}$$

Here g is the coupling between the Higgs boson and the fermion and Λ acts as a cut-off parameter for the effective standard model theory, which is assumed to be embedded in a more complete theory at scale Λ. As mentioned in Sec. 2.5, Λ can be smaller than the Planck scale. For example, calculations using renormalization group equations show [36] that the three gauge couplings approach each other at the energy

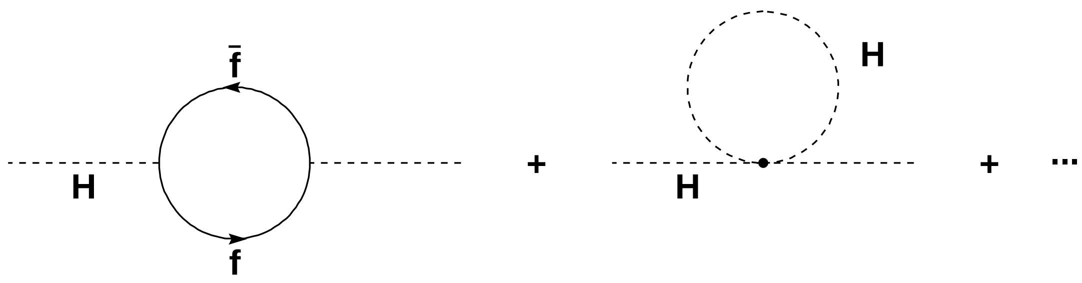

Figure 5.2: Feynman diagrams of loop graphs contributing to quantum corrections to the Higgs boson mass.

scale $\Lambda_{\mathrm{GUT}} \sim 10^{14} - 10^{16}$ GeV (*cf.* Fig. 5.3-left), therefore it is tempting to assume that a so-called grand unifying theory (GUT) sets in there.

GUTs (including the standard model) have two energy scales:

- the electroweak scale $v \sim 10^2$ GeV, which is also the scale where the mass of the Higgs boson is expected (*cf.* Sec. 2.5 on mass bounds),
- and the GUT scale $\Lambda_{\mathrm{GUT}} \sim 10^{16}$ GeV,

but radiative correction destabilize the Higgs mass, trying to make it of the order of Λ_{GUT}. Keeping the radiative corrections small with respect to much larger energy scales requires a procedure known as "fine-tuning", which implies iterative adjustment of the model parameters when going to higher order in perturbation theory. Of course

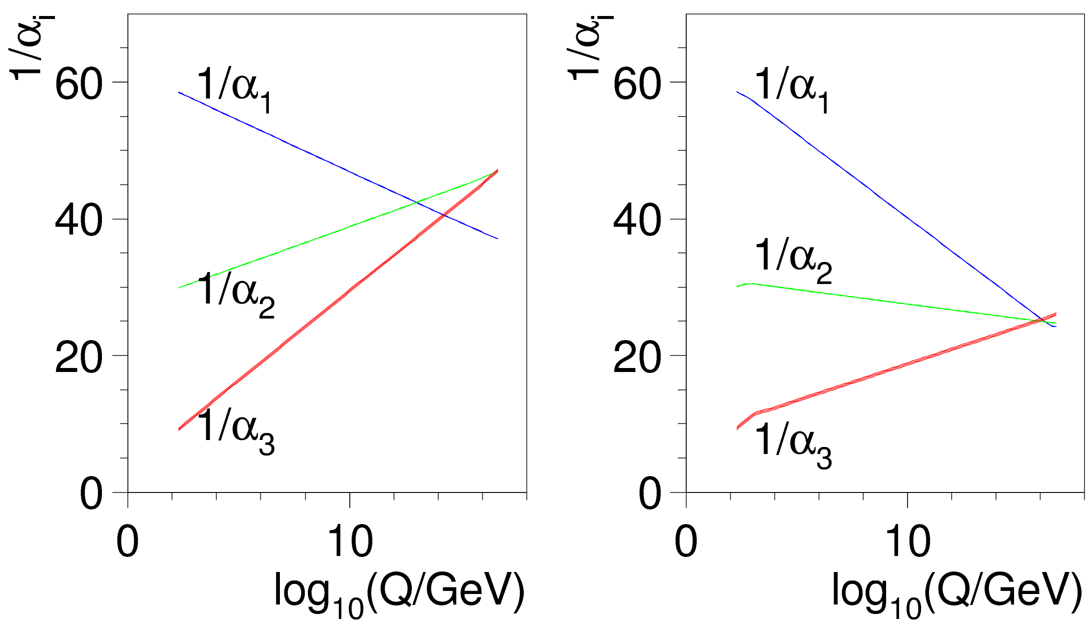

Figure 5.3: Running of the three gauge couplings in the standard model (left) and the MSSM (right). In the MSSM gauge coupling unification is possible due to threshold corrections from supersymmetric particles.

renormalization could be applied here. However, in each order of perturbation theory a fine tuning of $\mathcal{O}(10^{-14})$ would be needed, which is assumed to be "unnatural".

These consideration have led to the invention of supersymmetry [1] (SUSY) [14], which says that for each standard model particle there exists a so-called superpartner with the same mass and couplings, but with half a unit of spin less (or more, as in the case of scalar particles like the Higgs bosons). Table 5.1 displays the relationship between ordinary particles and their superpartners. Obviously this symmetry can not be exact since no scalar electron is known. Breaking the symmetry can be achieved by introducing additional terms, called soft supersymmetry breaking terms, into the Lagrangian of the theory. For the phenomenology of supersymmetry breaking (mSUGRA, GMSB) see Refs. [40, 41].

Anyway, a theory based on supersymmetry has to be structured in such a way as to maintain the success of the standard model in describing precision electroweak data. Consequently, this model is called the supersymmetric extension of the standard model (MSSM).

Among others, the MSSM has the following properties:

- gauge coupling unification becomes exact (*cf.* Fig. 5.3-right);
- it can be extrapolated up to the large energy scales in a well defined way;
- the Higgs mass is stabilized by the introduction of superpartners; fermion and boson contributions to δm_{H}^2 cancel in exact SUSY and naturalness is recovered.

In broken SUSY the correction to the Higgs mass is given by

$$\delta m_{\mathrm{H}}^2 \sim g^2 \left(\tilde{m}^2 - m^2\right), \tag{5.9}$$

where $\tilde{m}$ is the mass of the supersymmetric particle $\tilde{\mathrm{f}}$ (see Fig. 5.4). Therefore, for $\tilde{m} \lesssim \mathcal{O}(1\ \mathrm{TeV})$ any fine tuning is avoided.

The conclusion is that it is natural to have a light Higgs boson in the MSSM ($m_{\mathrm{H}} \sim v$) because of the presence of a higher symmetry that cures the fine-tuning and hierarchy problems. Moreover, the Higgs sector is stable at the electroweak scale even in the context of high energy GUT scales.

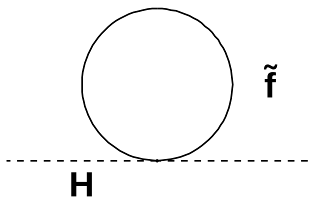

Figure 5.4: Feynman diagram in SUSY canceling the quadratic divergent contribution to δm_{H}^2 from the first diagram of Fig. 5.2 (the sfermion $\tilde{\mathrm{f}}$ is a boson).

[1] Very elementary, supersymmetry is defined as a symmetry that connects bosons and fermions.

5.2 The MSSM — its parameters and particles

As there is a section on the parameters and particles of the standard model (Sec. 2.4), the equivalent section for the MSSM is given here. Not counting the standard model paramters, the MSSM has 105 free parameters. With the assumption of universal masses[2] for superparticles of the same spin, the 105 parameters can be reduced to five free parameters. Usually they are chosen as the gaugino mass $m_{1/2}$ (unifying the mass parameters for the three types of gauginos — corresponding to the three gauge couplings), the scalar mass m_0 (unifying all squark and slepton masses), the (unified) trilinear Higgs-sfermion coupling A_0, $\tan\beta$ and the sign of the Higgs mixing parameter μ. In the literature this model is referred to as the constrained MSSM. The particle content of the MSSM is displayed in Table 5.1.

particles		spin	superpartners		spin
quarks	q	$\frac{1}{2}$	squarks	$\tilde{q}_L$,$\tilde{q}_R$	0
leptons	ℓ	$\frac{1}{2}$	sleptons	$\tilde{\ell}_L$,$\tilde{\ell}_R$	0
gauge bosons	γ,Z,$W^{\pm}$,g	1	gauginos		$\frac{1}{2}$
Higgs bosons	h,H,A,$H^{\pm}$	0	higgsinos		$\frac{1}{2}$

Table 5.1: Particle content of the MSSM. Since SU(2)×U(1) gauginos (photino, bino, winos) and higgsinos of the same electric charge have the same quantum numbers they can mix. The linear combinations forming the mass eigenstates are called neutralinos ($\tilde{\chi}_i^0$, i = 1,4) and charginos ($\tilde{\chi}_i^{\pm}$, i = 1,2).

5.3 The Higgs sector of the MSSM

The minimal supersymmetric extension of the standard model requires[3] two doublets of scalar Higgs fields to provide masses for the charged fermions. The first doublet Φ_1 (with hypercharge $Y = -1$) exclusively couples to charged leptons and down type quarks, whereas the second doublet Φ_2 ($Y = +1$) couples only to up-type quarks. Therefore the MSSM is a 2HDM of type II. Furthermore, supersymmetry imposes constraints on the Higgs sector of this model. For example, the terms of order four in the Higgs potential have to respect supersymmetry. This imposes relations between the λ_i of (5.1). Also the quartic couplings are not free but identical to the electroweak gauge couplings (in contrast to the quartic coupling λ of the Higgs potential in the

[2]Most models assume the masses of the particles to be identical (unified) at high energies (GUT) and only to differ at low energies.

[3]This requirement arises from a technical property of supersymmetric models.

standard model, which is a free parameter). As a consequence of the new symmetry two parameters are sufficient to parameterize the Higgs sector of the MSSM at tree level, *e.g.* m_{A} and $\tan\beta$ (also the combination m_{h} and $\tan\beta$ is used). Consequently, the other four parameters m_{h}, m_{H}, $m_{\mathrm{H}^\pm}$ and α are calculable as a function of m_{A} and $\tan\beta$ [13]:

$$m^2_{\mathrm{h,H}} = \frac{1}{2}\left(m^2_{\mathrm{A}} + m^2_{\mathrm{Z}} \mp \sqrt{(m^2_{\mathrm{A}} + m^2_{\mathrm{Z}})^2 - 4m^2_{\mathrm{A}} m^2_{\mathrm{Z}} \cos^2 2\beta}\right) \tag{5.10}$$

$$m^2_{\mathrm{H}^\pm} = m^2_{\mathrm{A}} + m^2_{\mathrm{W}} \tag{5.11}$$

$$\sin 2\alpha = -\sin 2\beta \left(\frac{m^2_{\mathrm{H}} + m^2_{\mathrm{h}}}{m^2_{\mathrm{H}} - m^2_{\mathrm{h}}}\right) \tag{5.12}$$

The mixing angle α is uniquely defined through (5.12), because by construction it lies in the range $-\pi/2 \leq \alpha \leq 0$.

5.3.1 Tree level mass bounds

A number of important inequalities can be derived from the expressions for the tree level Higgs boson masses given in (5.10) and (5.11):

- $m_{\mathrm{h}} < m_{\mathrm{Z}}$ $\quad (m_{\mathrm{h}} < \min\{m_{\mathrm{Z}}, m_{\mathrm{A}}\})$
- $m_{\mathrm{H}} > m_{\mathrm{Z}}$ $\quad (m_{\mathrm{H}} > \max\{m_{\mathrm{Z}}, m_{\mathrm{A}}\})$
- $m_{\mathrm{H}^\pm} > m_{\mathrm{W}}$ $\quad (m_{\mathrm{H}^\pm} > \max\{m_{\mathrm{W}}, m_{\mathrm{A}}\})$.

From the first line it follows that at least one light Higgs boson should exist in the MSSM. An interesting limiting case occurs when m_{A} gets large ($m_{\mathrm{A}} \gg m_{\mathrm{Z}}$ at fixed $\tan\beta$), then from the above relations it follows that also m_{H} and $m_{\mathrm{H}^\pm}$ get large and the three Higgs bosons A, H and $\mathrm{H}^\pm$ effectively decouple from the theory. Only the single CP-even scalar h is left in the Higgs sector, and it is found to be identical to the Higgs boson of the minimal standard model [4]. This scenario [38], referred to as the *decoupling limit*, is not restricted to the MSSM but also exists in general 2HDM.

The non-discovery of a Higgs boson at LEP would almost have ruled out the MSSM according to the tree level mass relation $m_{\mathrm{h}} < m_{\mathrm{Z}}$ (*cf.* the combined LEP limit $m_{\mathrm{h}} >$ 91.0 GeV/c^2 given in Table 1.1). However, when radiative corrections are included the upper bound on m_{H} is increased significantly, as shown in the next section.

5.3.2 Radiative corrections to the Higgs boson mass m_{h}

In lowest order the mass of a Higgs boson depends only on the masses of the gauge bosons as well as on the masses of the other Higgs bosons. Only in higher order corrections from the interactions with fermions come in. As the coupling to a fermion

[4] This follows because it can be shown that in this limit the couplings of the h boson to fermions and gauge boson are equivalent to those of the Higgs boson of the standard model.

is proportional to the mass of the fermion, the largest effect is expected from the top quark. Again, we are not interested in the value of the mass m_{h} itself but in the upper bound which, in one-loop [5] leading logarithmic approximation (LLA), is given by [39]

$$m_{\mathrm{h}}^2 \leq m_{\mathrm{Z}}^2 \cos^2\beta + \frac{3g^2 m_{\mathrm{t}}^4}{8\pi^2 m_{\mathrm{W}}^2} \ln \frac{m_{\tilde{\mathrm{t}}_1} m_{\tilde{\mathrm{t}}_2}}{m_{\mathrm{t}}^2}, \tag{5.13}$$

where $\tilde{\mathrm{t}}_1$ and $\tilde{\mathrm{t}}_2$ are the two top squark mass eigenstates. For $\cos\beta = 1$, $m_{\mathrm{t}} = 175$ GeV/c^2 and $m_{\tilde{\mathrm{t}}_1} = m_{\tilde{\mathrm{t}}_2} = 1$ (2) TeV one obtains

$$m_{\mathrm{h}} \lesssim 125\ (136)\ \mathrm{GeV}/c^2. \tag{5.14}$$

Actually this represents the strongest experimentally testable prediction of the MSSM. This limit is very sensitive to the top quark mass, but also the mixing in the stop sector, represented by the masses of the two top squarks, is important. Since the experimental results refer to this mixing when quoting exclusion limits in the two-dimensional $[m_{\mathrm{h}}, \tan\beta]$ parameter space, more details are given here. The masses of the physical top squarks are calculated by diagonalizing their mass matrix. The off-diagonal elements of this 2×2 matrix are given by $m_{\mathrm{t}}(A_t - \mu\cot\beta)$, where the parameters in the bracket have been mentioned in section 5.2 (A_t is the low energy value of A_0 for the case of the top squark). The scenario where the off-diagonal elements are small compared to the diagonal elements is called "no-mixing". On the other hand "maximal mixing" occurs when the off-diagonal elements are of comparable size to the diagonal elements. The definition used in paper 3 for "maximal mixing" is $(A_t - \mu\cot\beta) = \sqrt{6}M_{\mathrm{SUSY}}$ (and $|\mu| \ll M_{\mathrm{SUSY}}$), $M_{\mathrm{SUSY}} \sim 1$ TeV being the typical mass scale of the SUSY particles.

5.3.3 Mass bounds in the $[m_{\mathrm{h}}, \tan\beta]$ plane

In the preceding section an absolute upper bound on the mass of the lightest Higgs boson of the MSSM has been given. However, for certain sets of parameters of the model more restrictive bounds can be obtained (*cf.* Figure 2.4 for the case of the standard model, where the allowed range for m_{H} is shown as a function of the parameter Λ). While on tree level the bounds on m_{h} depend only on $\tan\beta$, more parameters are involved when higher order mass corrections are calculated. Usually the theoretically excluded region in the $[m_{\mathrm{h}}, \tan\beta]$ plane is shown for certain configurations of the additional parameters, called benchmarks sets. For example, the set of parameters which, for each value of $\tan\beta$, gives the largest possible upper bound on m_{h} is referred to as the $m_{\mathrm{h}}^{\mathrm{max}}$ scenario. Three important scenarios [37] used in the Higgs searches at LEP2 are shown in Figure 5.5. Looking at these figures one finds that the range shown for

[5] The two-loop corrections to m_{h} are typically $\mathcal{O}(20\%)$ of the one-loop corrections and they are negative.

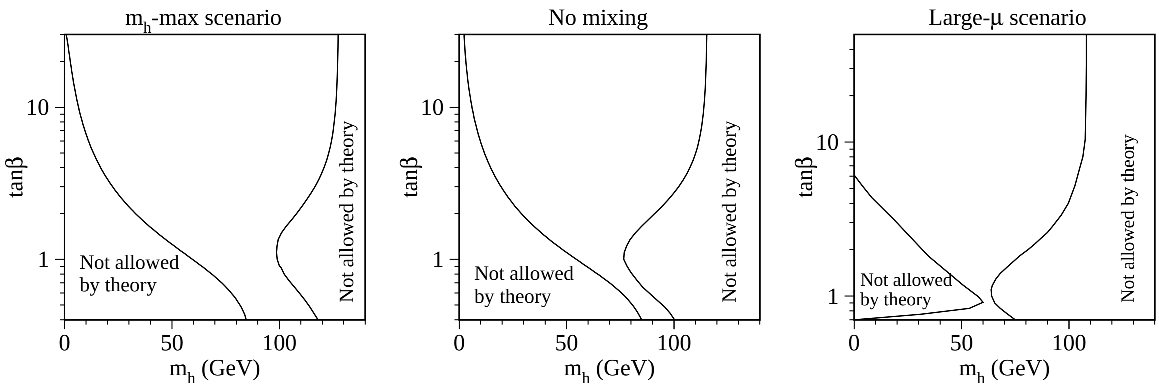

Figure 5.5: Theoretically disallowed regions in the $[m_\mathrm{h}, \tan\beta]$ plane for three MSSM benchmark scenarios. Left: In the $m_\mathrm{h}^\mathrm{max}$ scenario the parameters are chosen such as to obtain the maximum possible value for m_h as a function of $\tan\beta$. Middle: Same as before, but with no mixing in the stop sector. Right: This benchmark set is characterized by a relativ large value for $|\mu|$, the Higgsino mass parameter (from the superpotential).

$\tan\beta$ is not including zero, the reason being that theoretical considerations disfavor values of $\tan\beta$ smaller than 1. If $\tan\beta$ becomes too small then the Higgs coupling to top quarks $g_\mathrm{t} \sim m_\mathrm{t}/v_2$ becomes too strong, ultimately violating unitarity. Arguments similar to those of Sec. 2.5, namely the requirement that the Higgs-fermion Yukawa coupling remains finite when evolved (by means of the RGE) from the electroweak scale to some large scale Λ [39,42], lead to $1.5 \lesssim \tan\beta \lesssim 65$ (for $\Lambda = \Lambda_\mathrm{GUT}$ and $m_\mathrm{t} = 170\ \mathrm{GeV}/c^2$).

It is the task of experimental physicists to compare their results with the perdictions of theorists. In the case of the searches for neutral Higgs boson of the MSSM this is usually achieved by adding the experimentally excluded regions in the $[m_\mathrm{h}, \tan\beta]$ plane to the plots of Figs. 5.5 (or vice versa). This way of presenting the results is preferred because it can be shown that the experimental results are largely parameter independent when displayed in the $[m_\mathrm{h}, \tan\beta]$ plane.

5.3.4 Production and decay modes of neutral Higgs bosons in 2HDM and the MSSM

In two Higgs doublet models the production of the two neutral CP-even Higgs bosons h and H through the Higgs-strahlung process

$$\mathrm{e^+e^-} \to \mathrm{Z^*} \to \mathrm{hZ\,(HZ)} \tag{5.15}$$

is complemented by the so-called associated production of Higg bosons (*cf.* Fig. 5.1b)

$$\mathrm{e^+e^-} \to \mathrm{Z^*} \to \mathrm{hA\,(HA)}. \tag{5.16}$$

The cross sections for these processes are given by

$$\sigma(e^+e^- \to hZ) = \sin^2(\beta-\alpha)\,\sigma^{SM}_{HZ} \tag{5.17}$$

$$\sigma(e^+e^- \to hA) = \cos^2(\beta-\alpha)\,\sigma^{SM}_{HZ}\cdot x\,, \tag{5.18}$$

where σ^{SM}_{HZ} is the standard model cross section for Higgs-strahlung (given in Eq.3.1) and the factor $x = f_{hA}^{3/2}/[f_{hZ}^{1/2}(12m_Z^2/s + f_{hZ})]$ accounts for the correct suppression of the P-wave cross section near the kinematic threshold. The quantity $f_{ij} = [1-(m_i+m_j)^2/s)][1-(m_i-m_j)^2/s)]$ is the usual momentum factor of the two particle phase space. Here and in the following the corresponding formulae for the heavy Higgs boson H, which is to heavy to be produced at LEP2, can be obtained by making the substitution sin $\leftrightarrow$ cos in all trigonometric functions of the angles α and β that occur in the formulae for the light Higgs boson h. The factors $\sin^2(\beta-\alpha)$ and $\cos^2(\beta-\alpha)$ in (5.17) and (5.18) are a direct consequence of (5.6) and (5.7). Finally it is mentioned that the cross section for WW fusion of the h is reduced by the same factor $\sin^2(\beta-\alpha)$ as the cross section for Higgs-strahlung.

For the decay of the 2HDM Higgs bosons only decays into particles of the standard model are considered. Moreover, at LEP2 only decays into fermion pairs are relevant. The coupling of the standard model Higgs boson to fermions is given by m_f/v (*cf.* Eq. 2.28). As mentioned on page 72, v has to be replaced by v_1 for the coupling of the 2HDM Higgs bosons of type II to down type quarks and leptons, and by v_2 for the coupling to up type quarks. For example, the coupling to b quarks is given by

$$g_{hb\bar{b}} \sim \frac{m_b}{v_1}\,. \tag{5.19}$$

From (5.3) and (5.4) we have $v = v_1/\cos\beta = v_2/\sin\beta$. Using this in (5.19) yields

$$g_{hb\bar{b}} \sim \frac{m_b}{v\cos\beta}\,. \tag{5.20}$$

Down-type quarks exclusively couple to Φ_1, therefore their coupling to h includes a factor $\sin\alpha$, as can be seen from the definition of h in (5.5). Altogether, the decay width for 2HDM is given by

$$\Gamma_{hb\bar{b}} = \frac{\sin^2\alpha}{\cos^2\beta}\,\Gamma^{SM}_{Hq\bar{q}}\,, \tag{5.21}$$

where the standard model decay width $\Gamma^{SM}_{Hq\bar{q}}$ is defined in (3.6). The same result is obtained for the decay width into a lepton pair, but for up type quarks the substitution sin $\leftrightarrow$ cos has to be applied. If $\sin^2\alpha$ is small in (5.21) the otherwise dominant decay mode into $b\bar{b}$ can be highly suppressed. This is also true in the MSSM, where α and β are not independent but related through (5.12).

For 2HDM of type I an equation similar to (5.21) holds for all fermions. Then, for $\alpha = 0$ the lightest Higgs boson h cannot decay into fermions. This feature is commonly referred to as fermiophobic.

5.4 P3 [26]: Search for the neutral Higgs bosons of the MSSM in e^+e^- collisions at $\sqrt{s}$ from 130 to 172 GeV

In the search for the neutral Higgs bosons of the MSSM, signal topologies associated with the Higgs-strahlung process (*cf.* Fig. 3.6) are complemented with the $\mathrm{hA} \to \mathrm{b\bar{b}b\bar{b}}$ and $\mathrm{hA} \to \mathrm{b\bar{b}}\tau^+\tau^-$ search channels (*cf.* Fig. 5.6).

By taking into account the factor $\sin^2(\beta-\alpha)$ from (5.17) the results of the standard model Higgs boson searches can be directly combined with the results of the hA search analyses. The two hA search analyses are optimized for equal masses of the two neutral Higgs bosons, *i.e.* $m_\mathrm{h} = m_\mathrm{A}$, in which case they have similar branching ratios. It turns out [6] that for values of $\tan\beta \gg 1$ the neutral Higgs bosons h and A exclusively decay into b-quarks (branching ratio $\sim 92\%$) and τ-leptons (branching ratio $\sim 7.6\%$). The probability of having four b-jets in the final state therefore is $0.92^2 = 0.84.6$. Clearly b-tagging is very important for these analyses.

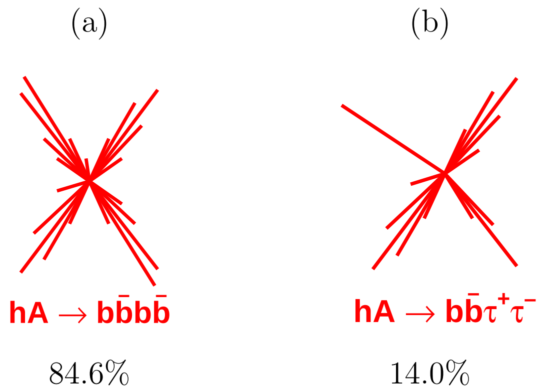

Figure 5.6: The neutral Higgs bosons h and A of the MSSM are searched for in these two event topologies (in addition to the Higgs-strahlung process). The branching ratios of the hA decay topologies are given below the figures for the case where $\tan\beta$ is large.

[6] For example, when the coupling of the h boson to down type fermions is large, the coupling to up type fermions is small, as explained in the previous section. The same holds for the A boson.

ELSEVIER

23 October 1997

PHYSICS LETTERS B

Physics Letters B 412 (1997) 173–188

Search for the neutral Higgs bosons of the MSSM in e^+e^- collisions at $\sqrt{s}$ from 130 to 172 GeV

ALEPH Collaboration

R. Barate [a], D. Buskulic [a], D. Decamp [a], P. Ghez [a], C. Goy [a], J.-P. Lees [a], A. Lucotte [a], M.-N. Minard [a], J.-Y. Nief [a], B. Pietrzyk [a], M.P. Casado [b], M. Chmeissani [b], P. Comas [b], J.M. Crespo [b], M. Delfino, [b], E. Fernandez [b], M. Fernandez-Bosman [b], Ll. Garrido [b,1], A. Juste [b], M. Martinez [b], G. Merino [b], R. Miquel [b], Ll.M. Mir [b], C. Padilla [b], I.C. Park [b], A. Pascual [b], J.A. Perlas [b], I. Riu [b], F. Sanchez [b], F. Teubert [b], A. Colaleo [c], D. Creanza [c], M. de Palma [c], G. Gelao [c], G. Iaselli [c], G. Maggi [c], M. Maggi [c], N. Marinelli [c], S. Nuzzo [c], A. Ranieri [c], G. Raso [c], F. Ruggieri [c], G. Selvaggi [c], L. Silvestris [c], P. Tempesta [c], A. Tricomi [c,2], G. Zito [c], X. Huang [d], J. Lin [d], Q. Ouyang [d], T. Wang [d], Y. Xie [d], R. Xu [d], S. Xue [d], J. Zhang [d], L. Zhang [d], W. Zhao [d], D. Abbaneo [e], R. Alemany [e], A.O. Bazarko [e,3], U. Becker [e], P. Bright-Thomas [e], M. Cattaneo [e], F. Cerutti [e], G. Dissertori [e], H. Drevermann [e], R.W. Forty [e], M. Frank [e], R. Hagelberg [e], J.B. Hansen [e], J. Harvey [e], P. Janot [e], B. Jost [e], E. Kneringer [e], J. Knobloch [e], I. Lehraus [e], G. Lutters [e], P. Mato [e], A. Minten [e], L. Moneta [e], A. Pacheco [e], J.-F. Pusztaszeri [e,4], F. Ranjard [e], G. Rizzo [e], L. Rolandi [e], D. Rousseau [e], D. Schlatter [e], M. Schmitt [e], O. Schneider [e], W. Tejessy [e], I.R. Tomalin [e], H. Wachsmuth [e], A. Wagner [e,5], Z. Ajaltouni [f], A. Barrès [f], C. Boyer [f], A. Falvard [f], C. Ferdi [f], P. Gay [f], C. Guicheney [f], P. Henrard [f], J. Jousset [f], B. Michel [f], S. Monteil [f], J-C. Montret [f], D. Pallin [f], P. Perret [f], F. Podlyski [f], J. Proriol [f],

[1] Permanent address: Universitat de Barcelona, 08208 Barcelona, Spain.
[2] Also at Dipartimento di Fisica, INFN Sezione di Catania, Catania, Italy.
[3] Now at Princeton University, Princeton, NJ 08544, USA.
[4] Now at School of Operations Research and Industrial Engineering, Cornell University, Ithaca, NY 14853-3801, USA.
[5] Now at Schweizerischer Bankverein, Basel, Switzerland.
[6] Supported by the Commission of the European Communities, contract ERBCHBICT941234.

PII S0370-2693(97)01112-X

P. Rosnet [f], J.-M. Rossignol [f], T. Fearnley [g], J.D. Hansen [g], J.R. Hansen [g], P.H. Hansen [g], B.S. Nilsson [g], B. Rensch [g], A. Wäänänen [g], G. Daskalakis [h], A. Kyriakis [h], C. Markou [h], E. Simopoulou [h], A. Vayaki [h], A. Blondel [i], J.C. Brient [i], F. Machefert [i], A. Rougé [i], M. Rumpf [i], A. Valassi [i,6], H. Videau [i], E. Focardi [j], G. Parrini [j], K. Zachariadou [j], R. Cavanaugh [k], M. Corden [k], C. Georgiopoulos [k], T. Huehn [k], D.E. Jaffe [k], A. Antonelli [l], G. Bencivenni [l], G. Bologna [l,7], F. Bossi [l], P. Campana [l], G. Capon [l], D. Casper [l], V. Chiarella [l], G. Felici [l], P. Laurelli [l], G. Mannocchi [l,8], F. Murtas [l], G.P. Murtas [l], L. Passalacqua [l], M. Pepe-Altarelli [l], L. Curtis [m], S.J. Dorris [m], A.W. Halley [m], I.G. Knowles [m], J.G. Lynch [m], V. O'Shea [m], C. Raine [m], J.M. Scarr [m], K. Smith [m], P. Teixeira-Dias [m], A.S. Thompson [m], E. Thomson [m], F. Thomson [m], R.M. Turnbull [m], O. Buchmüller [n], S. Dhamotharan [n], C. Geweniger [n], G. Graefe [n], P. Hanke [n], G. Hansper [n], V. Hepp [n], E.E. Kluge [n], A. Putzer [n], J. Sommer [n], K. Tittel [n], S. Werner [n], M. Wunsch [n], R. Beuselinck [o], D.M. Binnie [o], W. Cameron [o], P.J. Dornan [o], M. Girone [o], S. Goodsir [o], E.B. Martin [o], P. Morawitz [o], A. Moutoussi [o], J. Nash [o], J.K. Sedgbeer [o], P. Spagnolo [o], A.M. Stacey [o], M.D. Williams [o], V.M. Ghete [p], P. Girtler [p], D. Kuhn [p], G. Rudolph [p], A.P. Betteridge [q], C.K. Bowdery [q], P. Colrain [q], G. Crawford [q], A.J. Finch [q], F. Foster [q], G. Hughes [q], R.W. Jones [q], T. Sloan [q], E.P. Whelan [q], M.I. Williams [q], C. Hoffmann [r], K. Jakobs [r], K. Kleinknecht [r], G. Quast [r], B. Renk [r], E. Rohne [r], H.-G. Sander [r], P. van Gemmeren [r], C. Zeitnitz [r], J.J. Aubert [s], C. Benchouk [s], A. Bonissent [s], G. Bujosa [s], J. Carr [s], P. Coyle [s], C. Diaconu [s], A. Ealet [s], D. Fouchez [s], N. Konstantinidis [s], O. Leroy [s], F. Motsch [s], P. Payre [s], M. Talby [s], A. Sadouki [s], M. Thulasidas [s], A. Tilquin [s], K. Trabelsi [s], M. Aleppo [t], M. Antonelli [t], F. Ragusa [t,9], R. Berlich [u], W. Blum [u], V. Büscher [u], H. Dietl [u], G. Ganis [u], C. Gotzhein [u], H. Kroha [u], G. Lütjens [u], G. Lutz [u], W. Männer [u], H.-G. Moser [u], R. Richter [u], A. Rosado-Schlosser [u], S. Schael [u], R. Settles [u], H. Seywerd [u], R. St. Denis [u], H. Stenzel [u], W. Wiedenmann [u], G. Wolf [u], J. Boucrot [v], O. Callot [v,9], S. Chen [v], A. Cordier [v], M. Davier [v], L. Duflot [v], J.-F. Grivaz [v], Ph. Heusse [v], A. Höcker [v], A. Jacholkowska [v], M. Jacquet [v], M. Kado [v], D.W. Kim [v,10], F. Le Diberder [v], J. Lefrançois [v], A.-M. Lutz [v], I. Nikolic [v], M.-H. Schune [v], L. Serin [v], S. Simion [v], E. Tournefier [v], J.-J. Veillet [v], I. Videau [v], D. Zerwas [v], P. Azzurri [w], G. Bagliesi [w], S. Bettarini [w], C. Bozzi [w],

[7] Also Istituto di Fisica Generale, Università di Torino, Torino, Italy.
[8] Also Istituto di Cosmo-Geofisica del C.N.R., Torino, Italy.
[9] Also at CERN, 1211 Geneva 23,Switzerland.
[10] Permanent address: Kangnung National University, Kangnung, Korea.

R. Barate et al. / Physics Letters B 412 (1997) 173–188 175

G. Calderini [w], V. Ciulli [w], R. Dell'Orso [w], R. Fantechi [w], I. Ferrante [w], A. Giassi [w], A. Gregorio [w], F. Ligabue [w], A. Lusiani [w], P.S. Marrocchesi [w], A. Messineo [w], F. Palla [w], G. Sanguinetti [w], A. Sciabà [w], J. Steinberger [w], R. Tenchini [w], C. Vannini [w], A. Venturi [w], P.G. Verdini [w], G.A. Blair [x], L.M. Bryant [x], J.T. Chambers [x], Y. Gao [x], M.G. Green [x], T. Medcalf [x], P. Perrodo [x], J.A. Strong [x], J.H. von Wimmersperg-Toeller [x], D.R. Botterill [y], R.W. Clifft [y], T.R. Edgecock [y], S. Haywood [y], P. Maley [y], P.R. Norton [y], J.C. Thompson [y], A.E. Wright [y], B. Bloch-Devaux [z], P. Colas [z], B. Fabbro [z], W. Kozanecki [z], E. Lançon [z], M.C. Lemaire [z], E. Locci [z], P. Perez [z], J. Rander [z], J.-F. Renardy [z], A. Rosowsky [z], A. Roussarie [z], J.-P. Schuller [z], J. Schwindling [z], A. Trabelsi [z], B. Vallage [z], S.N. Black [aa], J.H. Dann [aa], H.Y. Kim [aa], A.M. Litke [aa], M.A. McNeil [aa], G. Taylor [aa], C.N. Booth [ab], R. Boswell [ab], C.A.J. Brew [ab], S. Cartwright [ab], F. Combley [ab], M.S. Kelly [ab], M. Lehto [ab], W.M. Newton [ab], J. Reeve [ab], L.F. Thompson [ab], K. Affholderbach [ac], A. Böhrer [ac], S. Brandt [ac], G. Cowan [ac], J. Foss [ac], C. Grupen [ac], P. Saraiva [ac], L. Smolik [ac], F. Stephan [ac], M. Apollonio [ad], L. Bosisio [ad], R. Della Marina [ad], G. Giannini [ad], B. Gobbo [ad], G. Musolino [ad], J. Putz [ae], J. Rothberg [ae], S. Wasserbaech [ae], R.W. Williams [ae], S.R. Armstrong [af], E. Charles [af], P. Elmer [af], D.P.S. Ferguson [af], S. González [af], T.C. Greening [af], O.J. Hayes [af], H. Hu [af], S. Jin [af], P.A. McNamara III [af], J.M. Nachtman [af], J. Nielsen [af], W. Orejudos [af], Y.B. Pan [af], Y. Saadi [af], I.J. Scott [af], J. Walsh [af], Sau Lan Wu [af], X. Wu [af], J.M. Yamartino [af], G. Zobernig [af]

[a] *Laboratoire de Physique des Particules (LAPP), IN2P3-CNRS, 74019 Annecy-le-Vieux Cedex, France*
[b] *Institut de Fisica d'Altes Energies, Universitat Autònoma de Barcelona, 08193 Bellaterra (Barcelona), Spain* [11]
[c] *Dipartimento di Fisica, INFN Sezione di Bari, 70126 Bari, Italy*
[d] *Institute of High-Energy Physics, Academia Sinica, Beijing, People's Republic of China* [12]
[e] *European Laboratory for Particle Physics (CERN), 1211 Geneva 23, Switzerland*
[f] *Laboratoire de Physique Corpusculaire, Université Blaise Pascal, IN2P3-CNRS, Clermont-Ferrand, 63177 Aubière, France*
[g] *Niels Bohr Institute, 2100 Copenhagen, Denmark* [13]
[h] *Nuclear Research Center Demokritos (NRCD), Athens, Greece*
[i] *Laboratoire de Physique Nucléaire et des Hautes Energies, Ecole Polytechnique, IN2P3-CNRS, 91128 Palaiseau Cedex, France*
[j] *Dipartimento di Fisica, Università di Firenze, INFN Sezione di Firenze, 50125 Firenze, Italy*

[11] Supported by CICYT, Spain.
[12] Supported by the National Science Foundation of China.
[13] Supported by the Danish Natural Science Research Council.
[14] Supported by the US Department of Energy, contract DE-FG05-92ER40742.
[15] Supported by the US Department of Energy, contract DE-FC05-85ER250000.
[16] Supported by the UK Particle Physics and Astronomy Research Council.
[17] Supported by the Bundesministerium für Bildung, Wissenschaft, Forschung und Technologie, Germany.
[18] Supported by Fonds zur Förderung der wissenschaftlichen Forschung, Austria.

176 R. Barate et al. / Physics Letters B 412 (1997) 173–188

[k] *Supercomputer Computations Research Institute, Florida State University, Tallahassee, FL 32306-4052, USA* [14,15]
[l] *Laboratori Nazionali dell'INFN (LNF-INFN), 00044 Frascati, Italy*
[m] *Department of Physics and Astronomy, University of Glasgow, Glasgow G12 8QQ, United Kingdom* [16]
[n] *Institut für Hochenergiephysik, Universität Heidelberg, 69120 Heidelberg, Germany* [17]
[o] *Department of Physics, Imperial College, London SW7 2BZ, United Kingdom* [16]
[p] *Institut für Experimentalphysik, Universität Innsbruck, 6020 Innsbruck, Austria* [18]
[q] *Department of Physics, University of Lancaster, Lancaster LA1 4YB, United Kingdom* [16]
[r] *Institut für Physik, Universität Mainz, 55099 Mainz, Germany* [17]
[s] *Centre de Physique des Particules, Faculté des Sciences de Luminy, IN2P3-CNRS, 13288 Marseille, France*
[t] *Dipartimento di Fisica, Università di Milano e INFN Sezione di Milano, 20133 Milano, Italy*
[u] *Max-Planck-Institut für Physik, Werner-Heisenberg-Institut, 80805 München, Germany* [17]
[v] *Laboratoire de l'Accélérateur Linéaire, Université de Paris-Sud, IN2P3-CNRS, 91405 Orsay Cedex, France*
[w] *Dipartimento di Fisica dell'Università, INFN Sezione di Pisa, e Scuola Normale Superiore, 56010 Pisa, Italy*
[x] *Department of Physics, Royal Holloway & Bedford New College, University of London, Surrey TW20 OEX, United Kingdom* [16]
[y] *Particle Physics Dept., Rutherford Appleton Laboratory, Chilton, Didcot, Oxon OX11 OQX, United Kingdom* [16]
[z] *CEA, DAPNIA / Service de Physique des Particules, CE-Saclay, 91191 Gif-sur-Yvette Cedex, France* [19]
[aa] *Institute for Particle Physics, University of California at Santa Cruz, Santa Cruz, CA 95064, USA* [20]
[ab] *Department of Physics, University of Sheffield, Sheffield S3 7RH, United Kingdom* [16]
[ac] *Fachbereich Physik, Universität Siegen, 57068 Siegen, Germany* [17]
[ad] *Dipartimento di Fisica, Università di Trieste e INFN Sezione di Trieste, 34127 Trieste, Italy*
[ae] *Experimental Elementary Particle Physics, University of Washington, Seattle, WA 98195, USA*
[af] *Department of Physics, University of Wisconsin, Madison, WI 53706, USA* [21]

Received 23 June 1997
Editor: K. Winter

Abstract

The process $e^+e^- \to hA$ is used to search for the Higgs bosons of the Minimal Supersymmetric Standard Model (MSSM), in the $b\bar{b}b\bar{b}$ and $\tau^+\tau^-b\bar{b}$ final states. The search is performed in the data collected by the ALEPH experiment at LEP, at centre-of-mass energies between 130 and 172 GeV and with a total luminosity of 27.2 pb^{-1}. No candidate events are found in either of the final states, in agreement with the expected background of 0.91 events from all Standard Model processes. Combined with searches for $e^+e^- \to hZ$, this results in a 95% C.L. lower limit on the masses of both h and A of 62.5 GeV/c^2, for $\tan\beta > 1$.

[19] Supported by the Direction des Sciences de la Matière, C.E.A.
[20] Supported by the US Department of Energy, grant DE-FG03-92ER40689.
[21] Supported by the US Department of Energy, grant DE-FG0295-ER40896.

1. Introduction

In minimal extensions of the Standard Model, two Higgs doublets are introduced in order to give masses to up-type quarks and down-type quarks separately. In these models, the Higgs sector therefore consists of five physical states, namely three neutral bosons – two CP-even h and H, and one CP-odd A – and a pair of charged bosons $H^{\pm}$. Six independent parameters are required: four Higgs boson masses, the ratio $v_2/v_1 \equiv \tan\beta$ of the vacuum expectation values of the two Higgs doublets, and α, the mixing angle in the CP-even sector.

Predictions can therefore only be made in specific models, of which the most popular is the Minimal Supersymmetric extension of the Standard Model

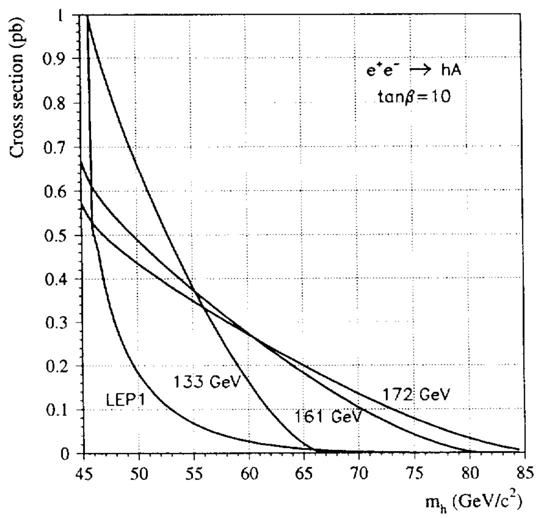

Fig. 1. The cross section for associated production $e^+e^- \to hA$ at LEP 1 and the three LEP 2 energies used in the analysis.

(MSSM). In this model, both H and $H^{\pm}$ are predicted to be too heavy to be discovered at LEP 2. The analysis presented in this letter is consequently restricted to the search for the lighter Higgs bosons, h and A, which can be produced by two complementary processes, the Higgs-strahlung process $e^+e^- \to hZ$ with a cross section proportional to $\sin^2(\beta - \alpha)$ and the associated pair-production $e^+e^- \to hA$ with cross section proportional to $\cos^2(\beta - \alpha)$. In Fig. 1 the hA cross section is shown for the LEP 1 energy of 91 GeV and the three LEP 2 energies: 133, 161 and 172 GeV.

At tree-level, only two parameters are needed to determine all the other relevant quantities (masses, couplings, and therefore cross sections). Here, these are chosen to be $\tan\beta$ and the mass m_h. When radiative corrections are included at the one [1] and two [2] loop levels, three other parameters are needed, namely M_{SUSY}, A_t and μ. In the stop sector, the overall mass scale is characterised by M_{SUSY} and the mixing is controlled by A_t and μ. In this letter the results are presented for $M_{SUSY} = 1\,\text{TeV}/c^2$ and for two extreme configurations of stop mixing: no mixing ($A_t, \mu \ll M_{SUSY}$) and maximal mixing ($A_t - \mu/\tan\beta = \sqrt{6}\, M_{SUSY}$), as suggested in [3]. The latter leads to the largest radiative correction to m_h and is therefore the most pessimistic choice for LEP, while the first is the most optimistic. Varying M_{SUSY} from 0.2 to $5\,\text{TeV}/c^2$ does not change the basic conclusions of this letter.

The analyses described in this letter search for associated hA production in data collected with the ALEPH detector at LEP at $\sqrt{s}$ from 130 to 172 GeV during the years 1995 and 1996. For m_h = 60 GeV/c^2 and $\tan\beta$ = 10 the branching fraction of h and A to $b\bar{b}$ is 92% and to $\tau^+\tau^-$ is 8%, giving $b\bar{b}b\bar{b}$ final states in 84% of the events and $\tau^+\tau^- b\bar{b}$ in 14%. Analyses of both these channels are performed. After describing the relevant aspects of the ALEPH detector in Section 2, the method used for tagging the b quark jets is described in Section 3. The event selections, detailed in Section 4, are optimized for $m_h = m_A$ = $60\,\text{GeV}/c^2$ with the procedure described in [4], using the reconstructed mass sum $m_h + m_A$ as the discriminating variable. In Section 5, the results from the hA modes of this letter are combined with the hZ modes of [4] and results are presented within the MSSM as a function of $\sin^2(\beta - \alpha)$ and as a function of $\tan\beta$.

2. The ALEPH detector

The ALEPH detector and its performance are described in [5] and [6]. In October 1995, the silicon vertex detector (VDET) described in these papers was replaced by a new device [7] which is used for the analyses described herein. This new VDET is twice as long as the previous detector, providing a larger acceptance and has less material in the active region.

With this modification the tracking system consists of the VDET, with two layers at average radii 6.3 and 11.0 cm measuring coordinates with a resolution of 12 μm in the rϕ dimension and 15–50 μm in the z dimension for incident angles between 0° and 70°, surrounded by the inner tracking chamber (ITC) and the time projection chamber (TPC). Charged particles are used in the analyses if they are reconstructed with at least four hits in the TPC (typically corresponding to a polar angle with respect to the beam $|\cos\theta| < 0.96$) and they originate from within a cylinder of length 20 cm and a radius of 2 cm coaxial with the beam and centered at the interaction point. Tracks with $|\cos\theta| < 0.94$ (0.85) pass through at least one (two) layer(s) of the new VDET. The resulting three dimensional impact parameter resolution can be parametrized as $(34 + 70/p)(1 + 1.6\cos^4\theta)\ \mu m$ (p in GeV/c). With the axial magnetic field of 1.5T the momentum resolution of the tracking system is given by $\sigma(p)/p = 6 \times 10^{-4} p_T \oplus 0.005$ (p_T in GeV/c). The TPC provides up to 338 measurements of the specific ionization, dE/dx, on the tracks.

The tracking chambers are surrounded by a lead/proportional-chamber electromagnetic calorimeter (ECAL) and a hadron calorimeter (HCAL) consisting of the iron magnet return yoke instrumented with streamer tubes. With two external streamer chamber layers the HCAL is also used for muon identification. The ECAL and HCAL have relative energy resolutions of $0.18/\sqrt{E} + 0.009$ and $0.85/\sqrt{E}$ (E in GeV). The calorimetry and tracking information are combined in an energy flow algorithm [6] which gives a measure of the total energy, and therefore the missing energy, with an error of $(0.6\sqrt{E} + 0.6)$ GeV. The various neutral particles reconstructed from the calorimeters together with the charged particle tracks used in this algorithm are referred to as "energy flow particles".

Lepton identification in ALEPH is described in [6,8]. Electrons are identified by comparing the energy deposit in the ECAL with the momentum measured in the tracking system, the shape and depth of the energy deposit in the ECAL and the specific ionization measurement. Muons are identified by requiring a hit pattern characteristic of a penetrating particle in the HCAL and at least one associated hit in the muon chambers. In all analyses described in this letter electron and muon candidates must have momenta greater than 2 GeV/c and 3 GeV/c, respectively.

3. b tagging

For the analyses of both the $b\bar{b}b\bar{b}$ and $\tau^+\tau^-b\bar{b}$ channels the b quark identification is an essential part of the signal extraction. In this letter b jets are identified mainly by exploiting the longer lifetime of b hadrons compared to other hadrons, but also by the presence in the jets of high p_T leptons from semileptonic decays. To use the lifetime information in a given jet, track impact parameters and secondary decay vertices are reconstructed relative to an event-by-event interaction point.

3.1. Interaction point determination

The algorithm used to determine the interaction point is similar to the one developed for the data taken at centre-of-mass energies close to the Z mass [9]. Well measured tracks are associated to their nearest jet and are projected into the plane perpendicular to this jet, to reduce the bias due to tracks coming from secondary vertices. The projected tracks are then combined with an average "beam spot" position, i.e., the location of the centre of the interaction region in the plane transverse to the beam axis. This beam spot is determined with relaxed cuts on the track selection compared to LEP 1 due to the much lower track rate at LEP 2 energies. Using groups of 120 tracks selected in consecutive events and with momenta down to 300 MeV/c, the beam spot position is determined with average accuracies of $\sim 27\mu m$ in the horizontal and $\sim 25\mu m$ in the vertical directions. The RMS dimensions of the beam luminous region were measured to be 135 (150) μm horizontally and 7.1 (6.6) mm along the beam direction in the 1995 (1996) data. The vertical dimension of the luminous region is small, of order 5 μm. Using these parameters as errors on the beam spot, the interaction point is found in each event with resolutions of typically 40, 20 and 40 μm in the horizontal, vertical and beam directions.

3.2. b tagging neural network

Six variables which discriminate between b jets and light quark jets are combined using neural networks to tag b quark jets. The first two variables are lifetime-based; the third is based on the transverse momentum of identified leptons and the last three are based on jet-shape properties. The quantities used are as follows:

1. $\mathscr{P}_{jet}$: probability of the jet being a light quark (uds) jet based upon impact parameters of tracks in the jet, similar to that described in Ref. [9] with modifications for the new VDET;

2. $\Delta\chi^2_{svx}$: the χ^2 difference between fitting tracks in the jet both to secondary and primary vertices compared to assuming all tracks come from the interaction point. This is based upon a secondary vertex pattern recognition algorithm which searches for displaced vertices via a three-dimensional grid point search [10];
3. p_T: the transverse momentum of identified leptons with respect to the jet axis [8];
4. $\mathcal{S}^b$: the boosted sphericity of the jet, defined to be the sphericity of energy flow particles in the rest frame of the jet;
5. Multiplicity/$\ln E_{jet}$: the energy flow particle multiplicity of the jet divided by the logarithm of the jet energy. Normalizing by $\ln E$ removes the expected energy dependence of the multiplicity;
6. Σp_T^2: the sum of the transverse momentum squared of each energy flow particle with respect to the jet axis.

For the hA analysis, a neural network based upon the first three variables ($\mathcal{P}_{jet}$, $\Delta\chi^2_{svx}$, and p_T) is used for identifying b-jets while all six variables are used in another neural network for the Higgs-strahlung process [4]. In this latter analysis, the extra variables which are efficient at discriminating between b-jets and light quark jets give higher b tagging efficiency at a given background; in the hA case, however, the six-variable neural network increases the background of bbgg events due to the similarity between gluon and b jets in the event shape variables [11].

The network architecture is multilayer feed-forward, consisting of four layers and is based upon the JETNET 3.4 package [12]. Detailed descriptions of theoretical aspects of neural networks are available elsewhere [13]. The neural network was trained, with the backward propagation method, using b and non-b jets in radiative returns to the Z from a sample of 400 000 Monte Carlo q$\bar{q}$ events generated at a centre-of-mass energy of 161 GeV. Radiative returns to the Z were used because the jets in such events are produced in a kinematic configuration similar to that of the signal; this was preferred to training the network using simulated signal events in order to reduce the associated systematic error in the signal efficiency.

An independent sample of 100 000 Monte Carlo events was used for testing. The resulting neural network output is shown in Fig. 2a for jets in the 161 GeV data and Monte Carlo, selected using the Durham jet finding algorithm with $y_{cut} = 0.008$. For

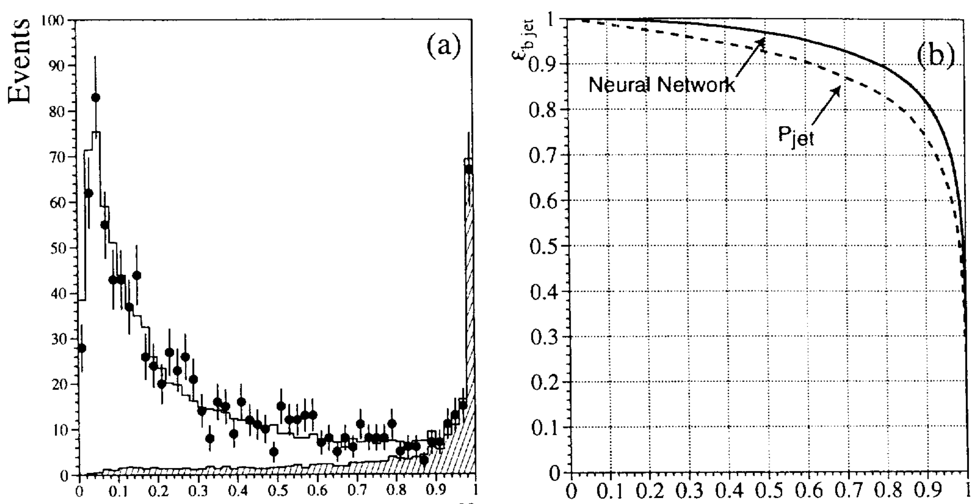

Fig. 2. (a) The output η of the neural network b tag for radiative returns to the Z for 161 GeV q$\bar{q}$ Monte Carlo (histogram) compared to the data at 161 GeV (points). The shaded region shows the contribution from generated b-jets. (b) The performance of the neural network b tag (solid line) for Monte Carlo events, presented in terms of the efficiency for identifying b-jets versus the efficiency for rejecting light quark jets. The performance of the single most powerful b tagging input variable to the neural network is shown for comparison (dashed curve).

events in the testing sample, it is possible to determine the efficiency for identifying b jets, ϵ_b^{jet}, as a function of the rejection for non-b jets, $(1-\epsilon_{udscg}^{jet})$, where ϵ_{udscg}^{jet} is the efficiency for wrongly identifying a light quark or gluon jet as a b jet. The resulting performance curve is shown in Fig. 2b; the curve for the single most powerful variable $\mathscr{P}_{jet}$ is also given, showing at a non-b rejection factor of 85% a gain in b efficiency from 78% to 87% by combining the extra information in the neural network.

3.3. Systematic studies of b tagging

The systematic uncertainty in the efficiency of the b tagging is evaluated from the Monte Carlo simulation and a consistency check is performed on efficiency and background using the calibration data taken at the Z peak during the 1996 data taking period.

The contribution to the b tagging systematics from the physics of b hadron decays has been estimated by varying the values of their lifetimes and decay multiplicities within the range allowed by existing experimental measurements [14]. The systematics due to track reconstruction have been studied by comparing track impact parameter distributions in data and Monte Carlo. The generated Monte Carlo distributions show impact parameter resolutions 10% better than in the data. A correction has been applied for this effect by smearing the track parameters in the Monte Carlo to calculate the analysis efficiency and half this correction is taken as a systematic error in the b tag efficiency.

After this correction is applied, the b tag efficiency is compared in Monte Carlo and data at the Z peak, by measuring the number of events with two and one hemispheres tagged by the algorithm. This method is a simplified version of that used to measure R_b in Ref. [9]. In that paper the equations for the number of double and single tags are solved to eliminate the b tag efficiency and extract R_b; here the value of R_b is input and the b tag efficiency is extracted. Fig. 3 shows the resulting comparison of the b tag efficiency as a function of the neural network output for one jet. Data and Monte Carlo agree within the statistical errors.

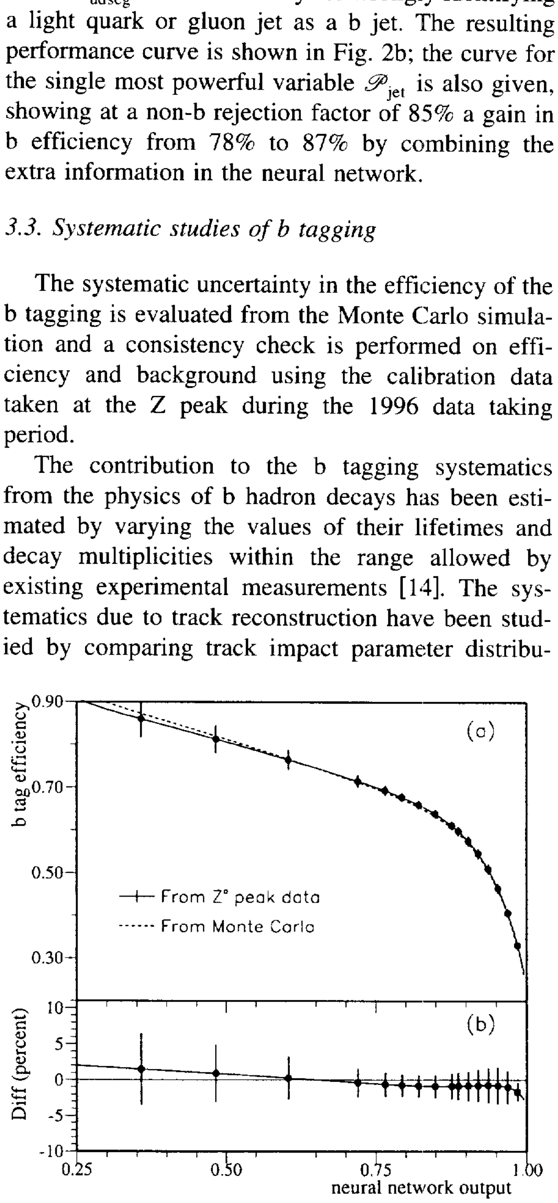

Fig. 3. Comparison of the neural network b tag efficiency for a single jet in Z peak data and Monte Carlo, after the smearing correction, as a function of the cut on the jet neural network output: (a) absolute tag efficiency; (b) difference between data and Monte Carlo.

4. Event selection

The data samples used in these analyses comprise 5.7 pb^{-1} at energies of $\sqrt{s}$ = 130.2 and 136.2 GeV recorded in November 1995, 10.9 pb^{-1} at 161.3 GeV in the summer of 1996, 1.1 pb^{-1} at 170.3 GeV and 9.5 pb^{-1} at 172.3 GeV in autumn 1996. The new VDET was completely installed for the 1996 data while for the November 1995 data the inner layer of the detector was complete but 5 out of 15 faces were missing in the outer layer. The appropriate detector geometries were used in the Monte Carlo for the two years.

For cut optimization and background estimates Monte Carlo samples were generated using the HZHA [15] program for the Higgs signal production and PYTHIA 5.7 [16] for the standard process production. The backgrounds considered are described in Ref. [4].

4.1. The $b\bar{b}b\bar{b}$ final state

The $b\bar{b}b\bar{b}$ final state is characterized by two clear signatures, the four-jet topology and a high b-quark content. These properties are the main handles for suppressing the background. The main source of

R. Barate et al. / Physics Letters B 412 (1997) 173–188 181

background is the two fermion process $e^+e^- \to q\bar{q}(\gamma)$, predominantly when the two primary partons are b quarks. At the higher centre-of-mass energies, two more processes, WW and ZZ (including $Z\gamma^*$) production, also become significant.

The first step in the analysis is a loose preselection intended to select hadronic events compatible with the four-jet topology and to suppress $q\bar{q}\gamma$ events with an energetic initial state radiation (ISR) photon. At least eight charged particles are required in the event comprising more than 10% of the centre-of-mass energy. To reject $q\bar{q}\gamma$ events with the ISR photon detected in the calorimeters, the electromagnetic energy in a cone of 1° around each energy flow particle in any jet must be less than 80% of the jet energy. To suppress these events when the photon escapes detection along the beam pipe, the missing longitudinal momentum is required to be less than $1.5 \times (M_{\text{vis}} - 90)$, where M_{vis} (in GeV/c^2) is the total visible mass in the event. The events are then clustered into four jets using the Durham algorithm. Events with y_{34}, the maximum y_{cut} value giving a four-jet event, smaller than 0.001 are rejected. The event thrust must be less than 0.85 and the smallest jet-jet angle, $\theta_{ij}^{\min}$, must be larger than 20°. The signal efficiency is 87% for $b\bar{b}b\bar{b}$ events at this level, while the $q\bar{q}$ background is reduced by a factor of ~ 40, the ZZ by a factor of almost 10 and the WW by more than 2. A total of 208 events are observed in the data, in agreement with the 188 events (112 $q\bar{q}$, 67 WW, 9 ZZ) predicted by the simulation. The excess of four-jet events reported in a previous paper [17] is present at this level of the analysis, but none of these events remain after the b tagging cut applied next.

The final selection combines the b tagging information in the event and a measure of compatibility with the four-jet topology. The b tagging variable uses the neural network outputs, η_j (described in the previous section), from all four jets, j, in the form

$$\mathscr{B}_4 = 4 - \sum_{j=1}^{4} \eta_j ,$$

while for the four-jet compatibility $\theta_{ij}^{\min}$ was chosen. These were combined linearly in a new variable $\mathscr{F}$:

$$\mathscr{F} = 90 \times \mathscr{B}_4 - \theta_{ij}^{\min} \; \left(\theta_{ij}^{\min} \text{ in degrees}\right).$$

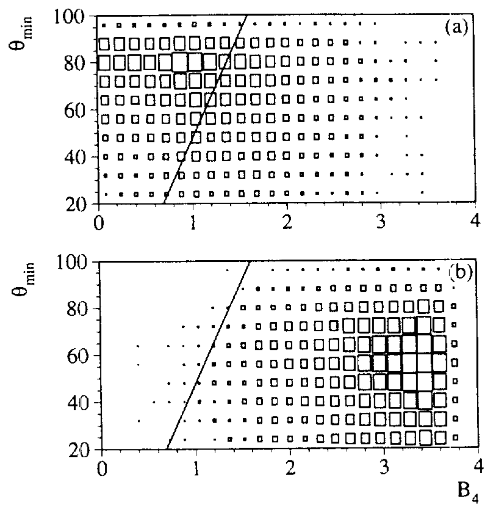

Fig. 4. Monte Carlo distribution of the minimum angle between jets $\theta_{ij}^{\min}$ versus the b tagging variable $\mathscr{B}_4$ (a) for the signal hA events, (b) for the background, $q\bar{q}$, WW and ZZ events. The line indicates the cut described in the text.

The choice of the coefficient of $\mathscr{F}$ was made with a linear discriminant analysis and the separation of signal and background is indicated in Fig. 4. Combining the b tag and four-jet compatibility information improves significantly the signal efficiency, compared to cutting independently on the individual variables, by saving some clear four-jet events with poorer b tagging information as well as some events with high content in b quarks but where two of the jets happen to be close in space.

The cut on $\mathscr{F}$ was placed at the point that minimizes the expected confidence level in the absence of signal, for the hypothesis $m_{\text{h}} = m_{\text{A}} = 60\,\text{GeV}/c^2$ [4]. This optimization procedure gave $\mathscr{F} < 49$, which corresponds to a signal efficiency of 55% at 172 GeV centre-of-mass energy. Fig. 7b shows the signal efficiencies for the three energies as a function of m_{h}. The distribution of $\mathscr{F}$ in the data and in the simulation is shown in Fig. 5a. For $\mathscr{F} < 49$, 0.87 ± 0.17 events (0.63 $q\bar{q}$, 0.07 WW, 0.17 ZZ) are expected in the simulation. No events were selected in the data. Fig. 5b shows distributions of the reconstructed signal mass sum $m_{\text{h}} + m_{\text{A}}$ which has been used as the discriminating variable in the cut optimization. This quantity is the sum of dijet masses for the pairing of jets with the minimum dijet

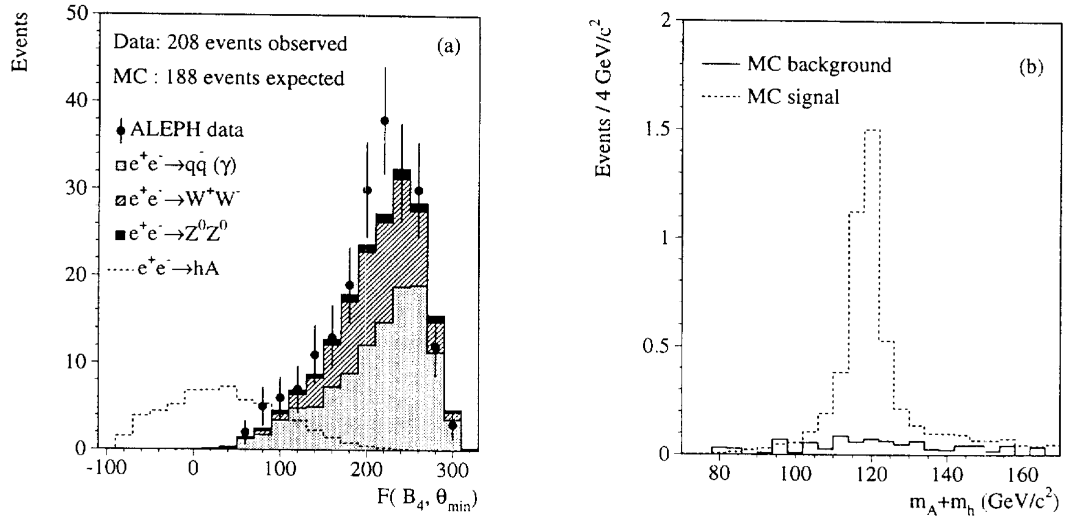

Fig. 5. (a) Distribution of data after the $b\bar{b}b\bar{b}$ preselection cuts at all energies as a function of the variable $\mathcal{F}(\mathcal{B}_4, \theta_{ij}^{min})$ described in the text. The background predictions from the Monte Carlo simulations are shown as cumulative shaded histograms and the dashed histogram is the signal for a luminosity 10 × that in the data. (b) Distribution of mass sum $m_h + m_A$ for signal and background Monte Carlo events, normalized to the recorded luminosity, after all cuts.

mass difference and uses jet energies rescaled with the beam energy constraint [17].

The b tagging cut, bringing the major loss in signal acceptance, gives the largest systematic uncertainty in the analysis efficiency. The b hadron lifetimes were varied within the ranges given by current world averages [18] by reweighting the generated hA signal Monte Carlo, giving a systematic error on the $b\bar{b}b\bar{b}$ efficiency of 0.7%. The systematics from other b physics sources are estimated to be 0.4%. The accuracy of the correction to the track resolution described in Section 3.3 is estimated from the comparison shown in Fig. 3 and a systematic of 0.8% is assigned to the efficiency, corresponding to 50% of the change due to the correction. With a contribution of 0.5% for Monte Carlo statistics the total systematic error is 1.2%. This is propagated to the final results using the method of Ref. [19] and changes the limits by negligible amounts.

4.2. The $\tau^+\tau^- b\bar{b}$ final state

The $\tau^+\tau^- b\bar{b}$ final state is selected by two complementary approaches. In the first approach, the tau decay products are first identified using charged particle tracks and tau candidates are constructed by the inclusion of neutral clusters in a cone around these tracks. In the second method, events are first clustered into four jets and jets consistent with tau decays are selected. In the following the first and second methods are referred to respectively as "track-based" and "jet-based".

4.2.1. Track-based selection

A preselection is first applied which selects high multiplicity hadronic final states and which rejects radiative returns to the Z peak. Hadronic events are selected by requiring at least ten charged particles which account for at least 20% of the centre-of-mass energy. Radiative returns with undetected photons down the beam axis are rejected by requiring the longitudinal missing momentum to be less than 30 GeV/c. The signal events are also characterized by missing energy and transverse momentum imbalance due to the undetected neutrinos. This is exploited by requiring the missing energy to be larger than 5 GeV and the momentum imbalance in the plane transverse to the beam axis to be larger than 5 GeV/c.

Tau leptons are identified by searching for identified electrons and muons, single charged particles and charged particle triplets with differing isolation requirements. To avoid the large potential contamination from background processes involving energetic leptons (e.g., eeZ, ZZ and WW), events with identified leptons with momenta larger than $40\,\mathrm{GeV}/c$ are rejected. Lepton candidates are required to be isolated by more than 10° using the isolation definition of the $\mathrm{H}\ell^+\ell^-$ channel described in Ref. [4]. Identified leptons which do not pass these criteria are not considered for the purposes of tau selection. The remaining tracks are rejected as tau candidates if another track falls within 10°. Charged particle triplets are identified by considering all combinations which have unit net charge and where no track except the three under consideration falls within 10° of the resultant vector. In all cases candidates with a net charged momentum less than $2\,\mathrm{GeV}/c$ are no longer considered. Tau candidates are constructed by adding the four-momenta of all the energy flow particles within 15° of the tau tracks. Tau candidates with a momentum less than $3\,\mathrm{GeV}/c$ or with a mass larger than $1.8\,\mathrm{GeV}/c^2$ are rejected.

In events with an identified lepton, background from W pair events is rejected by reconstructing the event as $\mathrm{WW} \to \mathrm{qq}\ell\nu$, where the missing four-momentum in the event is assigned to the neutrino and the remaining energy flow particles are assigned to the other W. Events in which the mass sum of the reconstructed W's is greater than $140\,\mathrm{GeV}/c^2$ and the mass of the hadronically-decaying W is less than $85\,\mathrm{GeV}/c^2$ are rejected.

Events are required to have at least two tau candidates of opposite charge, and at least one of the tau jets is required to have unit charged multiplicity. The sum of the isolation angles of the tau candidates is required to be larger than 80°. Energy flow particles not included in the tau jets are clustered into two jets using the Durham algorithm.

A fit is performed on the event, where the four jet directions are fixed to the measured ones and the jet momenta are determined from the fit. The masses of the tau jets are constrained to the nominal tau mass. The other two jets are rescaled keeping their velocities fixed to the measured values. The fit minimizes a χ^2 with contributions from energy-momentum conservation, the mass difference of the two dijet systems (in accordance with the $m_\mathrm{A} \approx m_\mathrm{h}$ hypothesis) and the estimated uncertainties on the measurements of the non-tau jets. In the fit the tau jet momenta are constrained to be larger than 90% of the measured values. Combinations in which either of the fitted values for the non-tau jet momenta is less than 75% of the measured energy are no longer considered. The distribution of χ^2 for the signal and background Monte Carlo is shown in Fig. 6a. Combinations with $\chi^2 > 20$ are rejected. If more than one combination passes the selection criteria, the combination with the smallest χ^2 is kept. In signal events the resolution on the tau dijet mass using this method is about $3\,\mathrm{GeV}/c^2$. The fitted mass of the tau pair is required to lie between $40\,\mathrm{GeV}/c^2$ and $70\,\mathrm{GeV}/c^2$.

The background is further reduced by means of the three-input neural network b tag. A requirement is placed on the sum of the outputs for the two non-tau jets, using an optimization procedure [4] which minimizes the expected confidence level of the $\mathrm{b\bar{b}b\bar{b}}$ analysis combined with that of the $\tau^+\tau^-\mathrm{b\bar{b}}$ analysis. The b tagging variable defined as

$$\mathscr{B}_2 = 2 - \sum_{i=1}^{2} \eta_i$$

is required to be smaller than 1.15.

Based on Monte Carlo simulation, the expected background is 0.02 ± 0.01 event. The efficiency to select $m_\mathrm{A} \approx m_\mathrm{h} \approx 60\,\mathrm{GeV}/c^2$ is 32% at 172 GeV and similar at 161 GeV.

4.2.2. Jet-based selection

Hadronic events are selected by requiring at least eight charged particles which account for more than 10% of the centre-of-mass energy. The longitudinal momentum of the event is required to be less than $40\,\mathrm{GeV}/c$, the reconstructed missing energy is required to be positive, and the transverse momentum must be larger than $5\,\mathrm{GeV}/c$. Events in which the thrust is greater than 0.9 are rejected.

The Durham algorithm is used to cluster the event into four jets, and the y_{34} value is required to be greater than 0.001. All four jets are required to contain at least one charged particle, and at least one jet must have less than seven energy flow particles.

The two lowest multiplicity jets are considered for tau selection. Only charged particles with momenta above $1\,\mathrm{GeV}/c$ are used in the following to select tau candidates. For these jets the total momentum of the charged particles is required to be larger than $2\,\mathrm{GeV}/c$, and the mass of each jet must be less than $1.8\,\mathrm{GeV}/c^2$.

The charged multiplicity of one of the tau candidates must be unity, and the sum of the charged multiplicities of the two jets is required to be six or less. The sum of the charges of the two tau candidates is required to be zero.

The four jets are fitted in the same way as for the track-based selection. The χ^2 of the fit, Fig. 6b, is required to be less than 20, and the reconstructed mass of the di-tau system must fall in the same mass range as for the track-based analysis. The same three-input neural network b tag is used, requiring $\mathscr{B}_2 < 0.85$. The cut is optimized to minimize the expected combined confidence level of the $\mathrm{b\bar{b}b\bar{b}}$, track-based and jet-based analyses.

From the Monte Carlo simulation, the expected background is 0.02 ± 0.01 events. The selection efficiency for $m_{\mathrm{A}} \approx m_{\mathrm{h}} \approx 60\,\mathrm{GeV}/c^2$ is 30% at 172 GeV and 27% at 161 GeV.

4.2.3. Combined $\tau^+\tau^-\mathrm{b\bar{b}}$ selection

The track-based and the jet-based analyses are combined by selecting events if they pass at least one of the selections. The overlap between the two selections for the signal is around 60%, with almost no common background. Fig. 6c shows the reconstructed m_{h} distribution for the signal and background. The final efficiency for the $\tau^+\tau^-\mathrm{b\bar{b}}$ combined selection is $\sim 45\%$ for $m_{\mathrm{A}} \approx m_{\mathrm{h}} \approx 60\,\mathrm{GeV}/c^2$ and is shown in Fig. 7c as a function of mass and centre-of-mass energy. The expected background is 0.04 ± 0.02 events. No candidates are observed by either analysis.

The two principal systematic uncertainties are common to the two $\tau^+\tau^-\mathrm{b\bar{b}}$ analyses: the energy flow reconstruction and the b tagging. Uncertainties on the efficiency can occur due to the simulation of reconstructed energy flow particles which can affect the efficiency of the cut on the χ^2 of the mass fit. The fit is recalculated with non-tau jet energies smeared within their errors. The effect is very small and gives a difference on signal efficiencies less than 0.2%. The b tagging effects are studied using a

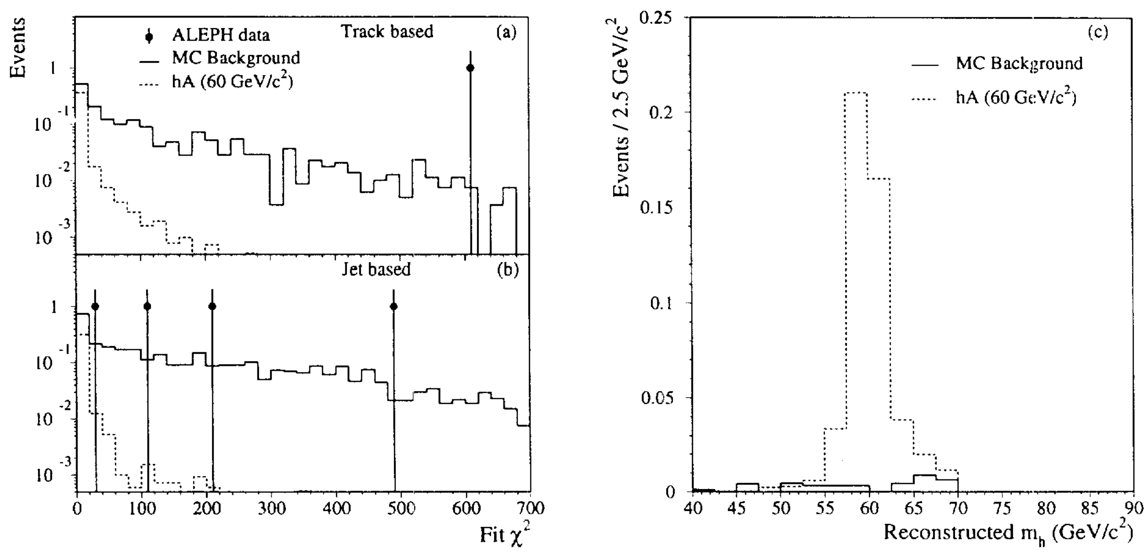

Fig. 6. The fit χ^2 variable in the $\tau^+\tau^-\mathrm{b\bar{b}}$ (a) track-based and (b) jet-based analyses with all cuts except those on the b tagging variable. The points are the data, the solid histogram is the total background prediction from the simulations and the dashed histogram is the expectation from $m_{\mathrm{A}} \approx m_{\mathrm{h}} \approx 60\,\mathrm{GeV}/c^2$ for a luminosity corresponding to the data. (c) Reconstructed mass m_{h} in the combined $\tau^+\tau^-\mathrm{b\bar{b}}$ analysis for signal and background after all cuts.

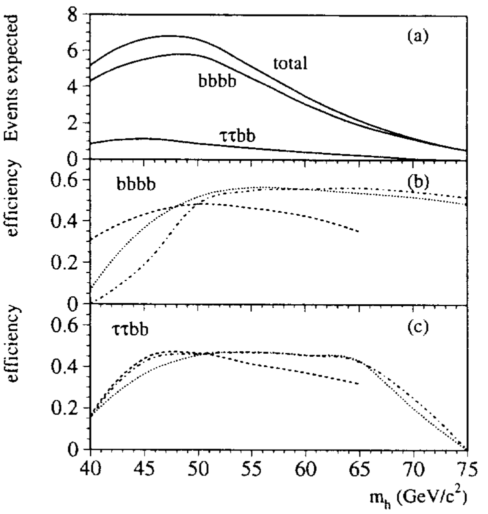

Fig. 7. Shown for $\tan\beta = 10$, where $m_A \approx m_h$, as a function of mass: (a) Expected number of events for the two channels and the total. (b) Efficiency for the $b\bar{b}b\bar{b}$ channel for the three energies: 133 GeV (dashed), 161 GeV (dotted), 172 GeV (dot-dashed). (c) Efficiencies for $\tau^+\tau^- b\bar{b}$ channel for the three energies.

similar approach as for the $b\bar{b}b\bar{b}$ channel. Reweighting generated signal events with different b hadron lifetimes changes the efficiency by less than 0.3% and the systematic due to the correction to the track resolution is evaluated to be 0.3%. Systematics are dominated by the 1.1% uncertainty due to Monte Carlo statistics. Adding all these effects in quadrature gives a total systematic error of 1.2% which has a negligible impact on the final result.

5. Combined results of hA and hZ analyses

No candidate events were retained by any of the selections presented in the previous sections, in agreement with the 0.91 ± 0.17 events expected from Standard Model processes. The results of the two selections were combined together, and then combined with the result of the search for the Higgs-strahlung process $e^+e^- \to hZ$ [4], in the following way [20].

First, the measured and expected confidence levels were computed both for the $b\bar{b}b\bar{b}$ and the $\tau^+\tau^- b\bar{b}$ final states, from the numbers of events expected from Standard Model processes and from signal (with $\cos^2(\beta-\alpha) = 1$), using the reconstructed mass sum $m_h + m_A$ as discriminating variable. Since no candidate events have been selected, the measured confidence level is simply $\exp(-s)$, where s is the number of events from signal expected to be

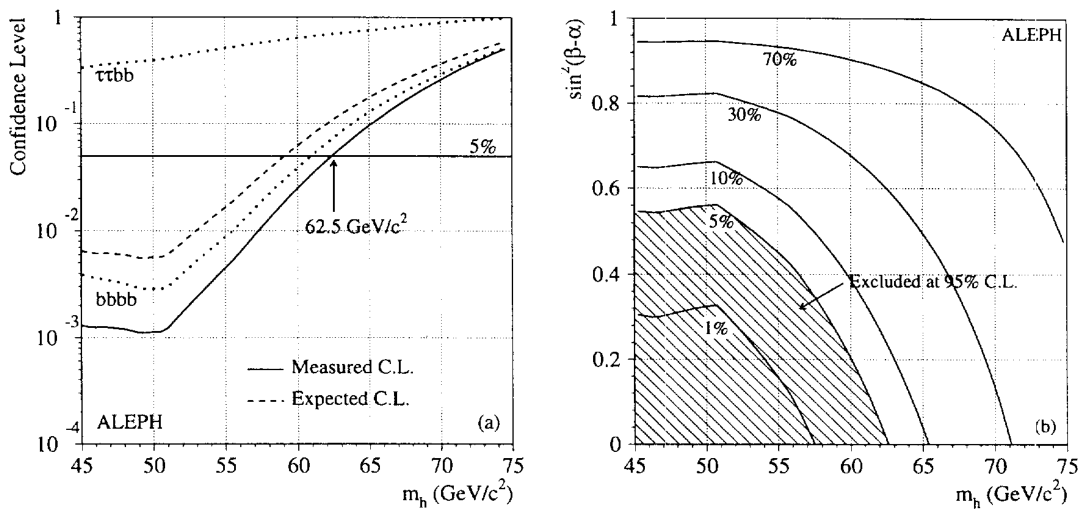

Fig. 8. (a) Measured confidence levels as a function of m_h (dotted curves) for the two final states produced by the $e^+e^- \to$ hA process, and for their combination (solid curve). Also shown is the combined expected confidence level (dashed curve). (b) Measured confidence level in the m_h,$\sin^2(\beta-\alpha)$ plane, obtained from the combined $e^+e^- \to$ hA search.

selected by each analysis (shown in Fig. 7a). The expected combined confidence level is displayed with the measured individual and combined confidence levels in Fig. 8a.

As a result of this combination, the m_h range between 45 and 62.5 GeV/c^2 is excluded at more than 95% C.L. for $\cos^2(\beta-\alpha)=1$, i.e., in a region of the MSSM parameter space in which $m_h = m_A$ and the decay branching ratios of h and A into $b\bar{b}$ and $\tau^+\tau^-$ are largest. The mass range below 45 GeV/c^2 was already excluded at much more than 95% C.L. by LEP 1 analyses [21,22]. The same operation was repeated varying $\cos^2(\beta-\alpha)$ from 1 to 0. The resulting confidence level curves are shown in Fig. 8b in the $[m_h,\sin^2(\beta-\alpha)]$ plane.

When $\cos^2(\beta-\alpha)$ becomes too small for the $e^+e^- \to$ hA searches to contribute, $\sin^2(\beta-\alpha)$ becomes large enough for $e^+e^- \to$ hZ searches [4] to play a significant rôle. The confidence level presented in Ref. [4] was therefore derived again by varying $\sin^2(\beta-\alpha)$ from unity (its value in the Standard Model) to zero. The resulting confidence level curves are shown in Fig. 9a in the $[m_h,\sin^2(\beta-\alpha)]$ plane.

Finally, the confidence levels obtained in the $[m_h,\sin^2(\beta-\alpha)]$ plane by the hZ and hA searches were combined. The result is displayed in Fig. 9b. All values of m_h below 62.5 GeV/c^2 can be excluded at more than 95% C.L.

These confidence levels in the $[m_h,\sin^2(\beta-\alpha)]$ plane can be translated into a 95% C.L. excluded region in the usual $[m_h,\tan\beta]$ plane, as shown in Fig. 10. The heavily shaded regions, theoretically not allowed, depend on the choice of parameters for stop mixing and on the top quark mass. (A value of 175 GeV/c^2[23] was used.) The experimentally excluded region is, however, identical in both cases of no mixing and maximal mixing.

When varying $\cos^2(\beta-\alpha)$, the hA production cross section was modified accordingly, but neither the m_A value nor the h and A branching fractions (and therefore hA selection efficiencies) were changed from their values at $\cos^2(\beta-\alpha)=1$. However, the hA analysis efficiencies have been checked to be unchanged at the level of 1% for mass differences of h and A below 10 GeV/c^2. With the choices of MSSM parameters given in Section 1, this is always the case when the $e^+e^- \to$ hA cross section is not vanishingly small. The h and A branching ratio variations have also been found to have a negligible effect.

The same holds true for hZ when varying $\sin^2(\beta-\alpha)$, except when m_A is small enough for the h → AA decay to occur. When $m_A > 2m_b$, however,

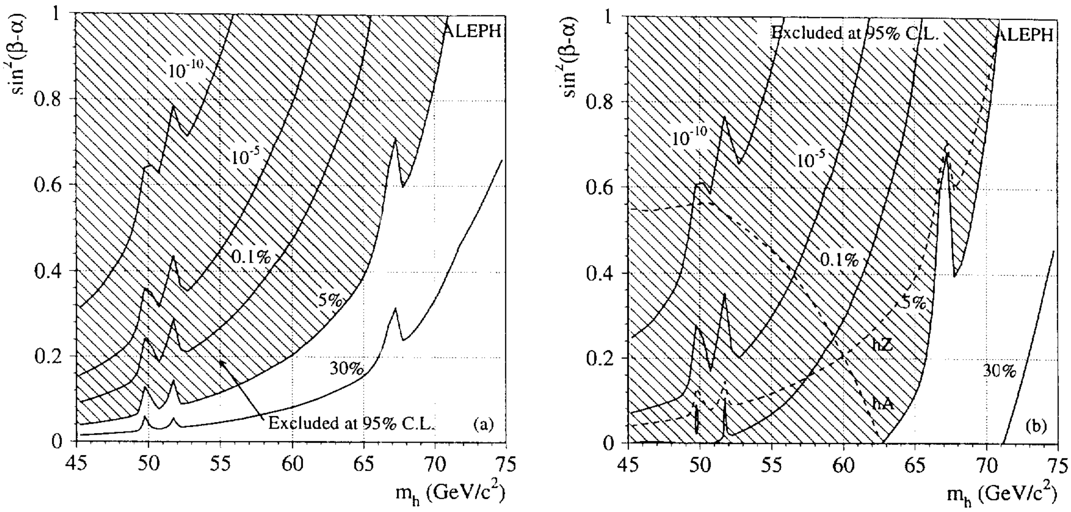

Fig. 9. Measured confidence levels in the $[m_h,\sin^2(\beta-\alpha)]$ plane (a) from $e^+e^- \to$ hZ searches, and (b) from the combination of $e^+e^- \to$ hZ and hA (solid curves) and again the 5% confidence levels for the hA and hZ analyses separately (dashed curves).

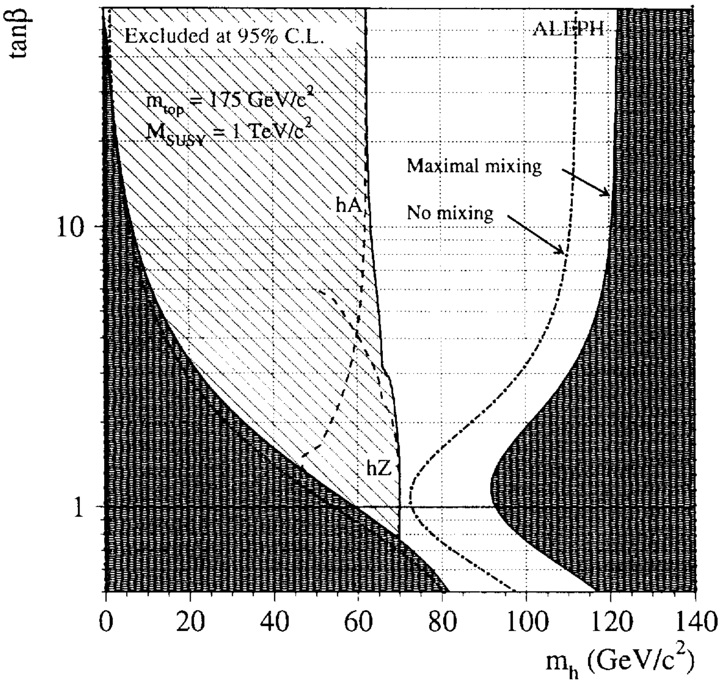

Fig. 10. The $[m_h, \tan\beta]$ plane in the maximal mixing configuration. The dark areas are theoretically disallowed. The hatched area is excluded at the 95% confidence level by the combined search for $e^+e^- \to hZ$ and $e^+e^- \to hA$. The dot-dashed lines show the change in the theoretically excluded region in the no mixing configuration.

A mostly decays into $b\bar{b}$ (and h into $b\bar{b}b\bar{b}$). This renders the hZ selections of Ref. [4] at least as efficient as when h decays into $b\bar{b}$ and the limits are conservative. This is no longer the case when $m_A < 2m_b$. This case must be dealt with by means of separate selections and is not addressed in this letter. Since such a light A has already been excluded by dedicated $e^+e^- \to hZ^*/hA$ searches at LEP 1 [21] for m_h values below $\sim 60\,\mathrm{GeV}/c^2$, the region corresponding to this configuration is a strip too narrow to be visible in Fig. 10, close to the theoretically forbidden domain and affecting only the $\tan\beta < 1$ region.

The invisible decay $h \to \chi\chi$ could also affect the validity of the result if the lightest neutralino χ were light enough. This possibility is excluded by the negative chargino searches performed at LEP 1.5 [24], when the GUT mass relations between charginos and neutralinos are satisfied [25].

To conclude, if the search is restricted to theoretically favoured $\tan\beta$ values in excess of unity, both m_h and m_A must be larger than 62.5 GeV/c^2 at the 95% confidence level.

6. Conclusions

A search has been made for the neutral Higgs bosons h and A of the Minimal Supersymmetric Standard Model using a total of 27.2 pb^{-1} of data collected at centre-of-mass energies from 130 to 172 GeV. For the associated production $e^+e^- \to hA$, searches have been performed in the $b\bar{b}b\bar{b}$ and $\tau^+\tau^- b\bar{b}$ final states. No candidate events were found in either channel with a total background expectation of 0.91 ± 0.17. This result was combined with the results reported in Ref. [4] on the search for $e^+e^- \to hZ$ to give exclusion limits on m_h as a function of $\sin^2(\beta - \alpha)$ and as a function of $\tan\beta$ for typical sets of MSSM parameters. For values of $\tan\beta > 1$, h and A are excluded for masses less than 62.5 GeV/c^2 at 95% confidence level.

Acknowledgements

We wish to thank our colleagues from the accelerator divisions for the successful operation of LEP at high energy. We are indebted to the engineers and technicians in all our institutions for their contribution to the excellent performance of ALEPH. Those of us from non-member countries thank CERN for its hospitality.

References

[1] Y. Okada, M. Yamaguchi, T. Yanagida, Progr. Theor. Phys. 85 (1991) 1;
J. Ellis, G. Ridolfi, F. Zwirner, Phys. Lett. B 257 (1991) 83; B 262 (1991) 477;
H.E. Haber, R. Hempfling, Phys. Rev. Lett. 66 (1991) 1815;
R. Barbieri, M. Frigeni, F. Caravaglios, Phys. Lett. B 258 (1991) 167;
R. Barbieri, M. Frigeni, Phys. Lett. B 258 (1991) 395.

[2] M. Carena, M. Quiros, C.E.M. Wagner, Nucl. Phys. B 461 (1996) 407;
M. Carena, J.R. Espinosa, M. Quiros, C.E.M. Wagner, Phys. Lett. B 355 (1995) 209;
H.E. Haber, R. Hempfling, A.H. Hoang, CERN-TH-95-216 (1995).

[3] M. Carena, P.M. Zerwas (Conveners) et al., Higgs Physics, in: Physics at LEP 2, Eds. G. Altarelli, T. Sjöstrand, F. Zwirner, CERN 96-01 (1996) p. 351.

[4] ALEPH Collaboration, Phys. Lett. B 412 (1997) 155.

[5] ALEPH Collaboration, Nucl. Instrum. Methods A 294 (1990) 121; B. Mours et al., Nucl. Instrum. Methods A 379 (1996) 101.

[6] ALEPH Collaboration, Nucl. Instrum. Methods A 360 (1995) 481.

[7] Construction and Performance of the new ALEPH Vertex Detector, D. Creanza et al., to appear in the Proceedings of the 5th International Conference on Advanced Technology and Particle Physics, Como, Italy (October 1996).

[8] ALEPH Collaboration, Nucl. Instrum. Methods A 346 (1994) 461.

[9] ALEPH Collaboration, Phys. Lett. B 313 (1993) 535.

[10] ALEPH Collaboration, Phys. Lett. B 322 (1994) 441.

[11] ALEPH Collaboration, Phys. Lett. B 384 (1996) 353.

[12] L. Lönnblad, C. Peterson, T. Rögnvaldsson, CERN-TH.7135/94.

[13] C. Peterson, T. Rögnvaldsson, CERN School of Computing, Ed. C. Verkerk (1991) p. 113;
L. Lönnblad, C. Peterson, T. Rögnvaldsson, Comp. Phys. Comm. 70 (1992) 167;
S.R. Amendolia, CERN School of Computing, Eds. C.E. Vandoni, C. Verkerk (1993) p.1.

[14] ALEPH, DELPHI, L3, OPAL Collaborations, Nucl. Instrum. Methods A 378 (1996) 101.

[15] P. Janot, The HZHA generator, in: Physics at LEP 2, Eds. G Altarelli, T. Sjöstrand, F. Zwirner, CERN 96-01 (1996) p. 309.

[16] T. Sjöstrand, The PYTHIA 5.7 and JETSET 7.4 Manual, LU-TP.95/20 and CERN-TH.7112/93.

[17] ALEPH Collaboration, Z. Phys. C 71 (1996) 179.

[18] Particle Data Group, Phys. Rev. D 54 (1996) 1.

[19] R.D. Cousins, V.L. Highland, Nucl. Instrum. Methods A 320 (1992) 331.

[20] P. Janot, F. Le Diberder, Combining 'Limits', CERN/PPE 97-053, LPNHE/97-01, to be submitted to Nucl. Instrum. Methods.

[21] ALEPH Collaboration, Phys. Rep. 216 (1992) 253; Phys. Lett. B 285 (1992) 309; B 313 (1993) 312; B 384 (1996) 427;
DELPHI Collaboration, Z. Phys. C 67 (1995) 69; Nucl. Phys. B 421 (1994) 3;
OPAL Collaboration, Z. Phys. C 73 (1997) 189;
L3 Collaboration, Z. Phys. C 57 (1993) 355; Phys. Lett. B 385 (1996) 454.

[22] P. Janot, Searching for Higgs bosons at LEP 1 and LEP 2, to appear in Perspectives on Higgs Physics II, Ed. G.L. Kane (World Scientific).

[23] J. Lys, S. Protopopescu, P. Tipton, proceedings of the 28th International Conference on High Energy Physics, Warsaw, Poland (25–31 July, 1996), Eds. Z. Ajduk, A.K. Wróblewski (World Scientific, 1997) pp. 23–32, 1192–1199.

[24] ALEPH Collaboration, Phys. Lett. B 373 (1996) 246.

[25] A. Djouadi, P. Janot, J. Kalinowski, P.M. Zerwas, Phys. Lett. B 376 (1996) 220.

5.5 P4 [27]: Higgs searches at LEP2 with the ALEPH detector

In the year 1998 ALEPH has taken 176 pb^{-1} of data at the single energy of 189 GeV. The results of the Higgs search analyses of this data sample are combined with results obtained at lower energies and presented in this paper.

Since the centre-of-mass energy is above the threshold of Z pair production, irreducible background from $ZZ \to b\bar{b}Z$ is expected in the search for the standard model Higgs boson. As a consequence, full background subtraction is performed.

This paper also presents the results of the searches for charged Higgs bosons in the context of two Higgs doublet models. The three characteristic final state topologies are shown in Fig. 5.7.

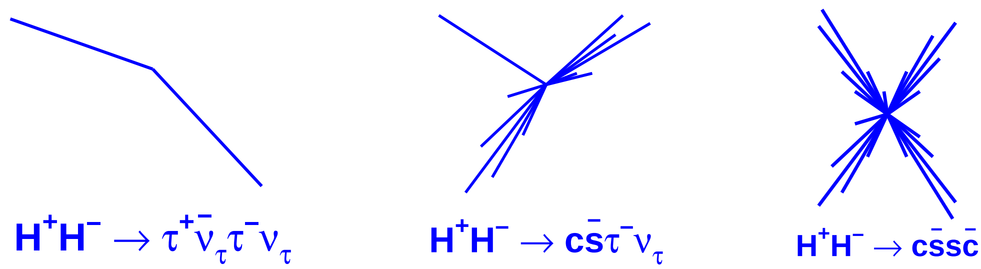

Figure 5.7: Graphical illustration of the three event topologies in which the charged Higgs bosons $H^\pm$ are searched for.

While the Z boson is invisible if it decays into neutrinos, the Higgs boson is invisible to the detector if it decays into, *e.g.* neutralinos, which it can do in certain extensions of the standard model. Figure 5.8 shows the dominant decay modes used in the search for an invisibly decaying Higgs boson when produced through the Higgs-strahlung process. The "acoplanar jets" final state is similar to the missing energy final state, and for 100% branching ratio into invisible decays a similar limit as in the standard model Higgs search is obtained.

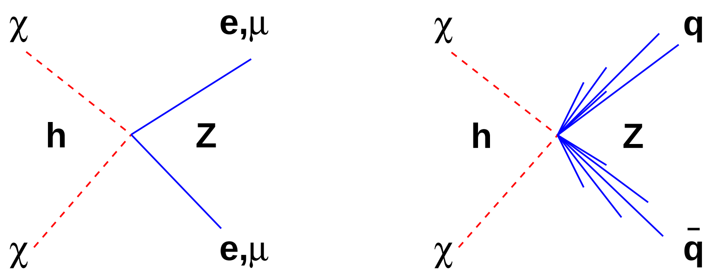

Figure 5.8: Signal topologies of invisible Higgs boson decays. The signatures are an acoplanar charged lepton pair (left) and an acoplanar pair of jets.

HIGGS SEARCHES AT LEP2 WITH THE ALEPH DETECTOR

E. KNERINGER
Institut für Experimentalphysik, Universität Innsbruck, 6020 Innsbruck, AUSTRIA
ALEPH Collaboration
E-mail: Emmerich.Kneringer@uibk.ac.at

Data collected with the ALEPH detector at centre-of-mass energies between 130 and 189 GeV are used to search for Higgs bosons of the standard model and its supersymmetric extensions. No evidence for a Higgs particle has been found in 256 pb^{-1} of LEP2 data. Mass exclusion limits were set.

1 Introduction

A neutral Higgs boson is required to complete the particle spectrum of the standard model. Fits to electroweak data [1] from LEP, SLC and Tevatron indicate that if the Higgs particle exists it has most probably a mass around 100 GeV/c^2. The situation at LEP, which is summarized in Fig. 1 (left), shows that we are getting more and more sensitive to this mass range.

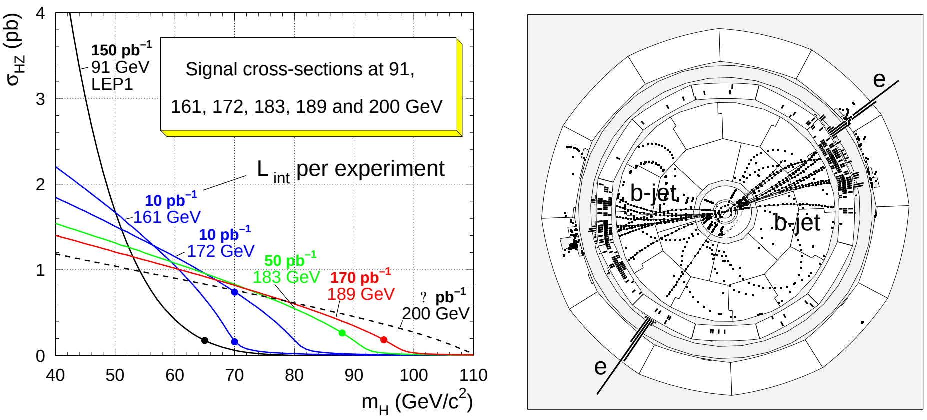

Figure 1: Left: cross section for the Higgs-strahlung process at the various LEP energies. For a given energy the point on the curve indicates the standard model Higgs boson mass exclusion limit obtained by a typical LEP experiment with the data taken at that energy. Right: Higgs boson candidate event in the H$\ell\ell$ channel (as seen by the ALEPH detector).

All mass exclusion limits given in this report are at 95% confidence level. To get an idea of the sensitivity of a specific analysis the expected mass exclusion limit [2] from gedanken experiments usually is also quoted. All the search analyses use cut-based selections and/or neural network methods. We make extensive use of Monte Carlo simulations for the neural net training and the setting of the selection cuts. No details of the preliminary analyses are given, however, the references always point to the corresponding latest published analysis.

2 The Standard Model Higgs Boson

At LEP2, the dominant Higgs production mechanism is the so-called Higgs-strahlung process $e^+e^- \rightarrow Z^* \rightarrow HZ$. There are also minor contributions from processes where the Higgs boson is generated through the fusion of two electroweak gauge bosons. In the mass range accessible at LEP2, the Higgs boson decays in 92% of the cases into two quark jets (91% of which are $b\bar{b}$) and in about 8% of the cases into $\tau^+\tau^-$. Combining these numbers with the branching fractions of the Z boson we obtain the branching fractions of HZ into the following four characteristic event topologies:

- four jet channel: $q'\bar{q}'q\bar{q}$ (64.6%)
- missing energy channel: $H\nu\bar{\nu}$ (20.0%)
- lepton channel: $H\ell^+\ell^-$, $\ell = e$ or μ (6.7%)
- τ–channel: either H or Z decays to $\tau^+\tau^-$ (8.7%)

Except for the lepton channel, a high b-quark content is required for the quark jets coming from Higgs boson decay. In all channels the invariant mass of the decay products of the Z must be compatible with m_Z. The results of the HZ analyses [3] applied to data taken with the ALEPH detector [4,5] at 189 GeV are summarized in Table 1.

Table 1: Signal efficiencies ϵ, expected number of signal events N_{95}^{exp} for $m_H = 95$ GeV/c^2, background expectation from standard model processes N_{bkg}^{exp}, background from ZZ events N_{ZZ}^{exp} (dominant background source; irreducible) and number of observed events in 170 pb^{-1} of ALEPH data taken at $\sqrt{s} = 189$ GeV for the HZ decay topologies.

Selection	ϵ	N_{95}^{exp}	N_{bkg}^{exp}	N_{ZZ}^{exp}	N_{obs}
$b\bar{b}q\bar{q}$	39.3%	7.7	18.5	10.1	20
$b\bar{b}\nu\bar{\nu}$	24.3%	1.6	3.7	3.1	7
$b\bar{b}\ell^+\ell^-$	72.9%	1.5	13.2	11.8	13
$b\bar{b}\tau^+\tau^-$	20.1%	0.2	0.8	0.6	2
$\tau^+\tau^-q\bar{q}$	18.9%	0.3	1.8	1.2	0
total		11.3	38.0	26.8	42

The analyses for the four individual channels are optimized in such a way that the combination of these analyses gives the best global HZ searches analysis. The definition used here for 'best analysis' is: the analysis which gives the highest expected Higgs mass exclusion limit under the hypothesis that there is no signal [2].

No signal is observed in 250 pb^{-1} of data (*cf.* m_{h} distribution in Fig. 2) which allows to exclude a standard model Higgs boson with a mass less than 90.4 GeV/c^2, as shown in Fig. 2 (right). The expected limit is 93.4 GeV/c^2.

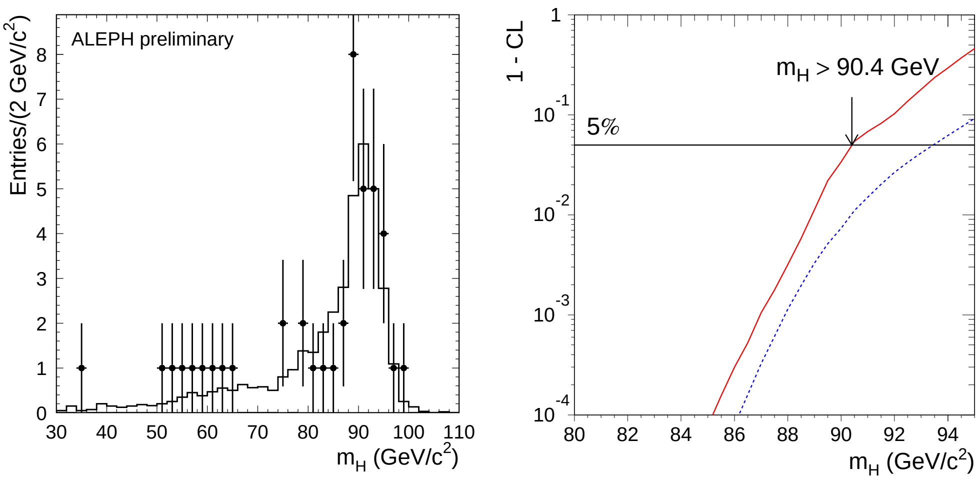

Figure 2: Left: distribution of m_{H} of the selected events (points) and the expectation from the standard model background processes (histogram) in HZ searches at $\sqrt{s}$ = 189 GeV. Right: observed (full line) and expected (dashed line) combined confidence levels for the standard model Higgs search.

3 Neutral Higgs Bosons of the MSSM

The particle spectrum of the Higgs sector of the minimal supersymmetric extension of the standard model (MSSM) consists of five physical states, two CP-even neutral bosons h and H (with mixing angle α and masses $m_{\mathrm{h}} < m_{\mathrm{H}}$), one CP-odd neutral boson A and two charged bosons $\mathrm{H}^{\pm}$. At tree level, the Higgs sector can be parameterized by two independent parameters, *e.g.* m_{h} and $\tan\beta = v_2/v_1$, the ratio of the vacuum expectation values of the two Higgs doublets. Only the h and A bosons are within the reach of LEP2. They are expected to be produced in Z decays via the Higgs-strahlung process $\mathrm{Z}^* \rightarrow \mathrm{hZ}$, with a cross section proportional to $\sin^2(\beta - \alpha)$, and via the associated pair production $\mathrm{Z}^* \rightarrow \mathrm{hA}$, with a cross section proportional to $\cos^2(\beta - \alpha)$.

These two processes are complementary, in the sense that if one cross section is maximal the other is minimal and vice versa. Thus both processes must be searched for. For the first process, the results from the hZ searches (Sec. 2) can be used. The second process is searched for in the following two decay channels:

- hA → $b\bar{b}b\bar{b}$ (85%)
- hA → $b\bar{b}\tau^+\tau^-$, $\tau^+\tau^- b\bar{b}$ (15%)

The performance of the two analyses [6] is reported in Table 2.

Table 2: Performance of the hA analyses at $\sqrt{s} = 189$ GeV: signal efficiencies, expected number of signal events for $m_{\rm h} = m_{\rm A} = 85$ GeV/c^2, background expectation and number of observed events.

Selection	ϵ	N_{85}^{exp}	N_{bkg}^{exp}	N_{obs}
$b\bar{b}b\bar{b}$	58.3%	3.4	9.0	13
$b\bar{b}\tau^+\tau^-$	24.0%	0.2	0.6	0

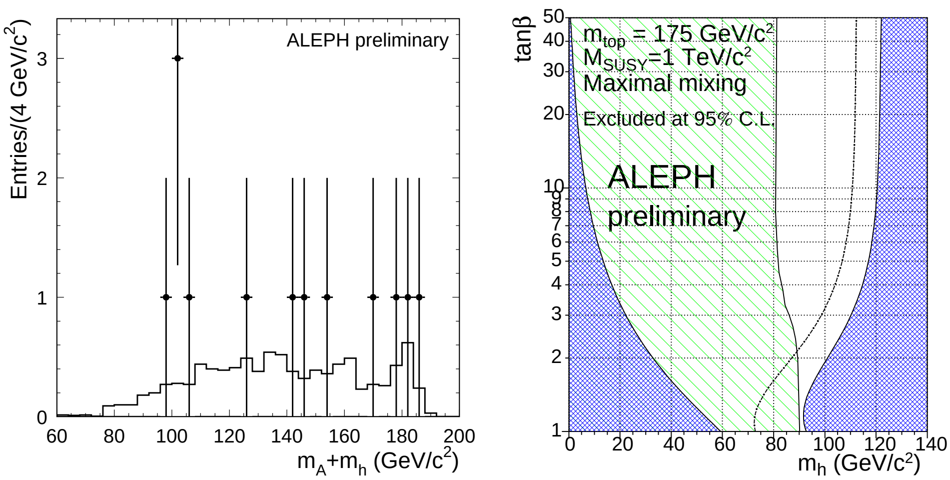

Figure 3: Left: distribution of $m_{\rm A}+m_{\rm h}$ of the selected events (points) and the expectation from the standard model background processes (histogram) in hA searches at $\sqrt{s} = 189$ GeV. Right: experimentally excluded region in the $[m_{\rm h},\tan\beta]$ plane (after combination with the hZ searches). The dark area represents the theoretically forbidden region for the case of 'maximal stop mixing' (dashed-dotted curve for the 'no stop mixing' case).

No signal is observed in the data, as can be seen in Fig. 3 (left). This allows to set an upper limit on the cross section for hA production as a function of

m_h, which implies an upper limit on $\cos^2(\beta - \alpha)$ as a function of m_h. On the other hand, the hZ searches interpreted in this way result in an upper limit on $\sin^2(\beta - \alpha)$ as a function of m_h. Combining the hZ and hA searches in an optimal way [2] leads to an excluded region in the two-dimensional parameter space $[m_h, \sin^2(\beta - \alpha)]$, which usually is translated to the $[m_h, \tan\beta]$ plane, as shown in Fig. 3 (right). For $\tan\beta \geq 1$ we find that ALEPH data up to centre-of-mass energies of 189 GeV exclude the h and A Higgs bosons of the MSSM with masses less than 80.8 and 81.2 GeV/c^2, respectively, *i.e.* the neutral Higgs bosons must be heavier than the W boson if $\tan\beta \geq 1$.

4 Charged Higgs Bosons

In the MSSM charged Higgs bosons are heavier than W bosons. This restriction does not hold for general two doublet models, which are very attractive theoretically because of the absence of flavor changing neutral currents and the relation $m_W = m_Z \cos\theta_W$ holding at tree level. The $H^\pm$ has the same decay modes as the $W^\pm$, but since its coupling is proportional to the charged fermion masses, it dominantly decays into the heaviest energetically allowed fermion pair of the quark and lepton families. Whether $H^\pm$ decay preferentially into quarks or leptons depends on other parameters of the model. Therefore, the search for pair-produced H^+H^- is performed in the following three channels:

- leptonic channel: $\tau^+\nu_\tau\tau^-\bar{\nu}_\tau$
- mixed channel: $c\bar{s}\tau^-\bar{\nu}_\tau$
- hadronic or four jet channel: $c\bar{s}s\bar{c}$

The performance of these analyses [7] is summarized in Table 3.

Table 3: Efficiencies ϵ, number of standard model background events expected N_{bkg}^{exp} and number of observed candidates N_{obs} for the three charged Higgs boson analyses at a centre-of-mass energy of 189 GeV, as functions of the charged Higgs mass. For the four jet channel, numbers are quoted within a ± 3 GeV/c^2 window around the assumed Higgs boson mass.

$m_{H^\pm}$	$\tau^+\nu_\tau\tau^-\bar{\nu}_\tau$			$c\bar{s}\tau^-\bar{\nu}_\tau$			$c\bar{s}s\bar{c}$		
(GeV/c^2)	ϵ (%)	N_{bkg}^{exp}	N_{obs}	ϵ (%)	N_{bkg}^{exp}	N_{obs}	ϵ (%)	N_{bkg}^{exp}	N_{obs}
50	33.5	15.5	20	35.6	9.4	11	40.1	15.1	18
55	35.2	15.5	20	37.2	9.4	11	38.4	22.8	23
60	38.2	15.5	20	37.4	9.4	11	37.6	28.0	19
65	35.2	15.5	20	34.8	9.4	11	37.2	30.6	28
70	39.9	15.5	20	28.1	9.4	11	36.4	32.7	35
75	40.8	15.5	20	19.1	9.4	11	34.6	55.1	40

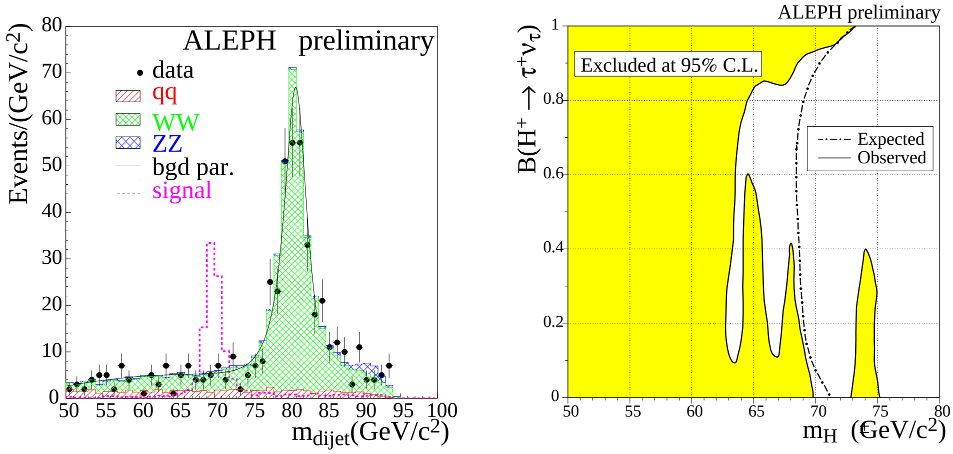

Figure 4: Left: distribution of the dijet mass distribution as obtained after applying all cuts of the $c\bar{s}s\bar{c}$ selection; shown are 189 GeV data (dots), background Monte Carlo (histogram) and the polynomial parameterization of the background (full line). Also shown is the Monte Carlo expectation for a signal with $m_{\mathrm{H}^\pm} = 70$ GeV/c^2 (dashed line) with arbitrary normalization. Right: limit on the mass of charged Higgs bosons as a function of $\mathcal{B}(\mathrm{H}^+ \to \tau^+\nu_\tau)$. Shown are the expected (dash-dotted) and observed (full) exclusion curves for the combination of the three charged Higgs boson analyses. The shaded area is excluded at 95% C.L.

The search for charged Higgs bosons in the three final states $\tau^+\nu_\tau\tau^-\bar{\nu}_\tau$, $c\bar{s}\tau^-\bar{\nu}_\tau$ and $c\bar{s}s\bar{c}$ has been performed using 175 pb^{-1} of ALEPH data collected at $\sqrt{s} = 189$ GeV. No evidence of Higgs boson production was found (Fig. 4 left) and mass limits were set as a function of the branching ratio $\mathcal{B}(\mathrm{H}^+ \to \tau^+\nu_\tau)$. The result of the combination of the three analyses is displayed in Fig. 4 (right) where the curves corresponding to expected and observed confidence levels of 95% exclusion are drawn. As can be seen from this figure, charged Higgs bosons with masses below 62.5 GeV/c^2 are excluded at 95% C.L. independently of $\mathcal{B}(\mathrm{H}^+ \to \tau^+\nu_\tau)$, where the expected mass exclusion limit is 68.5 GeV/c^2.

5 Invisible Higgs Boson Decays

Many extensions of the standard model allow for the Higgs boson to decay invisibly, *e.g.* into a pair of lightest neutralinos when the neutralino χ is light enough. Since the Higgs boson is produced through the Higgs-strahlung process hZ, this leads to the following two event topologies:

- a pair of acoplanar leptons, when $\mathrm{Z} \to \mathrm{e}^+\mathrm{e}^-$ or $\mathrm{Z} \to \mu^+\mu^-$

- a pair of acoplanar jets, when the Z decays hadronically

where the acoplanarity is defined as the azimuthal angle between the two lepton or jet directions. Two analyses [8] are designed for the two channels. When they are applied to ALEPH data taken at $\sqrt{s}$ = 189 GeV, 33 candidates are found, in agreement with 33.6 events expected from all background processes (*cf.* Table 4). The distributions of the reconstructed Higgs boson masses are shown in Fig. 5 (left).

Table 4: Performance of the acoplanar lepton and acoplanar jet pair analyses.

Selection	N_{bkg}^{exp}	N_{obs}
$h\ell^+\ell^-$	4.3	5
$hq\bar{q}$	29.3	28

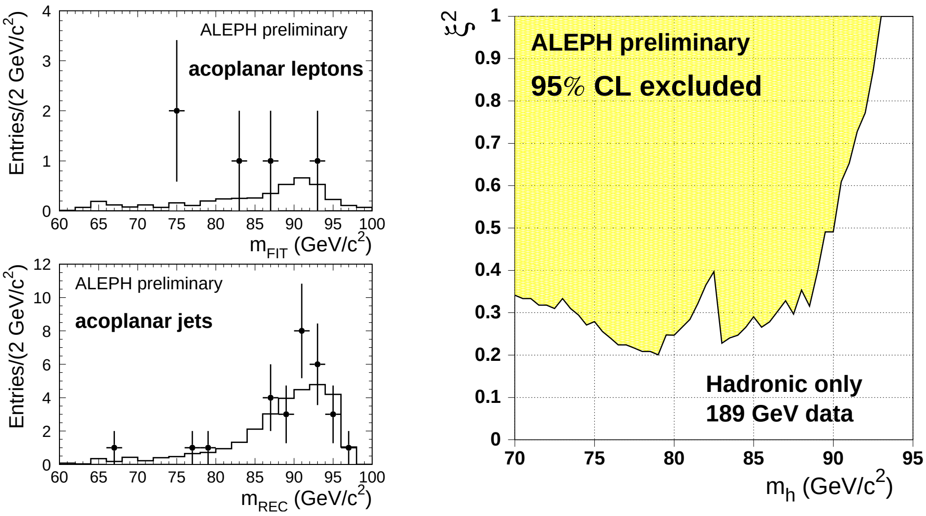

Figure 5: Left: distribution of the reconstructed Higgs boson mass of the selected events compared to the Monte Carlo expectation, for the acoplanar lepton and jet pair searches. Right: region in the $[m_h, \xi^2]$ plane excluded at 95% C.L. using only the hadronic channel at 189 GeV.

Quite generally, the production cross section for invisible Higgs boson decay can be parameterized as $\xi^2 \cdot \sigma_{SM}(e^+e^- \to hZ)$, where ξ^2 is a model dependent factor ranging from 0 to 1. One way of presenting the result of the negative searches is to calculate the 95% C.L. level upper limit on the production cross section of the invisibly decaying Higgs boson in units of $\sigma_{SM}(e^+e^- \to hZ)$ as a function of m_h, which is shown in Fig. 5 (right).

6 Summary

In this report, an overview has been given of the present status of Higgs boson searches with the ALEPH detector. The results are mainly based on the analysis of data taken at 189 GeV centre-of-mass energy. When the data taken at lower energies are included in the analyses the 95% confidence level exclusion limits improve slightly.

For the standard model Higgs boson we find $m_{\mathrm{H}} > 90.4$ GeV/c^2 at 95% C.L. using 250 pb^{-1} of data taken at $\sqrt{s} = 161$, 172, 183 and 189 GeV. This means that a Higgs boson with a mass equal to the Z mass just cannot be excluded at 95% C.L. with ALEPH data taken up to the year 1998.

Including all lower energy data, for the neutral Higgs bosons of the MSSM we obtain the limits $m_{\mathrm{h}} > 80.8$ GeV/c^2 and $m_{\mathrm{A}} > 81.2$ GeV/c^2 (valid for all values of $\tan\beta \geq 1$).

From the analysis of 175 pb^{-1} of ALEPH data collected in 1998, the charged Higgs bosons of general two doublet models are excluded below 62.5 GeV/c^2 independent of their decay mode.

Finally, using the same data, invisibly decaying Higgs bosons are searched for. For a production cross section equal to that of the standard model Higgs boson, *i.e.* $\xi^2 = 1$, masses below 92.8 GeV/c^2 are excluded.

Acknowledgments

I would like to thank all my colleagues from the ALEPH Higgs Task Force for the continuous effort to produce all these results.

References

1. LEP Electroweak Working Group, CERN-EP/99-15.
2. P. Janot and F. Le Diberder, *Nucl. Instrum. Methods* A **411**, 449 (1998).
3. ALEPH Collaboration, *Phys. Lett.* B **440**, 403 (1998).
4. ALEPH Collaboration, *Nucl. Instrum. Methods* A **294**, 121 (1990).
5. ALEPH Collaboration, *Nucl. Instrum. Methods* A **360**, 481 (1995).
6. ALEPH Collaboration, *Phys. Lett.* B **440**, 419 (1998).
7. ALEPH Collaboration, *Phys. Lett.* B **450**, 467 (1999).
8. ALEPH Collaboration, *Phys. Lett.* B **450**, 301 (1999).

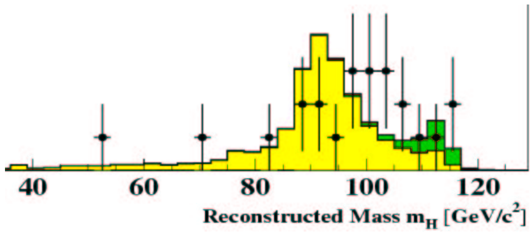

Is there a Higgs signal or not?

Chapter 6

Higgs Statistics

When an experiment is searching for a new particle several outcomes are possible. The main scenarios are:

(a) Nothing is found because the experiment is not sensitive enough.

(b) Nothing is found where an effect should be seen. This rules out the theory which predicts the particle.

(c) There is convincing evidence in the data for a new particle, which allows to claim its discovery. If this occurs, the next step is to check that the particle has all the properties predicted by the theory.

(d) The controversial case: there is an excess of events of a certain type, but this could also be due to a "background fluctuation". In this case the experiment has to be redone if possible, or even better, an independent experiment should be done.

In the search for the Higgs boson scenario (d) is actually the case at the end of LEP2. Pessimists rather say that scenario (a) is true. Optimists, on the other hand, vote for scenario (b) and say that all theories with $m_{\mathrm{H}} < 114.4$ GeV/c^2 [43] are ruled out (at the 95% confidence level), m_{H} being the mass of the standard model Higgs boson.

When an experiment is just at the limit of discovering a new particle the degree of belief that there is evidence for the particle in the data as well as the degree of belief that the data exclude the existence of the particle has to be quantified. Several statistical procedures have been developed to solve this problem in various contexts. Depending on the level of the expected background, for example, different methods seem to be optimal. Therefore it is not surprising that at the beginning of LEP2 all four LEP experiments used a different statistical method in their Higgs boson analyses (see Table 6.1). This was not an issue as long as the collaborations only published their own results. However, this became a problem when a combined result was requested. In the same way as the Higgs boson is searched for in various subchannels in a single

method	type	experiment
A	frequentist likelihood method	DELPHI
B	Bayesian likelihood method	L3
C	event weighting method	OPAL
D	confidence level combination	ALEPH

Table 6.1: Statistical methods used by the four LEP experiments to extract confidence limits from the findings of the Higgs boson searches. For a description of these methods, see Ref. [45]. Method A was finally chosen by the LHWG for combining the LEP results.

experiment, on a higher level, it can be seen as being searched for in sub-experiments of a global experiment *i.e.* the four LEP experiments together. Therefore it was obvious to apply the same techniques that were developed for combining subchannel results also to the task of producing a LEP-combined result. For this purpose the LEP working group for Higgs boson searches (LHWG) was established. When it compared the performances[1] of the four statistical methods in use it found them to be similar [46]. However, the LHWG wanted to converge to one single method (and maybe just another one, to be used for cross checks). In a meeting of the LHWG it was stated that the method to be selected should have certain properties. The method should

- be statistically correct (which is, of course, true for all methods);
- provide limits and discovery indicators;
- be applicable in the same way also for the various searches for other Higgs bosons (*e.g.* h, A or $H^{\pm}$);
- allow a detailed error handling to be implemented;
- be fairly easy to understand and use;
- allow a certain degree of "insight" into the experiments inputs (in case of any doubt on the result).

Finally, in February 2000 the LHWG decided to use method A (which fulfilled all the requirements) for producing the then future combined results. Since in the papers included in this *Habilitationsschrift* the statistical methods used are only briefly mentioned, the method preferred by the LHWG is described in more detail in the following section. This should allow to better understand the numbers and plots shown when the final LEP results on Higgs boson searches are quoted. It also gives credit to the huge amount of work that has been put into optimizing the individual analyses with respect to the statistical method used in order to obtain the best expected exclusion limit.

[1] The performance of a method was defined as the 95% confidence level mass exclusion limits (observed and expected on average) obtained, when combining the results of the four collaborations (higher numbers = better performance).

6.1 A statistical method for calculating confidence levels — the CL_s method

In this section the procedure, called the CL_s method [47], which was used to derive the final results of the Higgs boson searches at LEP2 is discussed. The emphasis is on the clarity and not on the complexity of the task. Often the question is raised, what is meant when somebody says: "We are 95% sure that $m_H > 114.4$ GeV/c^2." A more correct statement would be: "The 95% confidence level lower limit on the mass of the standard model Higgs boson is 114.4 GeV/c^2." This section is aimed at gaining a better understanding of what is behind this statement.

6.1.1 The discriminating variable

The starting point for calculating confidence levels is some data, usually available in the form of events. While originally an event is described by thousands of numbers ("raw data"), in the case of Higgs boson searches this information is condensed into a few (up to about 20) numbers, called event characteristics [2], which allow to discriminate in a statistical sense between signal events (events where a Higgs boson is produced at some intermediate step), and background events (events from known standard model processes). Candidates for signal events are selected by applying selection criteria, based on the event characteristics, to the data. In the next step so-called discriminating variables have to be defined. The distributions of these variables for the selected events should reveal whether signal events are present in the data, as described below. In the ALEPH analyses up to two such discriminating variables are used, namely the so-called reconstructed Higgs boson mass m_H^{rec} and a variable related to the b-quark contents [3] of the event. For simplicity, here only one variable is used, namely m_H^{rec}, which is the canonical discriminating variable for calculating confidence levels for the existence (or the non-existence) of the Higgs boson. It is obtained in the following way. First an event has to be selected by one of the analyses that differ mainly in the topology of the events they are looking for. Since for each topology a prescription exists on how to calculate m_H^{rec} (an example of such prescriptions is given in the introduction to the first paper in Sec. 3.3), this yields m_H^{rec}. When repeated for several events, a distribution like the one shown in Figure 6.1 is obtained. With the help of Monte Carlo simulations, the same distribution is calculated for signal and background events according to the standard model. Simulated signal and background events are also needed to optimize the selection criteria. This is achieved by maximizing the signal

[2] Mainly topological variables, like event shapes, and b-tagging information.

[3] In the mass range accessible at LEP2 the standard model Higgs boson decays predominantly into a $b\bar{b}$-pair — as shown in Sec. sec:decay-modes.

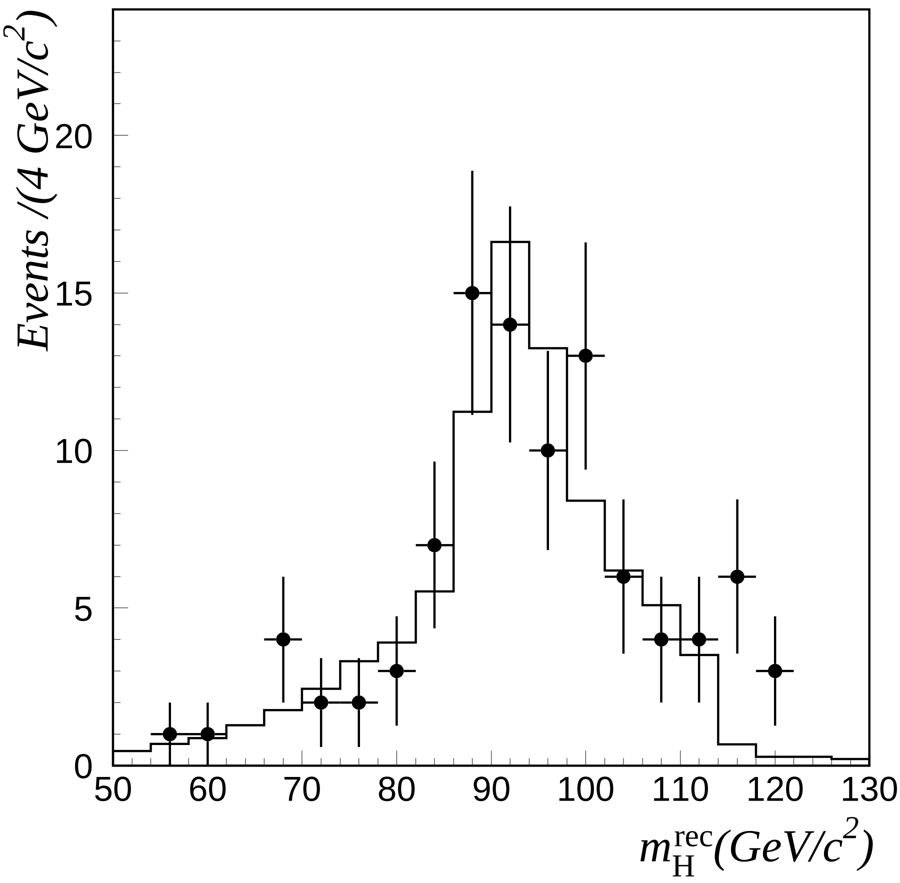

Figure 6.1: Distribution of the reconstructed Higgs boson mass (*i.e.* the discriminating variable) for the data collected by the ALEPH experiment in the year 2000 (dots with error bars) and the expected background (histogram) for the so-called cut stream analyses, after all cuts are applied. For the data $n = 95$ events are selected, where the expectation from the background distribution is $b = 87.6 \pm 2.4$, as obtained from Monte Carlo simulations.

efficiency and simultaneously reducing the background as much as possible for a given hypothesis on the mass of the Higgs boson. While this allows one to discriminate between competing analyses by selecting the analysis which has the highest efficiency for the same number of background events, still a working point on this efficiency vs. background curve has to be chosen. In other words, it has to be decided whether it is better to have the selection criteria very stringent (with moderate signal efficiency, but negligible background), or to have them rather loose (with high signal efficiency and a lot of background events in the selected event sample). A standard procedure is to choose the working point such as to obtain the best expected 95% exclusion limit for the signal under the hypothesis that there are no signal events in the data. What this means in the context of the $\mathrm{CL_s}$ method will be explained at the end of the section on confidence levels on page 116. The optimization of the analysis should be finished before the analysis is applied to the data, because otherwise there is the risk of introducing a bias by changing the selection criteria to "better suit the data".

6.1.2 Hypothesis testing

From the point of view of the theory of statistics [48], searches for new particles have to deal with the following problem: a test of a simple null hypothesis H_0 against a composite alternative hypothesis H_1 has to be performed, where a hypothesis consists of an assumption on the probability density function (p.d.f.) of some random variable ($m_{\mathrm{H}}^{\mathrm{rec}}$ in this case). A hypothesis is called simple if all the parameters of the p.d.f. are specified. A hypothesis is called composite if the general mathematical form of the p.d.f. is known, but the exact value of at least one parameter is not determined ($\hat{m}_{\mathrm{H}}$ in this case, where the caret is used to denote a specific hypothesis for the mass of the Higgs boson). The p.d.f. of the simple null hypothesis is shown in Figure 6.1 as the histogram [4]. The p.d.f. of the alternative hypothesis is obtained by adding the $\hat{m}_{\mathrm{H}}$-dependent number of signal events to the background analysis chain. Finally these events show up as a small peak [5] above the background around $\hat{m}_{\mathrm{H}}$ in the distribution of $m_{\mathrm{H}}^{\mathrm{rec}}$. Examples of such peaks are shown in Figs. 8.5 and 8.6. Concerning the "excess of ALEPH events" (*cf.* Fig. 6.1) one notes that a signal peak at $m_{\mathrm{H}}^{\mathrm{rec}} \approx 116$ GeV/c^2 would fit nicely in between the background expectation and the data.

Next a method has to be found, that allows to quantify the (dis)agreement of the data with either hypothesis. The well known Neyman-Pearson theorem (explained in [48] and [49]) states that the so-called likelihood ratio gives the most powerful test between two hypotheses H and H'. As a consequence, this test-statistic maximizes the discovery potential as well as the exclusion potential of a search for new particles.

H_0	=	simple null hypothesis	=	background-only	=	index b
H_1	=	composite alternative hyp.	=	signal+background	=	index s+b

Table 6.2: Notation used for the two hypotheses in the context of Higgs boson searches. All the terms in one row are used synonymously.

[4] In this histogram the p.d.f. is not normalized to unity but to the number of events corresponding to the integrated luminosity collected.

[5] The number of events in the peak is given by the usual formula $N = \epsilon\sigma\mathcal{L}_{int}$ and the width of the peak is determined by the mass resolution of the analysis.

6.1.3 The likelihood ratio

After the distribution of the discriminating variable is obtained for the data (Fig. 6.1), the probability P_i to observe n_i events in the data, where b_i events are expected from background processes, is calculated for each bin i. Since the number of entries in a bin of a histogram is distributed according to Poisson statistics, we have $P_i \equiv P(n_i|b_i) = \exp(-b_i) b_i^{n_i}/n_i!$. Thus the combined a posteriori probability $P(\text{data}|H_0)$ for obtaining the observed distribution of data events, under the hypothesis that it is a sample drawn from the background distribution, is

$$P(\text{data}|H_0) = \prod_{i=1}^{N_\text{bins}} P(n_i|b_i) = e^{-b} \prod_{i=1}^{N_\text{bins}} \frac{b_i^{n_i}}{n_i!}\,, \tag{6.1}$$

where $b = \sum b_i$ is the total number of background events and i runs over all analysis bins. The same probability is then calculated for the signal+background hypothesis H_1:

$$P(\text{data}|H_1) = e^{-(s+b)} \prod_{i=1}^{N_\text{bins}} \frac{(s_i + b_i)^{n_i}}{n_i!}, \tag{6.2}$$

where s_i is the number of signal events expected in bin i for the mass hypothesis $\hat{m}_\text{H}$, *i.e.* $s_i(\hat{m}_\text{H})$, and $s = \sum s_i$ is the total number of signal events.

If a “yes-or-no” decision has to be made on whether the observed histogram is more consistent with H_0 (background-only) or with H_1 (signal+background), the hypothesis which gives the higher probability should be chosen. Since the absolute value of the probability is irrelevant, it is more convenient to calculate the ratio Q of probabilities,

$$Q := \frac{P(\text{data}|H_1)}{P(\text{data}|H_0)} = e^{-s} \prod_{i=1}^{N_\text{bins}} \left(1 + \frac{s_i}{b_i}\right)^{n_i}, \tag{6.3}$$

and decide on whether this is larger or smaller than 1. With this definition an experiment is more signal+background-like than background-like if $Q > 1$.

Equation (6.3) is the definition of the likelihood [6] ratio estimator, which is the ratio of the probabilities of observing an event, an ensemble of events or an experimental outcome in general under the two search hypotheses H_1 and H_0. Q is multiplicative, which means that the estimator of an ensemble of events can be formed by multiplying the individual event estimators. This property is very useful for combining search analyses from subchannels and from different experiments.

Here only the binned version of the likelihood ratio is described, for which the distributions of the discriminating variable need to be available only as histograms. For the more general case of continuous distributions see Ref. [47].

[6] The term likelihood is used in the context of a posteriori probabilities — as compared to a priori probabilities.

For theoretical [7] and numerical reasons instead of Q its logarithm is used in practice:

$$X(\hat{m}_{\mathrm{H}}) := -2\ln Q = 2s(\hat{m}_{\mathrm{H}}) - 2\sum_{i=1}^{N_{\mathrm{bins}}} n_i \ln\left(1 + \frac{s_i(\hat{m}_{\mathrm{H}})}{b_i}\right), \tag{6.4}$$

where it is stressed that s and therefore X are functions of $\hat{m}_{\mathrm{H}}$. In the following the dependence of X on $\hat{m}_{\mathrm{H}}$ is not explicitly shown. X is called log-likelihood estimator or test-statistic and can be interpreted as a weighted sum over all selected events, where the weight of an event in bin i is defined as $\ln(1 + s_i/b_i)$. The event weight is always positive and can be thought of as being proportional to the signal to background ratio s_i/b_i, *i.e.* larger signal to background ratio means larger event weight.

Since the logarithm is a monotonic function, also X indicates how much the outcome of an experiment is signal-like, but because of the minus sign in the definition of X, an experiment favors the signal+background hypothesis if $X < 0$. Given a mass hypothesis $\hat{m}_{\mathrm{H}}$ for the Higgs boson, X starts out with the positive value $2s(\hat{m}_{\mathrm{H}})$ and is decreased whenever an event passes all the selection criteria of the analysis, thereby changing from favoring H_0 to favoring H_1, as more and more candidate events are observed.

The result obtained for the test-statistic of an experiment is called X_{obs} and it can be viewed as a random variable. To evaluate the statistical significance of X_{obs}, a common method is to do *Gedanken* experiments. Therefore in the next step a large number of Monte Carlo experiments is performed to obtain random distributions of the discriminating variable under the hypotheses H_0 and H_1. In these random experiments the number of events in each bin i of the distribution is generated assuming Poisson statistics with mean value b_i and $s_i(\hat{m}_{\mathrm{H}}) + b_i$ for the two hypotheses, respectively. The outcome of the Monte Carlo experiments is two distributions of X $(= -2\ln Q)$ for each mass hypothesis $\hat{m}_{\mathrm{H}}$, as shown in Figure 6.2. These two distributions are well separated for low values of $\hat{m}_{\mathrm{H}}$, mainly as a consequence of the higher cross section for Higgs boson production. This follows from (6.4), but quite general it can be said that selecting more events makes an experiment more signal-like. When the cross section decreases with increasing $\hat{m}_{\mathrm{H}}$, the distributions begin to overlap. For very large values of $\hat{m}_{\mathrm{H}}$ the two distributions coincide since $s_i(\hat{m}_{\mathrm{H}}) \sim 0$. This means that the two hypotheses are practically indistinguishable. In other words, from an experimental point of view "no Higgs boson" is equivalent to a very heavy Higgs boson.

---

[7] In the high statistics limit the distribution of $-2\ln Q$ is expected to converge to a $\Delta\chi^2$ distribution, where $\Delta\chi^2 = \chi^2(\mathrm{data}|H_1) - \chi^2(\mathrm{data}|H_0)$. For more information, see Ref. [50].

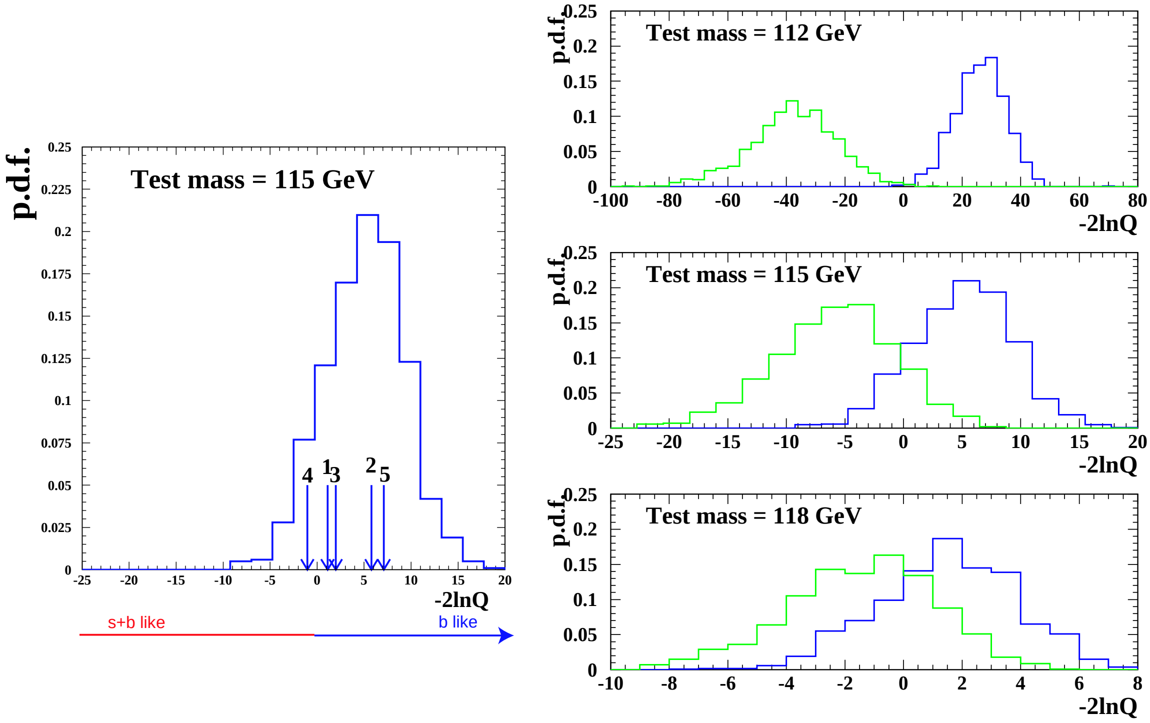

Figure 6.2: Distributions from Monte Carlo simulations of the test-statistic X. Left: Construction of the p.d.f. for the background-only hypothesis H_0. The result of the first five experiments and the final distribution is shown. Because of the statistical nature of the experiments a fraction of the background-only experiments favor the signal+background hypothesis H_1 (*e.g.* Monte Carlo experiment number 4, the reason being a downward fluctuation of the number of background events generated in the signal region of $m_{\mathrm{H}}^{\mathrm{rec}}$). Right: Comparison of the distributions for the two hypotheses H_1 (left histogram) and H_0 (right histogram), for various values of the test mass $\hat{m}_{\mathrm{H}}$. The separation between the distributions decreases with increasing $\hat{m}_{\mathrm{H}}$.

6.1.4 Confidence levels

The two distributions of the test-statistic are used to define the confidence levels for X_{obs} with respect to the two hypotheses H_0 and H_1. The definitions are

$$1 - \mathrm{CL_b} \quad := \quad P(X \leq X_{\mathrm{obs}}|H_0) \tag{6.5}$$

$$\mathrm{CL_{s+b}} \quad := \quad P(X \geq X_{\mathrm{obs}}|H_1) \tag{6.6}$$

A graphical illustration of the definitions of $1 - \mathrm{CL_b}$ and $\mathrm{CL_{s+b}}$ is shown in Figure 6.3. The background confidence level $1 - \mathrm{CL_b}$ (or $\mathrm{CL_b}$) measures the compatibility with the background hypothesis H_0. If $1 - \mathrm{CL_b}$ is small it can be used for establishing a discovery. The correspondence of $1 - \mathrm{CL_b}$ and the significance of the discovery is given in Table 6.3. On the other hand, $\mathrm{CL_{s+b}}$ measures the compatibility of the observation with the hypothesis that there are signal events in addition to the background events.

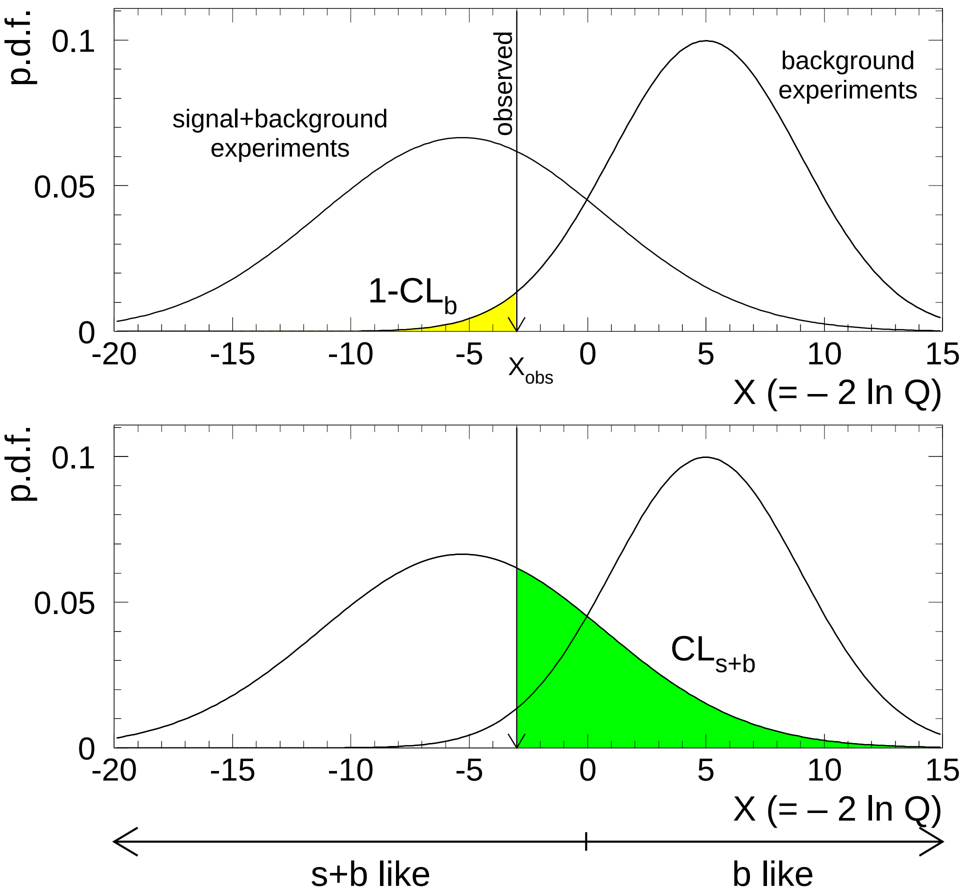

Figure 6.3: Illustrative example of the distributions of the log-likelihood estimator $-2\ln Q$ for signal+background and background experiments. The estimator of an observation, $X_{\mathrm{obs}} = -3$, is indicated by the vertical line.
Top: Definition of the confidence level $1 - \mathrm{CL_b}$ (light shaded area) which measures the compatibility of the observation with the background-only hypothesis H_0.
Bottom: Definition of the confidence level $\mathrm{CL_{s+b}}$ (dark shaded area) which measures the compatibility of the observation with the signal+background hypothesis H_1.

However, its main usage is as a measure of the incompatibility with H_1. This is not optimal, because $\mathrm{CL_{s+b}}$ only allows to exclude the signal+background hypothesis, where actually the signal part needs to be excluded. Since the number of expected background events from the standard model is known (although with some error), a straightforward solution would be to subtract the expected background from the number of observed events. The details of how this so-called background subtraction should be performed are a delicate point. In the case of the $\mathrm{CL_s}$ method for this purpose the ratio

$$\mathrm{CL_s} := \frac{\mathrm{CL_{s+b}}}{\mathrm{CL_b}} \tag{6.7}$$

$1-\mathrm{CL_b}$	error band	$1-\mathrm{CL_b}$	significance
0.16 ... 0.84	1σ	$2.7\cdot 10^{-3}$	3σ
0.023 ... 0.977	2σ	$5.7\cdot 10^{-7}$	5σ

Table 6.3: Correspondence between the confidence level $1-\mathrm{CL_b}$ and (left) the one and two σ error bands and (right) the statistical significance (*e.g.* for a discovery). This numbers are based on the fractiles of a two-sided Gaussian distribution.

is introduced and used to exclude the signal hypothesis. In this sense, one way of interpreting $\mathrm{CL_s}$ [47] is that it serves as an approximation of the confidence one might obtain if the background events could be removed of the sample of selected events. Strictly speaking, with the above definition $\mathrm{CL_s}$ is not a confidence level[8] but a ratio of confidences only. By construction, the following inequality holds for reasonable analyses (when $\mathrm{CL_b} \geq \mathrm{CL_{s+b}}$):

$$1 \geq \mathrm{CL_s} \geq \mathrm{CL_{s+b}}. \tag{6.8}$$

The signal hypothesis will be considered excluded at the confidence level CL (*e.g.* 95%), if[9] $\mathrm{CL_s} \leq 1-$ CL. As a consequence, the observation of a $\mathrm{CL_s}$ value smaller than 5% can be interpreted as an exclusion of the signal hypothesis at the 95% confidence level. Optimizing an analysis with respect to the selection criteria (*cf.* Sec. 6.1.1) in order to obtain the best exclusion limit therefore is equivalent to minimizing the signal confidence level $\mathrm{CL_s}$ for background-only experiments and for a specific mass hypothesis $\hat{m}_\mathrm{H}$. It is sufficient to do the optimization for one specific value of $\hat{m}_\mathrm{H}$, if that value is near the expected exclusion limit, which is a few GeV/c^2 (depending on $\mathcal{L}_{int}$) below the kinematic limit (defined as $E_\mathrm{cm} - m_\mathrm{Z}$) for Higgs boson production through $\mathrm{e^+e^-} \to$ HZ. For example, at $\sqrt{s}$ = 183 GeV the HZ analyses in ALEPH have been optimized for a Higgs boson with a mass of 85 GeV/c^2, where the kinematic limit is $\sim$ 92 GeV/c^2. In order to be insensitive to statistical fluctuations of $\mathrm{CL_s}$, the median value $\mathrm{CL_s^{median}}$ of the distribution of $\mathrm{CL_s}$ for background-only experiments is minimized.

6.1.5 Selected experimental results

Finally, in this section two important results of the standard model Higgs boson searches at LEP2 are presented. This also serves the purpose of "seeing Higgs statistics in action".

[8]The consequence of $\mathrm{CL_s}$ not being a true confidence is that the hypothetical false exclusion rate is generally less than the nominal rate of $1-$ CL.

[9]In the original publication, but also in [47], this equation reads $1-\mathrm{CL_s} \leq$ CL, which is wrong due to a typographical error ($\leq$ instead of the correct $\geq$)

The first interesting result is the observation of an excess of Higgs boson like events with the ALEPH detector. Figure 6.4-left shows the values of the test-statistic $-2\ln Q$

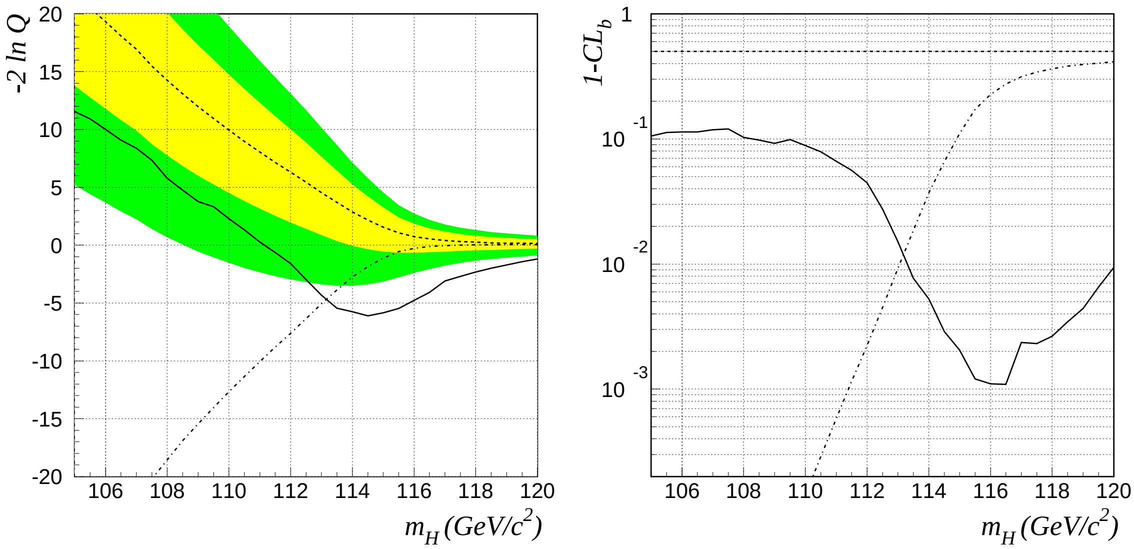

Figure 6.4: Results of the cut stream analysis with ALEPH data from the year 2000 [51]. Left: The log-likelihood estimator $-2\ln Q$ as a function of $\hat{m}_{\rm H}$ for the observation (solid curve) and the expectation for the null hypothesis H_0 (dashed curve). The light and dark grey regions around the background expectation represent the 1 and 2σ error bands, respectively (*cf.* Table 6.3). The dashed-dotted curve shows the expectation for the alternative hypothesis H_1. For the expected behaviors, the medians of the simulated distributions are shown. Right: Background confidence $1 - {\rm CL_b}$ as a function of $\hat{m}_{\rm H}$ for the observation (solid), the median for H_0 (dashed) and the median for H_1 (dashed-dotted). The minimum of the solid curve at $\hat{m}_{\rm H}$ at $\sim$ 116 GeV/c^2 corresponds to the observed excess of events, with a significance of $\gtrsim 3\sigma$.

as a function of the mass hypothesis $\hat{m}_{\rm H}$ for the observation and the median [10] expectation for the two distributions for the two hypotheses H_0 and H_1. The minimum at $\hat{m}_{\rm H}$ = 114.5 GeV/c^2 of the observation (with a value of $-2\ln Q = -6$, *i.e.* $Q = e^3$) means that the likelihood of observing this event configuration under the signal+background hypothesis is at least 20 times higher than observing it under the background-only hypothesis. When expressed in terms of the background confidence level $1 - {\rm CL_b}$ (as shown in Fig. 6.4-right), where the minimum of the observation is shifted [11] to $\hat{m}_{\rm H}$ $\sim$ 116 GeV/c^2, a probability as low as 10^{-3} is obtained. for observing this or a less background like event configuration. According to Table 6.3 this corresponds to a

[10]The median expected confidence level is used rather than the average expected confidence level because the CL distributions are typically asymmetric, and the medians are less sensitive to the CL distribution tails.

[11]The shift in the minimum is due to the fact that the width of the distribution of $-2\ln Q$ for H_0 gets quickly smaller for $\hat{m}_{\rm H} > 114$ GeV/c^2 (as indicated by the grey bands), thereby pushing $X_{\rm obs}$ further out into the tail of the distribution. This results in a smaller value of $1 - {\rm CL_b}$.

significance of more than 3σ.

While in the above example the use of the background confidence level as a means to exclude the background hypothesis was demonstrated (thereby indicating the possibility of a discovery), in the following an example of the use of the signal confidence level as a means to exclude the signal hypothesis is given. Figure 6.5 shows the confidence level on the signal hypothesis as a function of $\hat{m}_{\mathrm{H}}$ for the combination of the final results of all four LEP experiments. The intersection of the horizontal line for $\mathrm{CL_s} = 0.05$ with the observed curve at $\hat{m}_{\mathrm{H}} = 114.4$ GeV/c^2 is used to define the 95% confidence level lower bound on the mass of the standard model Higgs boson. The observed value of $\mathrm{CL_s}$ is larger than the median expected value in the absence of signal events (H_0) over the whole mass range shown. This is due to the presence of signal candidate events in the data with values of the reconstructed mass in the range from $\sim 100 - 117$ GeV/c^2 [44].

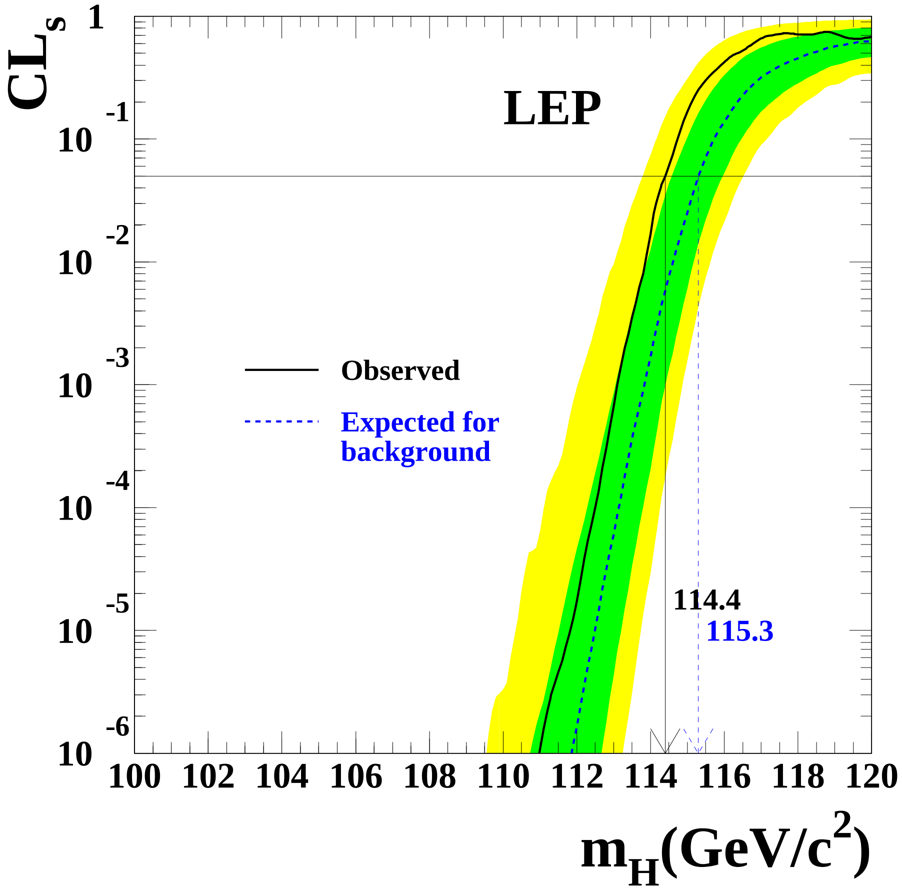

Figure 6.5: The ratio $\mathrm{CL_s} = \mathrm{CL_{s+b}}/\mathrm{CL_b}$ as a function of the test mass $\hat{m}_{\mathrm{H}}$ for the final LEP2 result [43]. Solid curve: observation; dashed curve: $\mathrm{CL_s^{median}}$ for the background-only hypothesis H_0. The dark and light shaded bands around $\mathrm{CL_s^{median}}$ correspond to the 68% and 95% probability bands (approximately the 1 and 2σ error bands).

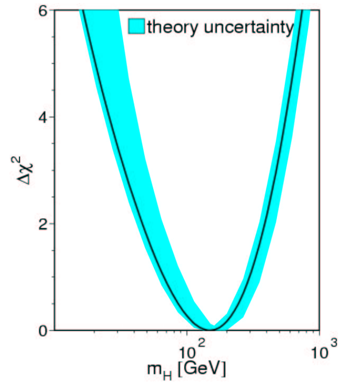

What does a χ^2 fit tell?

Chapter 7

Indirect Searches

7.1 The mass of the top quark

At the HEP summer conference in 1993 [52], a value of $m_{\rm t} = 162 \pm 27$ GeV/c^2 was quoted for the top quark mass as a result of a fit of the standard model parameters to electroweak data from LEP. Since $m_{\rm H}$ is a standard model parameter, it is also contained in such fits. But in contrast to $m_{\rm t}$, which occurs in a quadratic form, the dependence on $m_{\rm H}$ is only logarithmically (see Eq. 7.7 in the next section). Because of this, at the time the data were not precise enough to also make a prediction on $m_{\rm H}$. Instead fits have been done for fixed values of the Higgs boson mass ($m_{\rm H} = 300$ GeV/c^2 for the above result on $m_{\rm t}$). Only after the discovery of the top quark in 1995, when a reasonable precise measured value for $m_{\rm t}$ was available, it made sense to extract a prediction for $m_{\rm H}$ from the fit — as described in Section 7.3. For the evolution of the prediction for $m_{\rm t}$ between 1989 and 1995, see Ref. [53].

7.2 Radiative corrections and the mass of the standard model Higgs boson

In the standard model the mass of the Higgs boson is given by the relation $m_{\rm H} = \sqrt{2\lambda}\, v$, where v is the known vacuum expectation value of the Higgs field ($v = 246$ GeV) and λ is the unknown dimensionless quartic coupling constant in the Higgs potential (see Sec. 2.3). In the same way as the mass of the top quark was predicted before it was discovered, also the mass of the Higgs boson can be constrained in the context of the standard model by using precision electroweak measurements.

The starting point is the relation between the Fermi constant G_F (defined via the muon lifetime) and the parameters of the standard model:

$$m_{\rm W}^2 \sin^2\theta_W = \frac{\pi\alpha}{\sqrt{2}G_F}. \tag{7.1}$$

This equation only holds in lowest order of perturbation theory. When quantum effects are taken into account and when $\sin^2\theta_W$ is substituted by its defining relation in the on shell renormalization scheme, which is $\sin^2\theta_W = 1 - m_{\mathrm{W}}^2/m_{\mathrm{Z}}^2$ (valid in all orders of perturbation theory), Equation (7.1) changes to

$$m_{\mathrm{W}}^2\,(1 - m_{\mathrm{W}}^2/m_{\mathrm{Z}}^2) = \frac{\pi\alpha}{\sqrt{2}G_F}\,\frac{1}{(1-\Delta r)}, \tag{7.2}$$

where $\Delta r(m_{\mathrm{t}}, m_{\mathrm{H}}, ...)$ parameterizes the so-called radiative corrections. When the dominant loop corrections are included Δr depends linearly on m_{t}^2 and $\ln m_{\mathrm{H}}$. At LEP1, where m_{Z} was measured with high precision, (7.2) could be used to give a theoretical prediction for m_{W}, with the largest uncertainty coming from m_{t}. Since LEP2, where m_{W} was measured, this equation allows to make a prediction for m_{H}, because in the meantime the error on m_{t} has been reduced substantially by the measurement at Tevatron. In other words, with the experimental values of α, G_F, m_{Z}, and m_{W} a measured value of $\Delta r_{\mathrm{meas}} = 0.0355 \pm 0.0019$ [15] can be obtained. On the other hand, in 1-loop approximation Δr, which was first calculated in [54], can be written in the following way:

$$\Delta r_{1-\mathrm{loop}} = \Delta\alpha - \frac{c_W^2}{s_W^2}\Delta\rho + \Delta r_{\mathrm{rem}}(m_{\mathrm{H}}\,...), \tag{7.3}$$

where the abbreviations $s_W^2 \equiv \sin^2\theta_W$ and $c_W^2 \equiv \cos^2\theta_W$ have been used for the weak mixing angle in the on shell renormalization scheme. Here Δr is split into three terms, corresponding to pure QED corrections, electroweak corrections from Feynman diagrams including the W and Z bosons and the remainder part, where also the Higgs boson contributes. In the following each term of (7.3) is discussed separately.

- $\Delta\alpha$:
  This term is defined through the running QED coupling

$$\alpha(s) = \frac{\alpha(0)}{1-\Delta\alpha(s)} \quad (\text{with } \alpha(0) \equiv \alpha) \tag{7.4}$$

  at the energy scale $s = m_{\mathrm{Z}}^2$. This is conventionally considered to be the natural scale, not only for the Z resonance, but for all electroweak observables. The basic Feynman diagram for this correction (also known as vacuum polarization or photon self energy) is shown below. All fermions f that couple to the photon are allowed in the loop. For the running of α fermion one-loop insertions to the photon propagator are summed together with the photonic Born diagram. In leading order the QED part of the radiative corrections is given by [55]

$$\Delta\alpha(m_{\mathrm{Z}}^2) = \frac{\alpha}{3\pi}\sum_{\mathrm{f}\neq\mathrm{t}} Q_{\mathrm{f}}^2 N_{\mathrm{f}}^c (\ln\frac{m_{\mathrm{Z}}^2}{m_{\mathrm{f}}^2} - \frac{5}{3}) + \Delta\alpha_{\mathrm{t}}, \tag{7.5}$$

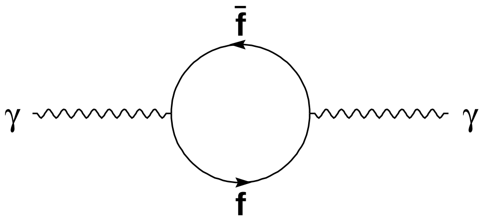

where Q_f is the charge and N_c^f is the color factor of the fermion f ($N_f^c = 3$ for quarks and $N_c^f = 1$ for leptons). The top quark contribution has to be given seperately, $\Delta\alpha_t = -\frac{\alpha}{3\pi}\frac{4}{15}\frac{m_Z^2}{m_t^2}$, because the light fermion approximation can only be used if $m_f \ll m_Z$. The contributions from the charged leptons and the top quark are calculated analytically with the above formulae (improved by including higher order terms), which is not possible for the light quarks, because their masses are not known well enough and because there are nonperturbative QCD effects (*e.g.* resonances). However, the light quark part $\Delta\alpha_{had}^{(5)}$ can be derived from experimental data with the help of a dispersion relation, with an error that is almost completely due to the experimental data. The final result is [56] $\Delta\alpha = \Delta\alpha_{lept} + \Delta\alpha_{had}^{(5)} + \Delta\alpha_t = 0.03150 + 0.02804 - 0.0000586 = 0.0595 \approx 6\%$.

- $\Delta\rho$:
  In analogy to the previous paragraph, this term describes the running of the weak couplings, which again is evaluated by inserting fermionic loops to the propagators (the contribution from gauge boson loops is small and therefore put into Δr_{rem}).

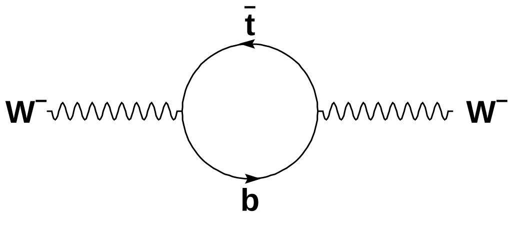

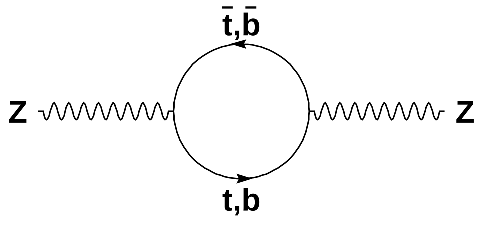

The net effect is a correction to the masses of the W and Z bosons, which is different for the two particles, because of the mass splitting between the isospin doublet fields. With the definition $\Delta\rho := \frac{\delta m_Z^2}{m_Z^2} - \frac{\delta m_W^2}{m_W^2}$ (where the mass corrections δm_Z^2 and δm_W^2 are defined in the context of renormalization [55, 57]) the 1-loop calculation gives [58]

$$\Delta\rho = \frac{\sqrt{2}G_F}{16\pi^2}\sum_d N_f^c \left(m_1^2 + m_2^2 - \frac{2m_1^2 m_2^2}{m_2^2 - m_1^2} \ln\frac{m_2^2}{m_1^2} \right). \quad (7.6)$$

Here the sum is over all weak doublets d and m_1 and m_2 are the masses of the members of a doublet. The term in the brackets is symmetric in m_1 and m_2 and it vanishes for $m_1 = m_2$ (no mass splitting). For $m_2 \gg m_1$ it can be approximated by m_2^2. Clearly the dominant contribution to $\Delta\rho$ is from the doublet (t,b). Its numeric value is $\Delta\rho_{\rm t} \approx 0.00952\ (m_{\rm t}/174.3\ {\rm GeV})^2$ [15], which gives a total contribution of -3.3% to $\Delta r_{1-\rm loop}$.

- $\Delta r_{\rm rem}$:
  The one-loop result for Δr contains two large terms: the running QED coupling (logarithmically enhanced by small fermion masses) and the parameter $\Delta\rho$ (enhanced quadratically by $m_{\rm t}^2$). By convention, all other (small) contributions are put into the remaining part. In the standard model the coupling of a particle to the Higgs boson is proportional to the mass of the particle for fermions and proportional to the mass squared for gauge bosons. Therefore the dominant correction involving loops of the Higgs particle comes from diagrams like the following (V = W or Z):

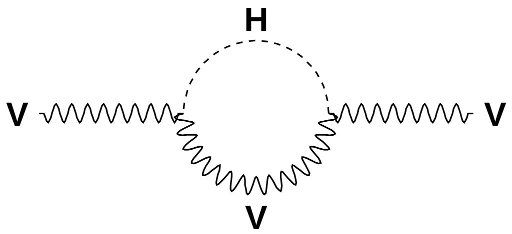

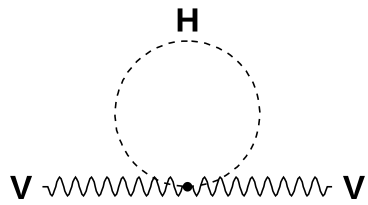

For $m_{\rm H} \gg m_{\rm W}$ the leading Higgs contribution to Δr is [57]

$$\Delta r_{\rm rem}^{\rm H} = \frac{\sqrt{2} G_F m_{\rm W}^2}{4\pi^2} \frac{11}{12} (\ln \frac{m_{\rm H}^2}{m_{\rm W}^2} - \frac{5}{6}) \tag{7.7}$$

While this expression vanishes for $m_{\rm H} \approx 122\ {\rm GeV}/c^2$ (where it is no longer a good approximation) the typical size of $\Delta r_{\rm rem}$ is 1%, which can be verified as follows: $\Delta r_{\rm rem} \approx \Delta r_{\rm meas} - \Delta\alpha + \frac{c_W^2}{s_W^2}\Delta\rho = 0.0355 - 0.0595 + 0.033 = 0.009$.

7.3 Fits of the LEP electroweak working group

Up to now not enough energy was available in experiments to produce real Higgs particles at their nominal mass. However, in the context of the standard model the Higgs particle manifests itself at lower energies through quantum effects, as was discussed in the preceding section. A precise measurements of the masses of the W and Z bosons is equivalent to a precise measurement of Δr (see Eq. 7.2), which in turn allows one to constrain m_H. This is done by the LEP electroweak working group (EWWG) by combining measurements from several experiments and performing various fits [59]. One of the aims is to test the consistency of the standard model and to infer information about its basic parameters. The procedure is as follows: more than 100 measurements (mainly from the Z resonance) are reduced to 20 precision (pseudo-)observables O_i. They depend on the standard model parameters $\alpha(m_\mathrm{Z})$, m_Z, α_S, m_t and m_H (and of course on G_F and all fermion masses). Then a χ^2 fit is performed, where the 20 observables are fitted to the most up to date standard model calculations. When χ^2 is plotted as a function of m_H (at the best fit values of all other parameters) curves like the ones shown in Figure 7.1 are obtained (besides showing the fit result, the two plots, from the years 1996 and 2003, should illustrate the improvement achieved since the beginning of LEP2). They allow one to predict the Higgs boson mass within the framework of the standard model. The standard error can be read off the x-axis where $\Delta\chi^2 = 1$. The quality of the most recent fit (2003) is $\chi^2/d.o.f = 25.5/15$ (5 standard model parameters varied for 20 data points = 15 degrees of freedom), where the probability for obtaining a χ^2 as large or larger than the observed one is only 4.4%. When the data-point with the largest contribution to χ^2 is removed from the fit (this corresponds to the curve denoted “Without NuTeV” in the right plot), the result is $\chi^2/d.o.f = 16.7/14$, with a probability of 27%.

Finally it should be mentioned that the results of the fit are correlated. The largest correlations occur between m_h and m_t (71%) and between m_h and $\Delta\alpha^{(5)}_\mathrm{had}$ (−48%). The signs of the correlations can easily be understood with the help of (7.3). Because of the different signs of the contributions to Δr, m_h and m_t are positively correlated (an increase in m_t also increases the best fit value of m_H). On the other hand, $\Delta\alpha^{(5)}_\mathrm{had}$ contributes with the same sign as m_H, therefore they are anti-correlated. This is reflected by the dark dashed curve in Figure 7.1-right, where a smaller value of $\Delta\alpha^{(5)}_\mathrm{had}$ (obtained by a more recent calculation [60]) shifts the $\Delta\chi^2$ curve to higher values of m_H. Because of the smaller error this parabola is tighter. Together with the shift in the minimum this results in the 95% C.L. upper limit staying practically the same.

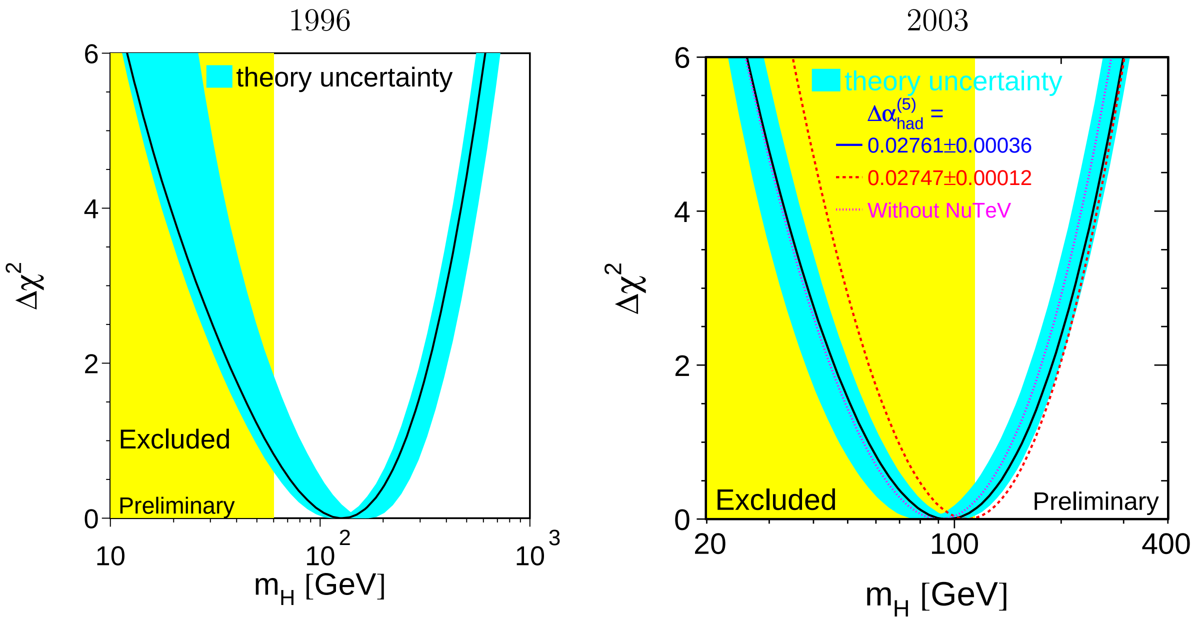

Figure 7.1: $\Delta\chi^2 = \chi^2 - \chi^2_{\rm min}$ vs. $m_{\rm H}$ curves of fits of the standard model parameters to electroweak data from LEP, SLC, Tevatron and NuTeV [59]. The bands along the curves (dark grey) represent an estimate of the theoretical error due to missing higher order corrections of the observables calculated in the framework of the standard model. They are obtained by comparing the results of two fit programs (ZFITTER [56] and TOPAZ0 [61]). The vertical bands (light grey) show the 95% confidence level exclusion limit form the direct search at LEP. Left: the best fit value using all data available in 1996 was $m_{\rm H}= 127^{+127}_{-72}$ GeV/c^2 with a 95% C.L. upper limit of 465 GeV/c^2. This fit did not include the lower limit on $m_{\rm H}$ from the direct search, which was 66 GeV/c^2 at 95% C.L. Right: the present best fit value on the Higgs boson mass is $m_{\rm H}= 91^{+58}_{-37}$ GeV/c^2 (from the solid curve) with a 95% C.L. upper limit of 211 GeV/c^2. Again the fit does not include the lower limit of 114.4 GeV/c^2 from the direct search at LEP2. The dashed curves are explained in the text.

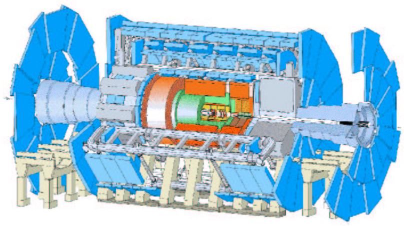

The ATLAS detector at LHC

Chapter 8

The Future of Higgs Boson Searches

The Higgs boson has not been discovered at LEP, but particle physicists will not give up until the question is resolved. If the standard model is not the correct theory for describing the origin of mass then some “new physics” effects should show up in future experiments.

In this chapter the short term future of Higgs Boson searches will be described. Experiments at three accelerators will be mentioned in this context. The accelerators are:

1. Tevatron: a $p\overline{p}$ collider presently running at Fermilab
2. LHC: a pp collider under construction at CERN
3. TESLA: an e^+e^- linear collider not yet approved

LEP has handed over the possibility to discover a Higgs Boson with a mass around 115 GeV/c^2 to the two experiments CDF and D0 presently taking data at the Tevatron collider at Fermilab. If these experiments are not able to collect sufficient data until LHC starts it may well be that the experiments at LHC will discover the Higgs boson first. Though the LHC experiments are capable of finding the Higgs boson over a wide range of masses (up to 1 TeV), here only the scenario is discussed in which the Higgs boson mass is below the threshold for the decay $H \rightarrow W^+W^-$. This is motivated by the observed excess of ALEPH events [51] at a mass around 115 GeV/c^2, and by the fact that fits of the standard model parameters to precision electroweak observables show preference for a light Higgs boson.

8.1 Tevatron

Tevatron produced its first $p\overline{p}$ collisions in 1985, but what came to be known as Run 1 only began in 1992. With the data collected in the following years (0.1 fb^{-1}) the two experiments CDF and D0 were able to announce the discovery of the top quark in 1995.

During Run 1 the injection system was installed in the same tunnel as the collider, which turned out to be a bottleneck by limiting the achievable luminosity to $1.6 \cdot 10^{31}\,\mathrm{cm}^{-2}\mathrm{s}^{-1}$. To overcome this the Main Injector was built as a separate synchrotron (see Fig. 8.1) and commissioned in 1999. In order to be able to increase the luminosity further (by about a factor of 2) an Antiproton Recycler was added (not commissioned yet). This device allows one to recuperate the antiprotons left over at the end of a store and re-use them.

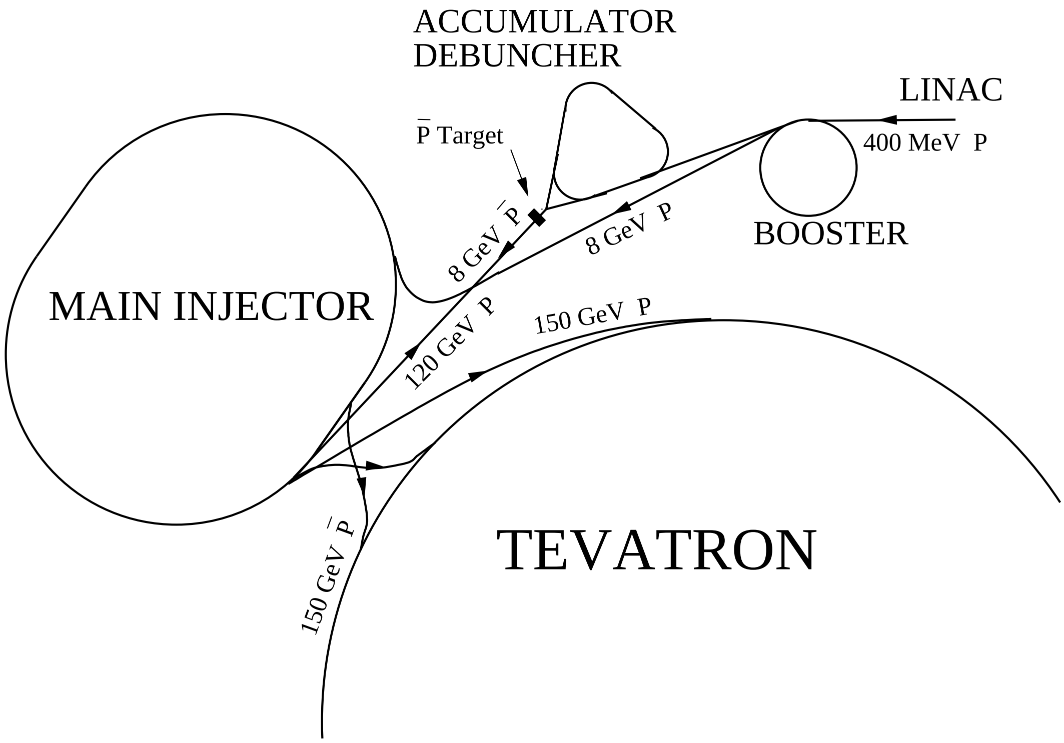

Figure 8.1: Layout of the Tevatron collider facility. The Main Injector is delivering protons and antiprotons at an energy of 150 GeV to the Tevatron.

In March 2001, when the upgrades of the detectors had been completed, Run 2 started at Tevatron. The centre-of-mass energy has been increased from 1.8 TeV to 1.96 TeV. The initial planning expected that each experiment should have collected $1-2\ \mathrm{fb}^{-1}$ of data by the end of the first phase, called Run 2a, at the end of 2004. This would allow one to exclude a Higgs boson of mass 115 GeV/c^2 at the 95% confidence level. Present expectations [62] are that the integrated luminosity for 2004 will be in the range 0.25 to 0.38 fb^{-1}, with the lower number including the expected effects of Recycler commissioning work. Since only 0.3 fb^{-1} have been collected so far (Aug. 2003), probably also the year 2005 is needed to achieve the Run 2a initial goal.

After further upgrades, mainly of the antiproton system, and by using more bunches in order to reduce beam-beam effects the second phase (Run 2b) should fully exploit the potential of the machine and ultimately collect 15 fb^{-1} per experiment before the end of the decade. If the Higgs boson exists, then this huge amount of data is needed to be able to discover it at Tevatron. For this to happen it is crucial that a luminosity of about $5 \cdot 10^{32}\,cm^{-2}s^{-1}$ can be attained. This is still lower than the initial (low) luminosity at LHC by a factor of two, but 30 times the luminosity achieved at Run 1. While the largest cross section for Higgs boson production at the Tevatron is through gluon-gluon fusion, this channel is hampered by an overwhelming background of QCD dijet events. Instead the process of associated production, with a cross section that is about ten times smaller, is used to search for the Higgs particle. Here a Z or W boson produced through quark-antiquark annihilation radiates a Higgs particle. In the case of ZH production the decay topologies studied are the same as at LEP2.

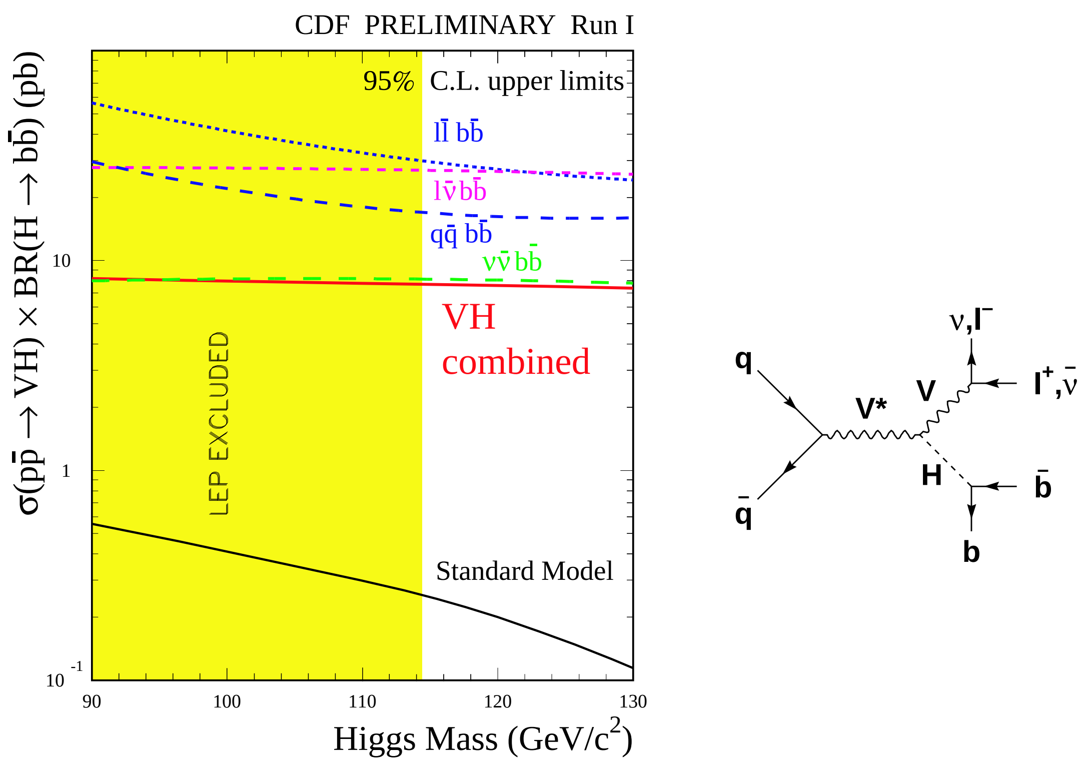

Figure 8.2: Left: CDF results of Higgs boson searches at Tevatron Run 1 [63, 64]. The "VH combined" curve shows the 95% C.L. upper limit on the cross section times branching ratio for the production of the standard model Higgs boson in association with a W or Z boson, with the Higgs decaying to $b\bar{b}$. The dashed curves give the limits for the various decay channels of the W and Z. Over the whole mass range shown the standard model prediction is smaller than the CDF limit by more than a factor of 10. The LEP exclusion region has been updated to the present limit. Right: Feynman diagram for associated production of the Higgs particle (V = W or Z).

With the data taken during Run 1 the CDF experiment obtained the Higgs boson exclusion limits shown in Figure 8.2. As an example, a Higgs boson of mass 115 GeV/c^2 is excluded at the 95% confidence level only if it has a production cross section that is 30 times higher than in the standard model (7.5 pb excluded compared to 0.25 pb in the standard model). The same factor appears as the increase in luminosity between Run 1 and Run 2b. However, since the sensitivity is given by s/$\sqrt{b}$, where s is the number of signal events and b is the number of background events and where both are proportional to the integrated luminosity $\mathcal{L}_{int}$, the sensitivity scales as $\mathcal{L}_{int}^{1/2}$. To increase the sensitivity by a factor of 30 therefore translates to a factor of 900 in increased $\mathcal{L}_{int}$ needed. Extensive studies have been performed [65] to estimate the discovery reach of the upgraded Tevatron. One of the results is displayed in Figure 8.3. This plot tells, for example, that the CDF and D0 experiments would have to collect 4 fb^{-1} (15 fb^{-1}) of integrated luminosity each in order to be able to discover the standard model Higgs boson with a mass of 115 GeV/c^2 at the 3σ (5σ) level.

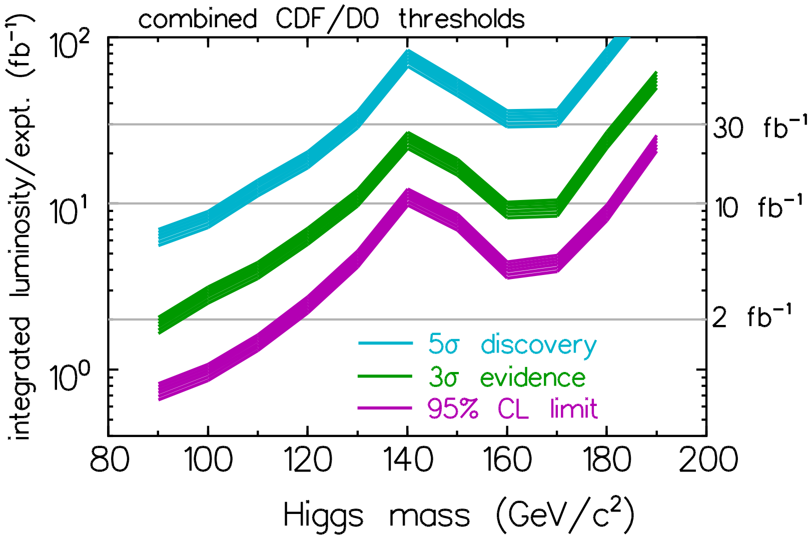

Figure 8.3: The integrated luminosity needed per experiment at Tevatron Run 2 to either exclude the standard model Higgs boson at 95% C.L. or to discover it at significances of 3σ or 5σ. The width of the bands represent an uncertainty of 30%, the lower end being the actual threshold.

8.2 LHC

The Large Hadron Collider is a proton-proton collider that is presently being constructed at CERN and installed in the former LEP tunnel. It should produce its first collisions in the year 2007 at a centre-of-mass energy of 14 TeV, initially at a luminosity of $10^{33}\,\mathrm{cm}^{-2}\mathrm{s}^{-1}$ and later at its design luminosity of $10^{34}\,\mathrm{cm}^{-2}\mathrm{s}^{-1}$.

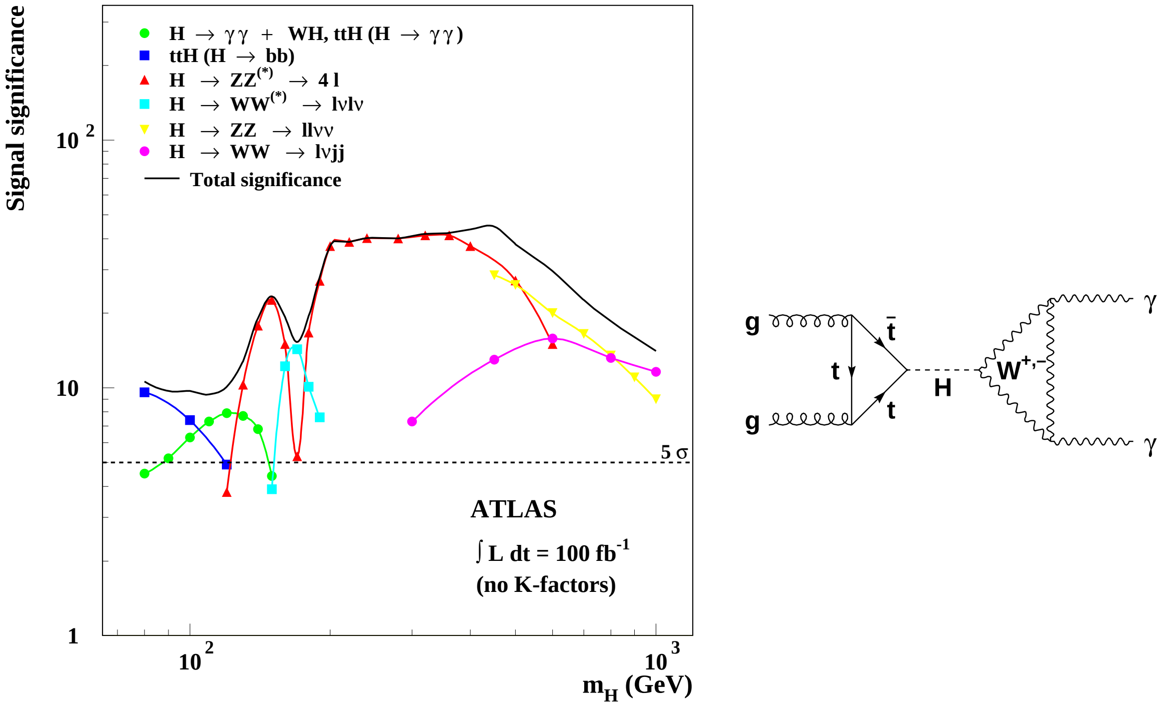

Figure 8.4: Left: Expected statistical significance of a standard model Higgs boson signal as a function of the Higgs boson mass for an integrated luminosity of 100 fb^{-1} collected with the ATLAS detector [66] (100 fb^{-1} is equivalent to running 10^7 s at the luminosity of $10^{34}\,\text{cm}^{-2}\text{s}^{-1}$). The solid curve gives the combined sensitivity of all the subchannels. The 5σ discovery limit is indicated by the dashed line. Right: Feynman diagram for the process of gluon fusion of the Higgs boson and the subsequent decay into two photons. To the first loop all quarks contribute and to the second loop in addition to the W bosons all charged fermions contribute (with a minus sign relative to the W's).

The experiments at LHC are expected to find the standard model Higgs boson (with a mass in the range from 100 to 1000 GeV/c^2) within the first year [1] of LHC running at its design luminosity. This can be concluded, for example, from Figure 8.4, which shows the Higgs search capabilities of the ATLAS experiment.

Should the mass of the Higgs boson be around 115 GeV, as motivated by the excess of events seen by ALEPH [51], then the highest sensitivity is achieved in the $\text{H} \to \gamma\gamma$ channel (see Fig. 8.4-left), where the Higgs particle is either produced through gluon-gluon fusion or associated production. The decay $\text{H} \to \gamma\gamma$ (Fig. 8.4-right) is a rare decay mode with a clean signature, but useful only over a limited higgs boson mass range (100 – 150 GeV/c^2). The maximum branching ratio is $2.2 \cdot 10^{-3}$ for $m_{\text{H}} = 130$ GeV/c^2. Below this mass the dominant decay mode is $\text{H} \to \text{b}\overline{\text{b}}$, but that channel is only

[1] In the context of CERN colliders one year of running actually means 10^7 seconds.

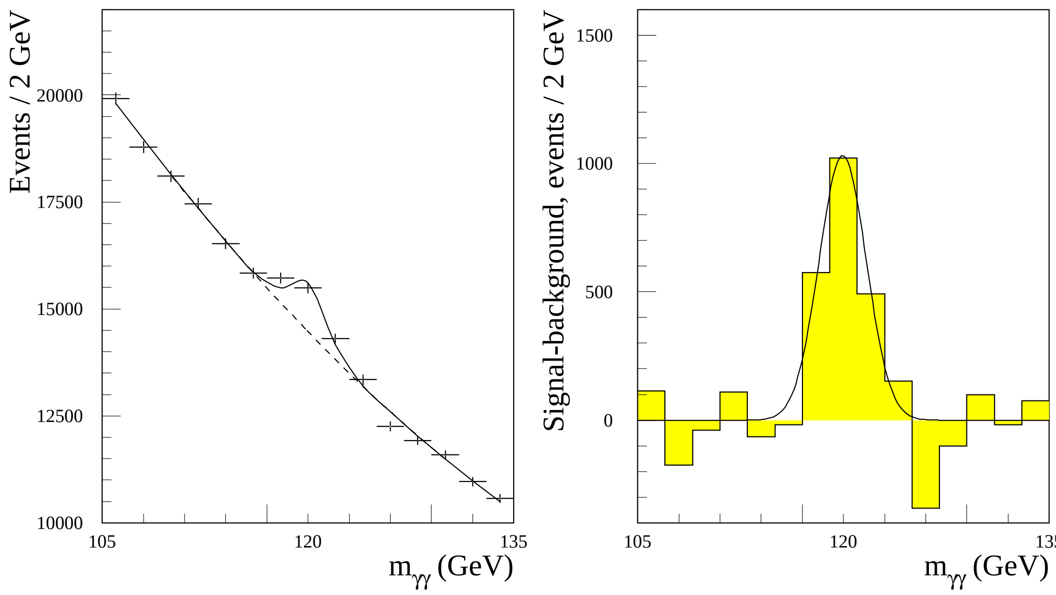

Figure 8.5: This is how a signal from a Higgs boson with mass 120 GeV/c^2 and reconstructed in the H $\rightarrow \gamma\gamma$ decay channel would look like with 100 fb^{-1} of data collected with the ATLAS detector. Left: the signal is on top of the irreducible background from prompt photons. Right: the background has been subtracted.

useful if the Higgs particle is produced together with another particle (W, Z or $t\bar{t}$), that can easily be tagged. Figure 8.5 shows that a typical general purpose detector at LHC (with excellent energy and angular resolution of the electromagnetic calorimeter) should be able to observe a clear Higgs mass peak above the background of the prompt $\gamma\gamma$ continuum if the collider can run for one year at its design luminosity.

8.3 TESLA

If LHC finds the Higgs boson or some other new physics in the energy range up to 1 TeV then very likely the next accelerator to be built will be an e^+e^- linear collider. This machine should then be able to perform precision measurements of the new phenomena in the same way as it was the case with LEP2. At the moment there are several competing projects: TESLA/DESY, JLC/KEK, NLC/SLAC and CLIC/CERN. The main differences are in the type of cavities used (copper versus superconducting), and their operation frequency (from 1.3 to 30 GHz), in the acceleration gradient (24 – 150 MV/m), in the maximum centre-of-mass energy (0.8 – 5 TeV). and in the luminosity (which is a function of the energy). One of the more advanced projects is TESLA. It uses superconducting cavities operating at 1.3 GHz and having an accelerating gradient of 24 MV/m. When running at the maximum energy of 800 GeV a luminosity of $5 \cdot 10^{34}$ cm^{-2}s^{-1} should be achieved. As an example of the superior signal to background ratio of e^+e^- colliders compared to hadron colliders, Figure 8.6 shows an invariant mass distribution of the standard model Higgs boson as expected at TESLA (to be compared to Fig. 8.5).

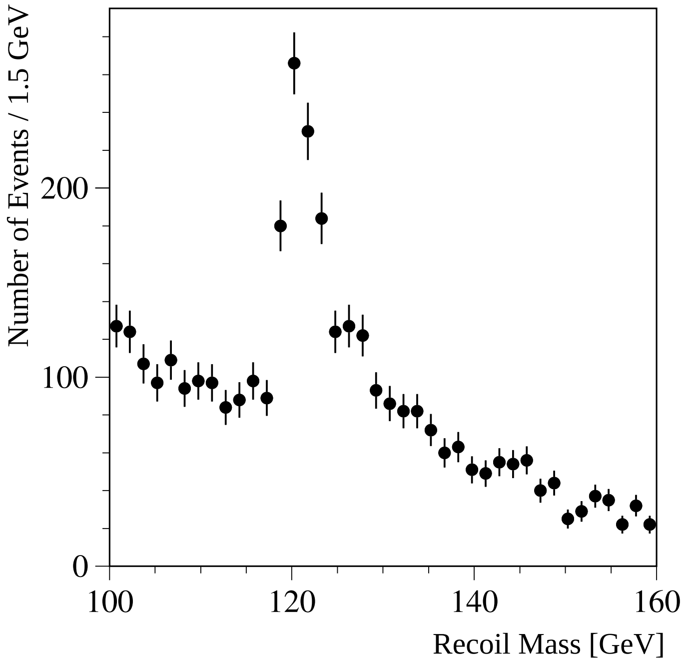

Figure 8.6: This plot [67] shows a simulation of the $\mu^+\mu^-$ recoil mass distribution of background and the signal process $e^+e^- \to HZ \to X\mu^+\mu^-$ for $m_H = 120$ GeV/c^2 with 500 fb^{-1} at $\sqrt{s} = 350$ GeV at the planned TESLA linear collider.

Simply stated, the roadmap for the next two decades is: the hadron colliders should reveal some new physics phenomena so that the next linear collider can be tuned to do precision studies of those new findings.

So when asked: what does "find the Higgs" mean, it should be clear that observing a bump in a $\gamma\gamma$, 4ℓ or $b\overline{b}$ invariant mass distribution is hardly sufficient. The Higgs boson is the agent responsible for electroweak symmetry breaking and fermion mass generation. It has a rich structure that must be confirmed by experiment.

Appendix A

A Higgs Boson Candidate Event

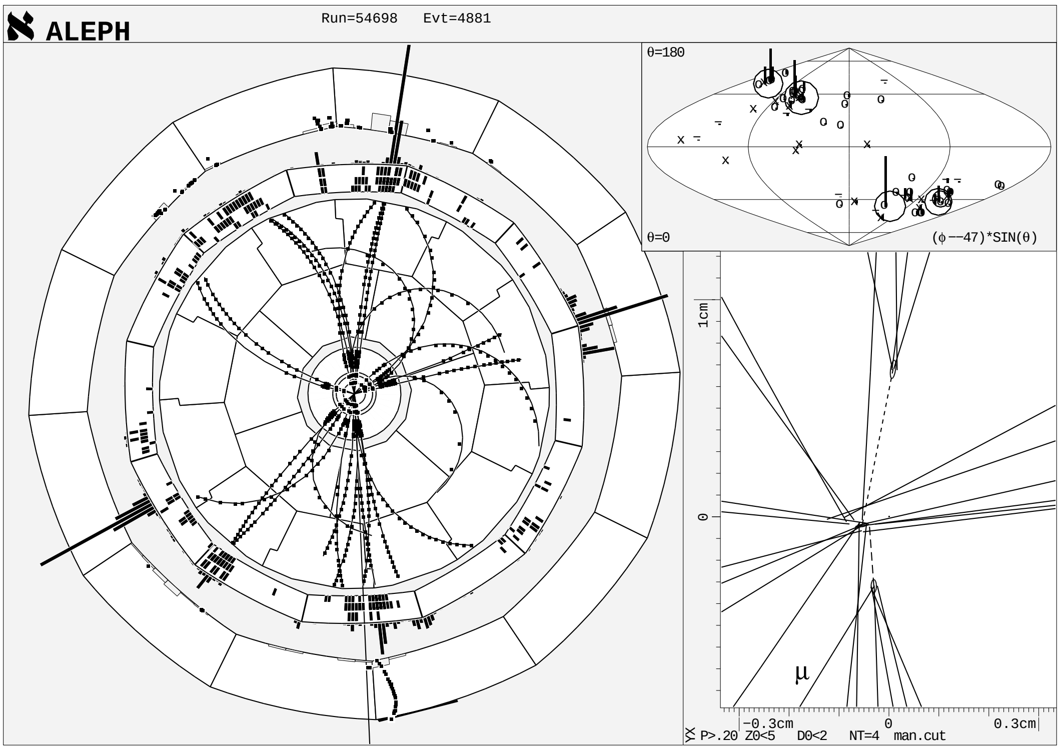

Figure A.1: A Higgs boson candidate event as seen with the ALEPH detector when looking along the beam line. This event has been recorded in the year 2000 (run # 54698, event # 4881) and contributes to the excess of events [51] at a reconstructed Higgs boson mass of $\sim 114\ \mathrm{GeV}/c^2$ observed in the data of that year. It has been selected by the four-jet analysis and can be interpreted as $\mathrm{e^+e^-} \to \mathrm{HZ} \to \mathrm{b\overline{b}q\overline{q}}$, because two of the jets are well b-tagged and the invariant mass of the other two jets is 92.1 GeV/c^2, consistent with m_{Z}. The reconstructed Higgs boson mass of this event is 114.3 GeV/c^2. In the inset shown at the lower right side one can see the two displaced vertices of the b-jets. One of these jets contains an identified muon, which is an indication of a semileptonic B-hadron decay. The inset at the upper right corner shows the energy depositions of the four jets in a so-called world map view (coordinates $\phi\cos\theta, \theta$).

Appendix B

The Waldegrave Challenge

- What is the Higgs boson, and why do we want to find it?
- Whoever answers this on one side of a single sheet of paper will be awarded a bottle of Champagne.

In 1993, the then UK Science Minister, William Waldegrave, issued a challenge to physicists to answer the questions 'What is the Higgs boson, and why do we want to find it?' on one side of a single sheet of paper. Bottles of champagne were awarded to the five winning entries at the annual meeting of the British Association for the Advancement of Science. The following contribution [1] is one of the winning entries (taken from Physics World Vol. 6, # 9).

1. The Higgs Mechanism

Imagine a cocktail party of political party workers who are uniformly distributed across the floor, all talking to their nearest neighbours (Fig. B.1). The ex-Prime Minister

Figure B.1: To understand the Higgs mechanism, imagine that a room full of people quietly chattering is like space filled only with the Higgs field ...

[1] By David Miller, Department of Physics and Astronomy, University College, London, UK.

enters and crosses the room (Fig. B.2). All of the workers in her neighbourhood are strongly attracted to her and cluster round her. As she moves she attracts the people she comes close to, while the ones she has left return to their even spacing (Fig. B.3). Because of the knot of people always clustered around her she acquires a greater mass than normal, that is she has more momentum for the same speed of movement across the room. Once moving she is hard to stop, and once stopped she is harder to get moving again because the clustering process has to be restarted.

Figure B.2:
... a famous person walks in, creating a disturbance as she moves across the room, and attracting a cluster of admirers with each step ...

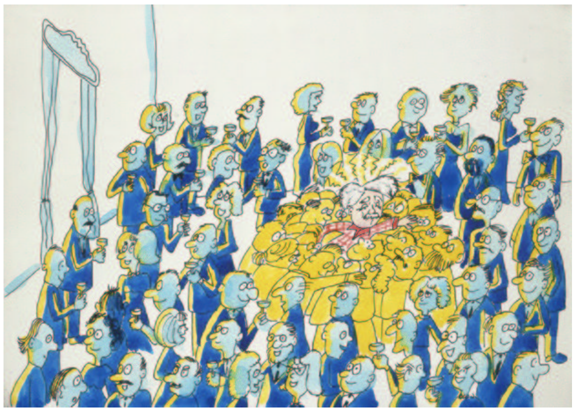

Figure B.3:
... this increases her resistance to movement, in other words, she acquires mass, just like a particle moving through the Higgs field ...

In three dimensions, and with the complications of relativity, this is the Higgs mechanism. In order to give particles mass, a background field is invented which becomes locally distorted whenever a particle moves through it. The distortion - the clustering of the field around the particle - generates the particle's mass. The idea comes directly from the physics of solids. instead of a field spread throughout all space a solid contains a lattice of positively charged crystal atoms. When an electron moves through the lattice the atoms are attracted to it, causing the electron's effective mass to be as much as 40 times bigger than the mass of a free electron.

The postulated Higgs field in the vacuum is a sort of hypothetical lattice which fills our Universe. We need it because otherwise we cannot explain why the Z and W particles which carry the weak interactions are so heavy while the photon which carries electromagnetic forces is massless.

2. The Higgs Boson

Now consider a rumour (Fig. B.4) passing through our room full of uniformly spread political workers. Those near the door hear of it first and cluster together to get the details, then they turn and move closer to their next neighbours who want to know about it too. A wave of clustering passes through the room (Fig. B.5). It may spread to all the corners or it may form a compact bunch which carries the news along a line of workers from the door to some dignitary at the other side of the room. Since the information is carried by clusters of people, and since it was clustering that gave extra mass to the ex-Prime Minister, then the rumour-carrying clusters also have mass.

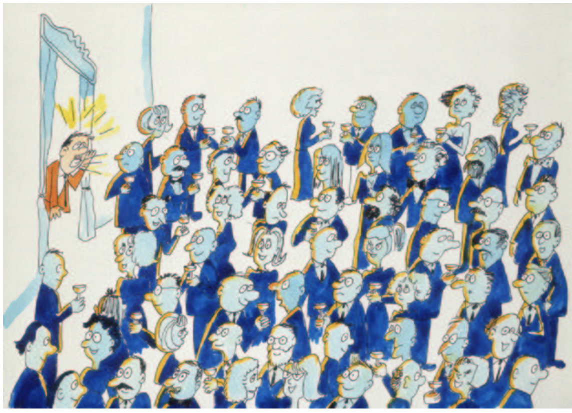

Figure B.4:
... if a rumour crosses the room ...

Figure B.5:
... it creates the same kind of clustering, but this time among the people themselves. In this analogy, these clusters are the Higgs particles.

The Higgs boson is predicted to be just such a clustering in the Higgs field. We will find it much easier to believe that the field exists, and that the mechanism for giving other particles is true, if we actually see the Higgs particle itself. Again, there are analogies in the physics of solids. A crystal lattice can carry waves of clustering without needing an electron to move and attract the atoms. These waves can behave as if they are particles. They are called phonons and they too are bosons.

There could be a Higgs mechanism, and a Higgs field throughout our Universe, without there being a Higgs boson. The next generation of colliders will sort this out.

Bibliography

[1] E. Fermi, Ricerca Scient. 2 (1933) issue 12 and Z. Phys. **88** (1934) 161.

[2] T.D. Lee, C.N. Yang, Phys. Rev. Lett. **4** (1960) 307.

[3] V.D. Barger, R.J.N. Phillips, *Collider Physics*, Frontiers in Physics, Addison-Wessely (1987)

[4] P.W. Higgs, Phys. Lett. **12** (1964) 132, Phys. Rev. Lett. **13** (1964) 508, Phys. Rev. **145** (1966) 1156;
F. Englert, R. Brout, Phys. Rev. Lett. **13** (1964) 321;
G.S. Guralnik, C.R. Hagen, T.W. Kibble, Phys. Rev. Lett. **13** (1964) 585.

[5] S.L. Glashow, Nucl. Phys. **20** (1961) 579;
A. Salam, in *Elementary Particle Theory*, ed. N. Svarthom, 1968;
S. Weinberg, Phys. Rev. Lett. **19** (1967) 1264;
G.'t Hooft, M. Veltman, Nucl. Phys. **44** (1972) 189.

[6] G. t'Hooft, Nucl. Phys. **33** (1971) 173 and Nucl. Phys. **35** (1971) 167.

[7] C.N. Yang, R.L. Mills, Phys. Rev. **96** (1954) 161.

[8] M. Baker, S.L. Glashow, Phys. Rev. **128** (1962) 2462.

[9] J. Goldstone, Nuovo Cim. **19** (1961) 154.

[10] J. Goldstone, A. Salam, S. Weinberg, Phys. Rev. **127** (1962) 965.

[11] F. Halzen, A. Martin, *Quarks and Leptons*, John Wiley & Sons (1984), New York.

[12] For details see, *e.g.* , p. 327 in Ref. [11].

[13] J. Gunion, H.E. Haber, G. Kane, S. Dawson, *The Higgs Hunter's Guide*, Addison Wesely (1990).

[14] For a review on Supersymmetry, see:
J. Wess and J. Bagger, *Supersymmetry and Supergravity*, Princeton Series in Physics.

[15] K. Hagiwara *et al.* (Particle Data Group), *Review of Particle Physics*, Phys. Rev. **D66** (2002) 01001.

[16] T. Hambye, K. Riesselmann, Phys. Rev. **D55** (1997) 7255.

[17] G. Altarelli, G. Isidori, Phys. Lett. **B337** (1994) 141;
J. Casa, J. Espinosa, M. Quiros, Phys. Rev. **B342** (1995) 171.

[18] B. Ioffe, V. Khoze, Sov. J. Part. Nucl. Phys. **9** (1978) 50;
B.W. Lee, C. Quigg, H.B. Thacker, Phys. Rev. **D16** (1977) 1519.

[19] W. Kilian, M. Krämer, P.M. Zerwas, DESY 95-216 (1995) and hep-ph/9512355.

[20] M. Carena, P.M. Zerwas, *Higgs Physics*, in *Physics at LEP2*,
Eds. G. Altarelli, T. Sjöstrand, F. Zwirner, CERN 96-01 (1996), Vol. 1, 351.

[21] M. Spira, P.M. Zerwas, *Electroweak Symmetry Breaking and Higgs Physics*, CERN-TH/97-397, DESY 97-261 and hep-ph/9803257.

[22] ALEPH Collab., D. Decamp *et al.*, *Searches for New Particles in Z Decays Using the ALEPH Detector*, Phys. Rev. **216** (1992) 253.

[23] P. Janot, *The HZHA Generator*, in *Physics at LEP2*,
Eds. G. Altarelli, T. Sjöstrand, F. Zwirner, CERN 96-01 (1996), Vol. 2, 309;
`http://alephwww.cern.ch/~janot/Generators.html`

[24] ALEPH Collab., R. Barate *et al.*, *Search for the Standard Model Higgs Boson in* e^+e^- *Collisions at* $\sqrt{s}$ *= 161, 170 and 172 GeV*, Phys. Lett. **B412** (1997) 155-172.

[25] ALEPH Collab., R. Barate *et al.*, *Search for the Standard Model Higgs Boson at the LEP2 Collider near* $\sqrt{s}$ *= 183 GeV*, Phys. Lett. **B447** (1999) 336-351.

[26] ALEPH Collab., R. Barate *et al.*, *Search for the Neutral Higgs Bosons of the MSSM in* e^+e^- *Collisions at* $\sqrt{s}$ *from 130 to 172 GeV*, Phys. Lett. **B412** (1997) 173-188.

[27] E. Kneringer, *Higgs Searches at LEP2 with the ALEPH Detector*,
in *Electroweak Physics*, Proceedings, Eds. A. Astbury, B.A. Campel, F.C. Khanna, J. Pinfold, M.G. Vincter, World Scientific (2000), 414-421, and hep-ex/0001037.

[28] K. Hübner, private communication

[29] J. D. Jackson, *Classical Electrodynamics*, John Wiley & Sons (1975), ISBN 0-471-43132-X.

[30] ALEPH Collab., D. Decamp *et al.*, *ALEPH: A Detector for Electron–Positron Annihilation at LEP*, Nucl. Instrum. Methods **A294** (1990) 121.

[31] ALEPH Collab., D. Buskulic *et al.*, *Performance of the ALEPH Detector at LEP*, Nucl. Instrum. Methods **A360** (1995) 481.

[32] D. Creanza et al., *The new ALEPH vertex detector*, Nucl. Instrum. Methods **A409** (1998) 157.

[33] E. Kneringer, *String Effect in* $e^+e^- \rightarrow$ *3 Jets at the Z Peak*, Dissertation (1995), Univ. Innsbruck, Austria.

[34] H.E. Haber, G.L. Kane, Phys. Rev. **117** (1985) 75.

[35] *The Standard Model Higgs Boson*, Ed. M.B. Einhorn, North-Holland, Amsterdam (1991).

[36] H. Georgi, H.R. Quinn, S. Weinberg, Phys. Rev. Lett. **33** (1974) 451.

[37] M. Carena, S. Heinemeyer, C.E.M. Wagner, G. Weiglein, *Suggestions for Improved Benchmark Scenarios for Higgs-Boson Searches at LEP2*, CERN-TH/99-374 (1999), DESY 99-186 and hep-ph/9912223.

[38] H.E. Haber, Y. Nir, Nucl. Phys. **B335** (1990) 363.

[39] *Perspectives on Higgs Physics II*, Ed. G.L. Kane, World Scientific (1997).

[40] For a review see:
G.F. Giudice, R. Rattazzi, *Theories with gauge-mediated supersymmetry breaking*, Phys. Rept. **322** (1999) 419;
S. Ambrosanio, G.D. Kribs and S.P. Martin, *Signals for gauge-mediated supersymmetry breaking models at the CERN LEP2 collider*, Phys. Rev. **D56** (1997) 1761.

[41] H.P. Nilles, *Supersymmetry, supergravity and particle physics*, Phys. Rev. **110** (1984) 1.

[42] B. Schrempp, M. Wimmer, Prog. Part. Nucl. Phys. **37** (1996) 1.

[43] The LEP Working Group for Higgs boson searches, *Search for the Standard Model Higgs Boson at LEP*, CERN-EP/2003-11 (2003), submitted to Phys. Lett. B.

[44] See Table 2 in Ref. [43].

[45] The LEP Working Group for Higgs boson searches, *Lower bound for the SM Higgs boson mass: combined result from the four LEP experiments*, CERN/LEPC 97-11, LEPC/M 115 (1997).

[46] The LEP Working Group for Higgs boson searches, *Lower bound for the Standard Model Higgs boson mass from combining the results of the four LEP experiments*, CERN-EP/98-046 (1998).

[47] A. Read, *Modified Frequentist Analysis of Search Results (The* $\mathrm{CL_s}$ *Method* in Workshop on Confidence Limits, eds. F. James, L. Lyons and Y. Perrin, CERN 2000-05 (2000) 81-99.

[48] S. Brandt, *Statistical and Computational Methods in Data Analysis*, North-Holland Publishing Company (1970).

[49] S.L. Meyer, *Data Analysis for Scientists and Engineers*, John Wiley & Sons (1975), ISBN 0-471-59995-6.

[50] S. Baker and R. Cousins, *Clarification of the Use of Chi-Square and Likelihood Functions in Fits to Histograms*, Nucl. Instrum. Methods **221** (437) 1984.

[51] ALEPH Collab., R. Barate *et al.*, *Observation of an Excess in the Search for the Standard Model Higgs Boson at ALEPH*, Phys. Lett. **B495** (2000) 1-17.

[52] G. Altarelli, *Precision Tests of the Standard Model: Theory*, Proceedings of the International Europhysics Conference on High Energy Phsics, Eds. J. Carr, M. Perrottet, Edition Frontieres (1994), 689-698.

[53] C. Quigg, *The State of the Standard Model*, hep-ph/0001145 (2000) p.8.

[54] A. Sirlin, Phys. Rev. **D22** (1980) 2695.

[55] W. Hollik, *Precision Tests of Electroweak Theory* in CERN Yellow Report 91-07 (1991) 50-102.

[56] D. Bardin *et al.*, *ZFITTER - A Semi-Analytical Program for Fermion Pair Production in* $\mathrm{e^+e^-}$ *Annihilation*, Comp. Phys. Comm. **133** (2001) 229 and hep-ph/9908433.

[57] F. Jegerlehner, *Renormalizing the Standard Model*, published in "Testing the Standard Model", p.476-590, TASI 1990, Eds. M. Cvetič, P. Langacker, World Scientific (1991); see also `http://www-zeuthen.desy.de/theory/fj/doc/tasi.ps.gz`.

[58] M. Veltman, Nucl. Phys. **B123** (1977) 89.

[59] D. Abbaneo *et al.* (LEP Electroweak Working Group), *A Combination of Preliminary Electroweak Measurements and Constraints to the Standard Model*, CERN-LEPEWWG/97-01, CERN-LEPEWWG/2003-01, `http://cern.ch/LEPEWWG`

[60] J.F. de Troconiz, F.J. Yndurain, Phys. Rev. **D65** (2002) 093002.

[61] G. Montagna *et al.*, *TOPAZ0 version 4.0i*, Nucl. Phys. **B401** (1993) 3.

[62] *The Run II Luminosity Upgrade at the Fermilab Tevatron*, (2003) `http://www.fnal.gov/pub/now/upgradeplan/`.

[63] F. Abe *et al.*, *Search for Higgs Bosons Produced in Association with a Vector Boson in* $\mathrm{p\overline{p}}$ *Collisions at* $\sqrt{s}$ *= 1.8* TeV, Phys. Rev. Lett. **81** (1998) 5748-5743.

[64] M. Kruse *et al.*, *Combined Standard Model VH production cross section limits for Run 1 at CDF*, CDF note 4985 (2000).

[65] M. Carena, J.S. Conway, H.E. Haber, J.D. Hobbs, *Report of the Tevatron Higgs Working Group*, Fermilab-Conf-00/279-T (2000) and hep-ph/0010338.

[66] *ATLAS Detector and Physics Perfomance – Technical Design Report*, Volume 2, ATLAS TDR 15, CERN/LHCC 99-15 (1999).

[67] *TESLA – Technical Design Report*, Part III, DESY 2001-011 (2001).